HYDRODYNAMIC ANALYSIS OF THE MOMENTUM-REVERSAL AND LIFT TIDAL TURBINE

Submitted by

Matthew James Berry

to the University of Exeter
as a thesis for the degree of
Doctor of Philosophy in Engineering
January 2017

I certify that all material in this thesis which is not my own work has been identified and that no material has previously been submitted and approved for the award of a degree by this or any other University.

Signature: .....

This page is intentionally left blank.

ABSTRACT

Tidal energy has the potential to make a valuable contribution to meeting future global energy demands. Converting the energy of tidal streams into useful electricity can be achieved with use of tidal-stream turbines, such as the Momentum-Reversal and Lift (MRL) device. This turbine utilises a blade motion where each blade rotates continuously through 180° about its own axis for every 360° of turbine rotation. The aim of the design is to harness both useful lift and drag forces when rotating at relatively slow speeds. However, no detailed analysis of the time-varying fluid dynamic behaviour of the turbine has been undertaken before this study.

The primary aim of this study has been to further understanding of the performance characteristics of the MRL turbine design, focusing on a laboratory-scale device. The study has analysed both the time-averaged and time-varying torque and power output, and the associated fluid-dynamic structure of flow through the turbine. A secondary aim was to generate data that can be used by other researchers who focus on the wake generation of the MRL tidal turbine.

This study has used OpenFOAM to develop a time-dependent RANS CFD model and investigate the performance of the MRL turbine. To allow validation of the CFD model, experiments were firstly undertaken in order to measure the cycle-mean torque and power output of the turbine when operating in a laboratory flume. Measurements of the flow velocity at a number of upstream and downstream locations were also taken, in order to allow comparison with the CFD simulation results, where appropriate.

Also, in order to allow validation of the CFD approach against time-varying data, the motion of the turbine blades was analysed. This allowed suitable experimental test cases to be identified from the literature and CFD simulation results have been compared to these.

A detailed sensitivity analysis of the MRL turbine CFD model was carried out, followed by two-dimensional simulations of the turbine involving a single-blade and three-blades. Three-dimensional simulations were also undertaken, with results compared to the gathered experimental results. Finally, the effect of varying turbine solidity was investigated with the CFD model.

Overall it was found that the CFD simulations successfully reproduce the rotational speed at which maximum torque and power are developed. However, the three-dimensional simulations significantly over-predict the magnitude of results in comparison to the gathered experimental results. Regardless, the two- and three-dimensional simulations have allowed detailed analysis of the flow behaviour and structures that are responsible for the development of blade forces and turbine torque.

ACKNOWLEDGEMENTS

This thesis represents a long, often difficult but ultimately rewarding journey and I would like to thank a number of people who have made it possible.

Thank you to my primary supervisor, Prof. Gavin Tabor for both his technical advice and feedback on the work undertaken, and for the patient and considerate support throughout. Also, thank you to my second supervisor, Prof. Lars Johanning, for his feedback on the completed thesis.

I would like to thank the staff at the University of Exeter, especially Rob O'Neale and Ian Moon who have provided computing and laboratory technical support respectively. I would also like to thank Prof. Mike Belmont of the University of Exeter and Prof. Deborah Greaves of Plymouth University for arranging access to the COAST laboratory.

For funding this study I would like to thank both the Kirby Laing Foundation and the Engineering and Physical Sciences Research Council.

Personal thanks must go to Rebecca Head, who gave me such support throughout my time in Exeter. Finally, thank you to my parents John and Gillian for their love and support, always.

This page is intentionally left blank.

CONTENTS

LIST OF FIGURES

LIST OF TABLES

This page is intentionally left blank.

LIST OF NOTATION

a	Flow induction factor
a_1	$k-\omega$ SST dimensionless constant
A_c	Cross-sectional area of channel
A_D	Empirical constant in static-plate drag coefficient correlation
a_d	Radius of turbine toothed timing-disk
a_e	Radius of turbine end-plate
A_{F_D}	Coefficient of turbine drag torque
A_{F_L}	Coefficient of turbine lift torque
a_h	Radius of turbine pulley-housing
A_i	Frontal area of turbine component i
a_i	Radius of turbine component i
A_L	Empirical constant in static-plate lift coefficient correlation
a_s	Radius of turbine spindle
B	Channel blockage ratio
B_D	Empirical constant in pitching-plate drag coefficient correlation
B_L	Empirical constant in pitching-plate lift coefficient correlation
C	CFD $k-\omega$ SST blended arbitary constant
c	Blade chord length
C_1	Wilcox $k-\omega$ arbitary constant
c_1	Moment coefficient laminar flow constant
C_2	Menter transformed $k-\varepsilon$ arbitary constant
c_2	Moment coefficient turbulent flow constant

C_D	Hydrodynamic drag coefficient
$C_{Dg,i}$	Drag coefficient of translating turbine component i
$CD_{k\omega}$	$k-\omega$ SST limited cross-diffusion term
$C_{Dr,i}$	Drag coefficient of rotating cylindrical surface of turbine component i
C_λ	Universal threshold coefficient
C_L	Hydrodynamic lift coefficient
$C_{M,i}$	Moment coefficient of rotating disk face of turbine component i
Co	Courant number
C_P	Turbine power coefficient
C_Q	Turbine torque coefficient
$C_{T,x}$	Turbine thrust coefficient (x-direction)
$C_{T,z}$	Turbine thrust coefficient (z-direction)
D	Turbine swept frontal height
D_a	Diameter of turbine bush shaft
D_b	Diameter of turbine blade shaft
D_c	Diameter of turbine central shaft
D_H	Hydraulic diameter of tunnel or channel
D_i	Diameter of turbine component i
D_m	Diameter of turbine bearing mount
E	Wall roughness parameter
F_1	$k-\omega$ SST blending function
F_2	$k-\omega$ SST blending function
F_D	Hydrodynamic drag force acting on turbine blade
$F_{Dg,i}$	Drag force acting on translating turbine component i
F_L	Hydrodynamic lift force acting on turbine blade
F_N	Force acting on turbine blade in direction normal to motion
F_T	Force acting on turbine blade in direction tangential to motion

F_x	Force acting on turbine blade in x-direction
F_z	Force acting on turbine blade in z-direction
g	Acceleration due to gravity
G_k	Generation of TKE per unit mass
$\tilde{G}_k$	Limited value of G_k
h	Blade central thickness
K	Reduced frequency of rotation
k	Turbulent kinetic energy per unit mass
k_{amb}	$k-\omega$ SST sustain ambient k value
k_{inlet}	k value at computational domain inlet
k_{TI}	Tolerance interval factor
l_b	Blade length or span
l_{char}	Characteristic length of body
l_e	Width of turbine end-plate
l_h	Width of turbine pulley-housing
l_i	Length or width of turbine component i
l_m	Width of turbine bearing mount
l_{mix}	Turbulent eddy mixing length
l_s	Length of turbine spindle
m	Load mass in turbine resistance characterisation experiment
n	Total number of turbine blades
$\mathbf{n}$	Surface normal vector
$\bar{N}$	Sample mean of value N
N_{da}	Rotary damper rotational speed (RPM)
N_t	Turbine rotational speed (RPM)
N_i	Rotational speed of turbine component i (RPM)
n_p	Total number of population variables

n_s	Total number of sampled variables
S_N	Sample standard deviation of value N
P	Turbine power
p	Static pressure of fluid
P_F	Flume pump power setting
q	Tolerance interval proportion of population
R	Darrieus turbine radius
R_b	Radius from turbine centre to blade centre
Re_c	Chord-based Reynolds number
$Re_{D,i}$	Linear Reynolds number for turbine component i
$Re_{\omega,i}$	Rotational Reynolds number for turbine component i
R_i	Radius of revolution of turbine component i
r_p	Rotary damper system pulley ratio
S	Invariant strain rate
s_e	Spacing from turbine end-plate to frame
s_h	Spacing from turbine pulley-housing to frame
s_i	Spacing from wall for turbine component i
$s_{i,j}$	Rate of strain tensor
t	Time
T_1	Turbine resistance torque due to rotary damper pulley system
T_2	Turbine resistance torque due to mechanical forces acting on rotating components
T_3	Turbine resistance torque due to hydrodynamic drag acting on rotating surfaces
T_4	Turbine resistance torque due to hydrodynamic drag acting on translating components
$T_{be,i}$	Resistance torque due to bearing friction acting on turbine component i
$T_{b,p}$	Driving torque acting on a single blade due to pressure forces

$T_{b,v}$	Driving torque acting on a single blade due to viscous forces
$T_{C,i}$	Resistance torque due to skin friction acting on cylindrical surface of turbine component i
T_d	Turbine driving torque
T_{da}	Rotary damper resistance torque
$T_{D,i}$	Resistance torque due skin friction acting on disk surface of turbine component i
$T_{E,i}$	Resistance torque due to drag acting on translating turbine component i
T_{F_D}	Turbine driving torque due to drag forces acting on blades
T_{F_L}	Turbine driving torque due to lift forces acting on blades
Ti	Turbulence intensity
T_l	Load torque in turbine resistance characterisation experiment
T_p	Resistance torque due to blade-pitch-control pulley system
T_r	Turbine total resistance torque
$T_{s,i}$	Resistance torque due to radial lip seal acting on component i
$\mathbf{u}$	Computational flow velocity vector
U	Experimental flow velocity (x-direction component)
u	Computational flow velocity (x-direction component)
U_0	Free-stream inflow velocity (x-direction component)
U_1	Inflow velocity local to blade (x-direction component)
U_b	Blade velocity (x-direction component)
u_{cell}	Fluid velocity at computational cell
U'	Turbulent velocity fluctuation (x-direction component)
U_i	Linear velocity of turbine component i
u_{inlet}	u value at computational domain inlet
u^+	Dimensionless velocity tangential to wall
U_R	Relative flow velocity magnitude

u_τ	Friction velocity
V	Experimental flow velocity (y-direction component)
v	Computational flow velocity (y-direction component)
V_0	Free-stream inflow velocity (y-direction component)
V'	Turbulent velocity fluctuation (y-direction component)
v_{inlet}	v value at computational domain inlet
Vo	Vorticity
W	Experimental flow velocity (z-direction component)
w	Computational flow velocity (z-direction component)
W_0	Free-stream inflow velocity (z-direction component)
W_b	Blade velocity (z-direction component)
W'	Turbulent velocity fluctuation (z-direction component)
w_{inlet}	w value at computational domain inlet
x_{max}	x co-ordinate of computational domain outlet boundary
x_{min}	x co-ordinate of computational domain inlet boundary
x_p	Distance from leading edge to plate/blade pitching axis
y_b	y co-ordinate of blade tip
y_{max}	y co-ordinate of computational domain front boundary
y^+	Dimensionless distance perpendicular to wall
Z_d	Number teeth on damper pulley
z_{max}	z co-ordinate of computational domain top boundary
z_{min}	z co-ordinate of computational domain bottom boundary
Z_t	Number teeth on turbine pulley
α	Blade angle of attack to relative inflow direction
α_ω	$k-\omega$ SST dimensionless constant
β	Angle between blade chord-line and x-axis
β^*	$k-\omega$ SST dimensionless constant

β_ω	$k-\omega$ SST dimensionless constant
Γ	Tolerance interval confidence level
γ	Angle between relative flow velocity and x-axis
δ	Boundary layer thickness
$\Delta\alpha$	Angle of attack change per computational time-step
$\Delta\theta$	Angular rotation per computational time-step
δ_{ij}	Kronecker delta
ΔS	Computational cell spacing (general)
ΔS_c	Surface-parallel cell spacing at blade chord-centre
ΔS_n	Surface-normal cell spacing at blade wall
ΔS_r	Cell spacing at rotor mesh boundary
ΔS_t	Surface-parallel cell spacing at blade tip
Δt	Computational time-step
ε	Dissipation rate of TKE per unit mass
ζ	Critical value of normal distribution
η_p	Efficiency of rotary damper pulley system
θ	Turbine rotor angle
κ	von Karman constant
λ_U	Universal threshold of variable U
μ	Dynamic viscosity of fluid
ν	Kinematic viscosity of fluid
ν_t	Turbulent eddy viscosity
ρ	Density of fluid
σ	Turbine solidity
σ_k	Turbulent Prandtl number
σ_U	Population standard deviation of variable U
σ_ω	Turbulent Prandtl number

τ_{ij}	Reynolds stress tensor
τ_{wall}	Wall shear stress
υ	Distance from computational cell to nearest wall
χ^2	Chi squared distribution value
ω	Turbulent frequency per unit mass
ω_0	Turbine rotational velocity
ω_{amb}	$k-\omega$ SST sustain ambient ω value
ω_i	Rotational velocity of turbine component i
ω_{inlet}	ω value at computational domain inlet
ω_{wall}	ω value at wall boundary
2D	Two-dimensional
3D	Three-dimensional
ACW	Anti-clockwise
ADV	Acoustic Doppler velocimetry
AMI	Arbitrary mesh interface
AOA	Angle of attack
AR	Aspect ratio
BEM	Blade element and momentum
BL	Baldwin-Lomax
BSR	Blade-speed-ratio
CCM	Computational continuum mechanics
CFD	Computational fluid dynamics
COAST	Coastal, ocean and sediment transport
CV	Control volume
CW	Clockwise
DES	Detached eddy simulation
DNS	Direct numerical simulation

FVM	Finite volume method
GHG	Greenhouse gas
GUI	Graphical user interface
HAWT	Horizontal-axis wind turbine
IBF	Immersed boundary force
IEA	International energy agency
IFREMER	Institut français de recherche pour l'exploitation de la mer
IPCC	Intergovernmental panel on climate change
LES	Large eddy simulation
LEV	Leading edge vorticity
LGV	Last good value
MAD	Mean absolute deviation
MITT	Multi-instrument turbulence toolbox
mPST	Modified phase-space threshold
MRL	Momentum-reversal and lift
NACA	National advisory committee for aeronautics
NREL	National renewable energy laboratory
NS	Navier-Stokes
OpenFOAM	Open source field operation and manipulation
PIMPLE	Combination of SIMPLE and PISO algorithms
PISO	Pressure implicit with splitting of operators
PIV	Particle image velocimetry
PSD	Power spectral density
PST	Phase-space threshold
RAM	Random access memory
RANS	Reynolds-averaged Navier-Stokes
RNG	Re-normalisation group

RPM	Revolutions per minute
SA	Spalart-Allmaras
SAS	Scale adaptive system
SIMPLE	Semi-implicit method for pressure-linked equations
SNR	Signal to noise ratio
SST	Shear-stress-transport
TEV	Trailing edge vorticity
TI	Tolerance interval
TKE	Turbulent kinetic energy
TSR	Tip-speed-ratio
TVR	Turbulent viscosity ratio
TV	Tolerance value
UAE	Unsteady aerodynamics experiment
URANS	Unsteady Reynolds-averaged Navier-Stokes
VAWT	Vertical-axis wind turbine

CHAPTER 1

INTRODUCTION

1.1 General Introduction to Tidal Stream Energy

1.1.1 The need for renewable energy

"*Warming of the climate system is unequivocal, and since the 1950s, many of the observed changes are unprecedented over decades to millennia. The atmosphere and ocean have warmed, the amounts of snow and ice have diminished, and the sea level has risen."*

This is one of the key findings from the Fifth Assessment Report of the Intergovernmental Panel on Climate Change (IPCC) *(Pachauri et al., 2014)*. Whilst the observed changes may be due to both natural and anthropogenic drivers, the IPCC report states that *"it is extremely likely that more than half of the observed increase in global average surface temperature from 1951 to 2010 was caused by the anthropogenic increase in greenhouse gas (GHG) concentrations and other anthropogenic forcings together".*

The impacts of a changing climate are wide ranging and varied, and the report states that *"in recent decades, changes in climate have caused impacts on natural and human systems on all continents and across the oceans." Furthermore, "continued emission of greenhouse gases will cause further warming and long-lasting changes in all components of the climate system, increasing the likelihood of severe, pervasive and irreversible impacts for people and ecosystems. Limiting climate change would require substantial and sustained reductions in greenhouse gas emissions which, together with adaptation, can limit climate change risks."*

Greenhouse gases include carbon dioxide (CO_2), methane and nitrous oxide, with emissions of the former contributing approximately 78% to the total GHG emission increase between 1970 and 2010 *(Pachauri et al., 2014).* Demand for energy, derived from the combustion of fuel, is the primary human activity responsible for production of CO_2 emissions, representing 61% of global GHG emissions in 2010. The uses of this energy are varied, although the greatest contribution currently comes from fuel combustion for providing electricity and heat (42% in 2014), with the primary energy sources being the fossil fuels coal, oil and gas (IEA, 2016a).

It is clear that in order to limit the risks posed by future climate warming, the use of fossil fuels for producing energy needs to be heavily reduced. However, total energy demand is highly likely to increase in the coming decades, with predicted global population and economic growth, and therefore alternative non-fossil fuel sources of energy are required. These alternatives can be broadly divided into biofuels, nuclear energy, hydro-electric and other renewables. These sources currently contribute about 19% of the world total energy supply, with biofuels (10.3%) and nuclear (4.8%) contributing the majority of this in 2014 (IEA, 2016b). However, these two energy sources provide their own problems, such as the conflict of land use for growing biofuels versus food, and the long-term safety and cost implications of storing nuclear waste.

Therefore, the increasing use of hydro-electric and other renewable energy sources, such as solar, wind, tidal and wave, is crucial. As the harnessing of renewable energy is typically more local than the purchase and import of fossil fuels, its use also increases energy security, and is not subject to future price increases due to depleting levels of fossil fuels.

The net installed capacity of renewables grew by 153 GW in 2015 (IEA, 2016c), which was over 50% of the total new capacity for the first time, showing that the use of renewables is increasing. The majority of new installations were photovoltaic solar panels and on-shore wind turbines, which have benefited from decreases in generation costs of up to 65% and 30% respectively since 2010 (IEA, 2016c). In the near future, it is likely the costs of these technologies will continue to fall and the number of installations will continue to rise. However, it should be noted that the suitability of these technologies is location specific, depending on the availability of resource. It is therefore important that a range of solutions for harnessing renewable energy continue to be developed, as

future global energy demand will likely need to be met by using a wide range of sources.

1.1.2 The case for tidal stream energy conversion

In comparison to the number of solar panels and wind energy turbines installed worldwide, the harnessing of tidal energy for electricity production is extremely limited at present. This is despite some clear advantages of tidal energy, such as reliability of resource (tides flood and ebb at predictable times twice each day) and the increased energy density of water compared to air.

The method of tidal energy conversion can generally be classified into two types: tidal range and tidal stream (or tidal current).

The former involves barrages that constrain the flow of water as the tide flows, before releasing the water through turbines and converting the stored potential energy into kinetic energy. The world's first large-scale tidal barrage began operating in 1966 in the Rance estuary, France and further power stations currently operate in Canada, Russia, South Korea and the Netherlands (O Rourke et al., 2010). However, this type of technology can pose significant risks to the local environment, such as silting of estuaries and impacts on marine ecosystems due to altered tidal ranges.

The second type of tidal energy technology solely relies on the kinetic energy of tidal currents, rather than potential energy of stored water. There is no requirement for a tidal barrage to be built, as the turbines are located directly in the tidal stream. This has the potential to significantly reduce construction costs and the environmental impact in comparison to tidal barrages. However, in order for current turbine technologies to operate effectively, significant peak tidal velocities of at least 1 m/s are typically required. Therefore potential locations for deployment are generally limited to estuaries and straits, where currents are accelerated by limited channel depths and/or widths. It is also important to note that in order to generate a significant amount of grid electricity from a particular tidal installation, a large number of turbines are required, similar to farms of wind turbines. Despite these limitations, the UK has a number of particularly suitable sites for tidal stream turbine farms, including the Pentland Firth between the Orkney Isles and mainland Scotland. Here tidal currents can exceed 5 m/s and recent studies have estimated that 1.9 GW of power,

averaged over the spring-neap tidal cycle, can be generated (Adcock et al., 2013). This is a significant amount of energy, and indicates the potential for tidal stream turbine deployment in the UK.

However, at present the cost of tidal stream turbine deployment is higher than other renewable technologies, in part due to the technological challenges associated with harsh marine environments. Until recently, the only grid-connected commercial-scale turbine in operation has been the Marine Current Turbines SeaGen device at Strangford Lough in Northern Island. This 1.2 MW device utilises two axial flow turbines (described in the following section) mounted on a single column and was installed in 2008. More recently, in 2016, a single 1.5 MW Atlantis MeyGen turbine (also axial-flow design) has been installed in the Pentland Firth, which is the first of a planned 269 devices, capable of generating 400 MW of electricity.

Although commercial deployment of tidal stream turbines is still at a relatively early stage, the field has attracted a significant amount of academic attention in the past decade. Studies have focused on a range of areas, at a number of different scales. These range from the analysis of tidal resources, to the impact of tidal farms on the environment, the interaction between multiple turbines in an array, the wake of individual turbines and the design of individual devices (Laws and Epps, 2016). It is the latter that this work focuses on, as described in the following sections.

1.2 Designs of Renewable Energy Turbines

Tidal stream turbine devices, both currently deployed and in development, are typically one of two types: axial flow or cross flow, which describes the direction of the incoming flow relative to the turbine axis of rotation. Diagrams of typical cross-flow and axial-flow turbine designs are shown in Figure 1.2.1. The working principles of these designs are the same as existing wind energy turbines, which is a much more mature field. Therefore, the following discussion of turbine designs refers to both wind and tidal energy devices in order to provide a broad overview.

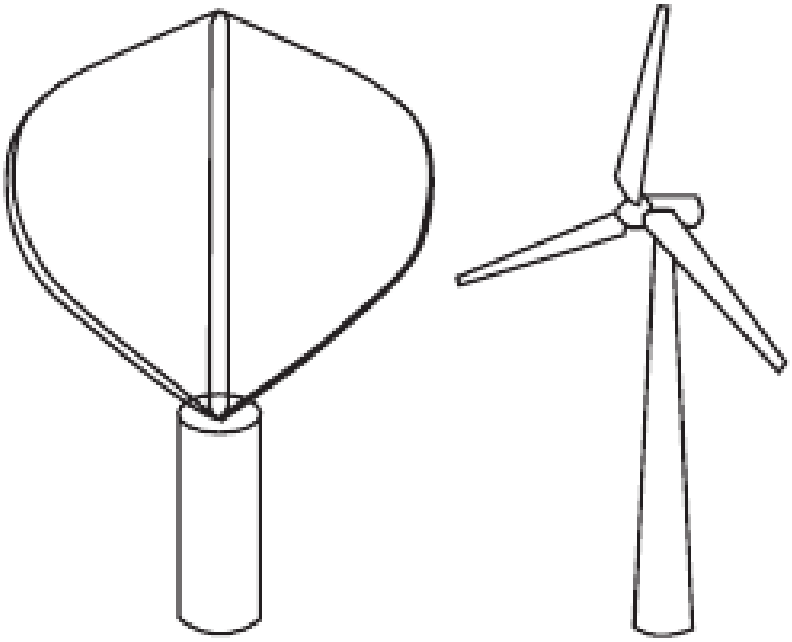

(a) Diagrams (MacPhee and Beyene, 2012)

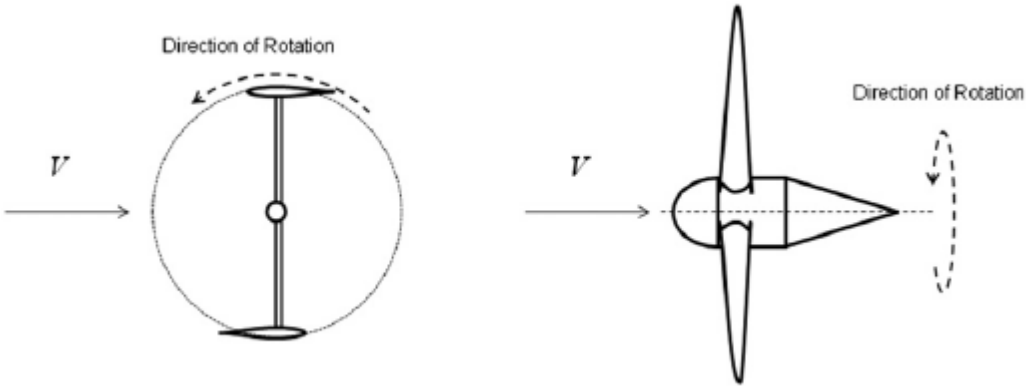

(b) Cross sectional views (Urbina et al., 2013)

Figure 1.2.1: Examples of cross-flow (left) and axial-flow (right) turbine designs

1.2.1 Brief history of renewable turbine design

Renewable energy turbines are not a new concept, with 'Panemone' cross-flow vertical-axis wind turbines (VAWTs) having been used as early as 900AD in Persia and axial-flow horizontal-axis wind turbines (HAWTs) used throughout Europe in the Middle Ages (Manwell et al., 2010).

In comparatively modern times, one of the most important early turbines was developed by Marcellus Jacobs in the early 1920's. In contrast to the traditional 'Dutch' or 'American' windmill-fan rotors, he developed a HAWT with aerofoil-section blades, in order to harness lift and achieve a faster rotational speed, suitable for generating electricity.

Key cross-flow turbine designs were developed by Sigurd Savonius, who patented a drag driven VAWT in 1929 (Savonius, 1929), and Georges Darrieus, who patented his troposkein, or 'egg-beater' shaped, lift driven VAWT in 1931 (Darrieus, 1931). The design of these turbines are discussed further in the following sections.

During the 1970s and 1980s, research and investment of wind turbine development increased, mainly driven by the dramatic increase in oil price in 1973, as discussed by Burton et al. (2011). This research covered both axial and cross-flow designs, with VAWT research in particular taking place at Sandia National Laboratories in the USA, where large scale prototype Darrieus turbines were built and tested (Worstell, 1979; 1980). However, interest and investment in VAWT development never matched that of HAWTs, with a number of factors in favour of the latter. These included their similarity with aircraft rotors, for which there were already established design tools in use during this period. Also, the nature of VAWTs means the rotor torque oscillates during each rotation, due to the constantly varying angle of attack of each blade, whereas HAWT blades are designed to ideally provide a constant rotor torque. This made HAWTs more attractive to develop, resulting in them being the most technologically advanced and widely used design today. In modern large off-shore wind farms, HAWT rotors can reach diameters of over 100 m with typical rated powers in excess of 6-8 MW.

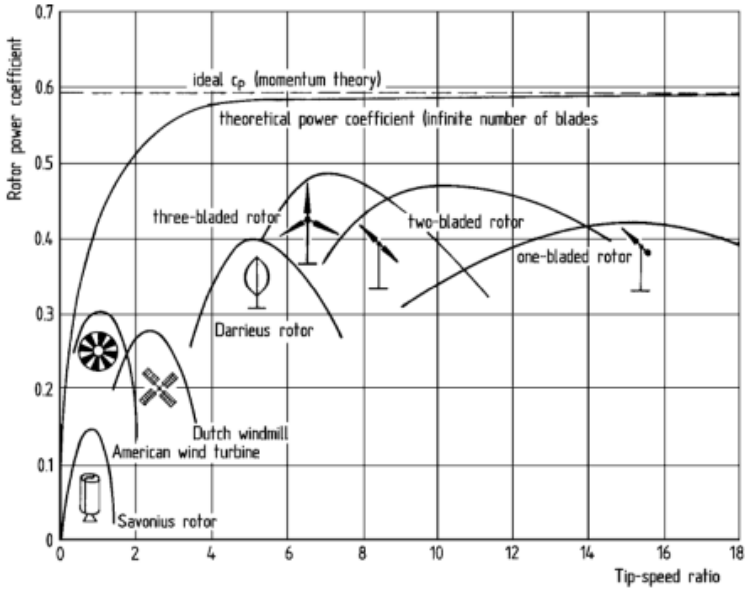

Figure 1.2.2: Typical power coefficient curves for various designs of axial- and cross-flow turbines (Hau, 2013)

1.2.2 Advantages of cross-flow designs

Modern three-blade HAWTs typically operate with power coefficients in the range of $C_P = 0.4 - 0.5$ (with the theoretical Betz limit set at 0.59) (Manwell et al., 2010), as indicated in Figure 1.2.2. However, Darrieus-type VAWTs have also been shown to operate at a peak efficiency of $C_P = 0.4$ and Paraschivoiu (2002) claims that the performance deficit of VAWTs compared to HAWTs is not as great as generally perceived.

Eriksson et al. (2008) evaluates the relative advantages of axial-flow and cross-flow wind turbine designs and concludes that the VAWT has many advantages over the HAWT, including lack of yaw error, simpler nacelle-less designs, smaller operational space and quieter operation. However, it is noted that a major disadvantage of VAWTs is the inability to self-start.

Research into the further development of VAWTs has increased over the past decade (MacPhee and Beyene, 2012) and their use is becoming more popular in certain applications, such as small-scale rotors for use in urban environments (Balduzzi et al., 2012; Tummala et al., 2016) and remote locations (Aslam Bhutta et al., 2012).

Regarding tidal energy turbines, the two grid connected devices currently in operation are both axial-flow design. One of the primary reasons may be that

these turbines are proven technology (in the wind energy sector) and their use presents lower risk to investors. However many alternative types of tidal turbine design have been researched in the past decade, including cross-flow designs (Khan et al., 2009; Lago et al., 2010).

The cross-flow design has the added advantage of orientation flexibility, i.e., the axis can be orientated vertically (as with most cross-flow wind turbines) or horizontally. The former potentially allows the generator mechanism to located above the water surface (Güney and Kaygusuz, 2010), while the latter allows both ends of the turbine to be moored, either to the sea bed or from a floating support, increasing structural stability. Both options allow the total capacity of the turbine to be increased by increasing the span, i.e., length of the turbine, rather than the overall diameter. When orientated horizontally, the turbines can therefore be located in relatively shallow water, and this potentially increases the extent of exploitable tidal resource.

1.2.3 Design of Darrieus turbines

Darrieus turbines, and related designs, generate torque due to the development of lift and drag forces acting on the blades as they pass through the incoming flow. The combination of the incoming flow velocity, and the relative motion of the blade through the flow, results in a resultant velocity magnitude acting on the blade, at a resultant angle of attack to the chord line. In standard Darrieus turbines, the orientation of each blade is fixed in relation to the turbine central axis i.e., the blade chord is always orientated tangentially to the turbine circumference. This results in continual variation of the resultant blade angle of attack as the turbine rotates. As lift and drag forces developed by foils vary with angle of attack, so does the torque developed about the turbine central axis.

Like axial-flow turbines, the operating speed of Darrieus turbines are usually represented by the tip-speed-ratio (TSR), as defined by:

$$TSR = \frac{\omega_0 R}{U_0} \tag{1.2.1}$$

where ω_0 is the turbine rotational velocity, R is the radius of blade path and U_0 is the incoming flow velocity. Darrieus turbines typically operate with TSR values in the range of $TSR = 3-7$ as here the resultant angle of attack typically varies

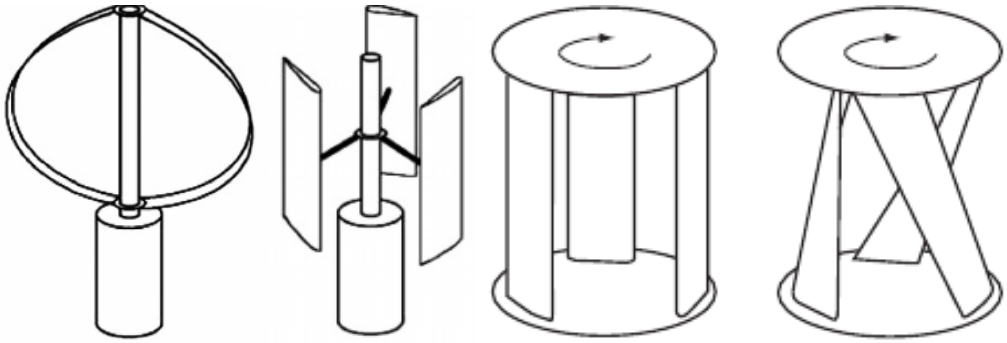

Figure 1.2.3: Typical variations of Darrieus turbines (from left to right): Troposkein, H-Darrieus, Caged and Gorlov (MacPhee and Beyene, 2012)

up to only 18° (Kirke and Lazauskas, 2011). Here foils typically operate in a pre-stall region, and lift forces dominate over drag. If the blades stall, lift suddenly reduces and drag dominates, which produces high levels of parasitic torque acting in the opposite direction to rotation. In order to avoid stall and generate positive turbine torque, the rotational velocity of the turbine needs to be high enough to ensure the resultant blade angle of attack remains low. Therefore, when at standstill, the turbine is generally unable to generate enough positive torque to self-start.

Since the invention of this turbine design in the 1920's a number of variations of blade arrangements have been developed (Tjiu et al., 2015), with some of the key designs illustrated in Figure 1.2.3.

These include the original troposkein design and straight bladed versions, either with open blade tips (H-Darrieus) or tips mounted to end plates (caged). The primary advantage of the latter is increased structural strength, although the end plates will inevitably influence the flow structure. A further version was developed by Alexander Gorlov (1995) and incorporates helical blades. This allows the rotational position of the blade section to constantly vary with span; this has the effect of reducing the variability of the total turbine torque and also improving the ability to self-start.

An alternative solution to the self-start and torque variation problem is to introduce periodic pitching of the blades about their own axis (Kirke and Lazauskas, 2011). A number of such designs have been proposed, with some known as cycloidal turbines (Hwang et al., 2009; Salter, 2012).

An illustration of the changing blade pitch is shown in Figure 1.2.4. This shows how the blades are pitched towards the incoming flow in the first quarter rotation,

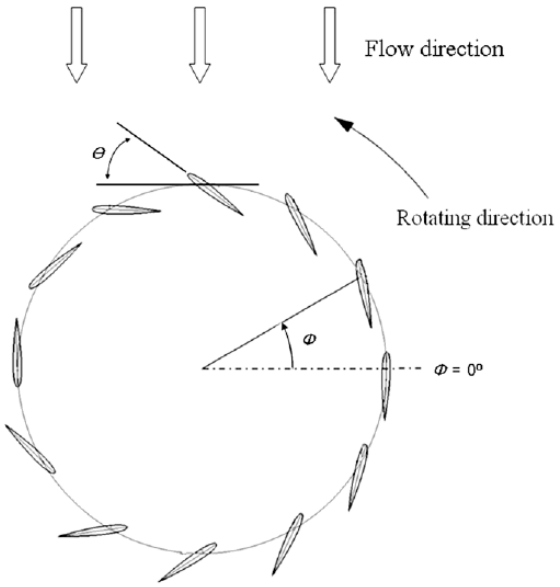

Figure 1.2.4: Blade path in a typical cycloidal Darrieus turbine (Hwang et al., 2009)

which effectively reduces the resultant angle of attack, avoiding stall. The maximum pitch angle can be controlled, depending on *TSR* value, although this adds considerable complication to the turbine mechanism and/or control systems.

1.2.4 Design of Savonius turbines

The Savonius turbine was designed to primarily harness the development of drag forces acting on rotating curved 'buckets', as illustrated in Figure 1.2.5.

This design of turbine operates at lower rotational speeds than Darrieus turbines, typically in the range of $TSR = 0 - 1$. The aim is to maximise drag forces acting on the buckets, but useful lift forces are generally not developed. This produces relatively low maximum power coefficients of approximately $C_P = 0.15$. As with Darrieus turbines, a number of developments have been trialled, such as the addition of end plates, the number and spacing of buckets, and the use of twisted buckets (Akwa et al., 2012). Despite this, use of this turbine is not common, although it is still the focus of many academic studies.

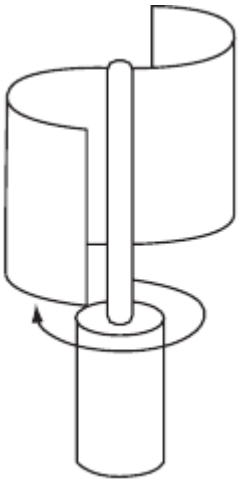

Figure 1.2.5: Typical Savonius VAWT design (MacPhee and Beyene, 2012)

1.2.5 Design of the momentum-reversal and lift turbine

1.2.5.1 General design intent

The momentum-reversal and lift (MRL) turbine is a novel design of cross-flow tidal-stream device developed by Aquascientific Ltd (Janssen and Belmont, 2009). A full size turbine is visualised in Figure 1.2.6, where it is shown suspended below a floating pontoon support.

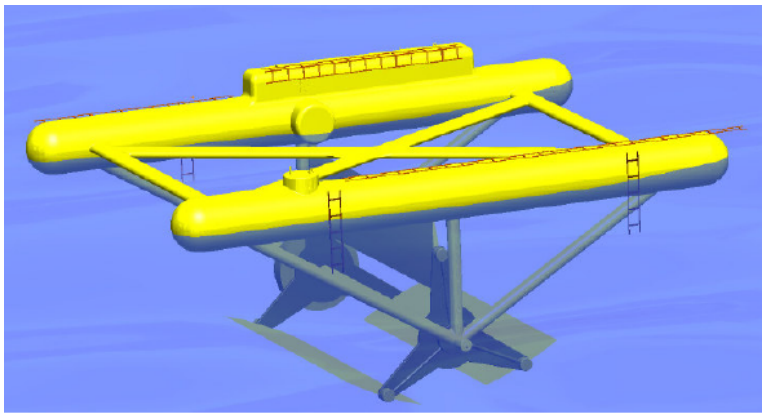

Figure 1.2.6: MRL tidal turbine supported below a floating pontoon support (Janssen and Belmont, 2009)

The design was originally conceived with the aim of harnessing both momentum-reversal (i.e. drag) and lift forces in order to develop useful torque. In order to achieve this, each turbine blade rotates about its own axis whilst rotating about the central axis. It is therefore a type of cycloidal turbine, although in contrast to the relatively small angle, periodic pitching described in Section 1.2.3, each

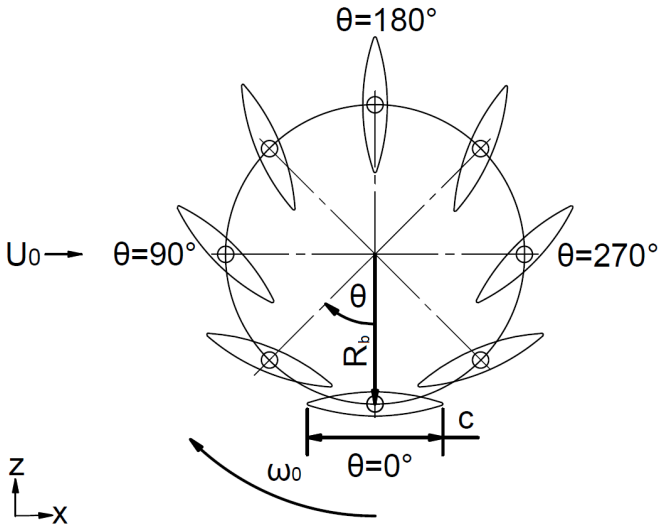

Figure 1.2.7: Diagram showing the orientation of a single MRL turbine blade as it rotates through a turbine cycle (shown in $\theta = 45°$increments)

blade rotates continuously through 180° about its own axis for every 360° of turbine rotation. This is achieved with a gear or pulley mechanism with ratio 1:2 between the central turbine shaft and each blade shaft. This results in the blade path shown in Figure 1.2.7.

The diagram shows how the frontal area of the blade facing the incoming flow is minimised at $\theta = 0°$ and maximised at $\theta = 180°$. The aim is to minimise parasitic drag at the former position and maximise useful drag at the latter position. The two half cycles between these points are defined as upstream ($0° < \theta < 180°$) and downstream ($180° < \theta < 360°$). In these ranges, the blade is pitched into the oncoming flow, with the aim of developing useful lift forces that contribute to positive torque about the central axis.

1.2.5.2 Definitions of turbine input and output parameters

A number of parameters are used to describe the geometry and operating conditions of the turbine:

- R_b: Radius from turbine centre to blade centre
- c: Blade chord length
- h: Blade central thickness
- l_b: Blade length, or span

- n: Number of blades
- θ: Turbine rotor angle
- ω_0: Turbine rotational velocity
- U_0: Nominal free-stream inflow velocity

The swept frontal height, D, of the turbine is defined as:

$$D = 2R_b + 0.5c + 0.5h \tag{1.2.2}$$

Furthermore, the solidity, σ, of the turbine is defined as:

$$\sigma = \frac{nc}{D} \tag{1.2.3}$$

Note that this is the standard form for solidity used for Darrieus turbines. However, care should be taken when comparing solidity values of MRL and Darrieus turbines, due to the different blade motions.

In a similar way to the TSR value defined for Darrieus turbines, the key operating condition of the MRL turbine is defined as the blade-speed-ratio (BSR):

$$BSR = \frac{\omega_0 R_b}{U_0} \tag{1.2.4}$$

Note, the use of 'blade' rather than 'tip' ensures the radius to the blade centre is used, rather than the changing radius to the outer tip of the blade. Similar to Savonius turbines, the useful operating range is restricted to $BSR = 0 - 1$, due to the angle of the blades in relation to the relative flow, as discussed in Chapter 4.

A chord based Reynolds number can be used to define the average flow conditions over a single blade, as defined by:

$$Re_c = \frac{\overline{U_R}c}{\nu} \tag{1.2.5}$$

where ν is the kinematic viscosity of the fluid and U_R is the relative flow velocity over the blade. This velocity varies throughout the turbine cycle and is dependent upon BSR, U_0 and rotor angle. Note that for Darrieus turbines where BSR (or TSR) is usually in the range of three to seven, then $\overline{U_R} \approx TSR\,U_0$. However,

for the MRL turbine, where *BSR* is typically in the range of zero to one, then $\overline{U_R} \approx U_0$.

The frontal area of the turbine relative to the cross-section area of channel is defined as the blockage ratio, *B*. For a turbine with no support structure (i.e. only blades) the blockage is defined as:

$$B = \frac{D\,l_b}{A_c} \tag{1.2.6}$$

where A_c is the cross-sectional area of channel at the turbine location. High blockage tends to increase flow velocities and therefore forces and torque acting on the turbine.

The cycle-mean generated torque, $\overline{T_d}$, that drives the rotation of the turbine about the central axis can be represented as a torque coefficient, C_Q, as given by:

$$C_Q = \frac{\overline{T_d}}{1/2\,\rho\,D\,l_b\,R_b\,U_0^2} \tag{1.2.7}$$

and likewise, the power coefficient, C_P, is given by:

$$C_P = \frac{\omega_0\,\overline{T_d}}{1/2\,\rho\,D\,l_b\,U_0^3} = C_Q\,BSR \tag{1.2.8}$$

where $\omega_0\,\overline{T_d}$ represents the cycle-mean power, *P*, generated by the turbine, ρ is the fluid density, $D\,l_b$ represents the frontal area swept by the turbine blades and therefore the denominator in Equation 1.2.8 represents the power contained in the fluid flowing through the turbine blade area.

In addition to the above parameters that define the turbine useful output, the cycle-mean forces acting on the turbine in both the x- and z-directions can be represented by thrust coefficients, as given by:

$$C_{T,x} = \frac{\overline{F_x}}{1/2\,\rho\,D\,l_b\,U_0^2} \tag{1.2.9}$$

$$C_{T,z} = \frac{\overline{F_z}}{1/2\,\rho\,D\,l_b\,U_0^2} \tag{1.2.10}$$

where $\overline{F_x}$ and $\overline{F_z}$ represent the cycle-mean forces acting on the turbine in the x- and z-directions respectively. Note, the denominator in both equations is the force acting on the frontal area of the turbine due to the incoming x-direction

(a) Sail Powered Energy wind turbine (SailPoweredEnergy)

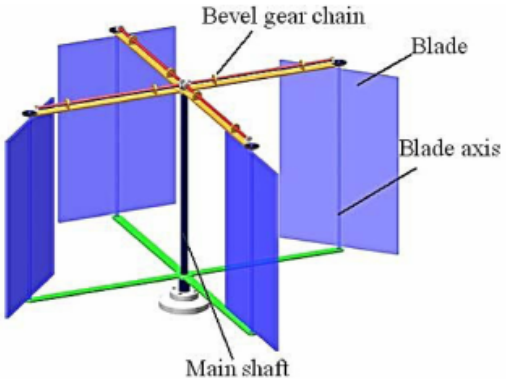

(b) Wollongong wind turbine (Mao et al., 2016)

Figure 1.2.8: Alternative cross-flow wind turbine designs

fluid flow (z-direction incoming flow is assumed to be zero). Using the same denominator in both equations allows a direct comparison to be made between each component of thrust.

1.2.5.3 Similar turbine designs

The type of blade motion employed in the MRL turbine is relatively rare, although two examples of wind turbines have been identified, as shown in 1.2.8.

The Sail Powered Energy (previously Tradewind) turbine (see SailPoweredEnergy) uses canvas sails instead of blades, and incorporates furling mechanisms in order to vary the area of the sail depending on wind speed. The sails also rotate about their own axis while the turbine rotates, in a similar fashion to the MRL turbine. No published research concerning this turbine design has been found.

The Wollongong design is also a vertical-axis wind turbine, with the same blade motion as the MRL turbine. This turbine was developed in Australia and primarily used as an undergraduate teaching device (Cooper and Kennedy, 2004), although researchers in Taiwan (Wang et al., 2010) and China (Zhang et al., 2011; Mao et al., 2016) have also focused on the design.

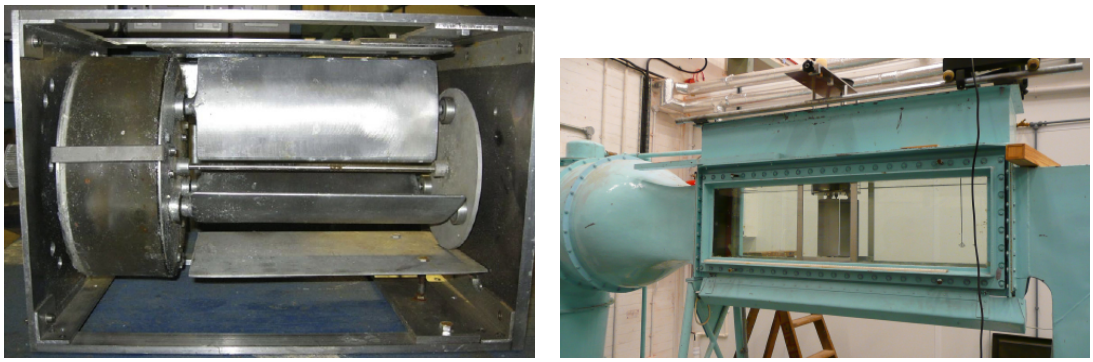

(a) Original MRL turbine experimental model **(b)** University of Exeter recirculating flume

Figure 1.3.1: Original MRL turbine experimental setup (Gebreslassie et al., 2013a)

1.3 Current State of MRL Turbine Research

1.3.1 Experimental work

At the outset of the work presented in this thesis, only limited experimental investigations of the MRL turbine had been undertaken, as presented in Gebreslassie et al. (2013a). These involved a laboratory scale model operating in the University of Exeter recirculating water flume, as shown in Figure 1.3.1. This model used blades of chord length $c = 0.095\,m$, radius of $R_b = 0.055\,m$ and a span of $l_b = 0.22\,m$, with the pitch control mechanisms located in a cylindrical housing at one end of the turbine. The cross-sectional area of the recirculating flume is relatively small, and therefore the area blockage ratio was approximately $B = 60\,\%$. Flow velocities were measured in the region of $U_0 = 0.60 - 0.875\,m/s$ with a peak power coefficient of approximately $C_P = 0.5$ found at $BSR = 0.5$, as shown in Figure 1.3.2.

No wake measurements were undertaken in the original flume experiments, although a study has since taken place at IFREMER, France, as reported in Gebreslassie et al. (2016). The results were gathered after the experimental work reported in this thesis, with the design of the turbine model being particularly influenced by the work presented here.

1.3.2 Computational simulations

The interaction of wakes from multiple MRL turbines has been simulated using a computational fluid dynamics (CFD) approach, as presented by Gebreslassie

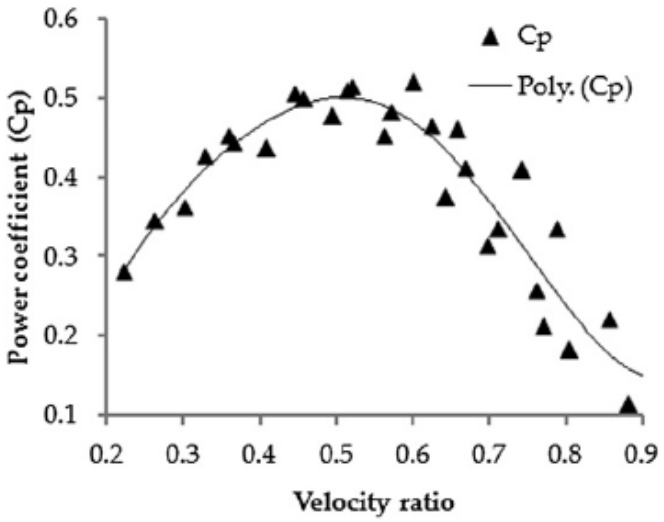

Figure 1.3.2: Original MRL turbine experimental results (Gebreslassie et al., 2013a) (Velocity ratio is equivalent to BSR)

et al. (2012; 2013a; 2013b; 2014; 2015). This Immersed Boundary Force (IBF) model uses a momentum-sink type approach to model the energy extracted by the turbine, and does not model the blades, or motion of the turbine directly. It does not provide any prediction of how forces and torque are developed by the turbine blades, nor give insight into the flow structure within the turbine region.

The purpose of the model is to induce a wake downstream of the turbine, which is modelled with a computationally expensive Large Eddy Simulation method. As the modelling of the turbine itself is very computationally inexpensive, it is possible to model a number of turbines operating together in an array and therefore assess the effect of turbine proximity on the size and shape of wakes, and performance of downstream devices. The energy extraction of the model is calibrated using experimental results and the wake compared to experimental measurements. Ideally energy extraction and wake results from the same experiments would provide a coordinated set of validation data.

1.4 Review of Cross-Flow Turbine Research

1.4.1 Aerodynamic issues and alternative design tools

Whatever the type of turbine design, many of the same aero- or hydro-dynamic issues affect the performance. These are summarised by Leishman (2002)

(albeit with a concentration on HAWTs) and include the important effects of turbulence in the inflow, and the dynamics of the turbine wake, both near and far from the turbine. The near wake is strongly affected by the turbine blade geometry and typically involves sharp velocity gradients and peaks in the turbulence intensity. The far wake is less affected by the rotor shape and here turbulence acts as a mixer, leading to recovery of the velocity deficit and reduction of the turbulent intensity. This far wake can greatly affect downstream turbines if situated too close together in farms. A third important phenomenon is dynamic stall, where the variation of lift and drag is altered for a continuously changing angle of attack in comparison to steady state results. This can occur due to varying wind velocities for HAWTs but is also intrinsic to VAWTs, as the blade angle of attack continuously varies during the turbine rotation. Therefore, understanding the effects of these phenomena is key to engineering efficient and reliable turbines for use in real world conditions.

Experimental testing of full scale turbines is unsuitable for providing flow field data due to the unpredictable and uncontrollable nature of the inflow wind conditions. The large size of turbines also provides the difficulties and expense of modifying blade designs for testing. Wind tunnel testing is generally impractical for full scale turbines, as the majority of wind tunnels are not large enough to accommodate them and therefore scale models must be used. This introduces further complications due to dimensional similarity requirements.

In order to maintain an equal Reynolds number at full size and wind tunnel conditions, the flow velocity must be increased to account for the reduced size of a turbine model (if using the same fluid properties, i.e. of wind). This results in an increased rotational speed of the blades, in order to maintain the desired tip speed ratio, and this could cause damage to the models. Also, if the blade tip speed is high enough in real world conditions, compressibilty effects may be introduced and therefore the added complication of matching the blade tip Mach number is introduced (this is more relevant to HAWTs than VAWTs).

Another issue is tunnel blockage that can occur if the tunnel walls are too close to the rotor to represent real world free-flow. Therefore the tunnel must be large enough to not affect the flow over the turbine. Although limited in use for design development, wind tunnel test results do prove invaluable for validation of mathematical design and analysis models. The role of mathematical modelling in the design and development process is therefore necessary due to the limitations and difficulties associated with experimental testing.

Mathematical models cover a range of complexities, from blade element and momentum models (BEM), vortex models and computational fluid dynamics as discussed in relation to VAWTs by Jin et al. (2015), Aslam Bhutta et al. (2012) and Islam et al. (2008). The former two types of model were developed in the 1970's for use with VAWTs (Templin, 1974; Larsen, 1975), when computing power was limited, and have been further developed since (Chapman et al., 2013; Tescione et al., 2016).

BEM models are based on the calculation of flow velocity through the turbine and have become the basis for performance prediction tools in the wind turbine industry. However, these models are based on experimental aerofoil measurements for angles of attack up to 180° and relatively low Reynolds numbers, and this data is not always readily available for a particular aerofoil profile. It has also been shown that these models are inadequate for VAWTs with high tip speed ratios and also high solidity. However, the method remains popular and with the inclusion of additional methods in order to account for unsteady aerodynamics and virtual camber, the model can be used to predict the performance of cycloidal rotors (Jain and Abhishek, 2016).

Vortex models are potential flow models based on the velocity field of the turbine through the influence of vorticity in the turbine wake. The blades are represented by bound vortices with strengths based on aerofoil coefficient datasets. However, although much more robust than BEM, vortex methods still rely on significant simplifications and also, known aerofoil coefficients. Also, both methods cannot visualise the basic flow structure within the rotor volume, which can be a powerful tool for rotor design and development (Delafin et al., 2017).

1.4.2 Computational fluid dynamics simulations

A more powerful tool for modelling flow through renewable energy turbines is computational fluid dynamics (CFD), based on the solving of the Navier-Stokes equations with the finite-volume method over a discretised flow domain. This allows more detailed modelling of turbine wakes as well as detailed modelling of the blade motion and therefore visualisation of the rotor-volume flow structure.

Modelling of flow through rotating turbines can be achieved using time-dependent sliding-mesh techniques, where different computational regions are defined for

rotating and stationary zones and the flow is interpolated across the interface at each time-step.

Different approaches exist with regards to modelling of the turbine rotors, as discussed by Sanderse et al. (2011) and Masters et al. (2015). One approach is to use an actuator line, surface or disc to model the rotor as a momentum sink and turbulence source, without the complication or expense of meshing the blades. However, this is a simplified approach that does not yield details of the near-blade flow structure. Alternatively and most physically sound, the blades can be modelled directly with a detailed mesh. This can lead to the accurate solving of the blade boundary layer, including phenomena such as transition, separation and stall.

The turbulence in the flow (including surface boundary layers) can be modelled with a Reynolds-Averaged Navier Stokes (RANS) approach, such as the $k-\varepsilon$ or $k-\omega$ models, which aim to model the effects of turbulence on the average flow. When employed in a time-dependent simulation the approach is often called unsteady-RANS, or URANS. A more advanced but computationally expensive approach is Large Eddy Simulation (LES), which directly models the largest eddies in the flow. A combination of the two techniques is called Detached Eddy Simulation (DES), where flow near to surfaces is modelled with RANS and the code switches to LES in other regions. A major drawback of LES and DES is the requirement for three-dimensional simulation domains, which is a major reason for the added computational expense over RANS, that can be run in two- or three-dimensions.

CFD has been used extensively for analysis of HAWT designs over the past two decades. Among many independent simulations, a coordinated set of research was undertaken by a range of authors worldwide, as reported by Masson et al. (2008). Here, CFD simulations (as well as other models) were validated against the Unsteady Aerodynamics Experiment (UAE) wind tunnel experiments conducted by the National Renewable Energy Laboratory (NREL) in the USA. In contrast to HAWTs, no large coordinated set of CFD research for VAWTs has taken place, in part due to the lack of modern, comprehensive wind tunnel measurements to validate against, such as the UAE. Typically, CFD models of VAWTs tend to be validated either against the experimental Sandia Darrieus turbine data, or against data from in-house small-scale experiments.

1.4.2.1 CFD of Darrieus turbines

A number of researchers have performed CFD studies of cross-flow wind and tidal turbines in the past decade. Details of the most notable studies of Darrieus turbines are given in Tables 1.4.1 and 1.4.2.

Early simulations

Hansen and Sørensen (2001) presented one of the earliest CFD studies of a VAWT, where the flow over a single NACA 0015 aerofoil blade in Darrieus motion was simulated, using $k-\varepsilon$ RANS turbulence modelling. The aim of this study was to demonstrate the basic ability of CFD to simulate VAWTs. In related work, Zhang and Sørensen (2004) used the actuator line technique to model a two bladed VAWT in a two-dimensional (2D) study. Here a line replaces the turbine blade and the pressure distribution along the line, at each discrete angle of attack, is set using results gained from aerofoil analysis software, such as XFOIL. The line tangentially follows a circular path, over-set on a simple uniform structured CFD grid. The turbine wake is modelled with the $k-\varepsilon$ RANS model. The results of tangential and normal blade forces are compared to experimental results from water tank tests of a VAWT but do not match well. It is noted that the effects of dynamic stall have not been modelled with this approach and this may contribute to the lack of accuracy. The authors did not pursue the modelling of VAWTs, primarily focusing on HAWT analysis over the subsequent years.

Vassberg (2005) aimed to revisit the VAWT design using advanced CFD analysis. Here an advanced time-spectral method was implemented with the aim of reducing computational time, taking advantage of the time periodic nature of the unsteady flow of a VAWT. This involved simulating a single aerofoil blade in cyclic motion. The model was validated against an experimental test case, where a NACA aerofoil is pitched in an oscillatory motion, and a close match of lift coefficient was achieved. Following this, three-dimensional (3D) unsteady simulations of both straight and troposkein bladed Darrieus turbines were run. The results of the straight bladed model were compared to a traditional mathematical model and it is seen the CFD code gives a significantly lower prediction of lift on the blade and therefore a lower power coefficient for the turbine. It is noted the traditional method is only a two dimensional model and by evaluating the span-wise variation of power coefficient it is concluded

Table 1.4.1: Details of CFD studies of Darrieus turbines (1 of 2)

Source	No. blades	Geometry	Flow medium	Re_c number	Solidity	TSR	Turbulence model	2D/3D	Output
Hansen and Sørensen (2001)	1	Straight	Air			3-5	$k-\varepsilon$	2D, 3D	C_P
Vassberg (2005)	1	Straight, Troposkein	Air	1000k	0.035-0.165	1-14	Spectral BL	3D	C_P
Ferreira et al. (2007)	1	Straight	Air	50k	0.063	2	SA, $k-\varepsilon$, LES, DES	2D	Vorticity (Vo)
Amet et al. (2009)	2	Straight	Air	38k	0.2	2, 7	$k-\omega$	2D	Vo, C_L, C_D
Gretton et al. (2009)	3, 4	Straight, Cycloidal	Water	500k	0.24	2-3.6	$k-\omega$ SST	2D	C_P, C_Q, C_T
Hwang et al. (2009)	3, 4, 6	Cycloidal	Water	17k	0.08-0.15	1.4-3.4	$k-\varepsilon$	2D	C_P
Gupta and Biswas (2010)	3	Straight	Air	50k	0.75	1.2-1.8	$k-\varepsilon$	2D	C_P
Howell et al. (2010)	3	Straight	Air	33k	1.0	1.3-2.6	RNG $k-\varepsilon$	2D, 3D	Vo, C_P
Qin et al. (2011)	3	Straight	Air	160k	0.24	1.3-2.6	RNG $k-\varepsilon$	2D, 3D	Vo, C_L, T
Beri and Yao (2011a; 2011b)	3	Straight	Air	270k	0.375	0.1-4.0	RNG $k-\varepsilon$	2D	C_P, C_Q,
Raciti Castelli et al. (2011; 2012c)	3, 4, 5	Straight	Air	170k	0.25-0.42	1.4-3.3	Real. $k-\varepsilon$, $k-\omega$ SST	2D	C_P
Raciti Castelli et al. (2012b; 2012a)	4, 5	Shrouded	Water	450k	0.33-0.42	0.5-3.2	$k-\omega$ SST	2D	C_P
Almohammadi et al. (2012; 2013b; 2013a)	3	Straight	Air	1000k	0.48	0.5-5	Transitional $k-\omega$ SST	2D	C_P
McLaren et al. (2012)	3	Straight	Air	360k	0.48	0.4-2.4	$k-\omega$ SST	2D	Velocity, C_P
Li et al. (2013)	3	Straight	Air	360k	0.48	0.4-1.9	$k-\omega$ SST, LES	2D, 2.5D	C_P

Table 1.4.2: Details of CFD studies of Darrieus turbines (2 of 2)

Source	No. blades	Geometry	Flow medium	Re_c number	Solidity	TSR	Turbulence model	2D/3D	Output
Rossetti and Pavesi (2013)	3	Straight	Air	100k	0.33	0.1-4	SAS	2D, 3D	C_Q
Lanzafame et al. (2014)	3	Straight	Air	53k-270k	0.50	0.2-2.2	Transitional $k-\omega$ SST	2D	C_P
Maître et al. (2013)	3	Straight	Water	270k	0.55	1-3	$k-\omega$ SST	2D	Vo, C_P
Pellone et al. (2014)	3	Straight	Water	270k	0.55	1-3	$k-\omega$ SST	3D	Vo, C_P
McNaughton et al. (2014)	3	Straight	Water	180k	0.55	0.2-2.7	Low Re $k-\omega$ SST	2D	C_P
Mohamed et al. (2015)	3	Straight	Air	23k	0.1	2-9	$k-\omega$ SST	2D	C_P, C_Q
Lee and Lim (2015)	3	Straight, Helical	Air	160k	0.4, 0.6, 0.8	1.2-3.2	RNG $k-\varepsilon$	3D	Vo, C_P, C_Q
Alaimo et al. (2015)	3	Straight, Helical	Air	140k	0.45	0.4-2.2	$k-\omega$ SST	2D, 3D	Vo, C_P, C_Q
Elkhoury et al. (2015)	3	Straight, Cycloidal	Air	100k	0.75	0.25-1.5	LES	3D	Vo, C_P
Balduzzi et al. (2016)	3	Straight	Air	200k	0.44	1.1, 2.2	$k-\omega$ SST	2D	Vo, C_P, C_Q
Bhargav et al. (2016)	3	Straight	Air	450k	0.5	0.8-2.3	Transitional $k-\omega$ SST	3D	Vo, C_P
Chowdhury et al. (2016)	3	Straight, Tilted	Air	56k	0.21	2.9-3.4	RNG $k-\varepsilon$, $k-\omega$ SST	3D	Vo, C_P, C_Q
Gorle et al. (2016)	4	Straight	Water	80k	0.53	0.5-5	$k-\omega$ SST	2D	Vo, C_P
Sengupta et al. (2016)	3	Straight	Air	20k	0.5	0.9-2.5	RNG $k-\varepsilon$	2D	Vo, C_P, C_Q
Asr et al. (2016)	3	Straight	Air	34k	0.33	0-4.2	$k-\omega$ SST	2D	Vo, C_P, C_Q

tip losses contribute greatly to the lower power prediction of the 3D CFD model. The effect of turbine solidity was also evaluated, and it was found high values of solidity, for a given TSR value, were the most efficient. This highlights the advantage of CFD over other models that are unable to simulate high solidity turbines. Although successful in many regards, the authors note that the simulations only considered an impractical single-blade turbine and importantly, no consideration of how to best resolve the blade wake was given. It was recognised the wake would likely have a significant impact on performance as, for multi-blade turbines the blades would pass through the downstream wake of other blades in each rotation.

LES and DES simulations

Ferreira et al. (2007) recognised that dynamic stall plays a significant part in VAWT performance, especially at low values of TSR. The authors noted that modelling the dynamic stall of a VAWT involves a number of challenges. These included the inability to simplify the geometry and computational expense with radial symmetry (as can be done with HAWTs) and also the need for a fine spatial mesh within the whole of the rotor, in order to correctly model the development of the shed vortices that interact with downstream blades. Also, the correct use of a turbulence model and near wall models is crucial to accurately model both the lift and drag acting on the aerofoils. This is because drag becomes dominant on each blade at a certain period in the rotation and actually decelerates the rotor, especially at low values of TSR, during turbine start up for example. Ferreira et al. aimed to compare various turbulence models including the Spalart-Allmaras (SA) and $k-\varepsilon$ RANS models and the LES and DES approaches. The results were validated against experimental flow visualisation results, e.g. particle image velocimetry (PIV) data. This is an approach also taken by Amet et al. (2009), who used the $k-\omega$ model instead of LES or DES. The latter author found the vortex shedding behaviour of the RANS simulation to qualitatively match the experimental results. However, the results of Ferreira et al. showed the two RANS models used did not sufficiently predict either the amount of vorticity shed from the leading edge, or the roll up of the trailing edge shed vorticity, which were both clearly visualised by the experimental work. In contrast, the LES simulation did predict these, but not at accurate aerofoil positions or rotational times. The DES model, using the SA model in the near wall region, was found to give the most accurate results, with

the position and timing of vorticity shedding matching the PIV results. It was also found that the DES model was less sensitive to both space and time grid refinements. When considering the tangential and normal forces on the blades, as is done with most CFD studies, it was found that the choice of turbulence model did not greatly affect the results. This implies that, although a simulation may give a good match of overall power performance, the physical phenomena within the rotor space may not be modelled correctly.

Further LES studies have only recently been reported by Li et al. (2013) and Elkhoury et al. (2015). The former performed '2.5D' simulations, where a finite blade span was modelled, but with periodic boundary conditions at the tips. Therefore fully 3D effects such as tip losses were ignored. LES was compared to URANS and was found to better model the breakdown of larger vorticity into smaller structures. This resulted in better prediction of the occasion of dynamic stall and therefore the magnitude of turbine torque developed throughout the cycle. The latter author performed fully three-dimensional simulations and also found satisfying results, with the power coefficient very well predicted over a range of TSR values. However, none of the above authors have reported the computational expense involved in carrying out the LES simulations, which was likely high. Also, all LES simulations were either directly compared to, or extended from previously reported URANS simulations, which are a much less computational expensive approach.

URANS simulations

Although not as advanced as LES or DES techniques, many authors have found URANS simulation results can match well to validation data. For example, the study of Howell et al. (2010) reports both 2D and 3D CFD models of a 3-blade H-Darrieus VAWT, with results validated against wind tunnel data from in-house measurements. Unlike the study by Ferreira et al. (2007), no comparison of turbulence models was carried out, with the Re-Normalisation Group (RNG) $k-\varepsilon$ RANS model chosen as it is known to predict flow separation more accurately than the standard $k-\varepsilon$ model. However, the chosen approach of modelling boundary layer behaviour was to use non-enhanced wall functions, rather than a wall resolved approach favoured by other researchers. Comparison between the 2D and 3D results does show the importance of the latter, with power coefficients over a range of TSR values matching the experimental data more accurately. This is attributed to the modelling of blade tip vortices, making

the simulation more physically accurate. However, the results for the 3D model did tend to diverge from the experimental results at higher TSR values, which is unexpected. This inaccuracy may be a result of the choice of turbulence model and the relative accuracy of the vortex shedding simulation. The vorticity of the simulation is visualised in the study, although there is no experimental PIV data to validate against, and it is noted the interaction of downstream blades with shed vortices is likely to affect the transition of the boundary layers on the blade, but it is not possible to capture this with the chosen RANS model.

Qin et al. (2011) furthered this work, but focused only on the peak performance conditions. Again, the 3D model reduced the torque produced throughout a cycle, when compared to 2D results, due to modelling of tip losses. By calculating the theoretical angle of attack (AOA) and resultant flow velocity onto a blade as it rotates about the turbine axis, the variation of lift coefficient with AOA was calculated from the simulations results. This highlighted that the maximum turbine torque is produced at an angular location when the blade is stalled, which is significantly different from the dynamic stall behaviour of aircraft wings or helicopter rotors.

Further authors report the use of the RNG $k-\varepsilon$ URANS model (e.g. Beri and Yao (2011a); Lee and Lim (2015); Sengupta et al. (2016)) but the majority of recent authors have used the $k-\omega$ shear-stress-transport (SST) turbulence model. This combines the standard $k-\omega$ model in near wall regions with the standard $k-\varepsilon$ model in the free stream. The advantage of this approach is the combination of several desirable aspects of other two equation methods; namely the improved ability of the $k-\omega$ to model separated flow, but with the stability of the $k-\varepsilon$ model in the free-stream. The first use of this model in cross-flow turbine simulation is found in Gretton et al. (2009), where performance of a tidal turbine is analysed. The selection of this model is due to its success in predicting accurate lift and drag coefficients for static and pitching foils.

The $k-\omega$ SST model was also chosen by McLaren et al. (2012), who found it to well-predict the static lift and drag coefficients of a NACA 0015 aerofoil up to angles of attack of 45°, although VAWT power coefficient results were significantly over-predicted by a 2D simulation. Further researchers have selected the model (e.g. Maître et al. (2013); Mohamed et al. (2015); Alaimo et al. (2015); Balduzzi et al. (2016); Chowdhury et al. (2016); Gorle et al. (2016); Asr et al. (2016)) with many finding it to give superior results to the RNG $k-\varepsilon$ RANS model favoured by some earlier studies. These have included three-

dimensional simulations, with all the support structure modelled (Pellone et al., 2014), that very well match to experimental torque results. In particular, three-dimensional modelling of support arms at the blade tip introduced horse-shoe vortices that strongly affected the flow over the majority of the blade span. These eliminated the 35% overestimation of torque predicted by 3D simulations without the support arms. This highlights the need to simulate the full experimental setup if simulations are expected to match to experimental results.

Other researchers have used transitional RANS models such as the $k-\omega-\gamma-Re_\theta$ SST model (Almohammadi et al., 2013a; Lanzafame et al., 2014; Bhargav et al., 2016). This type of model was developed to improve the prediction of laminar to turbulent boundary layer transition and the associated effect on separation. However, the model requires calibration through the optimisation of local variables, and this requires prior knowledge of some physical result. For example, Lanzafame et al. (2014) calibrates against static lift and drag coefficients for a given blade profile. It is then reported that the VAWT 2D simulation power coefficient results match very well to 3D experimental results through the full TSR range, whilst the standard $k-\omega$ SST model yields a significant over-prediction. The results of Bhargav et al. (2016) also show excellent agreement with the experimental results of McLaren et al. (2012), but the calibration technique is not reported.

Daróczy et al. (2015) compares 2D simulation results, for four different VAWTs, when using a number of RANS models, including Spalart-Allmaras, Realizable and RNG $k-\varepsilon$ models, the standard $k-\omega$ and $k-\omega$ SST models and the transitional $k-\omega-\gamma-Re_\theta$ SST model. It was found that the transitional model gave very mixed results, highlighting the challenge presented by the need for calibration. Only the Realizable $k-\varepsilon$ and $k-\omega$ SST models gave results that were comparable to experimental results through the full range of tested TSR values. The former model always gave a constant offset and the latter gave an offset that varied with the cube of TSR. It was suggested the offsets are the result of neglected 3D phenomena such as tip losses and support structure drag.

Sensitivity analysis

A large number of authors have highlighted the need for a thorough sensitivity analysis when designing the computational setup (e.g. Gretton et al. (2009); Maître et al. (2013); Pellone et al. (2014); Balduzzi et al. (2016)). When using

wall-resolved RANS modelling, it is especially important to assess the effect of mesh resolution at the blade wall, in order to model boundary layer behaviour as accurately as possible. Other important simulation parameters that are considered include the domain size and time-step.

Gretton et al. (2009) highlighted that a building-block approach can be used in order to find simple test cases that represent some part of the physical behaviour of a turbine blade. For example, single static blades at multiple angles of attack can be simulated, or even blades continuously pitching through a range of angles. By performing detailed sensitivity analyses on these simple cases, computational expense can be reduced. However, this is not possible without both an understanding of the conditions encountered by turbine blades, and the availability of suitable test case results. Even with these, the simple test cases will not account for complexities encountered in the full turbine environment.

Other researchers have shown how the choice of monitored parameter is important in sensitivity analyses. For example, if only the cycle-mean torque or power coefficient is compared, variations in behaviour that occur throughout a cycle can be obscured. Therefore the variation of torque through a cycle should also be monitored.

Simulation of alternative designs

A number of authors have utilised CFD to model novel VAWT designs, including variations in aerofoil profiles, number of blades, chord length and also the use of pitching plates (i.e. cycloidal turbines).

Carrigan et al. (2012) used CFD in an automated process to optimise the blade aerofoil profile from the baseline NACA 0015. An automated geometry creation and meshing procedure allowed a large number of CFD simulations to be run. A time-dependent sliding mesh simulation was used, where the rotor domain physically rotates within the far-field domain, at each time step. A 2D simulation was chosen in order to give manageable computation times. The resulting optimised aerofoil blade was found to give a 6% increase in power coefficient at the chosen TSR. Likewise, Beri and Yao (2011b) used a 2D simulation with an aerofoil modification involving the ability of the trailing edge to open, with the aim of increasing drag for increased performance at very low TSR values. The CFD simulation was able to compare different geometries and

it was concluded little advantage was gained from the novel design. Gupta and Biswas (2010) simulated a VAWT with a twist at the trailing edge of each aerofoil, and an optimum degree of this twist was shown to increase the power coefficient. The simulation was validated against wind tunnel results for a blade with an arbitrarily-set amount of twist. However, in contrast to the majority of other studies discussed, Gupta does not use a time-dependent sliding mesh simulation, but instead a steady-state moving reference frame model. Here a stationary domain is used, but the Navier-Stokes equations are solved in the rotating reference frame. This results in an additional Coriolis term being introduced to the momentum equations, in order to simulate the effects of rotation on the flow. The results approximately match the wind tunnel results and prove adequate in comparing the effect of trailing edge twist on the rotor power. However, the method is unable to predict the time dependant vortex shedding behaviour.

A follow up study by Raciti Castelli et al. (2012c) used a CFD model to investigate the effect of increasing the number of turbine blades from three to four or five. It was found that the increase resulted in a lowering of the peak efficiency and also a re-positioning of the peak to lower TSR values. CFD proved to be more cost effective than manufacturing and wind tunnel testing of alternative turbine designs. Similar investigations were undertaken by Hwang et al. (2009) and Gretton et al. (2009), who found the same relationship. Increasing the number of blades increases the solidity, but this can also be achieved by increasing the chord length or reducing the turbine radius, as also investigated by Hwang et al. (2009) and additionally Lee and Lim (2015). Again, the same relationship is observed, i.e., decreasing peak power (and corresponding TSR value) with increasing solidity.

Gretton et al. (2009), Hwang et al. (2009) and Elkhoury et al. (2015) also investigate the use of pitching blades to delay or avoid stall. This is achieved by the use of multiple rotating mesh regions (one for for each blade) embedded within a larger rotating mesh region (for the rotor). The simulations were used to find optimal amplitudes and phase positions for the pitching, in order to maximise power coefficient values. Again, this is something that would be time-consuming and expensive to attempt with physical experiments, but can be achieved relatively inexpensively with 2D RANS simulations.

Note, this multiple rotating zone approach for CFD modelling of cycloidal rotors has also been used by Esmailian et al. (2014), Gagnon et al. (2014) and Xisto

et al. (2014), albeit for propulsion applications such as the Voith Schneider Propeller. When compared to experimental results, Xisto et al. (2014) reported the thrust was over-predicted and the power under-predicted, although the variation of results with rotor speed was correct.

A shroud, or duct, modification to Darrieus turbines was investigated by Raciti Castelli et al. (2012b) and Roa et al. (2010). The shrouds were designed to funnel water flow into the turbine and increase performance. The authors found peak power coefficients were increased by up to 60%, which is primarily a result of increased torque developed by blades in the downwind half of rotation. However, the frontal area of the turbine is increased by the use of the funnel shaped shrouds, and therefore the definition of the power coefficient should account for this.

Simulation of alternative operating conditions

In real life situations, the operating conditions of turbines will rarely be constant or consistent with the limited number of cases measured in wind tunnels or water flumes. Therefore, a powerful use of CFD is assessing the impact of alternative conditions on the performance of a turbine.

Such studies have been undertaken by Bhargav et al. (2016), who investigated the effect of fluctuating inlet flow velocity, and Chowdhury et al. (2016), who modelled a VAWT tilted into the wind. The latter is directly analogous to a horizontally aligned cross-flow turbine with a yaw error relative to the incoming flow.

Asr et al. (2016) modelled the start-up behaviour of a VAWT, which is potentially a major drawback of cross-flow turbine designs. This was achieved with use of a six degree of freedom solver coupled to the torque output of the CFD simulation. This allowed the rotor zone to accelerate from standstill until a TSR value where driving forces are in equilibrium to resistance forces. The results were compared to experimental behaviour and matched very well in shape, with four distinct zones of behaviour. The simulation results were generally over-predicted, but this is likely due to the lack of 3D tip losses. The simulations were also used to adjust the blade fixed pitch angle and/or thickness in order to improve the start-up behaviour.

1.4.2.2 CFD of MRL-type turbines

The only published CFD study focused on MRL-type turbines has very recently been reported by Mao et al. (2016). The cross-flow wind turbine incorporates four flat blades located at a rotor radius of $R_b = 0.5\,m$. Seven chord lengths between $c = 0.3\,m$ and $c = 0.6\,m$ were trialled, giving solidity values in the range $\sigma = 1.0 - 1.8$. 2D simulations were undertaken, using the standard $k-\varepsilon$ model and a wall-function approach. The results are not directly compared to any experimental results, although a similar model setup is shown to well predict the performance of a Savonius turbine. A peak power coefficient of approximately $C_P = 0.36$ is predicted in the range of $BSR = 0.4 - 0.5$ for the maximum solidity turbine, with lower values of solidity resulting in lower peak power values.

1.4.3 Conclusion of review

It has been found that the use of CFD for modelling the flow through cross flow turbines is a powerful tool and offers advantages over traditional mathematical models, mainly in the ability to model the vortex shedding behaviour within the rotor volume, which is particularly important as blades periodically pass through this turbulence during the turbine rotation. The ability of CFD to accurately model the vortex shedding behaviour is therefore important for yielding accurate results. Another advantage is the ability to reliably model high solidity rotors, which some traditional methods cannot, especially as high solidity turbines give better performance at low tip speed ratios.

The use of CFD for modelling of cross-flow turbines has increased over the past decade, as has the complexity of the simulations used. If computing power is adequate, the most accurate model appears to be a 3D time-dependent study using a sliding mesh approach and either an advanced RANS model, LES or DES to model the turbulence. However, 2D simulations using two-equation RANS techniques are still used by the majority of researchers as they provide a relatively inexpensive insight into the flow structures that occur at the centre span of high aspect ratio turbines. It is not unusual for 2D RANS simulations to yield average torque or power coefficients significantly higher than 3D experimental results, and this may be due to neglecting 3D flow aspects such as tip losses or vortices induced by support structures. Alternatively,

the simplifications inherent in RANS modelling may not correctly model the breakdown of shed vortices or delay the onset of vortex shedding and therefore overestimate the forces developed by blades.

In any simulation, a thorough and methodical sensitivity analysis is required in order to verify results are as reliable as possible for the selected modelling approach. As a minimum, the analysis should focus on cell sizes, especially near blade surfaces and in the rotor zone, time-step and domain size.

Ideally simulations should be compared or validated against reliable experimental results. High aspect ratio experimental models, with minimal support structure yield the most suitable data, as this can be most easily approximated with 2D simulations. As well as cycle averaged torque and power results, time-resolved torque and flow visualisation provide the most comprehensive validation data. However, these are relatively rare in the reported studies and usually the variation of C_P and/or C_Q with TSR is compared.

An alternative validation approach is to identify simple test cases that represent the turbine blade behaviour, and perform relevant CFD simulations to compare to experimental results. This can provide confidence that the chosen CFD approach can model some fundamental aspect of the flow physics.

Fully verified and validated CFD models can be used to assess alternative designs, such as changing solidity, blade profiles or blade pitch, as well as varying operating conditions, such as inflow velocity magnitude and direction.

1.5 Introduction to Current Work

1.5.1 Motivation and objectives

The motivation for the work presented in this thesis is two-fold:

- To gain a better understanding of the performance characteristics of the MRL tidal turbine and the physical flow phenomena responsible for this
- To generate data that can be used by other researchers who focus on the wake generation of the MRL tidal turbine

From this, the following objectives have been set:

1. Undertake experimental results that measure the torque and power developed by the laboratory-scale MRL turbine model when operating at a range of BSR values
2. Measure the velocity profiles in the flow downstream of the operating MRL turbine model, in order to characterise the wake
3. Develop a computational fluid dynamics model of the MRL turbine that provides an insight into the behaviour over a range of BSR values
4. Ensure the model is thoroughly verified and compare results against the gathered experimental results
5. Model the effect of varying turbine geometry parameters and compare to results of the reference case (the experimental model)

1.5.2 Thesis layout

1.5.2.1 Experimental work

Chapter 2 presents experimental work focused on the energy conversion performance and wake characteristics of a laboratory scale MRL turbine model. Firstly a detailed description of the turbine experimental model is given, followed by the method used to estimate the resistance torque of this model. The energy conversion experimental method and results are given, before wake measurement methods and results are presented.

1.5.2.2 Simulation work

The CFD simulation theory, setup and a detailed sensitivity analysis are presented in Chapter 3.

In order to better understand and reliably simulate the behaviour of the MRL turbine model, an analysis of the blade motion has been undertaken, in order to give insight into the flow conditions encountered by an individual blade throughout its motion about the turbine central axis. This has allowed the identification of test cases that have been simulated and validated against experimental data from the literature, as presented in Chapter 4.

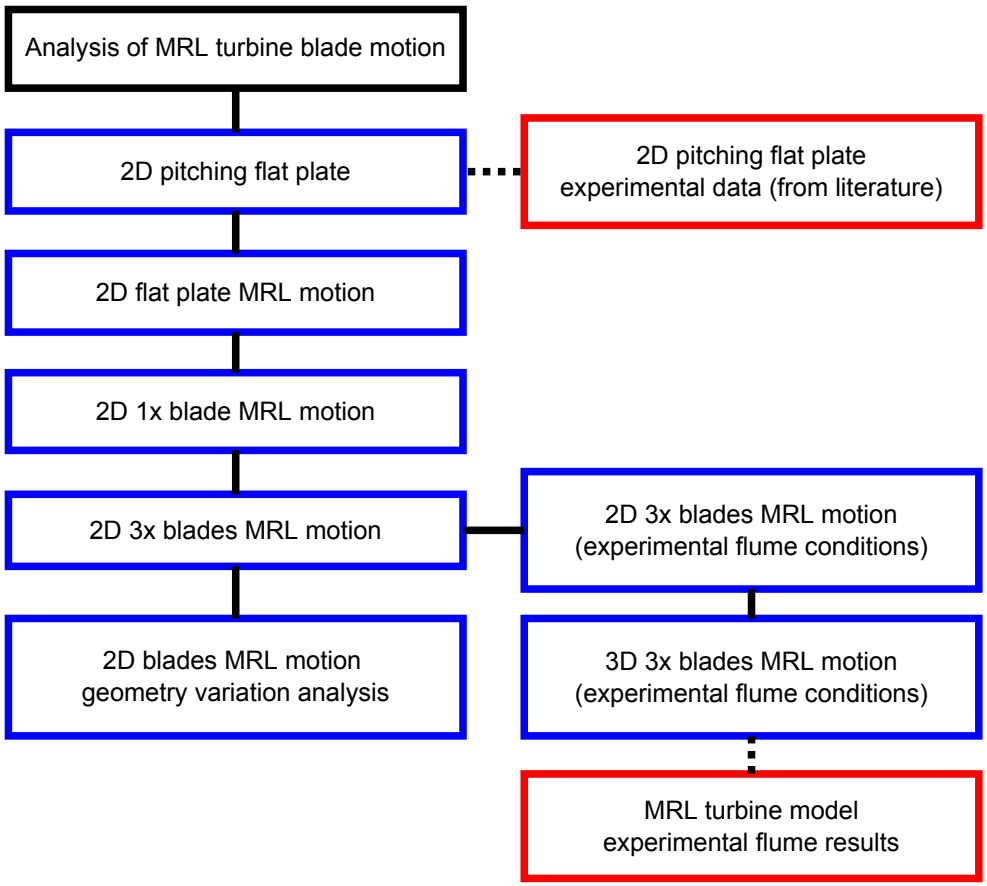

Figure 1.5.1: Flow chart showing the building block approach used in the computational analysis of the MRL tidal turbine. Red and blue boxes indicate experimental and simulation results respectively

Following this, a building block approach has been taken where the complexity of the simulations has been increased in stages, in order to fully understand how the results develop. This building block approach is presented in Figure 1.5.1. Simulations of single blades are presented in Chapter 4 and simulations of three-blade turbines, with comparison to experimental data, are presented in Chapter 5. This chapter also presents results for varying turbine geometries.

Finally, conclusions to the thesis and recommendations for future work are given in Chapter 6.

CHAPTER 2

EXPERIMENTAL ANALYSIS

2.1 Chapter Introduction

This chapter presents the experimental hydrodynamic analysis of a single laboratory-scale model of the MRL turbine. The analysis primarily focuses on the energy conversion performance of the turbine, and the variation of this with operating conditions. Further experimental work, focusing on characterisation of the downstream wake production, is also presented.

The majority of the testing was carried out in a laboratory flume where inlet flow velocity and turbine rotational resistance were controlled. Turbine rotational speed was measured, allowing torque and power coefficients to be calculated. Preliminary experiments were also carried out in order to characterise the total rotational resistance of the turbine over a range of rotational speeds.

This chapter firstly gives an overview of the turbine model used throughout the experiments, before presenting an analysis of the turbine's rotational resistance sources. Following this, the resistance characterisation experiment and the flume experiment work is presented, firstly focusing on energy conversion and secondly wake characterisation.

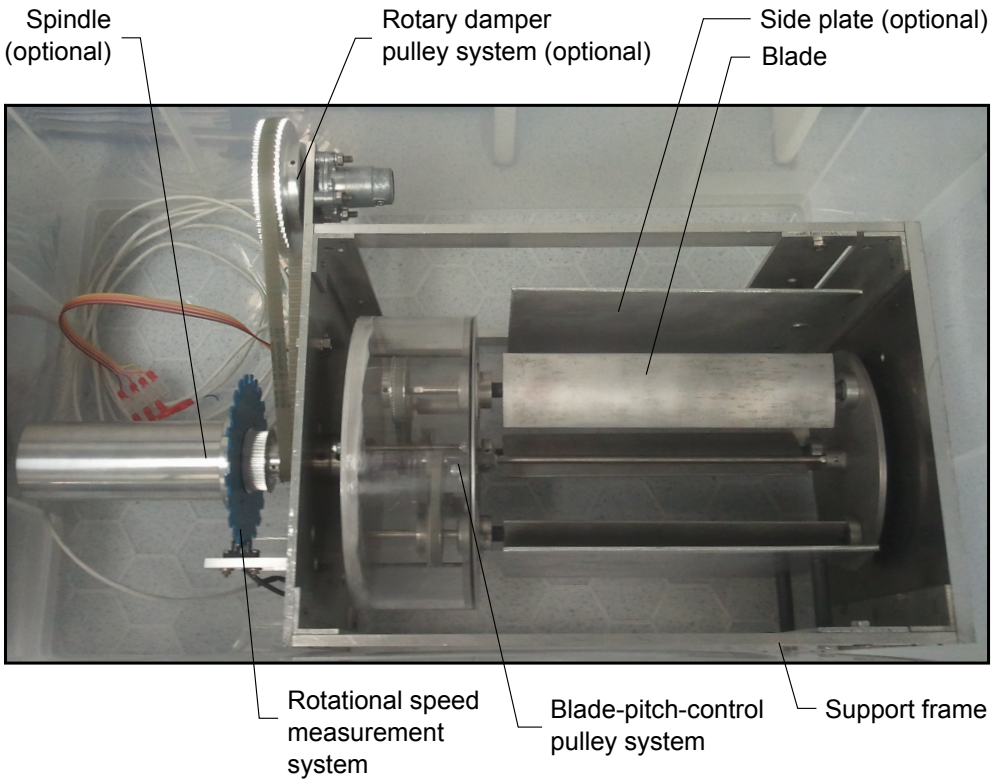

Figure 2.2.1: Image of MRL turbine experimental model with major components indicated (shown with characterisation experiment support frame)

2.2 MRL Turbine Experimental Model

2.2.1 Model diagrams and definitions

This section describes the physical characteristics of the experimental MRL turbine model. The following diagrams and tables give an overview of the model, which is then described in more detail in the following sub-section.

Firstly, an image of the model can be seen in Figure 2.2.1, with the major components indicated.

A detailed drawing of the model is shown in Figure 2.2.2, with particular attention given to the rotational mechanism that drives the rotation of the blades as the turbine rotates. Components of particular interest are numbered, with the definitions and quantities given in Table 2.2.1.

Figure 2.2.3 shows a diagram of the model, with all optional components present, but with the blades replaced with plain shafts as used in the characterisation ex-

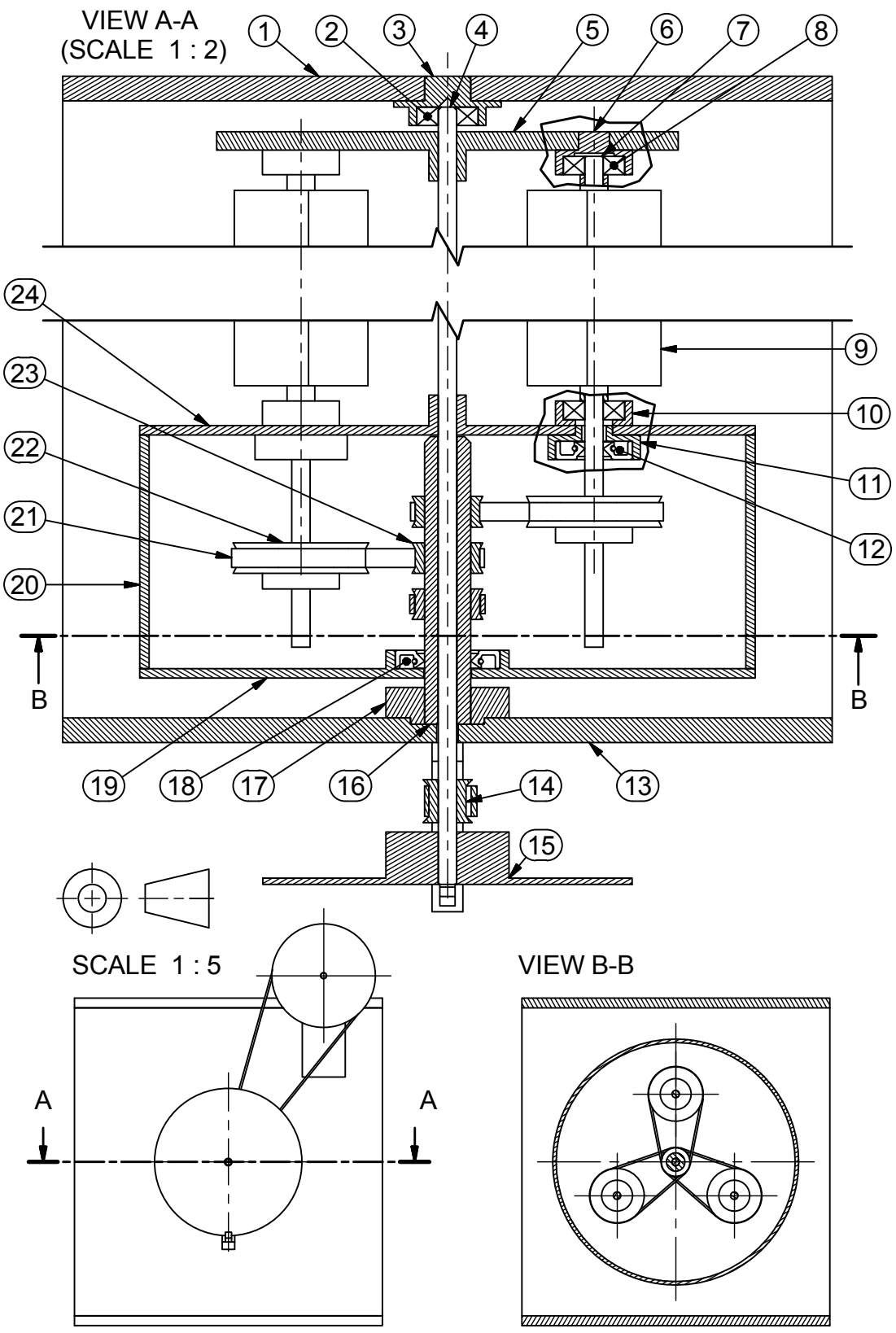

Figure 2.2.2: Detailed drawing of the experimental model focusing on the rotational mechanism

Table 2.2.1: Component parts list for model rotational mechanism (numbers shown in Figure 2.2.2)

Number	Component Description	Quantity
1	Support frame 1	1
2	Central shaft bearing	1
3	Bearing mount (support frame)	1
4	Central shaft	1
5	End plate	1
6	Bearing mount (end plate)	3
7	Blade shaft	3
8	Blade shaft bearing	6
9	Blade	3
10	Bearing mount (housing)	3
11	Seal mount (housing)	3
12	Blade shaft seal	3
13	Support frame 2	1
14	Central turbine pulley	1
15	Toothed timing-disk	1
16	Bush shaft	1
17	Mounting boss	1
18	Bush shaft seal	1
19	Housing outer plate	1
20	Housing cylinder	1
21	Blade timing belt	3
22	Blade pulley	3
23	Bush shaft pulley	3
24	Housing inner plate	1

Table 2.2.2: Experimental model component dimensions

Dimension	Symbol	Value m
Blade axial length	l_b	0.220
Blade revolution radius	R_b	0.055
Blade shaft diameter	D_b	0.006
Central shaft diameter	D_c	0.006
Bush shaft diameter	D_a	0.015
Housing radius	a_h	0.100
Housing width	l_h	0.082
Housing to frame spacing	s_h	0.012
End-plate radius	a_e	0.075
End-plate width	l_e	0.006
End-plate to frame spacing	s_e	0.010
Bearing mount diameter	D_m	0.025
Bearing mount width	l_m	0.008
Spindle radius	a_s	0.027
Spindle length	l_s	0.140
Toothed timing-disk radius	a_d	0.060

periments described in Section 2.4. The diagram defines important dimensions relating to the model's components, with values given in Table 2.2.2.

2.2.2 Model description

The model of the MRL turbine used in the experimental analysis can be described as laboratory-scale and is sized for use in recirculating water flume systems. The rotational motion of the three blades is controlled by the blade-pitch-control pulley system, which is enclosed in a watertight housing. The turbine is mounted into a rigid support frame that can be fixed into the water flume, so that the turbine is completely submerged.

The three turbine blades, of chord length $c = 0.05m$, each incorporate a shaft which is mounted at each end by bearings mounted onto the end plate and the housing inner plate. A central shaft passes through both the end plate and housing inner plate, but is rigidly fixed to both. This central shaft is mounted at one end by the central bearing, which is mounted to the support frame. The

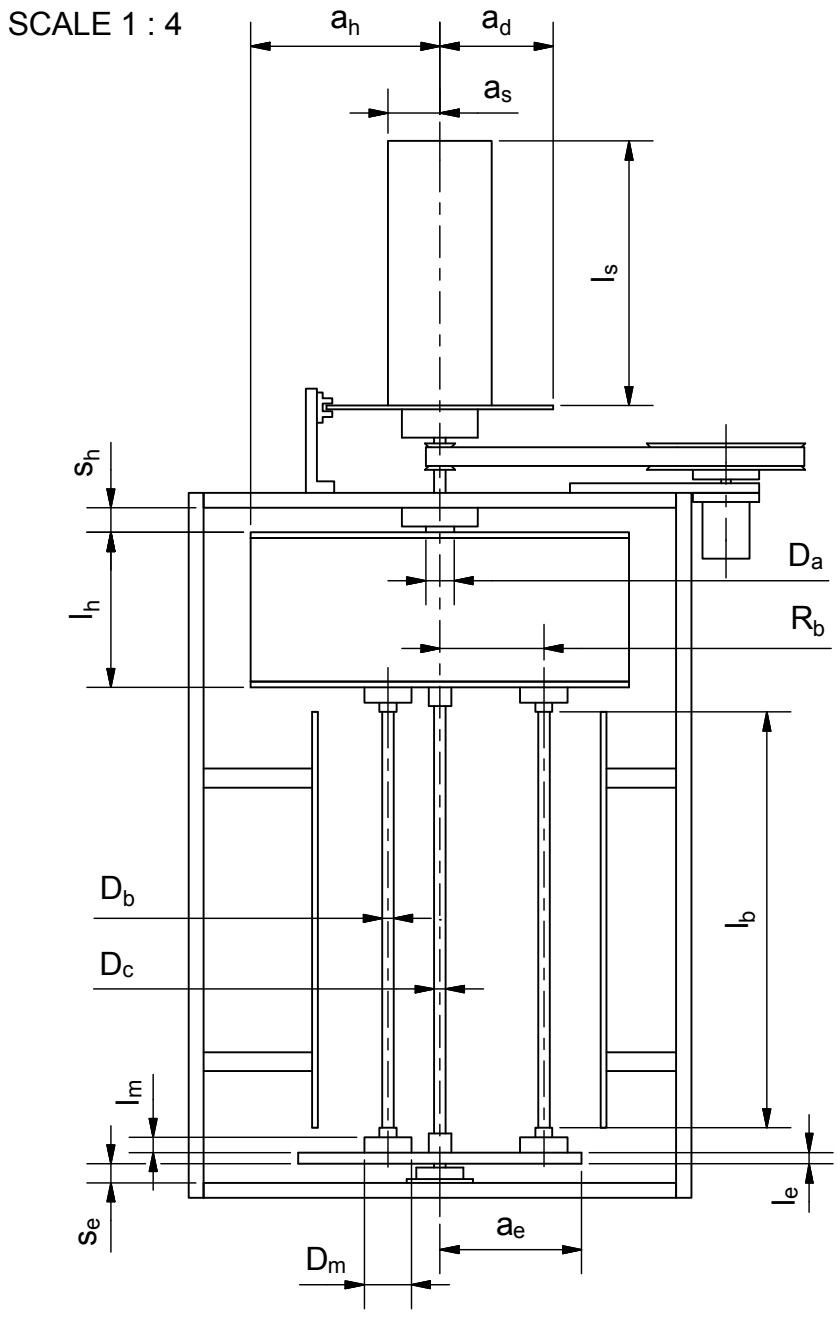

Figure 2.2.3: Diagram of the experimental model with important component dimensions defined

other end of the central shaft passes through the bush shaft, which is fixed rigidly to the support frame by the mounting boss, enabling smooth rotation of the turbine.

The bush shaft also passes through the housing outer plate, which is free to rotate about it. This outer plate is connected to the inner plate by the transparent housing cylinder. Each blade shaft also passes into the housing, through the inner plate, and has a pulley wheel fixed to it. Each of these pulley wheels, located at different axial positions, is linked via a timing belt to a smaller pulley wheel fixed to the outside of the bush shaft. It is important to recognise that the bush shaft itself does not rotate with the turbine and therefore as the blades rotate about the central shaft, the timing belts drive the rotation of the individual blades about their own axes. The ratio of number of teeth on the blade pulley wheels to number on teeth on the bush shaft pulley wheels is set at 2:1. This ensures the blades rotate once for every two rotations of the turbine, thus enabling the MRL blade motion described in Chapter 1 to be achieved.

The purpose of the housing is to keep the blade-pitch-control pulley system from being exposed to the water flow when operating in a flume tank. This ensures a constant rotational resistance is applied by the uniform housing, rather than irregularly shaped pulley system, rotating in the flow. It also prevents contamination of the pulley system with particles that may be present in the recirculating flume flow.

To ensure the housing is watertight, radial lip seals are used around the bush shaft where it passes through the outer plate, and also around each of the blade shafts where they pass through the inner plate.

After passing through the bush shaft, the central shaft continues to the outside of the support frame, where the rotational speed measurement system is located, as well as the optional rotary damper pulley system and spindle.

The rotational speed measurement system comprises a toothed disk, mounted to the central shaft, and a hall effect sensor through which the teeth pass. The hall effect sensor is linked, via a control box, to a laptop. By measuring the rate at which the teeth pass through the sensor, the rotational speed of the turbine is measured and recorded.

The optional rotary damper system comprises a viscous damper linked to the central shaft via a timing belt. The ratio of number of teeth on the damper pulley

and central pulley can be varied in order to control the total rotational resistance of the turbine.

The optional spindle was used only for the resistance characterisation experiments described in Section 2.4. This is rigidly attached to the central turbine shaft and is used to drive the rotation of the turbine by an externally applied torque.

2.3 Analysis of Rotational Resistance Sources

2.3.1 Aim of analysis

This section presents an analysis of the rotational resistance that develops when the turbine model is rotating in water. The aim is to characterise the multiple sources of this resistance, and develop relationships that estimate the variation of resistance with rotational speed.

2.3.2 Definition of rotational resistance sources

When operating at a constant rotational speed, the torque driving the rotation is equal to the resistance torque, as given by:

$$T_d = T_r \tag{2.3.1}$$

where T_d is the driving torque and T_r is the resistance torque. When the turbine is operating in a fluid flow, the driving torque is generated from forces acting upon the blades due to their motion through the fluid. It is this torque that is investigated by the computational analysis presented in Chapter 5. However, during the experimental analysis it is not possible to measure this torque directly with the given experimental model. Therefore it is necessary to measure, or at least estimate, the resistance torque during the experimental analysis and equate this to the driving torque generated by the blade motion. The purpose of this section is to analyse the possible sources of rotational resistance that effect the experimental model, in order to allow reliable prediction of the resistance torque.

When operating at steady rotational speed, and therefore ignoring inertial effects, the total resistance torque originates from a number of sources, as described by:

$$T_r = T_1 + T_2 + T_3 + T_4 \tag{2.3.2}$$

where the numerical subscripts refer to:

1. Mechanical resistance at the central turbine shaft due to the optional rotary damper pulley system.
2. Mechanical resistance of the rotational turbine components, such as bearings, bushes, radial lip seals and the blade-pitch-control pulley system.
3. Hydrodynamic resistance due to skin friction affecting all submerged, rotating surfaces.
4. Hydrodynamic resistance due to body and skin friction drag affecting components that translate through the water.

T_1 is the only resistance torque that is controllable for the given model and its calculation is described in Section 2.3.3. If the turbine model was linked to an electrical generator instead of the rotary damper, this torque would be the useful output.

T_2, T_3 and T_4 can be seen as losses and are unable to be controlled for the given model. The total of these resistances was measured by the characterisation experiments described in Section 2.4. As detailed later, the turbine model is placed in stationary water in the resistance characterisation experiments and flowing water in the flume experiments, and so the rotational resistance due to hydrodynamic forces is expected to be different for the two conditions. It is therefore important to have an understanding of the origins of the rotational resistance and an estimate of their magnitude in relation to each other, in order to inform the uncertainty analysis for the flume experiments. Each source of resistance torque is now treated separately in Sections 2.3.4, 2.3.5 and 2.3.6.

2.3.3 Mechanical resistance of the rotary damper system

The rotary damper used throughout the experimental analysis is a Kinetrol model Q-CRD. This device is designed for small applications and provides rotation to resistance due to the viscosity of a fluid contained within the housing. A

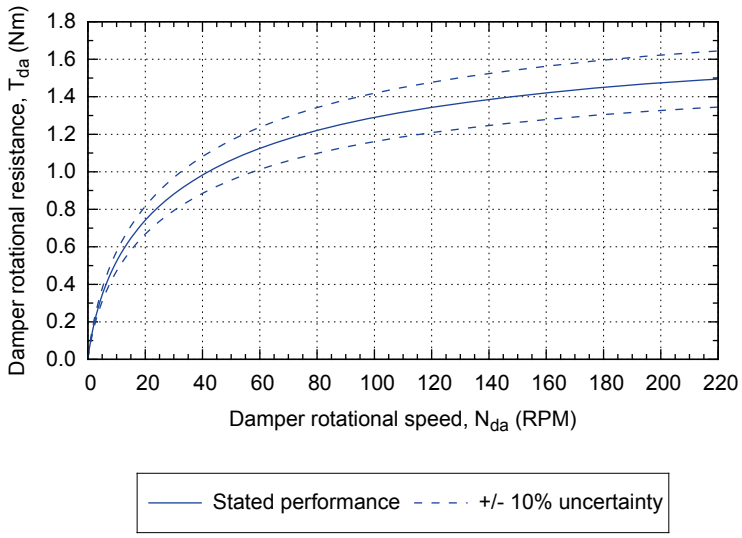

Figure 2.3.1: Variation of rotary damper rotational resistance with rotational speed

viscosity of 500,000 cSt has been used, which is the highest viscosity available for the particular model. The resistance torque provided is dependent upon rotational speed, with the characteristic curve shown in Figure 2.3.1 given by the manufacturer. This data is valid for operation at 20 °C and is stated to be accurate within $\pm$10%.

The central turbine shaft and the damper are linked via a synchronous pulley system, avoiding the risk of belt slip and ensuring reliable transmission of resistance torque to the turbine. The torque required at the central shaft to drive the damper pulley system, is given by:

$$T_1 = \frac{1}{\eta_p} T_{da} r_p \tag{2.3.3}$$

where η_p is the efficiency of the pulley system (typically 95%), T_{da} is the torque required to rotate the damper and r_p is the pulley ratio, given by the number of teeth on the turbine and damper pulleys (Z_t/Z_d).

Via selection of the the pulley ratio, the resistance torque provided by the damper system is able to be controlled. However, as the pulley ratio is varied, so too is the relationship between turbine rotational speed, N_t and damper rotational speed N_{da}, as given by:

$$N_{da} = N_t r_p \tag{2.3.4}$$

Therefore, if the rotational speed of the turbine is known, Equations 2.3.3 and 2.3.4, and Figure 2.3.1 can be used to determine the rotational speed of the

damper, the torque provided by the damper at this speed and the torque requirement at the central turbine shaft.

2.3.4 Mechanical resistance of rotating components

Frictional forces originating from the relative motion of shafts and components in the turbine model contribute to the total mechanical resistance torque. These components include the bush shaft, bearings, radial lip seals and the blade-pitch-control pulley system. The total rotational resistance originating from these can be described by:

$$T_2 = \sum T_{be,i} + \sum T_{s,i} + T_p \tag{2.3.5}$$

where $\sum T_{be,i}$ is the total resistance torque from the bearings and bush shaft, $\sum T_{s,i}$ is the total resistance torque from the radial lip seals and T_p is the resistance torque originating from the blade-pitch-control pulley system. Each of these is discussed in the following sections.

2.3.4.1 Bearings and bushes

The turbine model incorporates seven bearings and a bush shaft that mount each of the three blade shafts and the central turbine shaft. Bearings and bushes are of course designed to minimise rotational resistance and therefore their effect is neglected here, i.e $\sum T_{be,i} = 0$. However, it is important to note that during the course of the flume experiments in particular, contaminants, especially sand particles, may have entered the bearings and led to increased resistance to rotation. However, it is not possible to estimate the magnitude of this effect here.

2.3.4.2 Radial lip seals

Four radial lip seals, or rotary shaft seals, are used in the turbine model. As radial lip seals are designed to prevent penetration of fluid (or other contaminants) from the outside, it is necessary that the seals exert a contact force on the shafts, in turn causing resistance to rotation. The performance of radial lip seals is complex and has been a topic of great interest in the field of tribology over

a number of decades (Stakenborg, 1988; Horve, 1992). A large number of parameters effect sealing performance and include seal geometry, material, fluid viscosity, fluid pressures, temperatures, shaft rotational speed, shaft surface roughness and time in service (Plath et al., 2005). It is therefore very difficult to predict the resistance torque provided by a radial lip seal and only empirical data for a particular use conditions can give an accurate value, despite attempts to computationally model their behaviour (Frölich et al., 2014). Despite this, radial lip seal manufacturer Parker gives the following as an approximation for resistance torque from a single seal acting on component i (Parker, 2006):

$$T_{s,i} \approx 14\, D_i^2\, N_i^{1/3} \tag{2.3.6}$$

where $T_{s,i}$ is the rotational resistance acting on the component (i.e., shaft), D_i is the shaft diameter and N_i is the shaft rotational speed measured in revolutions per minute (RPM). However, it is noted that there is a large uncertainty of $\pm 50\%$ in order to account for different levels of lubrication. Although this equation cannot be use to give an accurate estimation of the rotational resistance provided by the radial lip seals, it can be used to give an indication of the approximate magnitude of the resistance in relation to that originating from other sources.

2.3.4.3 Blade-pitch-control pulley system

The synchronous pulley system used to control the variation of blade-pitch with rotation of the turbine is a major source of mechanical rotational resistance in the turbine model. This is because of the frictional forces generated from the wrapping of the three timing belts around the central pulley wheels as each belt tooth engages and disengages with the pulley teeth.

It is necessary that the timing belts are kept relatively tight, in order to avoid slip in the system which would cause misalignment of the blades in relation to each other and the direction of the flow. Therefore, wheels are also incorporated into the design that keep the belts under tension (but are not shown in Figure 2.2.2 to aid clarity). Prior to the experiments the location of the wheels and therefore tension in the belts was set manually and although steps were taken to achieve consistent tension in each belt, it is probable that a variation existed between them. This would have led to an asymmetric load acting on the central turbine

shaft as the turbine rotated and introduced further resistance, due to contact between the shaft and inside of the bush for example.

Unfortunately it is not possible to analytically estimate in any reliable way the rotational resistance caused by the blade-pitch-control system. However, from manual inspection and handling of the turbine model, it is noted that the resistance to rotation greatly increases when the system is engaged (i.e. the timing belts are attached) compared to when not engaged. This indicates that the rotational resistance originating from this system is significantly greater than from the other mechanical sources.

2.3.5 Hydrodynamic resistance of rotating surfaces

All components of the turbine model that simply rotate about the central axis (i.e. not the blade shafts or bearing mounts that revolve about the central axis), experience a resistance to rotation due to the skin friction drag generated on their surfaces. These surfaces include the housing inner and outer plates, the housing cylindrical surface, the end-plate inner and outer surfaces, both toothed disk surfaces and in the characterisation experiment only, the cylindrical surface of the spindle. The central turbine shaft also experiences skin friction on its rotating surface, but this is negligible in comparison to the other surfaces and is therefore ignored. This effect may be negligible if the turbine was operating in air, but not so in water due to the much greater density, and it is therefore important to estimate the magnitude.

The rotating surfaces that experience skin friction drag can be described as either disks (i.e. flat circular faces) or cylinders, so that the total resistance torque due to skin friction is given by:

$$T_3 = \sum T_{D,i} + \sum T_{C,i} \tag{2.3.7}$$

where $\sum T_{D,i}$ is the total torque originating from the disk surfaces and $\sum T_{C,i}$ is the total torque originating from the cylinder surfaces. The following sections describe methods for estimating the resistance torques for both of these.

2.3.5.1 Rotating disk skin friction

The rotational resistance torque, or moment, generated by skin friction acting on a single face of a rotating disk can be calculated by integrating the drag force, acting at a particular radial position, over the entire face of the disk. This leads to the definition of a moment coefficient for the rotating disk, from which the resistance torque, $T_{D,i}$, can be calculated:

$$T_{D,i} = {}^{1}/_{2}\,\rho\,\omega_i^2\,a_i^5\,C_{M,i} \tag{2.3.8}$$

where ρ is the fluid density, ω_i is the disk rotational velocity, a_i is the disk radius and $C_{M,i}$ is the moment coefficient for the rotating disk. Momentum analysis for this type of problem was first performed by Von Kármán (1921) who obtained expressions for the moment coefficient, in the following form for laminar flow:

$$C_{M,i} = c_1\,Re_{\omega,i}^{-1/2} \tag{2.3.9}$$

and the following form for turbulent flow:

$$C_{M,i} = c_2\,Re_{\omega,i}^{-1/5} \tag{2.3.10}$$

Here c_1 and c_2 are constants and $Re_{\omega,i}$ is the rotational Reynolds number, as given by:

$$Re_{\omega,i} = \frac{\omega_i\,a_i^2}{\nu} \tag{2.3.11}$$

where ν is the fluid kinematic viscosity.

Cochran (1934) adjusted von Kármán's coefficient value for the laminar flow expression, to give $c_1 = 1.935$, whilst von Kármán gave the value $c_2 = 0.073$ for turbulent flow. Theodorsen and Regier (1944) confirmed these relationships with experimental results over a range of Reynolds numbers and various sized disks. It was found that transition from laminar to turbulent flow occurred at a maximum Reynolds number of 310,000 although the theoretical minimum (the intersection of the two relationships) is 57,000.

The above given values of c_1 and c_2 are only valid for disk surfaces rotating in open environments with no account taken of the proximity of walls to the rotating surfaces. Numerous authors have attempted to address this problem, including Daily and Nece (1960) who presents momentum coefficient expressions for

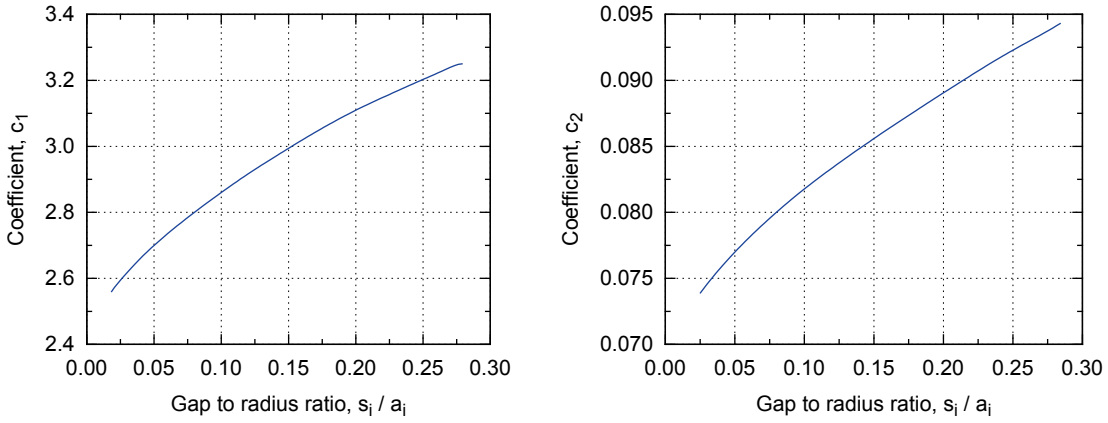

(a) Laminar flow

(b) Turbulent flow

Figure 2.3.2: Variation of momentum coefficient constant with gap to radius ratio for rotating disks in close proximity to stationary walls

four types of flow regimes occurring between a rotating disk and stationary wall. These regimes are the combinations of merged boundary layer and separate boundary layer conditions, for both laminar and turbulent flows, and are dependant upon the ratio s_i/a_i, where s_i is the spacing between disk and wall. Daily and Nece found that for $s_i/a_i > 0.05$ only the separate boundary layer regimes occur at all but the lowest Reynolds numbers. The expressions describing the momentum coefficient for these regimes take the same form as Equations 2.3.9 and 2.3.10, but now the constants c_1 and c_2 are functions of s_i/a_i, as shown in Figure 2.3.2 for both laminar and turbulent regimes. Daily and Nece also present experimental results that match the expressions to within 3% and confirmed their validity in the range $10^3 < Re_{\omega,i} < 10^7$.

The values of c_1 and c_2 values are therefore dependent upon both component rotational velocity and the spacing from adjacent faces, as discussed further in Section 2.3.5.3.

2.3.5.2 Rotating cylinder skin friction

The rotational resistance torque, $T_{C,i}$, generated by the skin friction acting on a cylindrical face rotating about its axis can be calculated from the product of drag force acting on the surface and the radius of the cylinder, leading to the following relationship:

$$T_{C,i} = \rho\,\omega_i^2\,\pi\,l_i\,a_i^4\,C_{Dr,i} \tag{2.3.12}$$

where l_i is the component (i.e., cylinder) width, a_i is the cylinder radius and $C_{Dr,i}$ is the drag coefficient for the force acting upon the surface. Lamb (1932) gives the following relationship for laminar flow:

$$C_{Dr,i} = \frac{4}{Re_{\omega,i}} \tag{2.3.13}$$

Theodorsen and Regier (1944) presents experimental results that confirm this relationship to be accurate at the very lowest Reynolds numbers, but above $Re_{\omega,i} \approx 80$ transition to turbulent flow occurs, with the drag coefficient given by the logarithmic relationship:

$$\frac{1}{\sqrt{C_{Dr,i}}} = -0.6 + 4.07 \log(Re_{\omega,i} \sqrt{C_{Dr,i}}) \tag{2.3.14}$$

2.3.5.3 Prediction of total skin friction resistance

Using Equations 2.3.8 to 2.3.14 and the model dimensions given in Table 2.2.2, the variation of resistance torque due to rotating surfaces has been estimated over an appropriate range of turbine rotational speeds. These estimations are valid for the experimental model rotating in a tank of stationary water, as in the resistance characterisation experiment.

The housing and end-plate inner surfaces are taken to be in an open environment, with no wall proximity effects, whereas the outer surfaces are in close proximity to the support frame and so the appropriate relationships are used. Where necessary, transition from laminar to turbulent flow is assumed to take place at the theoretical minimum Reynolds number, as discussed in Section 2.3.5.1.

The results of this analysis are presented in Figure 2.3.3 and it can be seen that the housing cylindrical surface provides the dominant contribution to the rotational resistance, followed by the housing circular faces, end-plate faces, toothed disk faces and the spindle cylindrical face. The difference in resistances provided by the inner and outer faces of the housing, although of the same diameter, is due to the proximity of the outer plate to the support frame wall. The same is true for the end-plate inner and outer surfaces which, due the reduced diameter in comparison to the housing, contribute less rotational resistance. It should be noted that each of these plates has been treated as

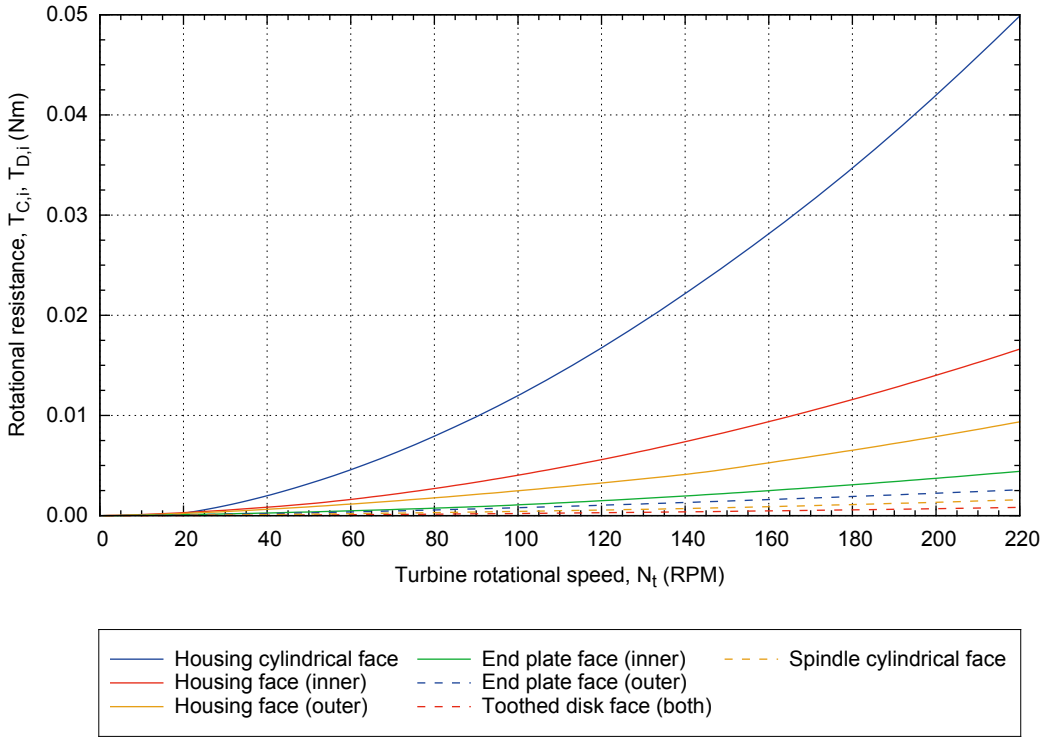

Figure 2.3.3: Estimated variation of skin friction resistance with turbine rotational speed, for a number of component surfaces in the experimental model

being a plain smooth surface and the effects of the bearing housings attached to the inner surfaces in particular, have been ignored.

Note, the variation of moment coefficient (used to predict the rotational resistance due to disk skin friction) assumed the lowest theoretical transition point (i.e., $Re_{\omega,i} = 57,000$). This gave the highest possible prediction of resistance at higher rotational speeds, as turbulent boundary layers are associated with increased skin friction. The maximum transition point ($Re_{\omega,i} = 310,000$) was also trialled and this reduced the predicted resistance due to the various disk faces. For example, the maximum inner housing face resistance was reduced by 35%. The uncertainty in transition point therefore results in an uncertainty in the predicted rotational resistance. However, the dominant contribution to the rotational resistance is due to skin friction acting on the housing cylindrical face, where there is no such uncertainty in transition point. Therefore the overall uncertainty is negligible and is ignored.

2.3.6 Hydrodynamic resistance of translating components

The primary component parts that translate through the fluid as the turbine rotates are, of course, the blades. However, when operating in a fluid flow, these provide the driving torque and are not of interest here. Instead, this section concerns the components that provide resistance to the rotation as they revolve about the central turbine axis. These include a low number of exposed bolt heads, on the housing surface for example, as well as the bearing mounts on the housing and end-plate inner surfaces. Also, in the characterisation experiments the blades are replaced with plain shafts, which contribute to the rotational resistance. The drag from small components, such as the bolt heads, is ignored in this analysis, as their frontal area is much less than those of the dominant translating components, the cylindrical bearing mounts and shafts.

The total resistance torque due to hydrodynamic drag affecting components that translate through the water can be given by:

$$T_4 = \sum T_{E,i} \tag{2.3.15}$$

where $T_{E,i}$ is the torque due to drag acting on an individual component. This torque is given by:

$$T_{E,i} = F_{Dg,i} R_i \tag{2.3.16}$$

where R_i is the radius of the component's revolution about the central axis and $F_{Dg,i}$ is the linear drag force acting upon it, as given by:

$$F_{Dg,i} = {}^1\!/_2 \rho U_i^2 A_i C_{Dg,i} \tag{2.3.17}$$

Here A_i is the frontal area of the component facing the direction of movement, U_i is the linear velocity of the component, given by:

$$U_i = \omega_0 R_i \tag{2.3.18}$$

and $C_{Dg,i}$ is the drag coefficient, dependant upon shape, aspect ratio (AR) and diameter-based Reynolds number, $Re_{D,i}$, as given by:

$$Re_{D,i} = \frac{U_i D_i}{\nu} \tag{2.3.19}$$

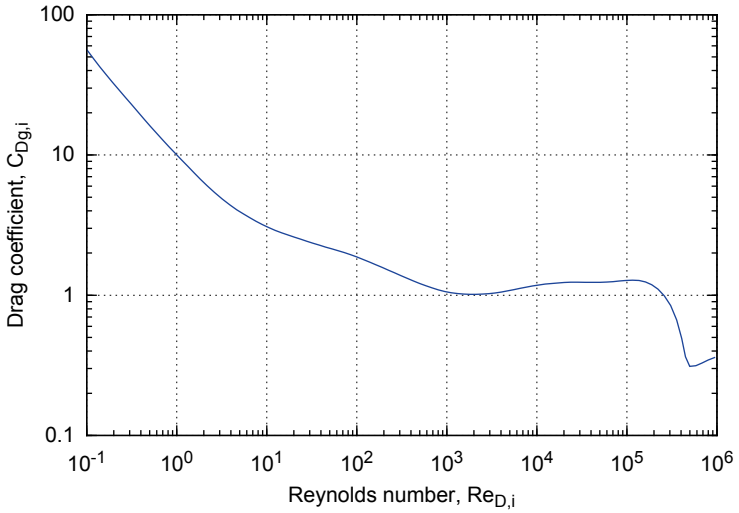

Figure 2.3.4: Variation of drag coefficient with Reynolds number for an infinite length smooth cylinder (adapted from Schlichting (1979))

For a circular cross-section cylinder of infinite length, the variation of drag coefficient $C_{Dg,i}$ with Reynolds number $Re_{D,i}$ is shown in Figure 2.3.4.

White (2008) gives values for finite aspect ratio cylinder drag coefficients, indicating they are valid for laminar flow from approximately $10^3 < Re_D < 10^5$. For example, for the blade shaft aspect ratio of $AR = l_b/D_b = 37$, the drag coefficient is approximately 81% of the infinite length value. For the bearing mount aspect ratio of $AR = l_m/D_m = 0.3$, it can be extrapolated that the drag coefficient is approximately 50% of the infinite length value. However, it should also be noted that these values correspond to cylinders with open ends and the shafts of the turbine model are situated between the bearing mounts, which themselves are mounted onto the housing or end plate inner surfaces. Therefore there is an uncertainty in the estimation of the drag coefficient for these components, which will be further considered in Section 2.4.4.3.

Using Equations 2.3.16 to 2.3.19 and the model dimensions given in Table 2.2.2, the variation of resistance torque due to the drag forces acting on components translating through stationary water has been estimated over an appropriate range of turbine rotational speeds, as presented in 2.3.5. The effect of varying the drag coefficient depending on the cylinder aspect ratio is also shown for the shaft resistance. It can be seen that the estimated resistance torque due to the three plain blade shafts is dominant over that from the six blade bearing mounts and also the values of resistance due to rotating surfaces, as presented previously in Figure 2.3.3. Therefore it is estimated that the resistance due to

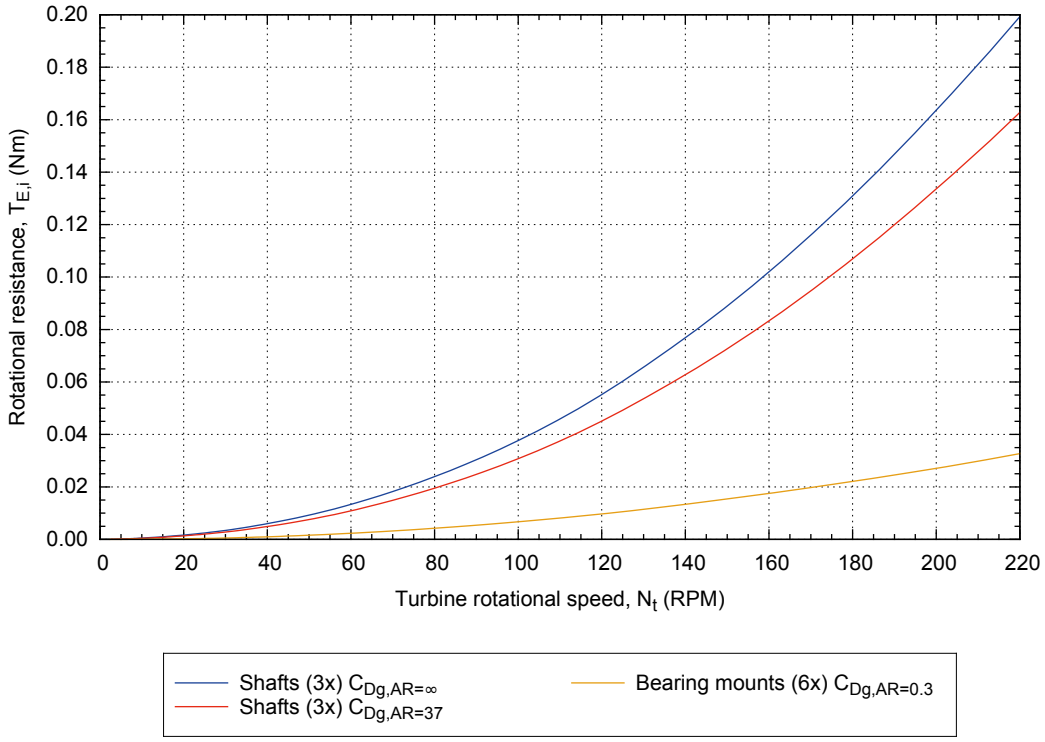

Figure 2.3.5: Estimated drag resistance due to component part translation versus turbine rotational speed

all hydrodynamic forces acting on the turbine model's components as it rotates in stationary water will be dominated by the drag acting on the plain shafts.

2.3.7 Conclusion of section

This section has presented analysis of the multiple sources of rotational resistance that exist within the experimental MRL turbine model. These include mechanical and hydrodynamic resistances, both controlled and uncontrolled. A number of relationships that describe the variation of resistance with turbine rotational speed have been developed; these predict that the resistance due to translating shafts (used as blade replacements) will provide the dominant resistance torque when the turbine is rotating within a tank of stationary water. Unfortunately, no analytical estimation of the mechanical resistance due to the blade-pitch-control pulley system has been possible, and this will be estimated indirectly from experimental work presented in the following section.

2.4 Resistance Characterisation Experiment

2.4.1 Aim of the experiment

During the laboratory flume experiments described in Section 2.5, the turbine model's inherent resistance to rotation was augmented and varied by use of the rotary damper system previously described. In addition to the variable resistance provided by this system, resistance to rotation was also caused by both hydrodynamic forces effecting the wetted turbine components and mechanical forces inherent to the turbine's operation, as discussed in Section 2.3.

Therefore, the aim of the experiments presented in this section was to measure the total hydrodynamic and mechanical rotational resistance and in particular, the variation of these with rotational speed. This enables a value for the total rotational resistance to be estimated for each test condition used in the flume experiments described in Section 2.5 and therefore enable more reliable comparison to be made with computational results presented in Chapter 5.

2.4.2 Experimental approach

The basic approach used in this experiment was to apply a known load torque to the central turbine shaft and measure the rotational speed of the turbine once it reached an approximately constant value. By doing this, the total rotational resistance of the turbine for the particular rotational speed is found.

The experiment was set up as shown in Figure 2.4.1. The turbine model, supported by the frame shown in Figure 2.2.1, was fixed into a tank of stationary water and the driving torque applied by a mass and pulley system. The rotational speed was measured at a rate of 5 Hz by the toothed disk and hall sensor system linked to a control box outside of the tank.

When the turbine is operating in a fluid flow, it is the forces generated by the fluid flowing over the blades that of course act to drive the rotation of the turbine. However, in this experiment the aim is to measure only the rotation to resistance caused by the mechanical and hydrodynamic forces acting upon the components of the turbine, not including the blades. Therefore it would have been ideal if the blades, including shafts, were removed completely for this experiment. However, in order to assess the rotational resistance caused by

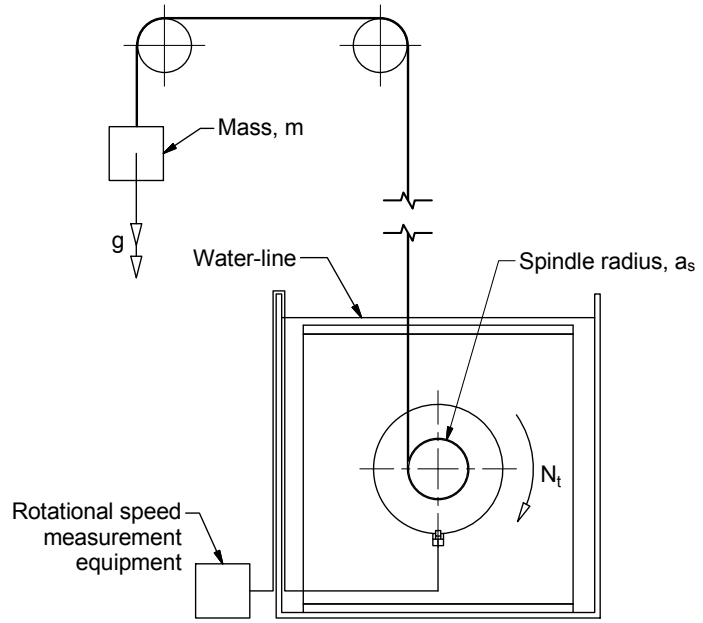

Figure 2.4.1: Turbine resistance characterisation experimental setup

the blade-pitch-control pulley system, the blade shafts needed to be included in this area. In addition, the frictional resistance due to the blade shafts rotating in the radial lip seals mounted to the housing inner plate also needed to be assessed. It was not possible to mount blade shafts only in the housing section of the turbine and therefore full length blade shafts were used, which ran from the bearings in the end-plate to the blade pitch-control system.

In order to drive the rotation of the turbine in the absence of the blades or a water flow, a torque was applied to the turbine from an external force. As the aim of the experiment was to assess the variation of rotational resistance with rotational speed, it was important that the external source of torque did not also prescribe the rotational speed. Therefore the external torque was provided by a mass free to drop from height due to the acceleration of gravity. The mass was attached via string and a pulley wheel to the turbine spindle, directly attached to the central turbine shaft. Pulley slip was not possible, as the end of the string was directly attached to the spindle. As the mass was released from height, the constant torque applied to the turbine caused its rotational acceleration until a constant speed was reached, where the load torque equalled the resistance torque of the turbine at this rotational speed. This relationship is given by:

$$T_l = m g a_s = T_r \tag{2.4.1}$$

where T_l is the load torque, provided by the mass, m, gravity, g, and spindle radius a_s.

By repeating the experiment with various values of m, the relationship between resistance torque and rotational speed was assessed. The experiment was firstly conducted without the additional rotary damper system attached, in order to measure only the rotational resistance of the turbine components themselves. The experiment was then repeated with the addition of the damper system and two different pulley ratios in order to vary the total resistance torque. By comparison of these results to those without the damper system, the resistance torque provided by the damper is able to be compared to the values given by the damper manufacturer's data.

It is also important to note that, for practical reasons, this experiment was conducted with the turbine located in a tank of non-flowing water. It would have been preferable if the experiment was conducted with the turbine in a recirculating flume, in order to more accurately assess the resistance due to hydrodynamic forces acting upon the components rotating in a flow of water, rather than nominally stationary water. The velocity of the flow could have also been varied in order to assess the effect of this and directly link to the flow velocities used in the experiments presented in Section 2.5. However, this was not practically possible due to both available time at the experimental flume facility and the limited space available for the dropping mass system to be set up above the flume.

2.4.3 Experimental results

2.4.3.1 No additional damper load

The turbine, without the optional damper system engaged, was subjected to a range of external torques as detailed in Table 2.4.1 along with the qualitative result for each, in terms of whether the turbine reached an approximately constant rotational speed. It can be seen that for the lowest applied load torque the turbine did not start to rotate, indicating the approximate starting torque due to mechanical resistances. For the next two incremental increases in load torque (due to approximate 0.1kg increases in load mass), the turbine started to rotate, but did not reach a constant rotational speed in the time it took the mass to reach the ground from the available drop height. The highest six load

Table 2.4.1: External driving torques and qualitative results (no additional damper load, i.e. $r_p = 0$)

Mass, m *kg*	Load torque, T_l *Nm*	Turbine rotation?	Constant speed reached?
0.810	0.219	N	N
0.912	0.246	Y	N
1.012	0.273	Y	N
1.114	0.301	Y	Y
1.214	0.328	Y	Y
1.320	0.356	Y	Y
1.421	0.383	Y	Y
1.522	0.411	Y	Y
1.622	0.438	Y	Y

torques did however accelerate the turbine to reach an approximately constant rotational speed, with the variation over time shown in Figure 2.4.2 for three repeat readings at each load torque. It can be seen that for each of the load torque results presented, the turbine rotational speed accelerates at a high rate from rest and then trends towards an approximately constant value until it suddenly decelerates back to rest due to the mass reaching the ground and no load torque being applied.

2.4.3.2 Addition of damper load

The experiments were repeated with the additional resistance torque (T_1) provided by the damper and pulley system. Two pulley ratios of $r_p = 0.3$ and $r_p = 0.5$ were used, in order to confirm the behaviour of the damper and pulley system was as expected. Five different load torques, with three repeat readings for each, were used for each of the pulley ratios. The resulting variation of measured rotational speed with time is shown for each of the load torques in Figures 2.4.3 and 2.4.4. As with the $r_p = 0$ results, the applied load torque caused the turbine to accelerate from rest to a relatively constant speed before decelerating once the mass reached the ground.

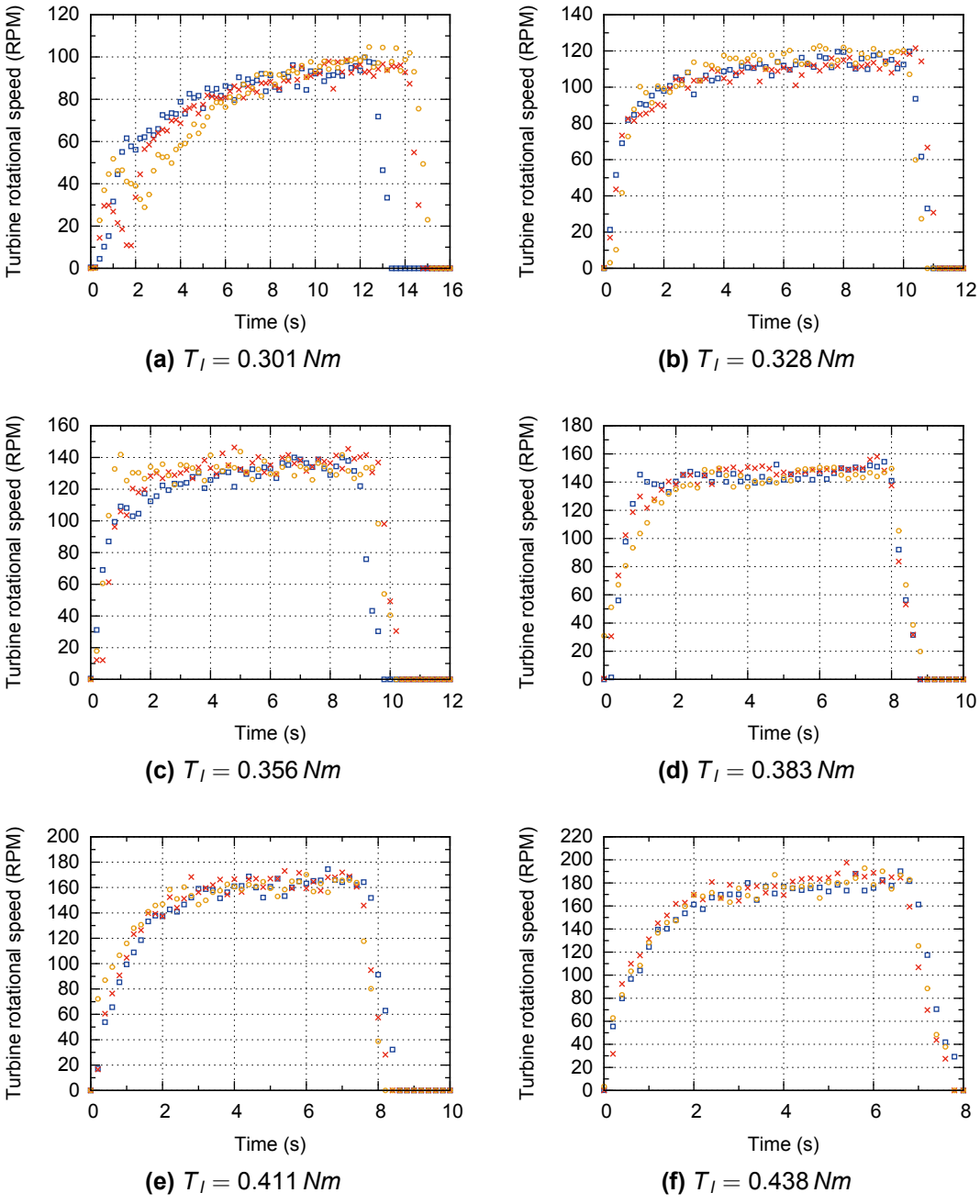

(a) $T_l = 0.301\,Nm$ **(b)** $T_l = 0.328\,Nm$

(c) $T_l = 0.356\,Nm$ **(d)** $T_l = 0.383\,Nm$

(e) $T_l = 0.411\,Nm$ **(f)** $T_l = 0.438\,Nm$

Figure 2.4.2: Variation of turbine rotational speed with time (no additional damper load, i.e. $r_p = 0$)

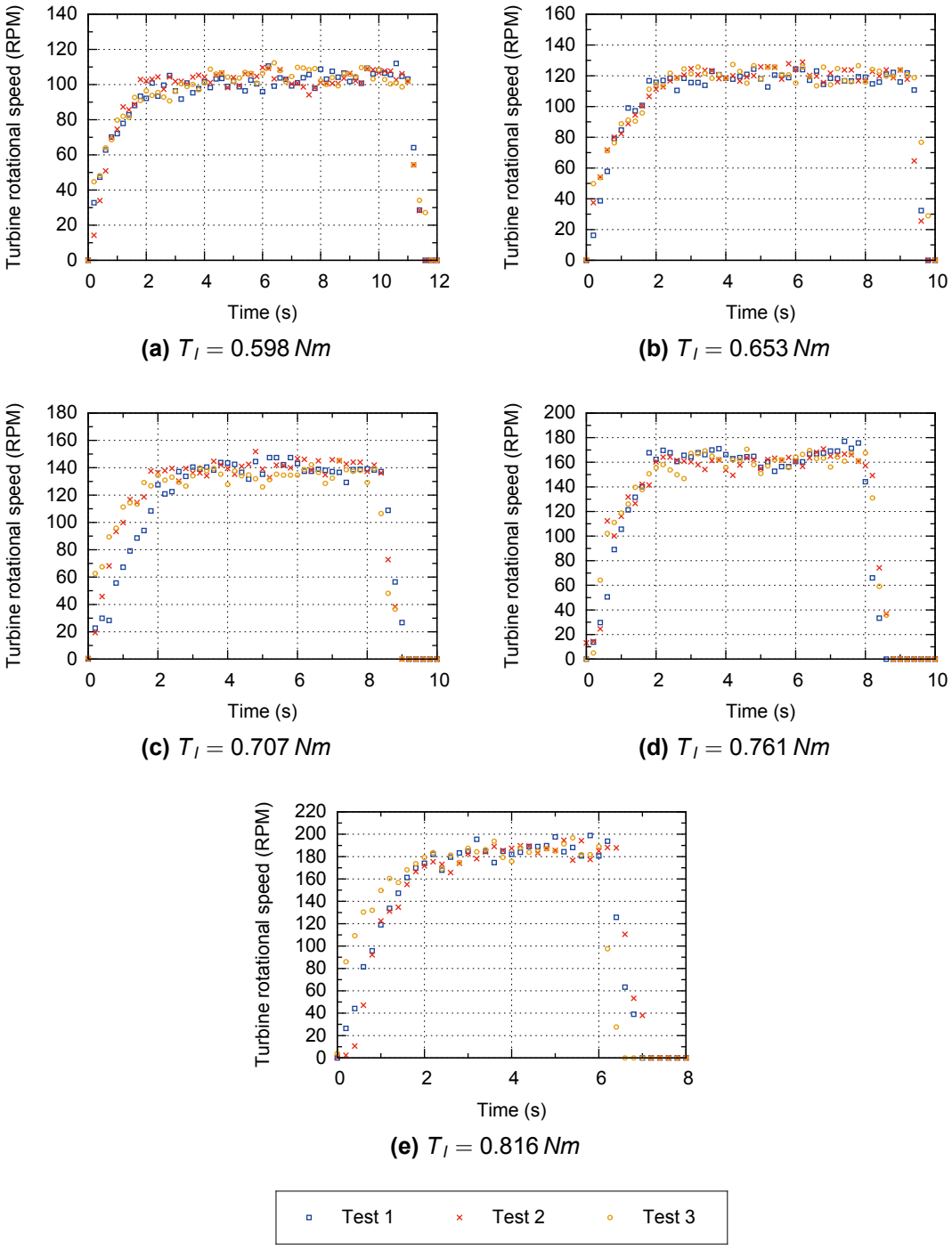

(a) $T_l = 0.598\,Nm$ **(b)** $T_l = 0.653\,Nm$

(c) $T_l = 0.707\,Nm$ **(d)** $T_l = 0.761\,Nm$

(e) $T_l = 0.816\,Nm$

Figure 2.4.3: Variation of turbine rotational speed with time (with pulley ratio $r_p = 0.3$)

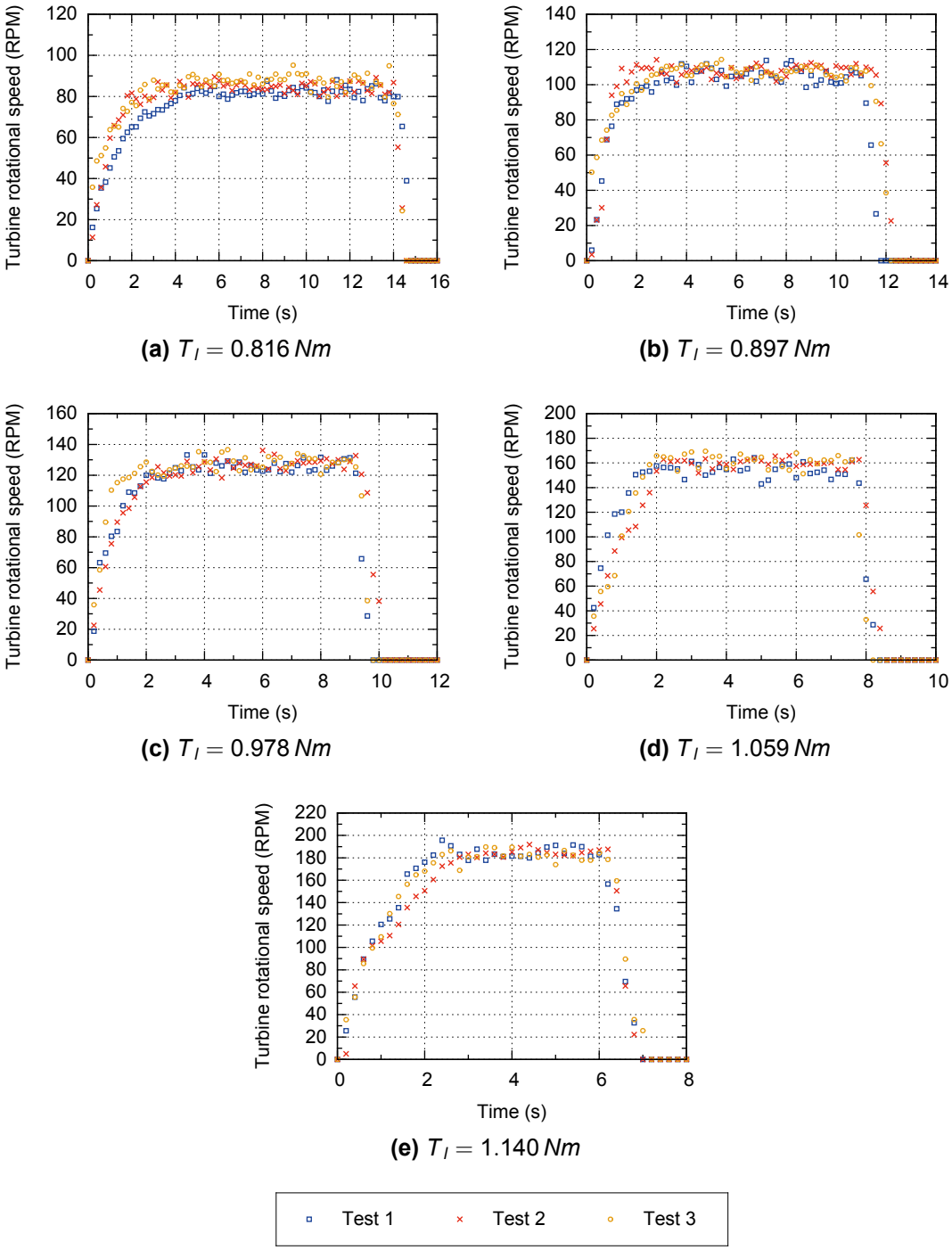

(a) $T_l = 0.816\,Nm$ **(b)** $T_l = 0.897\,Nm$

(c) $T_l = 0.978\,Nm$ **(d)** $T_l = 1.059\,Nm$

(e) $T_l = 1.140\,Nm$

Figure 2.4.4: Variation of turbine rotational speed with time (with pulley ratio $r_p = 0.5$)

2.4.4 Analysis of experimental results

2.4.4.1 Variations in measurement of rotational speed

The experimental results show that when a relatively constant rotational speed was reached there was still a fluctuation over time in the measured readings for each of the forty-eight tests carried out. In order to compare results and perform further analysis it is therefore necessary to calculate a mean value of rotational speed over the 'constant' speed range, which lasted for approximately three or four seconds in each test. As the rotational speed was measured, or sampled, at a rate of only 5 *Hz* and the mean value calculated over a range of between three and four seconds, it is recognised that this sample mean does not necessarily represent the true mean rotational speed of the turbine in the 'constant' region for each specific test. However, it is believed this method is sufficient for this analysis. Therefore, the mean rotational speed results from all the individual tests are presented in Figure 2.4.5, where the values are plotted against the load torque applied to the turbine.

The results show that for all three tested values of damper pulley ratio, the mean turbine rotational speed reached increases with increasing load torque. In general, with each incremental increase in load torque, an incremental increase in rotational speed was measured. However, there is also a variation between the mean rotational speeds calculated from the three repeat tests at each load torque. As the purpose of this analysis is to allow an estimation of turbine resistance torque to be made for any given rotational speed and damper pulley ratio combination, this variation in the mean rotational speed must be taken into consideration in any further analysis.

In order to do this, the (sample-averaged) mean value is calculated from the three (time-averaged) mean rotational speeds measured at each applied load torque. Tolerance intervals have then been calculated in order to indicate the statistical uncertainty in the rotational speed measured for each applied load.

The calculation of a tolerance interval *TI*, centred around a sample mean is given by:

$$TI = \bar{N} \pm k_{TI} S_N \tag{2.4.2}$$

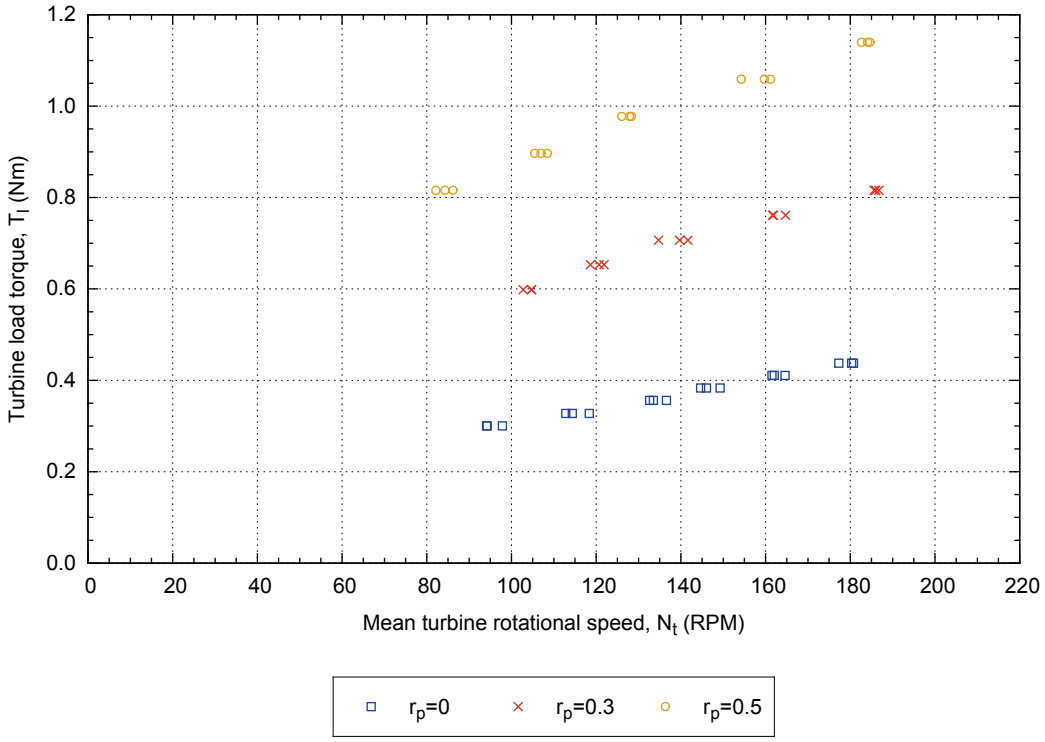

Figure 2.4.5: Applied load torque versus mean measured rotational speed

where $\bar{N}$ is the sample mean value, S_N is the sample standard deviation and k_{Tl} is a factor chosen so that the interval covers a proportion, q, of the population with confidence level Γ (Croarkin and Tobias, 2006). The value of $k_{Tl} S_N$ is also called the tolerance value or TV. Assuming the data is sampled from a normally distributed population, κ can be approximated by:

$$\kappa = \sqrt{\frac{(n_s - \frac{1}{n_s})\,\zeta^2_{(1-q)/2}}{\chi^2_{1-\Gamma,\,n_s-1}}} \tag{2.4.3}$$

where $\chi^2_{1-\Gamma,\,n_s-1}$ is the critical value of the chi-square distribution with $n_s - 1$ degrees of freedom that is exceeded with probability Γ, $\zeta_{(1-q)/2}$ is the critical value of the normal distribution associated with cumulative probability $(1 - q)/2$ and n_s refers to the sample size (Howe, 1969). Typically, proportion and confidence levels varying from 90% to 99% are used. Of course, as the level of confidence or the proportion of the population to be covered increases, the tolerance interval increases in size. Also, as the sample size increases, the tolerance interval will decrease in size.

For this study the three repeat measurements of mean rotational speed at each

load torque can be seen as a sample size of three, where the total population would be the measured mean rotational speeds from a very large number of tests that could be undertaken at that load torque. Using proportion and confidence levels of 90%, κ is found to be 5.85 and from this tolerance values have been calculated as shown in Table 2.4.2. These indicate the range of values below and above the sample mean that 90% of the (time-averaged) mean rotational speeds from repeated tests would be expected to lie, with a 90% level of confidence. As the sample sizes are only three in all cases, the tolerance intervals are seen as being conservatively large and therefore proportion and confidence values of 90% are seen as sufficiently high for this study. The results show that the tolerance intervals vary between 3.4 and 21.3 RPM, or between 1.8 and 15.1% of the mean value, reflecting the range of variations between (time-averaged) mean rotational speeds measured in all sets of three tests undertaken.

2.4.4.2 Estimation of the turbine model rotational resistance

The sample mean values of rotational speed and corresponding tolerance intervals are shown in Figure 2.4.6a, plotted against the corresponding load torque, or turbine rotational resistance, for $r_p = 0$. Also shown are curves that predict the variation of the turbine model's rotational resistance with rotational speed. These have been derived by adjusting each of the tested load torque values by the mechanical and hydrodynamic resistance torques estimated by the methods described in Section 2.3 (the individually adjusted results are not shown in order to aid clarity).

In order to construct the curves, each total load value has firstly been adjusted by subtracting the total estimated resistance torque due to drag forces acting on the revolving shafts and bearing mounts (T_4). Next each torque value has been further adjusted by subtracting the total estimated resistance torque due to skin friction forces acting on rotating surfaces (T_3). This leaves the estimated resistance forces due to all mechanical resistances (T_2). From this, an estimation of the rotational torque due to the radial lip seals ($\sum T_{s,i}$) has been subtracted, leaving only the estimated mechanical resistances from the blade-pitch-control pulley system (T_p). The line of best fit through the individually adjusted results is linear and approximately constant. By extrapolating these lines back across the entire rotational speed range, the intercept of the y-axis

Table 2.4.2: Sample mean, standard deviation and tolerance values for measured turbine rotational speed

Damper ratio, r_p	Load torque, T_l *Nm*	Mean of sampled speeds *RPM*	St. dev. of sampled speeds *RPM*	Tolerance value *RPM*	TV / mean %
N/A	0.301	95.4	2.1	12.4	13.0
	0.328	115.2	2.9	16.7	14.5
	0.356	134.2	2.1	12.2	9.1
	0.383	146.7	2.4	13.8	9.4
	0.411	162.7	1.7	9.7	5.9
	0.438	179.5	1.9	11.0	6.1
0.3	0.598	104.1	1.1	6.6	6.3
	0.653	120.4	1.6	9.5	7.9
	0.707	138.7	3.6	20.9	15.1
	0.761	162.7	1.7	10.1	6.2
	0.816	186.1	0.6	3.4	1.8
0.5	0.816	84.2	2.0	11.8	14.0
	0.897	107.0	1.5	8.8	8.2
	0.978	127.4	1.2	7.1	5.6
	1.059	158.4	3.6	21.3	13.4
	1.140	183.8	1.0	6.0	3.3

indicates a load torque of approximately 0.225 Nm is required for the turbine to start rotating. This corresponds favourably with the experimental findings, where a load torque of 0.219 Nm did not initiate rotation, but a load torque of 0.246 Nm did. From this linear line of best fit, curves for the addition of $\sum T_{s,i}$, T_3 and T_4 have been added, confirming the derived curve for the total resistance fits with the mean measured experimental results.

It can be seen that at lower rotational speeds the estimated resistance torque due to the blade-pitch-pulley system is highly dominant over both other mechanical resistances and the hydrodynamic resistances. As the rotational speed increases, the hydrodynamic resistances increase until both the predicted hydrodynamic and mechanical resistances are approximately equal at the highest rotational speed of interest. As mechanical friction forces do not generally vary with speed, and the hydrodynamic forces vary with the square of speed, the predicted behaviour is as expected.

2.4.4.3 Uncertainties in the estimation of rotational resistance

There are a number of sources of uncertainty in the predicted curves of rotational resistance. These primarily include uncertainty in the estimation of resistance from the hydrodynamic and mechanical sources detailed in Section 2.3, but the uncertainty in the measured mean rotational speeds is also taken into account. Uncertainty limits for the estimation of resistance from each of the hydrodynamic and mechanical sources are detailed below.

Mechanical resistance from rotary damper system, T_1 The performance curve shown previously in 2.3.1 shows $\pm 10\%$ uncertainty bands for the damper torque, as stated by the manufacturer. The validity of these performance bands are confirmed in Section 2.4.4.4.

Mechanical resistance from rotating components, T_2 The resistance due to the radial lip seals, $\sum T_{s,i}$ is predicted by equation 2.3.6, which is stated with $\pm 50\%$ uncertainty. The blade pitch control pulley system resistance, T_p is derived from this process and therefore the uncertainty bands are also derived. While the uncertainty in $\sum T_{s,i}$ is large and the use of equation 2.3.6 is acknowledged to be unreliable (as the performance of radial lip seals is difficult

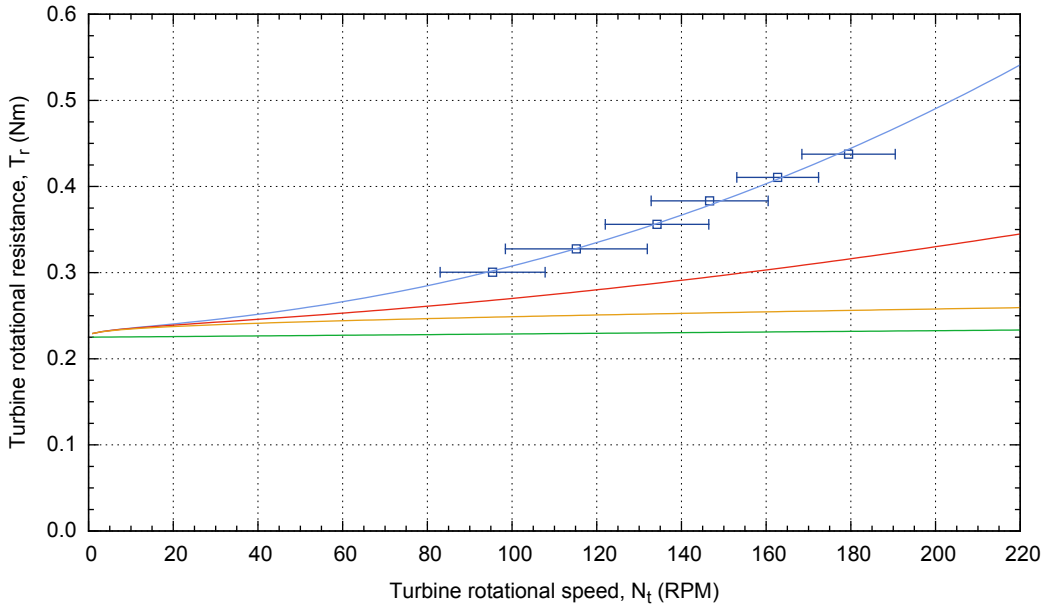

(a) Showing best estimate curves only

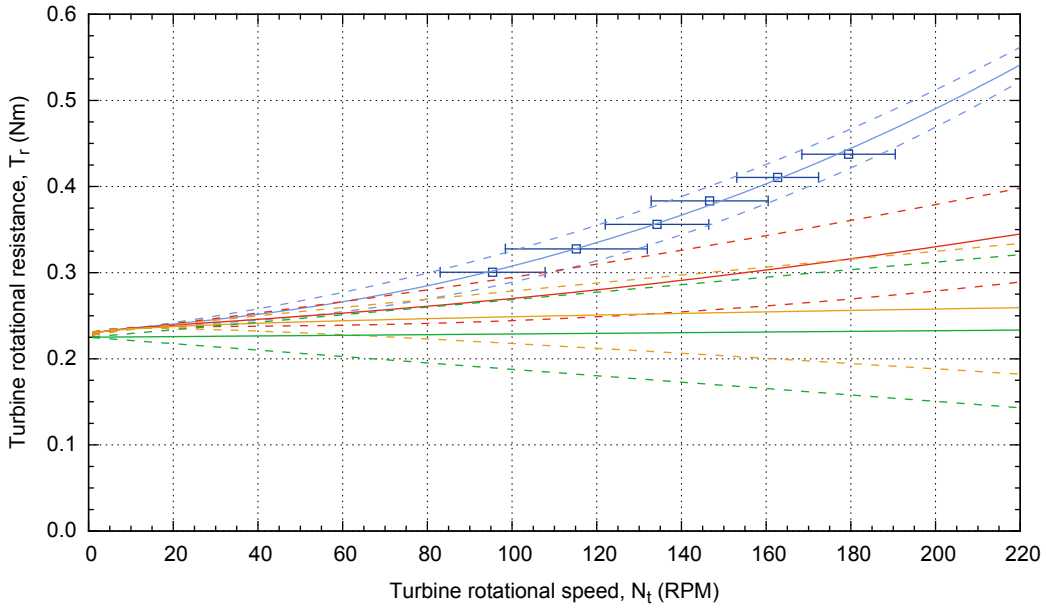

(b) Showing cumulative uncertainty curves (dashed lines)

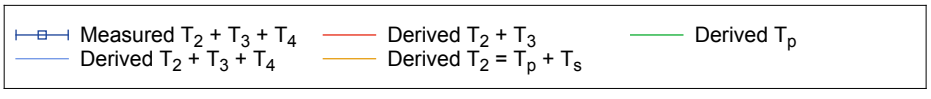

Figure 2.4.6: Measured and predicted turbine rotational resistance versus rotational speed (without optional damper, i.e. $r_p = 0$)

to predict), this prediction is not crucial to the study and is only used to suggest a comparison of the relative magnitude of the radial lip resistance in relation to the other mechanical sources.

Hydrodynamic resistance from rotating surfaces, T_3 The prediction of resistance torque due to skin friction acting on rotating surfaces of the model is reliant on the accurate prediction of drag coefficients for both rotating disks and cylinders. Also, the model has been simplified by ignoring the presence of the bearing mounts on the inner surfaces of the housing and end plate, and also the interaction between the various rotating surfaces. There is no uncertainty given for the analytical and empirical equations used to predict this resistance and so an uncertainty of $\pm 25\%$ of the total predicted resistance from this source has been used for safety.

Hydrodynamic resistance from translating components, T_4 For the resistance provided by the shafts and bearing mounts revolving about the central axis, there is an uncertainty in the choice of drag coefficients used. For the shafts, the maximum drag coefficient is that of an infinite aspect ratio shaft and the minimum value is that for an aspect ratio of 37 (i.e. 81% of the upper limit). For the bearing mounts, there is greater uncertainty, as the estimation of 50% of the infinite aspect ratio value (for an aspect ratio of 0.3), is itself an extrapolation from the data in White (2008) and may not be reliable. It should be also noted that one end of each mount is located on a flat surface, which would tend the drag coefficient towards that of an infinite aspect ratio cylinder, although the other end is open, which would lead to reduced drag. There is also the interaction between the mount wakes and the boundary layer of the rotating plates to consider, which may negate the drag caused by the wake of the low aspect ratio mounts. Therefore a drag coefficient value of 50% of the infinite aspect ratio value is taken as a maximum estimate for the bearing mounts, and neglecting this drag altogether is taken as a minimum value estimate.

For the total resistance caused by the drag of translating components, the minimum predicted value therefore uses the lower drag coefficient for the shafts, while ignoring the bearing mounts drag, and the maximum uncertainty limit uses an infinite aspect ratio drag coefficient for the shafts and 50% of the infinite aspect ratio value for the bearing mount drag.

As a best estimate for the total resistance, the drag coefficient for an infinite aspect ratio cylinder is used for the shaft drag, and the mount drag is neglected. It is believed this accounts for the fact that the shafts are located between two plates and therefore the end losses would be reduced in comparison to open ended shafts, and the bearing mounts are located on the rotating disks, where the boundary layer would strongly interact with the mount wakes and therefore reduce their drag towards zero.

Combination of uncertainties The uncertainties described above have been combined in order to derive the uncertainty bounds shown in Figure 2.4.6b. The upper uncertainty bounds for the predicted curves have been derived by using the lower tolerance limits of each set of rotational speeds. Likewise, the lower uncertainty bounds have been derived from the upper tolerance limits. The uncertainty curves are cumulative as they are derived in the same order as the best estimate curves. For example, the lower uncertainty limit for T_p is derived by subtracting the maximum predicted values of T_4, T_3 and $\sum T_{s,i}$ using the upper tolerance limits of rotational speed. The derived uncertainty curves have then been used as a baseline in order to reconstruct the uncertainty curves around the predicted total resistance ($T_2 + T_3 + T_4$). These curves can also be seen as lines of best fit through the lower and upper tolerance limits. The uncertainty curves, like the best estimate curves, are only of interest here in order to derive a baseline T_p curve from which the prediction for total resistance over the full range of rotational speeds is constructed. However, the uncertainty in the prediction of resistances from the different sources becomes more important during the analysis of results from the flume experiments, as discussed in Section 2.5.2.2.

2.4.4.4 Confirmation of predicted rotary damper performance

The sample mean values of rotational speed and corresponding tolerance intervals, for the tests with and without the optional damper system attached, are shown in Figure 2.4.7, plotted against the corresponding load torque, or turbine rotational resistance. The predicted best estimate and uncertainty curves are shown for the $r_p = 0$ experiment. To these curves, the predicted additional torque from the damper system (T_1) has been added, as calculated in Section 2.3.3. The uncertainty of $\pm 10\%$ in this additional load has been added to the

corresponding $r_p = 0$ uncertainty curves in order to derive the uncertainty curves for the $r_p = 0.3$ and $r_p = 0.5$ results.

It can be seen that the mean experimental results, and all but one of the calculated tolerance limits, lie within the bands of uncertainty for the predicted curves when using the damper system. This confirms that the damper performed as expected, with resistance torques matching the stated values in the tested rotational speed range. Although rotational speeds lower than 80 RPM were not tested in this experiment, there is nothing to suggest the damper performance will not also match to the manufacturer's stated curve in this speed range. Therefore this method of estimating the total rotational resistance will be used to analyse the flume experimental results, with twelve different values of r_p , as described in Section 2.5.

2.5 Flume Experiment: Energy Conversion

2.5.1 Aims of the experiment

This section presents experimental work conducted at Plymouth University's COAST laboratory, focusing on the energy conversion performance of the MRL turbine. During the experiment, the MRL turbine model was mounted in the constant-velocity water stream of a laboratory water-current flume. The aim of this experimental work was to measure the rotational speed of the turbine for a range of resistance torques, in order to characterise the turbine's energy conversion performance over a range of rotational speeds, or blade-speed-ratios. The effect of varying the flow velocity was investigated, as well as the effect of adding of the optional side plates to the model.

2.5.2 Experimental approach

2.5.2.1 General experimental setup

The experimental MRL turbine model shown previously in Section 2.2.1 was re-fitted into a new support frame, suitable for use in the COAST laboratory's 30 m long and 0.6 m wide recirculating water-current flume. The frame incorporated longer, narrower supports at either end of the turbine and again had optional

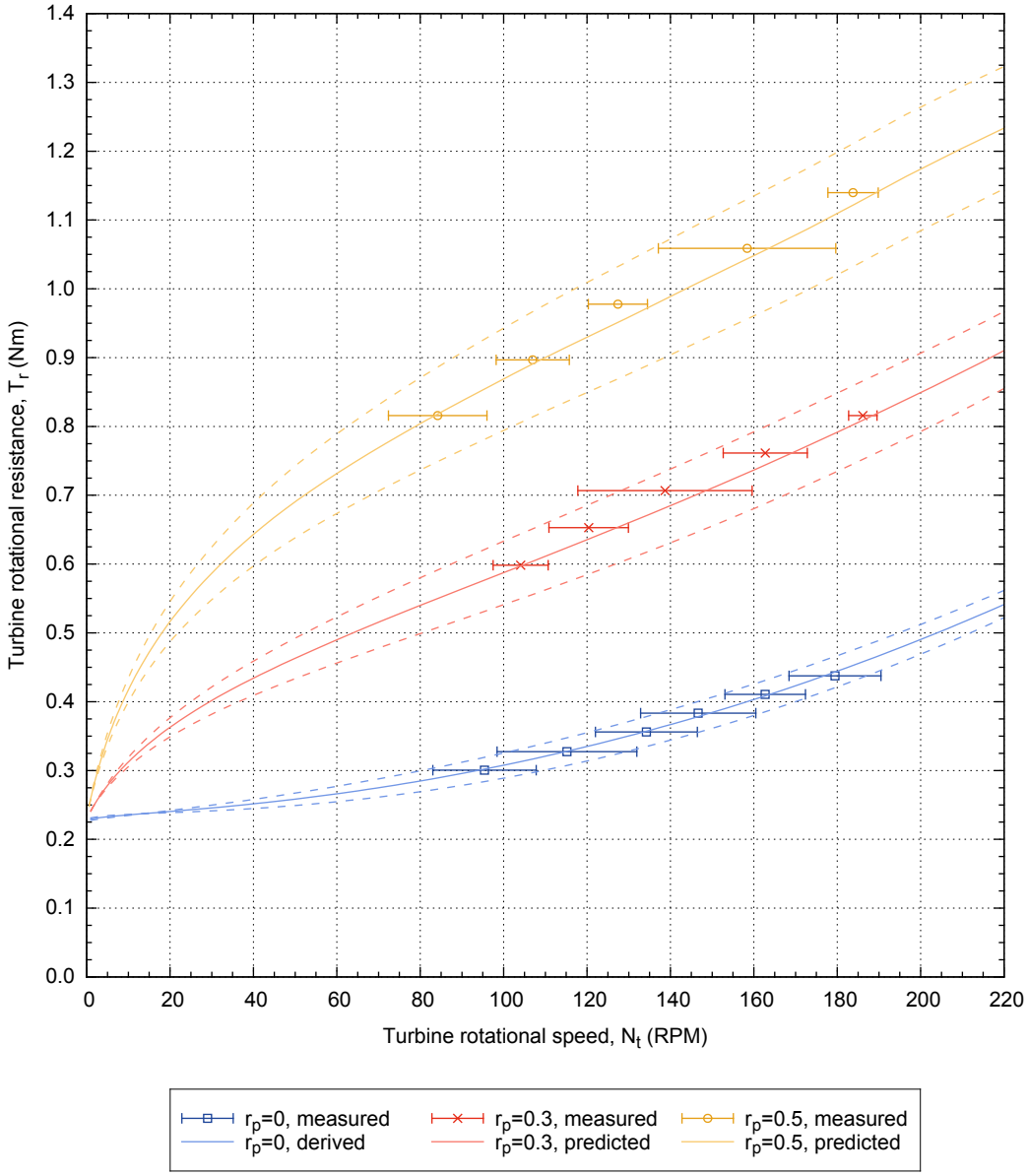

Figure 2.4.7: Variation of measured and predicted turbine rotational resistance with rotational speed (uncertainties shown with dashed lines)

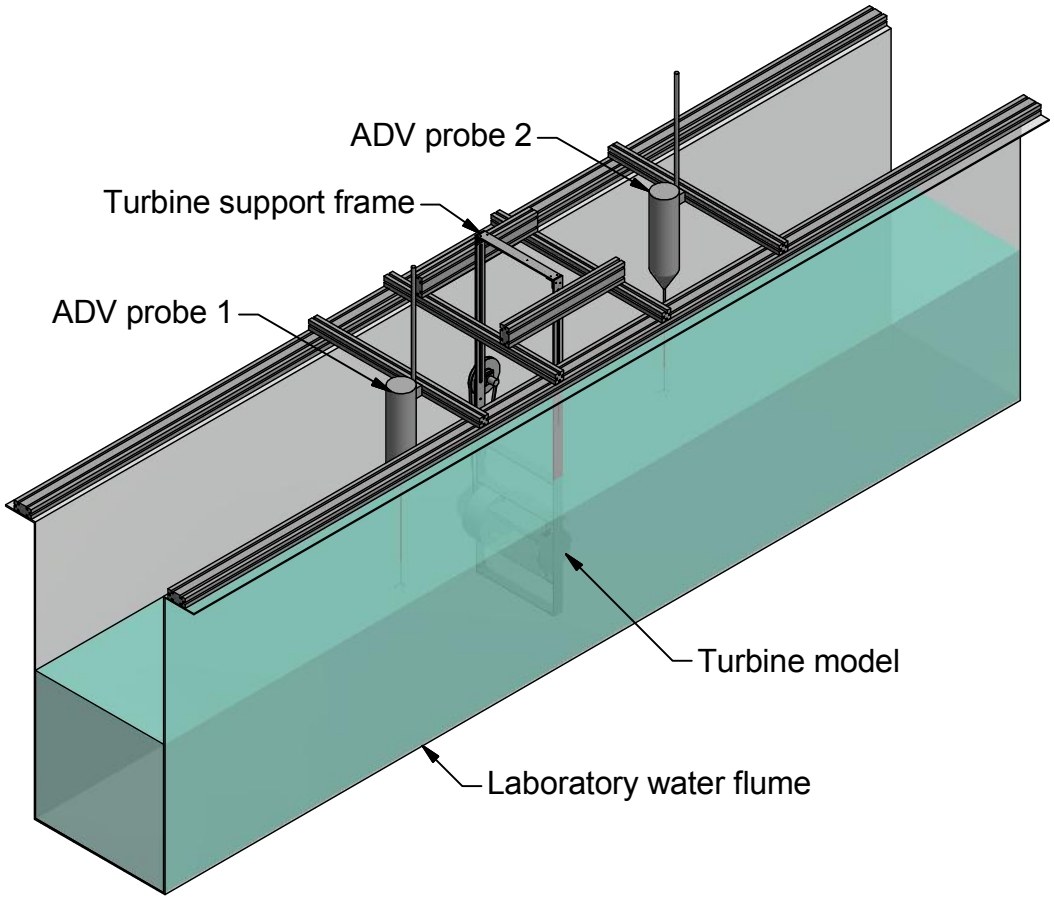

Figure 2.5.1: Isometric representation of the flume experimental setup (full length of flume is not shown)

mounts for the side plates. The optional spindle was now removed but otherwise the turbine mechanism was identical to as described earlier. A graphical representation of the experimental setup is shown in Figure 2.5.1, showing the turbine suspended in the flume by the support frame, which is fixed to the top of the flume by aluminium struts spanning the flume width. Also shown are two Nortek Vectrino II downward-facing acoustic Doppler velocimetry (ADV) probes, used to measure the current velocity in each physical dimension, both upstream and downstream of the turbine. The turbine model was positioned approximately 20 *m* from the flume inlet and 10 *m* from the outlet. This position was determined by the location of the computer equipment used to record both the turbine rotational speed and flow velocities, and ensured the flow was fully developed when reaching the turbine.

2.5.2.2 Resistance variation and uncertainty

In order to vary the resistance torque of the turbine, the damper system pulley ratio was varied, thus changing T_1, as described in Section 2.3.3. Eleven different pulley ratios, ranging between $r_p = 0.12$ and $r_p = 0.90$, were used in order to provide a wide range of load torques and therefore allow a wide range of rotational speeds to be measured. In addition, the turbine was tested with the damper pulley system disengaged (i.e. $r_p = 0$), which provided the minimum resistance possible for the given experimental model.

It is important to note there are number of differences between the flume experimental setup and that used to characterise the rotational resistance of the model in Section 2.4. A discussion of these differences and the possible effects on the rotational resistance is given below:

Unchanged The pulley system used to control the rotation of the blades is unchanged from the resistance characterisation experiment, and as it is protected by the cylindrical housing, it is unaffected by the state of the surrounding water. Therefore it is predicted that the resistance due to this system, T_p will be equal to that predicted in Section 2.4.4.2. Likewise, the radial lip seals should be unaffected by the flume environment, although they will now be running for much longer continuous periods and so the resistance provided may vary over time. However, any changes are unpredictable, and as the resistance predicted from the radial lip seals is much lower than that predicted from other mechanical sources, any variations over time are neglected.

Changed The only changes to the turbine model that certainly affect its rotational resistance are the replacement of the plain shafts with blades and removal of the spindle. Figure 2.3.3 showed that the predicted resistance due to skin friction acting on the spindle is negligible in comparison to other sources and therefore this change will be ignored. However, the removal of the shafts is highly significant as this was predicted to be a major contributor to the rotational resistance, especially at the higher rotational speeds of interest here. Therefore the curves predicting the relationship between rotational speed and total resistance must be altered to take this into account.

A further certain change to the experimental set up is the fact the model will now operate in a flow of water instead of a stationary tank. Therefore it is predicted

that the rotational resistance due to skin friction acting on the rotating faces will be altered from that predicted for a stationary fluid environment. However, no analytical or empirical relationships have been found that can predict skin friction resistance acting on surfaces rotating in a flow. Therefore, there is a large amount of uncertainty related to the prediction of resistance from this source. As an upper bound for the predicted resistance of the turbine, the skin friction contribution will be included, and for a lower bound this contribution will be ignored.

Overall uncertainty Taking into account the changes to the model and conditions described above, uncertainty limits of rotational resistance have been chosen for the turbine operating with $r_p = 0$. These limits have been selected from the curves in Figure 2.4.6b shown previously. For the upper limit, the minimum predicted resistance due to the plain shafts has been removed, resulting in the curve of maximum predicted resistance for $T_2 + T_3$. For the lower limit, the maximum predicted resistance due to both the shafts and bearing mounts has been removed, as well as the maximum prediction due to skin friction acting on the rotating surfaces. This results in the curve of minimum predicted resistance for T_2 only. For the best estimate of rotational resistance, the mean value of the upper and lower limits is used.

The predicted variation of total rotational resistance with turbine rotational speed for the range of damper pulley ratios used is shown in Figure 2.5.2. The uncertainty limits for the turbine rotating without the damper system are shown ($r_p = 0$), and it can be seen that as rotational speed increases, so does the magnitude of the uncertainty. The uncertainty in the predicted performance for higher values of r_p incorporates both the uncertainty from the $r_p = 0$ estimation and the uncertainty in the estimated resistance provided by the damper (T_1). However, only the best estimate curves are shown in order to aid clarity.

2.5.2.3 Velocity measurement

The water depth in the channel was variable, and after initial testing of the available flow velocities and turbulence levels with different water depths, a value of $0.6\,m$ was chosen that allowed four flow velocities between approximately $0.87\,m/s$ and $1.40\,m/s$ to be tested (by variation of the power setting, P_F, for the flume pump). This ensured a wide range of turbine rotational speeds could

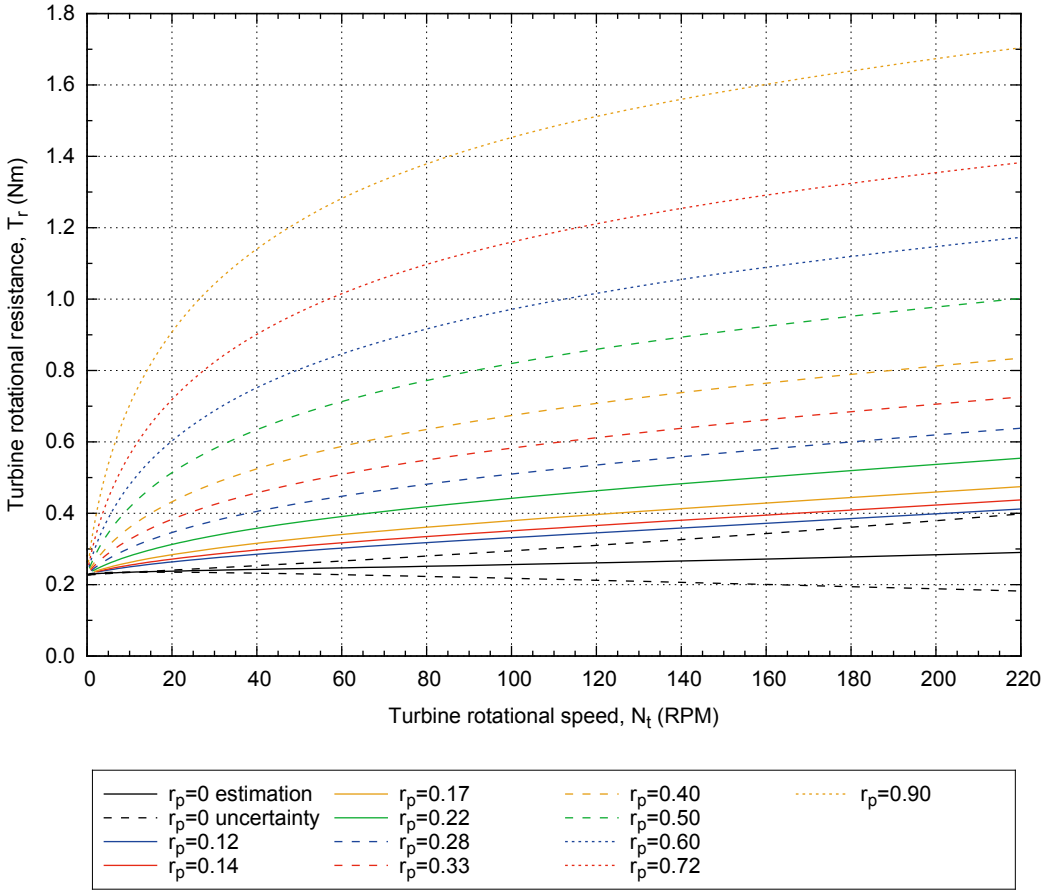

Figure 2.5.2: Predicted turbine rotational resistance for a range of damper system pulley ratios

be measured by variation of the rotary damper pulley ratio. This also resulted in a blockage ratio of approximately $B = 13\,\%$, based on the total frontal area of the turbine (swept blade area and pulley housing) compared to the wetted cross-sectional area of the channel.

The position of the turbine within the flume channel was set by aligning the central shaft at the mid-depth of the water flow and the mid-span of the blades at the mid-span of the channel. From this a co-ordinate system was derived, in order to describe the position in the flow of the ADV probe measurement cells, as shown in Figure 2.5.3. It should be noted that the ADV probes simultaneously measured the flow velocity at thirty adjacent cells of 1 *mm* height, located between 40 *mm* and 70 *mm* vertically below the physical extent of the probe. Therefore the z co-ordinate position refers to the location of a single measured cell and not the location of the probe head.

In order to characterise the profile of the free-stream flow in the flume, velocity measurements were firstly taken with ADV probe 1, located at $x = -1.4\,m$. This corresponded to an upstream position of $x = -10\,D$, where D represents the swept frontal height of the turbine blade path, as described in Chapter 1 (for the turbine model with a blade chord of $c = 0.05\,m$ and $R = 0.055\,m$, $D = 0.140\,m$). Measurements were taken at multiple positions through both the depth of the channel (at $y = 0\,m$) and across its width (at $-0.015 < z < 0.015\,m$), with the results presented in Section 2.6.4.1. Unfortunately, only the flow from three of the four flume power settings was characterised in this way, although it is assumed that the cross sectional flow profiles for the highest setting ($P_F = 80\%$) follow a similar pattern to the lower three settings ($P_F = 50$, 60 and 70%).

During the remainder of the experimental work, ADV probe 1 was positioned at a constant upstream location of $x = -10\,D$, $y = 0\,m$ and $-0.15 < z < 0.15\,m$, i.e. in-line with the centre of the turbine. At this position the flow was least disturbed by the presence of the turbine and the flume walls, and the measured values are taken to be characteristic of the upstream flow. By constantly measuring the velocity for the entire period of each rotational speed measurement, any longer timescale variations could be captured, in order to ensure the inflow to the turbine was approximately consistent over all the tests. Velocity measurements at this location are denoted by a zero subscript (i.e. U_0).

During this phase of the experiment, concerned with only measuring the energy

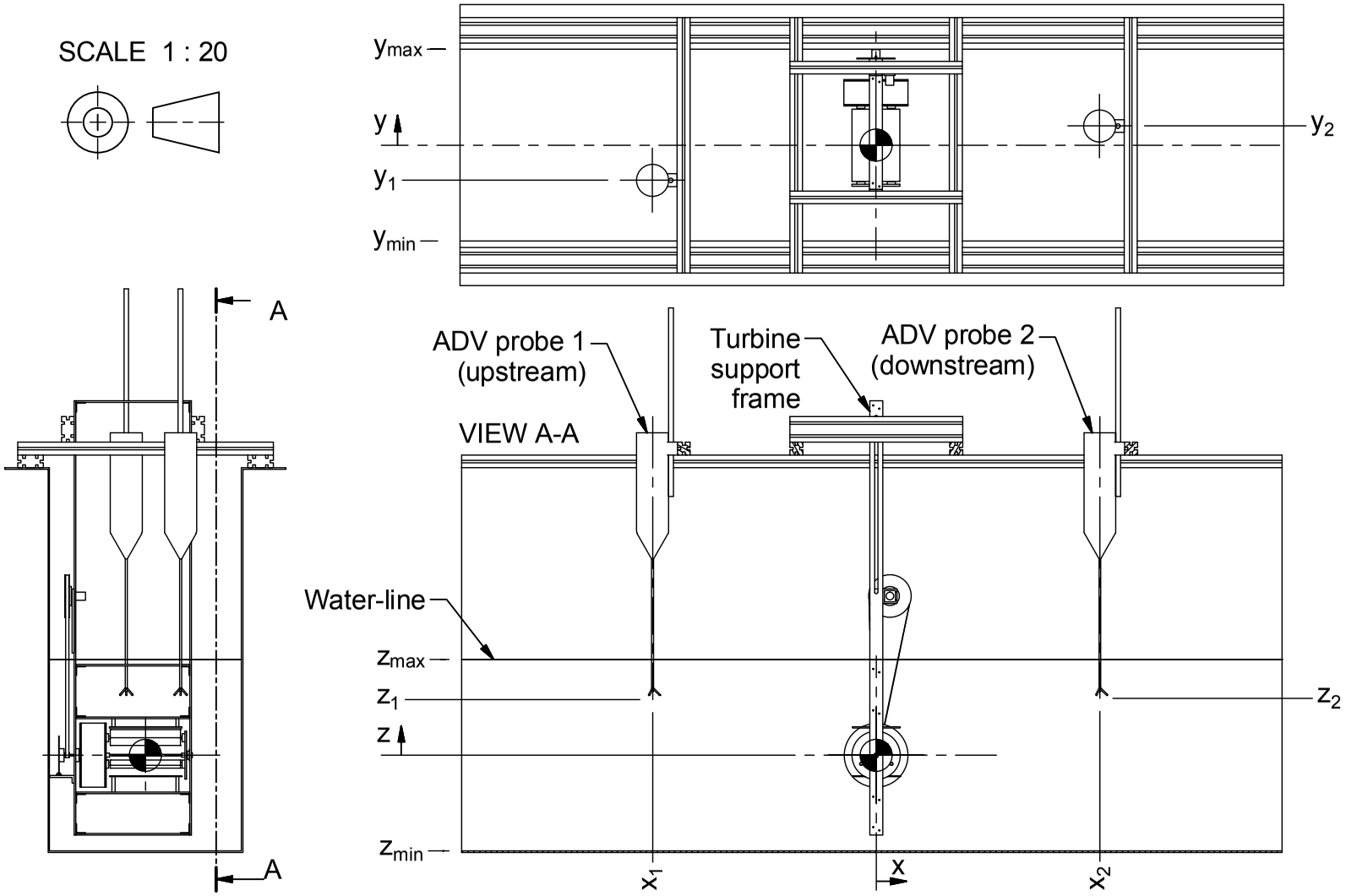

Figure 2.5.3: Diagram of the flume experimental setup defining the co-ordinate system used to position the ADV probes

conversion performance, ADV probe 2 was removed, as only the incoming flow velocity and rotational speed of the turbine were measured. During the wake measurement experiment presented in Section 2.6, ADV probe 2 was used to measure the flow velocity at a number of upstream and downstream positions.

Noise contamination of the measured velocity time-series is inevitable with use of ADV probes and therefore a process of noise removal is required for all velocity measurements taken in this experiment. The process is described in Section 2.6.3 and allows more reliable calculation of the mean and standard deviation of the velocity time series, for all three components (i.e. x-, y- and z-direction).

This enables the following relationship to be used to calculate the turbulence intensity, *Ti*, of the free-stream flow:

$$Ti = \frac{\sqrt{\frac{1}{3}\left(S_{U_0}^2 + S_{V_0}^2 + S_{W_0}^2\right)}}{\sqrt{\left(\bar{U}_0^2 + \bar{V}_0^2 + \bar{W}_0^2\right)}} \tag{2.5.1}$$

where $\bar{U}_0$, $\bar{V}_0$ and $\bar{W}_0$ are the mean values of the x-, y- and z- direction velocity time series and S_{U_0}, S_{V_0} and S_{W_0} are the standard deviation of the same velocity time series, all measured at the set upstream position as denoted by the zero subscript. The turbulence intensity is expressed as a percentage. For the four free-stream velocities tested, turbulence intensity was approximately $Ti = 4.0\,\%$.

2.5.2.4 Rotational speed measurement

The rotational speed of the turbine was again measured by the toothed disk and hall-effect sensor system and recorded on computer equipment near to the flume. Each measurement was taken at a rate of 10 Hz for a period of 60 seconds. The mean value of the resulting time series, N_t, was taken as the representative rotational speed for each test. The results were checked for any long time-scale variations that may have resulted from changing flow velocity and any such readings were rejected and retaken.

For the power conversion phase of the experiments, three repeat readings were taken for each load torque setting at each inlet flow velocity tested. When measuring the wake velocities, the rotational speed of the turbine was also measured for the duration of each velocity reading.

2.5.2.5 Calculation of torque and power coefficients

For each test undertaken, Figure 2.5.2 was used to predict the total rotational resistance of the turbine for the particular combination of damper pulley ratio and mean rotational speed. This resistance torque is assumed to equal the driving torque generated by the turbine blades. The driving torque, T_d, mean rotational speed, N_t and mean incoming flow velocity, $\bar{U}_0$, were used to calculate the blade speed ratio, torque coefficient and power coefficient as defined in Chapter 1. In this case, the mean turbine rotational speed, ω_0, expressed in rad/s, is calculated from:

$$\omega_0 = \frac{\pi N_t}{30} \tag{2.5.2}$$

2.5.2.6 Testing regime

Table 2.5.1 shows the combinations of measured inlet flow velocity, turbine resistance setting and side plate attachment that were tested. It shows that at the lowest inlet velocity, the highest four resistance settings were not trialled, as the turbine was unable to rotate. Also, side plates were only tested with two resistance settings, due to time constraints.

2.5.3 Experimental results

Experimental results describing the power conversion characteristics of the MRL turbine model are presented in different formats by Figures 2.5.4, 2.5.5 and 2.5.6, and are discussed in the following sections.

2.5.3.1 Variation of driving torque with rotational speed

Figure 2.5.4 shows the mean rotational speed of the turbine measured when various total resistance torques were applied at four inlet flow velocities. The dashed grey curves show the predicted rotational resistances for the twelve damper pulley ratios used, as shown previously in Figure 2.5.2. The majority of results were gathered with the turbine operating without the optional side plates attached, although two damper pulley ratios of $r_p = 0.33$ and $r_p = 0$ were also used with the side plates attached, again with four different inlet flow velocities. By measuring and calculating the mean rotational speeds and matching these

Table 2.5.1: Energy conversion experiment testing regime

Side plates	r_p	$\bar{U}_0$ (m/s)			
		0.87	1.05	1.22	1.40
No	0.00	x	x	x	x
	0.12	x	x	x	x
	0.14	x	x	x	x
	0.17	x	x	x	x
	0.22	x	x	x	x
	0.28	x	x	x	x
	0.33	x	x	x	x
	0.40	x	x	x	x
	0.50		x	x	x
	0.60		x	x	x
	0.72		x	x	x
	0.90			x	x
Yes	0.00	x	x	x	x
	0.33	x	x	x	x

values to the predicted total rotational resistances, clear relationships between rotational resistance and rotational speed have been revealed, and can be seen for all four inlet flow velocities tested.

As the chosen damper pulley ratio increased (and therefore total rotational resistance generally increased), the turbine rotated at a lower speed until any further increase in resistance prevented the turbine from continuously rotating. At the lowest flow velocity tested ($\bar{U}_0 = 0.87\,m/s$), only eight of the chosen pulley ratios resulted in continuous rotation, at the next flow velocity, ($\bar{U}_0 = 1.05\,m/s$) eleven of the pulley ratios allowed rotation and at the two highest flow velocities ($\bar{U}_0 = 1.22\,m/s$ and $\bar{U}_0 = 1.40\,m/s$) all twelve ratios allowed rotation.

For each inlet flow velocity tested, the relationship between rotational resistance and rotational speed appear to follow a peaked curve shape, with the results taken for $\bar{U}_0 = 1.05\,m/s$ best capturing this. This particular set of results show the peak torque to be generated at approximately 43 *RPM*. Below and above this speed, the rotating blades generate a lower torque, with the majority of data points at higher rotational speeds.

This overall relationship between rotational resistance and rotational speed is repeated for all four inlet flow velocities tested. However, the measured rotational speed also increased with increasing inlet flow speed for each particular damper pulley ratio used. Therefore, for a given rotational speed of the turbine, the driving torque generated by the blades increases with increasing inlet flow velocity.

When comparing the results for a given combination of damper pulley ratio and inlet flow speed, the results show that adding the optional side plates caused the turbine to rotate at a higher rotational speed. The effect on the result is similar to increasing the overall inlet flow velocity and therefore could show the side plates increase the flow velocity encountered by the turbine blades. However, the increase in the rotational speed (when adding side plates) is less significant for results that lie near to the peak driving torques generated without the plates attached (e.g. the results for $\bar{U}_0 = 0.87\,m/s$ and $r_p = 0.33$) and larger for results that lie towards the upper ends of the apparent curves (e.g. the results for $\bar{U}_0 = 0.87\,m/s$ and $r_p = 0$). As the inlet flow velocity increases, the results from both damper settings tend to lie further away from the peak no-plates results, and therefore the increases in rotational speed

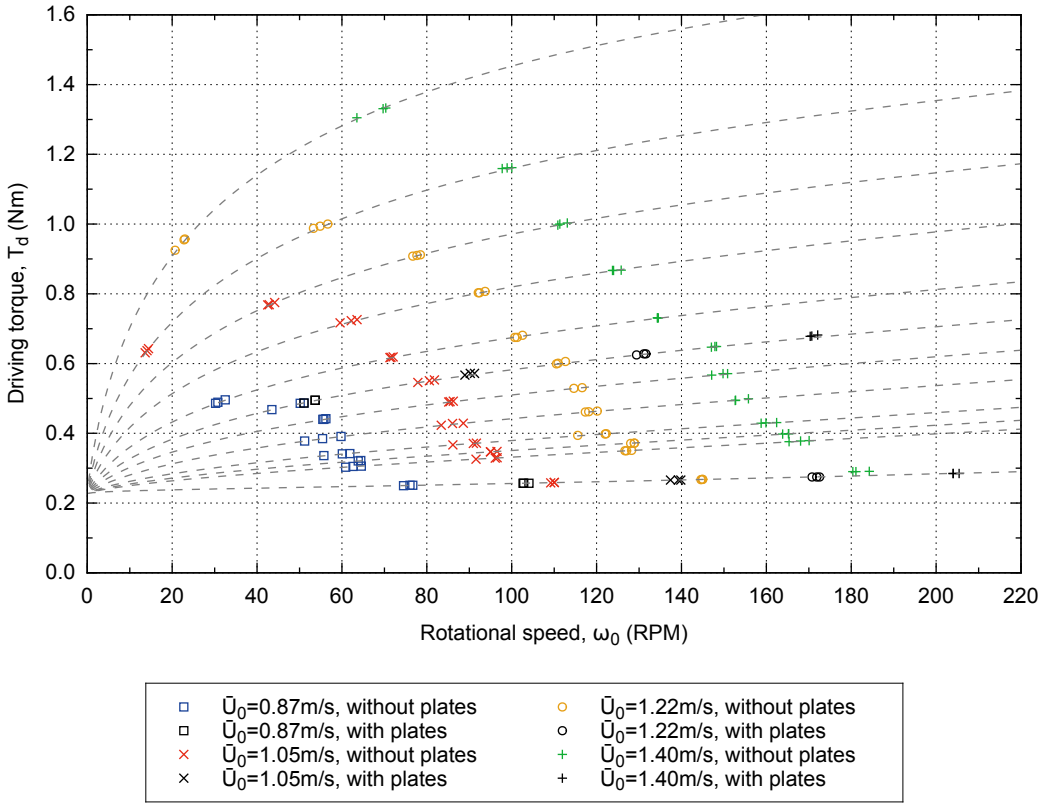

Figure 2.5.4: Variation of turbine driving torque with rotational speed
(Dashed lines represent predicted resistance to rotation at various damper pulley ratios)

become larger and more similar to each other. Therefore the effect of adding the side plates appears to be more complex than simply increasing the flow velocity encountered by the blades and also depends on the rotational speed of the turbine.

2.5.3.2 Variation of driving torque with blade speed ratio

Figure 2.5.5a shows the driving torque results plotted against blade speed ratio and also indicates the level of uncertainty that results from the torque prediction method. In general, the magnitude of the uncertainty increases with increasing resistance torque and rotational speed; therefore the results for the highest inlet flow velocity have the largest predicted uncertainties and likewise, the lowest inlet velocity results have the smallest levels of uncertainty. Although the rotational speed results have now been modified to account for the inlet flow velocity, the four sets of inlet flow velocity results are still distinct from each

other, with large differences in the magnitude of driving torque generated at a given blade speed ratio.

However, when expressed as torque coefficient, as shown in Figure 2.5.5b, the results for the different inlet flow velocities are more closely matched in terms of magnitude. The peak torque coefficient for all four sets of results lies in the approximate range $0.73 < C_Q < 0.93$ (when accounting for uncertainty), at a blade speed ratio in the range of $0.2 < BSR < 0.3$. As the blade speed ratio increases from this value, the torque coefficient continuously decreases and trends towards zero at a value of $BSR > 0.9$.

When comparing the effect of adding side plates to the turbine, Figure 2.5.5b shows the torque coefficient results for all four flow velocities increase in magnitude compared to the no-plates results and also appear to correlate closely with each other. Again, the increase in magnitude is larger as the value of blade speed ratio increases and the results lie further from the peak torque coefficient.

2.5.3.3 Variation of power with blade speed ratio

Figure 2.5.6a shows the variation of turbine power with blade speed ratio, for the four inlet velocities tested. Again, the results for the turbine operating with side plates are also shown. The relationship for each particular flow velocity is distinctly more curve shaped than the torque results, which is due to the individual torque results now being multiplied by the relevant rotational speed. A clear distinction in the magnitudes of the power can be seen between the results for each inlet flow velocity, from a peak power of approximately $P = 2.8\,W$ for the lowest inlet velocity and $P = 12\,W$ for the highest (best estimate values, not accounting for uncertainty). The peak power also appears to shift to slightly higher values of blade speed ratio as the inlet velocity increases, from approximately $BSR = 0.35$ for the lowest inlet velocity to a value in the range of approximately $0.40 < BSR < 0.45$ for the two highest velocities tested.

The results for the turbine operating with the side plates attached mostly show the power generated to be shifted to higher values, when compared to the no-plates results at the same inlet flow velocity and blade speed ratio. Again, the effect is more significant if the results lie further from the no-plates peak power generation results.

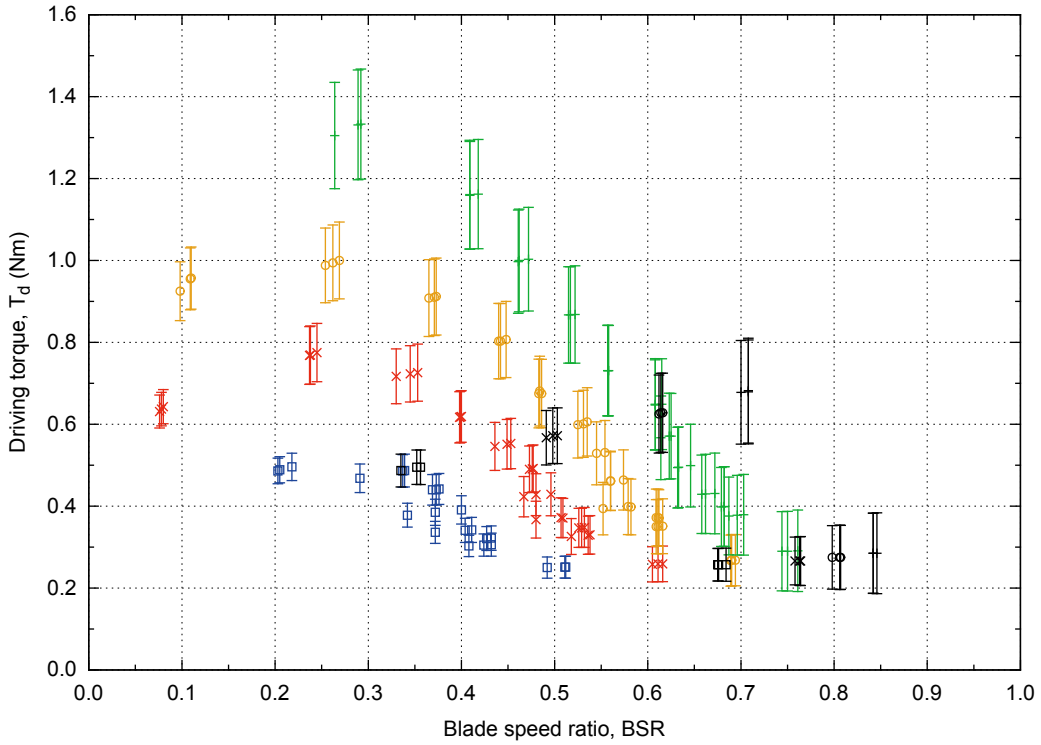

(a) Torque

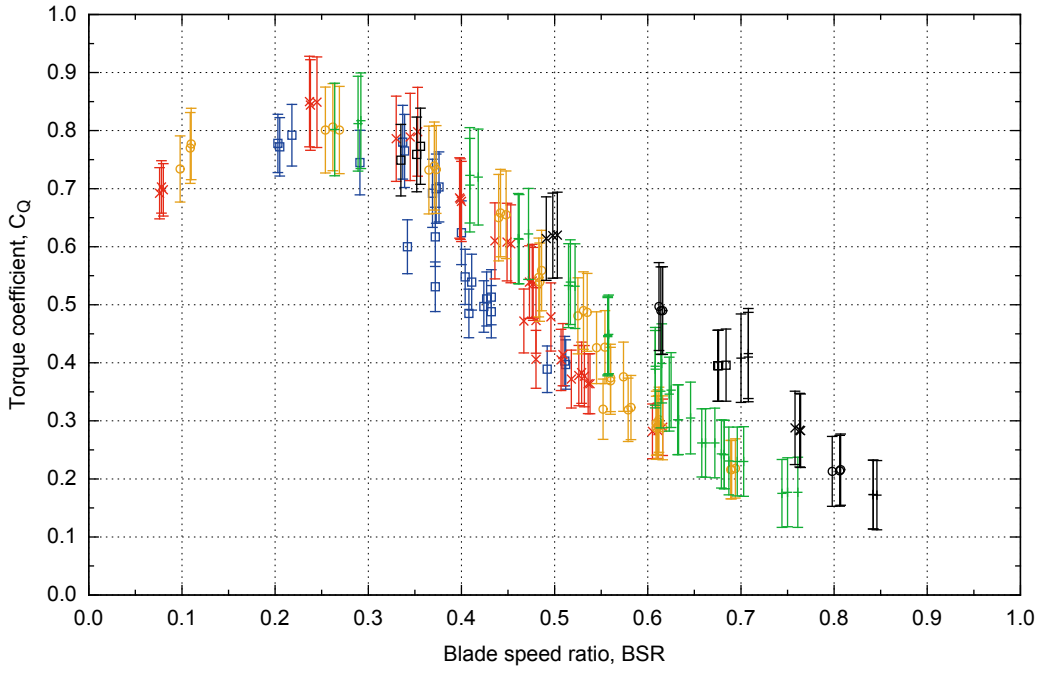

(b) Torque coefficient

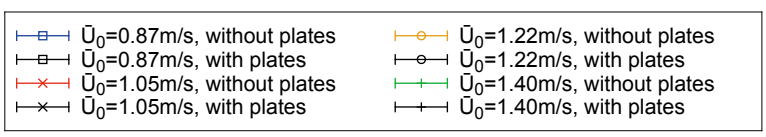

Figure 2.5.5: Variation of turbine driving torque with blade speed ratio, for four values of inlet velocity, with and without side plates ($Ti = 4.0\,\%$ and $B = 13\,\%$)

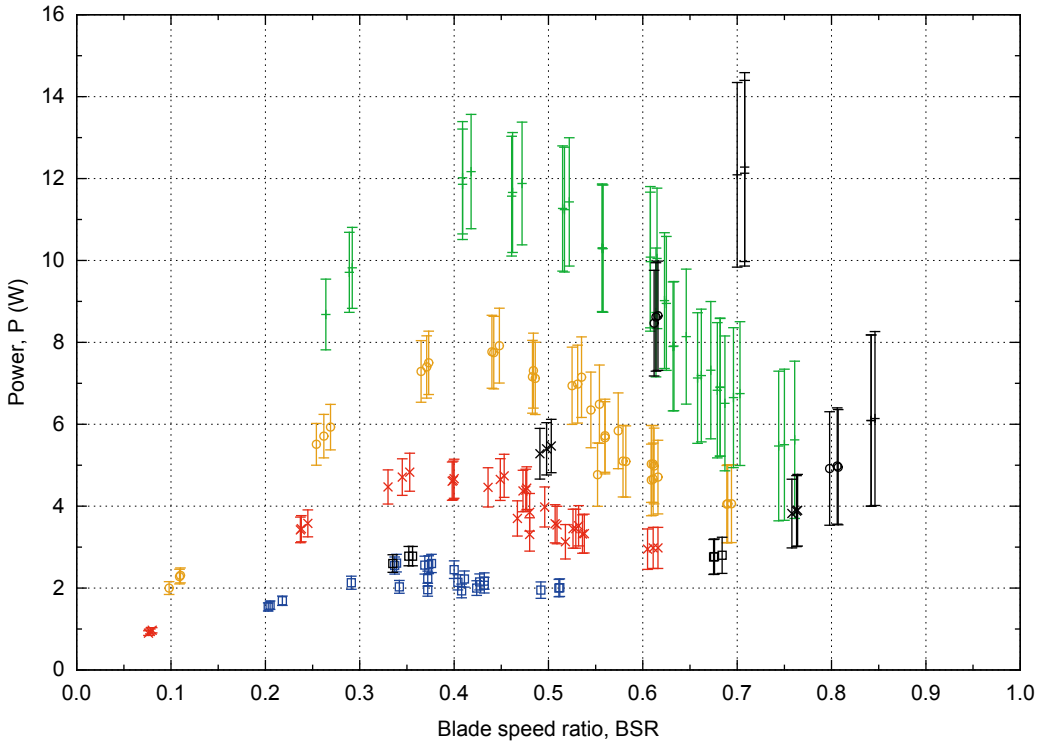

(a) Power

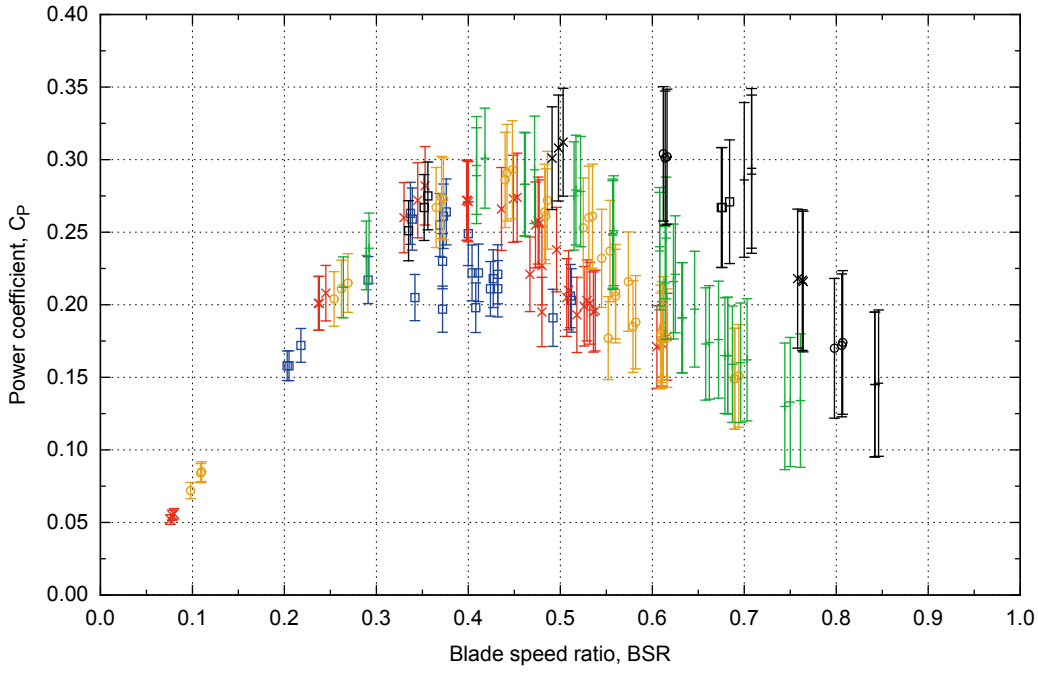

(b) Power coefficient

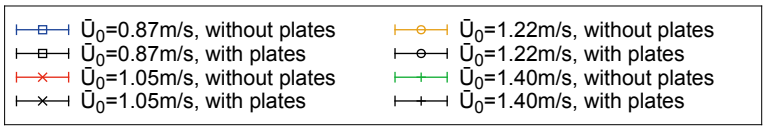

Figure 2.5.6: Variation of turbine power with blade speed ratio, for four values of inlet velocity, with and without side plates ($Ti = 4.0\,\%$ and $B = 13\,\%$)

Figure 2.5.6b shows the power values converted to power coefficients, again plotted against blade speed ratio. This brings the magnitude of the results for each inlet flow velocity closer together. The peak values of power coefficient, for the turbine operating without side plates, fall in the approximate range of $0.24 < C_P < 0.33$ when taking into account all four flow velocities and uncertainties. The maximum measured power coefficient and the value of blade speed ratio that it occurs increases with each increase in flow velocity.

Power coefficient results at blade speed ratios lower than the peak show a strong correlation at all four flow velocities, and trend towards the origin. The results at blade speed ratios higher than the peak are not as well matched for all four flow velocities, with increases in flow velocity shifting the curves to the right. However, the results do appear to move closer together at the higher blade speed ratios reached, as they possibly trend towards a power coefficient value of zero at a blade speed ratio in the range $0.9 < BSR < 1.0$.

The results for inlet velocity of $\bar{U}_0 = 0.87\,m/s$ show the most variation in power coefficient values for a given blade speed ratio, especially in the range $0.34 < BSR < 0.41$ where some results show a best estimate value of power coefficient as low as $C_P = 0.19$ and some results as high as $C_P = 0.26$. This is a result of the relatively large variation between the three mean rotational speeds calculated for tests with damper pulley ratios of $r_p = 0.17$ and $r_p = 0.22$, as shown previously in Figure 2.5.4. The cause of these variations is unknown, although it can be assumed the rotational resistance of the turbine was elevated for the tests that gave lower mean rotational speeds, when compared to the predicted values. This increase in rotational torque may have resulted from a misalignment of the timing belt in the damper pulley system, which would have reduced the pulley efficiency.

The power coefficient results for the turbine operating with side plates appear to strongly correlate for all four inlet velocities tested, with the results shifted to higher values when compared to tests conducted without the plates, especially at blade speed ratios higher than the peak. The overall effect of adding the plates appears to shift the peak power coefficient generated to higher values of blade speed ratio, in the approximate range $0.5 < BSR < 0.6$, where the power coefficient is predicted to lie in the range $0.30 < C_P < 0.35$. Although this peak value of power coefficient is not greatly increased compared to the no-plates results (especially for the higher flow velocities tested), the curve peak appears to be widened. Therefore the turbine is able to generate a relatively

high power coefficient (e.g. greater than 75% of the peak value) over a wider range of blade speed ratio values.

2.5.4 Conclusions of experiment

The presented experimental work has characterised the MRL turbine model's energy conversion performance at a range of rotational speeds, or blade-speed-ratios. The effect of varying the flow velocity has been investigated, as well as the effect of adding of the optional side plates to the model. Unfortunately, forces acting on the turbine were not measured, and therefore thrust coefficients could not be calculated.

The results show the peak torque coefficient lies in the approximate range $0.73 < C_Q < 0.93$ at a blade speed ratio in the range of $0.2 < BSR < 0.3$. At higher rotational speeds the driving torque reduces significantly, towards zero at $BSR = 0.9 - 1.0$.

The power coefficient follows a peaked curve relationship with *BSR* value. The maximum values lies in the range $0.24 < C_P < 0.33$ and occur in the range $0.35 < BSR < 0.45$. At higher values, the power coefficient also reduces towards zero at $BSR = 0.9 - 1.0$.

The effect of inlet flow velocity is not clear, with results well correlated at lower values of *BSR*, but more variation (and uncertainty) occurring at higher values. However, in comparison to the raw torque and power results, the calculation of coefficients brings the four sets of results relatively in line with each other.

The use of side plates does not appear to increase the peak torque or power coefficient values, but extends the width of the peak region to higher values of *BSR*, before reduction occurs towards zero.

2.6 Flume Experiment: Wake Characterisation

2.6.1 Aims of the experiment

The work presented in this section aims to characterise the wake produced downstream of the turbine model by measurement of a number of velocity profiles. Whilst wake characterisation is not the primary aim of the wider work,

measurement of velocity profiles upstream and downstream of the turbine can be valuable when comparing experimental and simulation power results, as presented in Chapter 5. The results may also be of use to others who are researching simulation of tidal turbine wake formation.

2.6.2 Experimental approach

The experimental setup used was as described in Section 2.5.2, with ADV probe 2 inserted into the flow at various upstream and downstream positions.

Firstly, ADV probe 2 was used to measure the velocity through both the depth of the channel (at $y = 0$) and across its width (measuring a batch of cells at $-0.15 < z < 0.15\,m$), at various longitudinal locations ($x = 1\,D$, $x = 2.5\,D$, $x = 5\,D$ and $x = 10\,D$). This required 108 separate measurements to be taken and for each of these readings, the velocity at the constant upstream location was also measured, as well as the rotational speed of the turbine. The turbine operated with a rotational resistance setting of $r_p = 0$, and the flume power was set at $P_F = 50\%$. From monitoring the inlet flow and rotational speed of the turbine, approximately constant operating conditions for all wake measurements were achieved. Each set of velocity readings was measured at a rate of 100 Hz for a period of 60 seconds, and the results post-processed as described in Section 2.6.3.

A number of wake velocity measurements were also taken along the 'centre-line', i.e at $y = 0$ and a batch depth of $-0.15 < z < 0.15\,m$, at various downstream positions in the range $-1\,D \leq x \leq 20\,D$. These profiles were measured for a range of operating conditions, resulting from the use of two rotational resistance settings and three flow velocities.

2.6.3 Post-processing of velocity measurements

2.6.3.1 Acoustic Doppler velocimetry probe operation

Acoustic Doppler velocimetry (ADV) probes are designed to sample instantaneous velocity components at a single point, i.e. cell, with a relatively high frequency. The Vectrino II probe head includes one central transmitter, located on the bottom end of the probe shaft, and four receivers located on angled

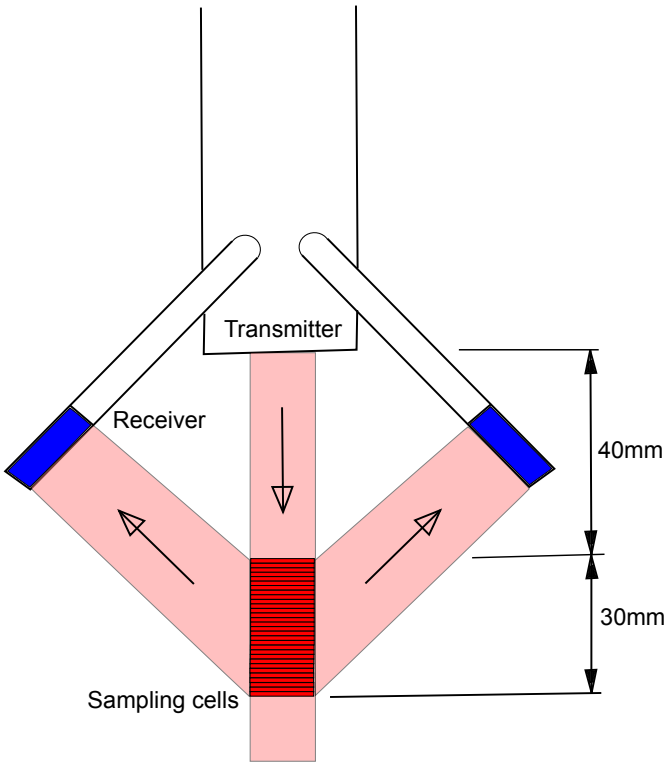

Figure 2.6.1: Diagram showing sampling arrangement of Vectrino ADV probe

extensions arranged in a circular pattern at 90° intervals. The probe can simultaneously sample velocities in a batch of thirty cells of 1 *mm* height, beginning 40 *mm* from the probe transmitter. Each cell is approximately cylindrical in shape with a diameter of 6 *mm*. This arrangement ensures the probe is non-intrusive in the volume to be sampled. A diagram of this setup is shown in Figure 2.6.1.

ADV probes work on the principle of the Doppler shift, where transmitted sound waves bounce off a moving object and undergo a phase shift proportional to the velocity of the object. The four receivers record the reflected, or back-scattered, waves and calculate the flow velocity based on this phase shift, as described in detail by Voulgaris and Throwbridge (1998). In the case of a probe operating in a fluid environment, the object is a particle carried in the fluid and therefore it is required that the flow is seeded in some way. For this experiment the seeding was provided by a fine sand periodically added to the water flow at the inlet of the flume and allowed to mix evenly before measurements taken.

The ADV system simultaneously records the three velocity components at each cell, as well as signal strength values and correlation values. The signal strength value is related to the intensity of the acoustic reflections and is therefore related

to the concentration of suspended particles in the measurement cell, at the instantaneous time of a measurement.

2.6.3.2 The requirement for post-processing

Each velocity time series measured by the ADV probe will inevitably be contaminated with noise, or 'spikes', possibly due to a number of reasons:

- Aliasing errors: the phase shift of acoustic waves can only be measured in the range $-180°$ to $+180°$ and any shift that lies outside of this will cause a spike in the time series due to the wrapping of the signal.
- Doppler noise: An approximately Gaussian white noise that is inherent in devices using Doppler back-scattering techniques. This noise appears over all frequencies and is caused by (i) particles entering the sampling cell during the interval between acoustic pulses, (ii) turbulence at scales smaller than the sampling cell causing particle scattering, and (iii) beam divergence (Khorsandi et al., 2012).

These spikes will likely bias the statistical measurements of the flow, such as mean and standard deviation (i.e. turbulence), that will be used to characterise the flow. It is therefore necessary to clean the time-series of contamination, where it can be identified. As the ADV probes record a very large amount of data (i.e. 6000 data points for each of the three velocity components, at each of the thirty cells in every batch, and numerous batches were measured in positions throughout the flume), a systematic method of post-processing is required, as it is not practical to inspect and correct every time-series individually.

2.6.3.3 Overall post-processing approach

In order to post-process the velocity time series, the following approach has been used:

- Assess the quality of typical raw time-series from different measurement locations, in order to decide whether post-processing is necessary
- 'De-spike' contaminated raw time-series from each individual cell, in order to reject noise readings

- Classify the de-spiked results in order to identify the most reliable time-series within each batch of thirty cells, and reject time-series that do not meet the criteria
- Calculate statistical results from each de-spiked (and accepted) time-series
- Calculate the sample-averaged results from the accepted statistical results in each batch of thirty cells

The above steps are explained in more detail in the following sections.

2.6.3.4 Examples of raw data series

Typical raw time-series data, at cells located upstream ($x = -10\,D$) and downstream ($x = 1\,D$), are shown in Figure 2.6.2 (in the time domain) and Figure 2.6.3 (in the frequency domain).

The time domain results show much greater fluctuation in velocity measurements at the location directly downstream of the turbine, when compared to the far-upstream location. This is somewhat expected, as the flow directly downstream of the turbine is likely to have much greater levels of turbulence than the inlet free-stream. However, a relatively large number of spikes also appear in the downstream results, and these appear to be superimposed upon the general level of turbulence. This behaviour is observed in all three velocity-components, although it appears significantly more pronounced in the x- and y-direction results.

The frequency domain results show the same sets of data, but plot the power spectral density (PSD) of the data at a range of frequencies. Lines representing the rotational velocity of the turbine are shown, as well as the blade pass frequency (i.e, three times the turbine frequency). These indicate that the large spike in PSD observed at an approximate frequency of $4.5\,Hz$ in the downstream results (x- and z-direction components in particular) are likely due to large scale flow structures formed by an individual blade.

Also shown are lines representing a -5/3 gradient; the Kolmogorov turbulence scaling law (Kolmogorov (1941)) predicts velocity time series should follow this gradient in the inertial sub-range of frequencies. Noise tends to flatten the power spectra, especially at higher frequencies and therefore comparison to a -5/3 gradient can be used to assess noise levels.

The frequency domain results generally shows the PSD trend decreases with increasing frequency, for both sets of results. However, the upstream results generally follow a steeper gradient, much closer to a value of -5/3, in comparison to the downstream results, indicating that a significant amount of noise is present in the latter. This data therefore requires use of a noise removal technique, in order to make calculated statistical values more reliable. As discussed above, the downstream z-direction results appear to be less contaminated than the x- and y-direction results, as the PSD plot appears to follow a steeper gradient in the higher frequency range. This indicates less noise removal is required in this time-series.

2.6.3.5 De-spiking of velocity time series

A number of researchers have contributed to the development of different de-spiking techniques, but the most widely is the Phase-Space Threshold (PST) method developed in Goring and Nikora (2002), Wahl (2003) and Goring and Nikora (2003). This is based on phase-space plots of the the turbulent velocity fluctuations and the first and second derivatives (i.e. U', $\Delta U'$ and $\Delta^2 U'$ for the x-direction velocity component). Goring and Nikora recognised that when plotted in this manner, good data should lie within an ellipsoid cluster in three-dimensional phase-space. They used the Universal Threshold, λ_U, as first proposed by Donoho and Johnstone (1994), to determine the limits of the ellipsoid when projected onto three two-dimensional planes. This estimates the absolute maximum value that should occur in a normally distributed population of n_p variables, with a mean of zero ($\bar{U} = 0$) and standard deviation of σ_U, and is calculated as follows:

$$\lambda_U = \sigma_U \sqrt{2 \ln n_p} \tag{2.6.1}$$

Alternatively, the mean absolute deviation (MAD_U) can be used in place of the standard deviation. The algorithm of Goring and Nikora calculates the size of each ellipse, identifies values that lie outside of these, removes them and then replaces them with a suitable values. The latter step maintains the total number of values in the sample and therefore allows more reliable calculation of statistical properties. Values can be replaced with a number of methods, including the overall sample mean, the last 'good' value (LGV), or an interpolation between a number of adjacent points. The process is iterative and repeats until the number of spikes detected is reduced below a certain limit.

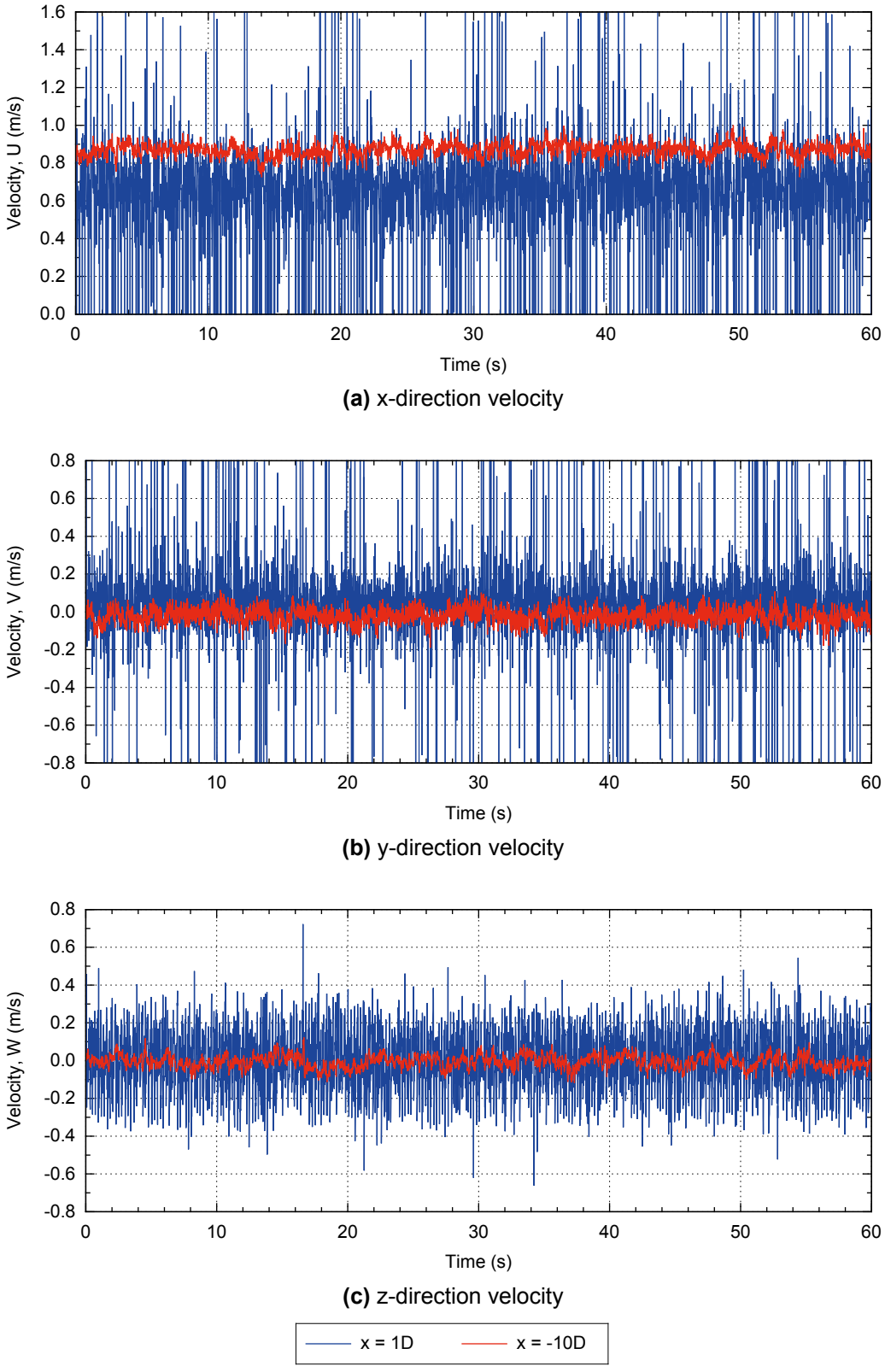

Figure 2.6.2: Raw velocity time series measured at upstream and downstream cell positions (both at $y = 0$, $z = 0.018\,m$). The turbine was operating at $BSR = 0.6$ with $\bar{U}_0 = 0.87\,m/s$ and no side plates attached

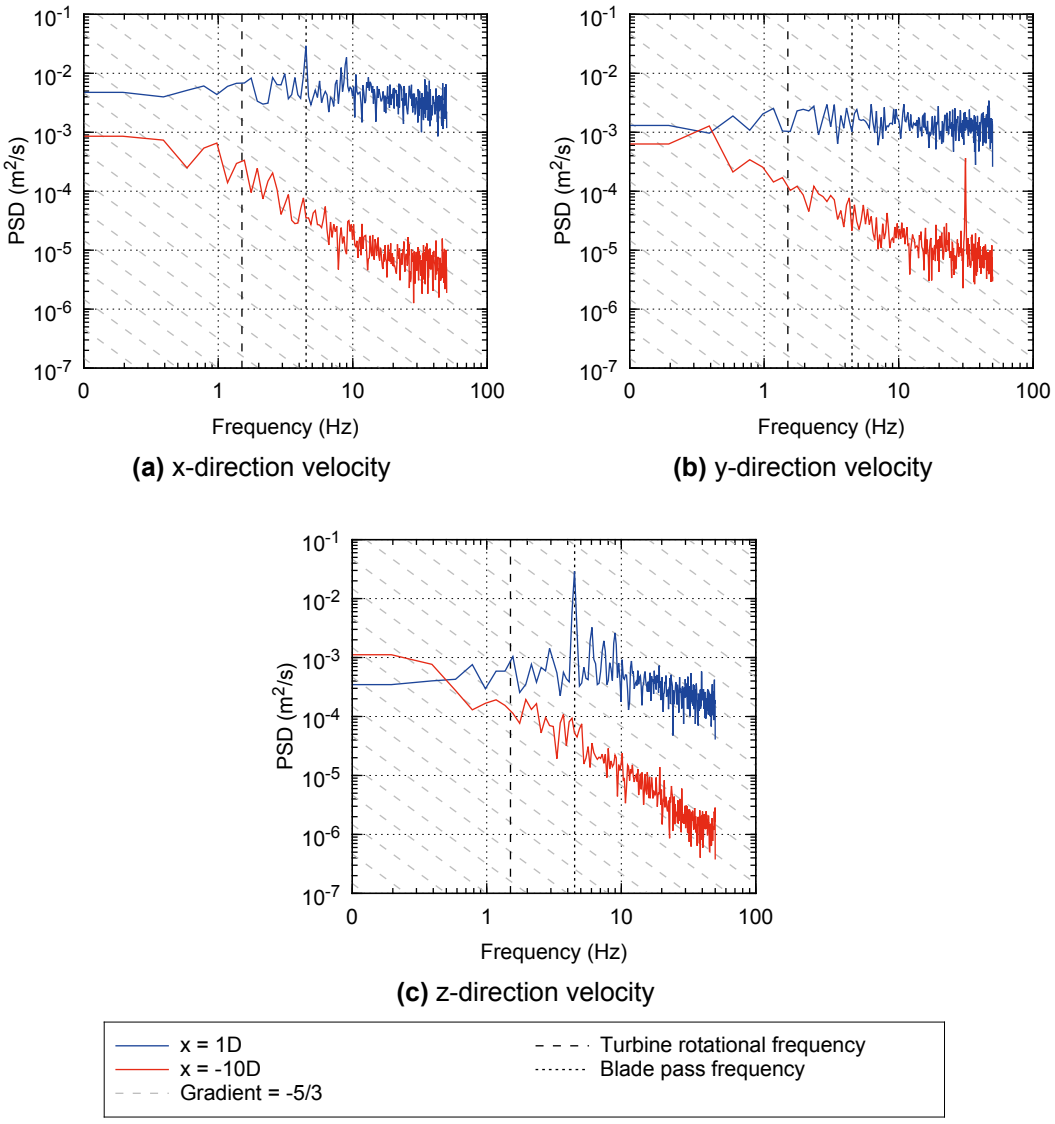

Figure 2.6.3: Estimates of power spectral density for raw velocity series measured at upstream and downstream cell positions (both at $y = 0$, $z = 0.018\,m$). The turbine was operating at $BSR = 0.6$ with $\bar{U}_0 = 0.87\,m/s$ and no side plates attached

A modification to the method, denoted as mPST, was developed by Parsheh et al. (2010) in order to minimise the number of valid data points that get identified as spikes. This can occur at data points adjacent to spikes, due to high values of $\Delta U'$, although the data points are not spikes themselves. Therefore, in the mPST method, points next to spikes are protected from removal.

An alternative method to PST was developed by Cea et al. (2007), where the velocity fluctuations for the three components (i.e. U', V' and W') are plotted against each other, and an ellipse is again used for filtering. This method is not iterative, but does not benefit from the advantage that differentiation of the signal brings; namely amplification of spike values that aids identification.

The effectiveness of the methods described above, including a number of value replacement methods, were assessed by Jesson et al. (2013), who identified the mPST method is most suitable for highly contaminated data. In addition, the LGV replacement method is most appropriate for use with mPST, as these give the best reconstruction of the spectral density distribution.

Examples of two-dimensional phase-space plots are shown in Figure 2.6.4, for the same upstream and downstream data as discussed previously (the y-direction component result has been omitted, as it is similar to the x-direction result). These show the upstream results are tightly clustered in all plots, indicating low levels of noise contamination. In contrast, the downstream results show a number of results that lie outside of the central cluster. There are relatively few of these in the z-direction results, but the x-direction results show a highly significant amount, with 'spokes' of noise appearing. Therefore, the mPST de-spiking method, with LGV replacement has been used during post-processing of these results.

In order to apply the chosen de-spiking method, the Multi-instrument turbulence toolbox (MITT) developed by MacVicar et al. (2014) has been used. This open-source sets of algorithms is written in the software Matlab, and therefore could be easily integrated with further post-processing procedures (i.e. calculation of statistical values). The toolbox has the added capability of data classification, enabling the reliability of de-spiked data sets to be further assessed. This is discussed further in Section 2.6.3.6.

All sets of results were processed in batches, with all results post-processed in the same way so that manual inspection of results was not necessary. There-

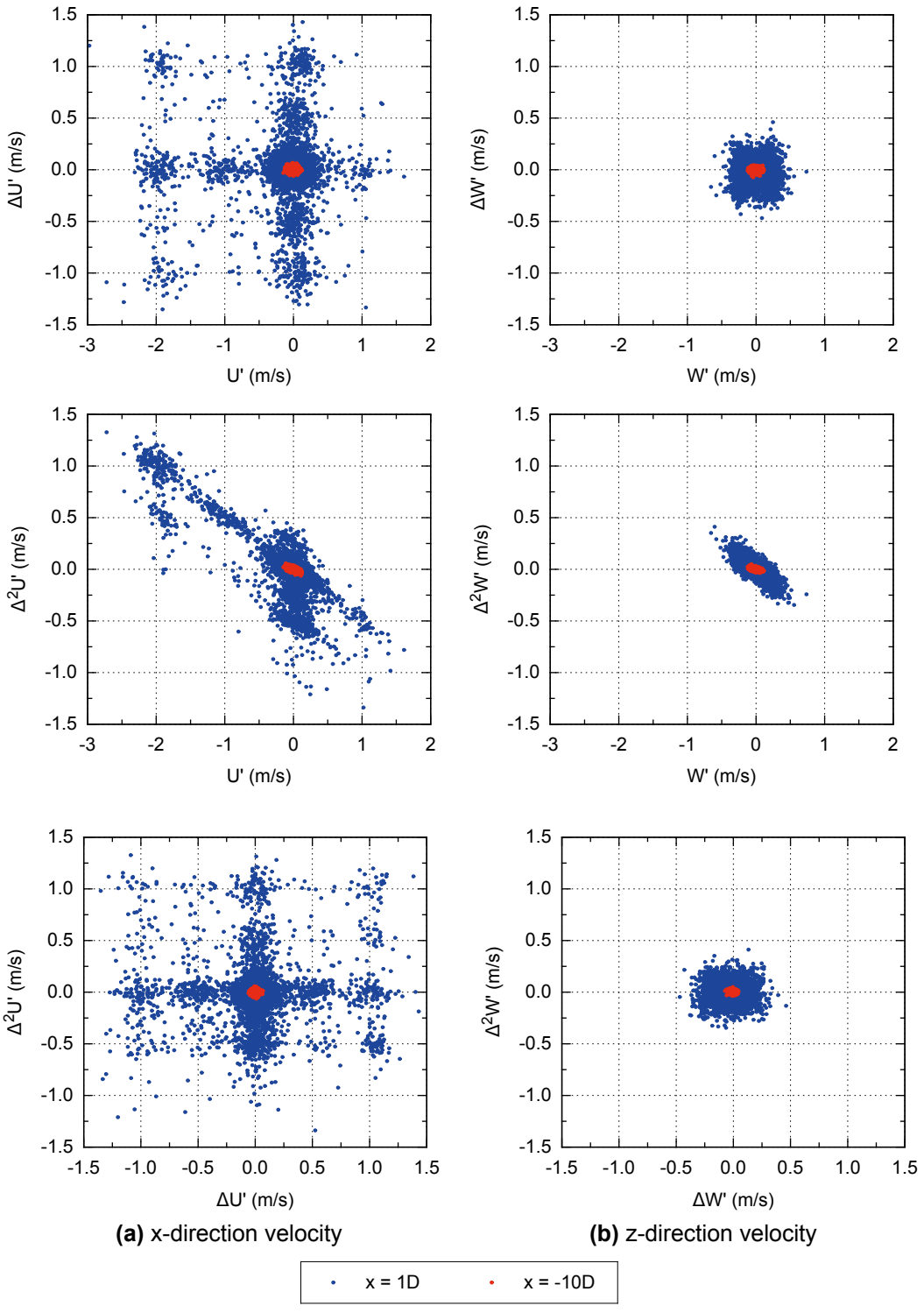

Figure 2.6.4: Phase-space plots for velocity series measured at upstream and downstream cell positions (both at $y = 0$, $z = 0.018\,m$). The turbine was operating at $BSR = 0.6$ with $\bar{U}_0 = 0.87\,m/s$ and no side plates attached

fore, it was necessary to ensure both relatively clean data and highly noisy data could be de-spiked effectively with the same method, as explored below.

The mPST method programmed in MITT uses an additional user-defined coefficient (C_λ) as a multiplier to the universal threshold (with default value of 1.0). This is to allow flexibility, as the universal threshold alone does not always remove all significant noise data. Figure 2.6.5 shows the phase-space plots of the typical upstream and downstream raw data, for the x-direction velocity component only. Note the difference in axis scales, which indicate the relative levels of turbulence and noise between the sets of results. Also shown are ellipses sized using the the universal threshold and three values of C_λ. The value of $C_\lambda = 1.0$ excludes very few data points in the upstream results, but is very effective in excluding a significant amount of noise data in the downstream results. However, it is conservative and does also allow a number of results in the 'spokes' of the downstream results to be accepted. Therefore two lower values of C_λ were also trialled; of these, $C_\lambda = 0.5$ appears to be overly selective, but $C_\lambda = 0.75$ gives a balance between the two, and also appears suitable for both sets of results.

The raw data, and de-spiked data corresponding to all three values of C_λ are shown in frequency space in Figure 2.6.6. The upstream results show little variation between raw and de-spiked results, but the downstream results show a significant reduction in PSD at all frequencies, and a notable increase towards a gradient of -5/3. Results from using $C_\lambda = 1.0$ and $C_\lambda = 0.75$ are very similar, but $C_\lambda = 0.5$ gives a further reduction in PSD throughout the full frequency range, including at low frequencies where noise is less likely.

The downstream results show the large spike in PSD that occurs at the blade pass frequency remains significant after the de-spiking process, and the reduction in PSD at this frequency is significantly less than throughout the general frequency range. The de-spiking process also reveals a significant spike in PSD at the turbine rotational frequency, and this was not immediately clear in the raw results. This shows the mPST approach is successfully retaining good data, corresponding to flow structures created by the turbine rotation.

In order to further assess the suitability of the trialled C_λ values, the mean, standard deviation and skew of raw and de-spiked data series are presented in Figure 2.6.7, for three batches of thirty cells each, measured in the vertical plane. De-spiking has a significant effect on the downstream data results, with

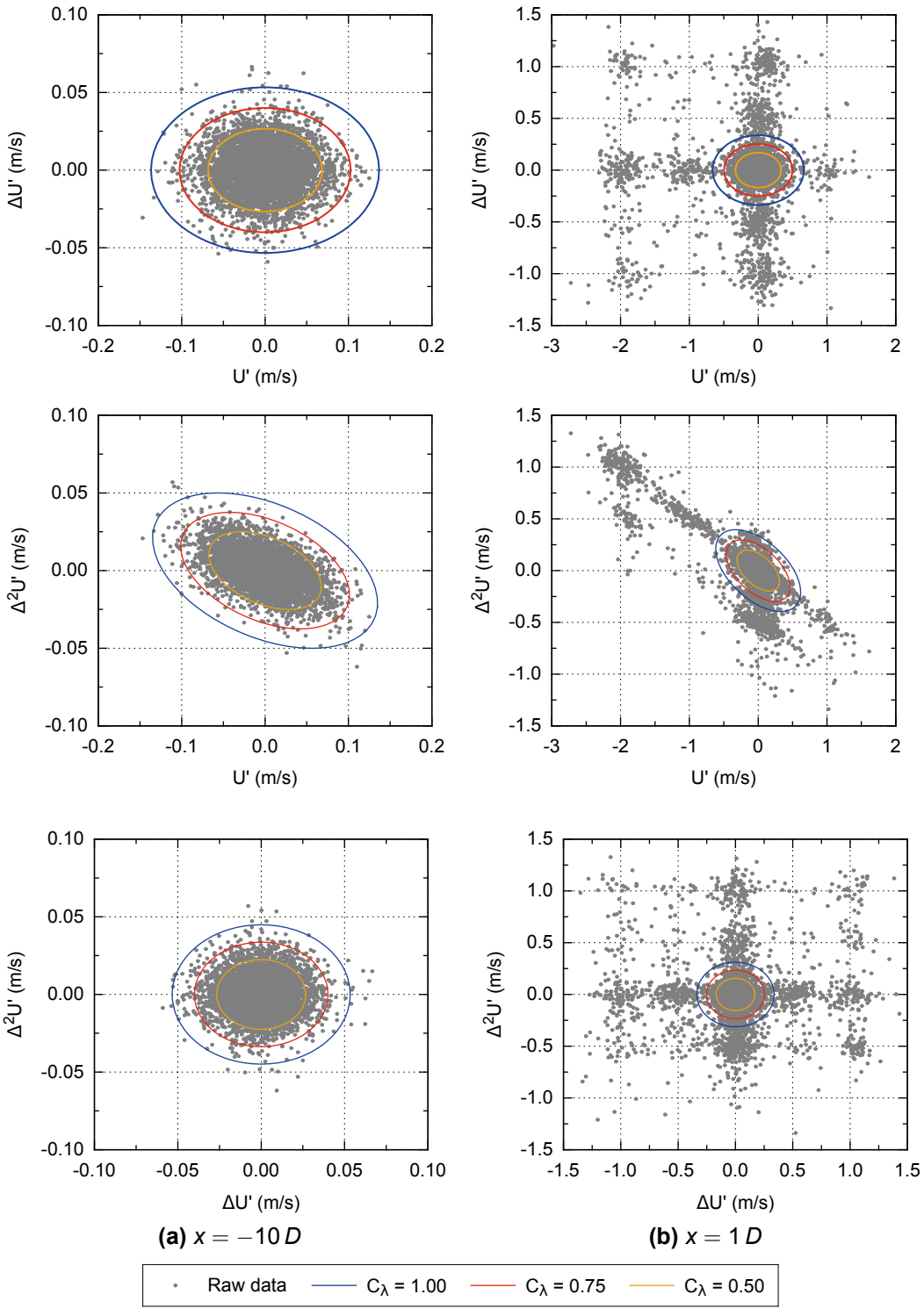

Figure 2.6.5: Phase-space plots for x-direction velocity series, showing various mPST thresholds ($C_\lambda \lambda_U MAD_U$), measured at upstream and downstream positions (both at $y = 0\,m$, $z = 0.018\,m$)

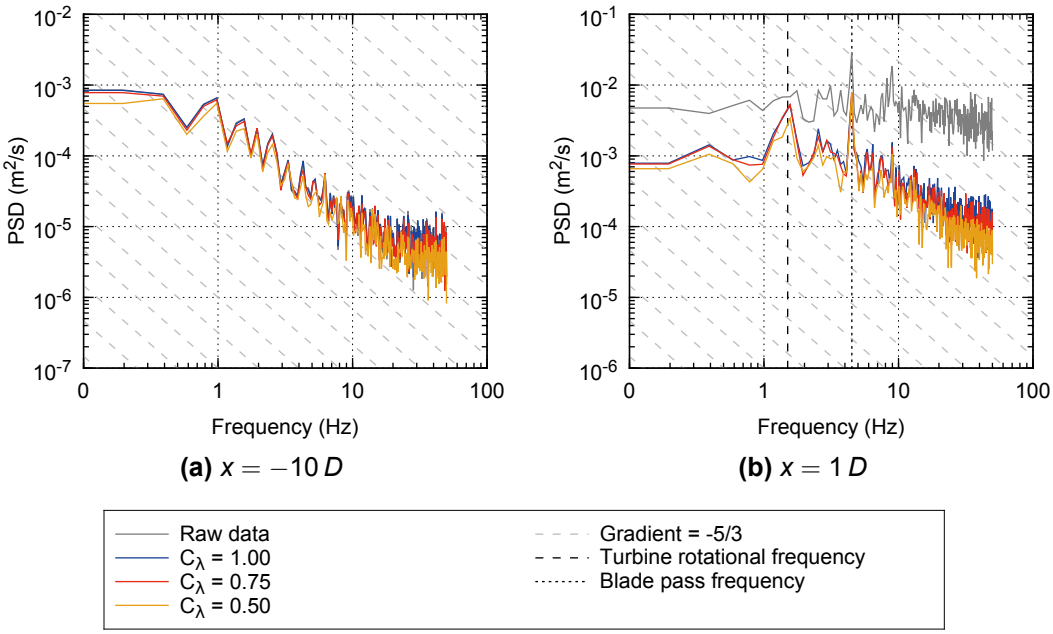

Figure 2.6.6: Estimates of power spectral density for x-direction velocity series, showing raw data and the effect of various mPST threshold coefficients (C_λ) on de-spiked data, measured at upstream and downstream positions (both at $y = 0\,m$, $z = 0.018\,m$)

mean values increased by approximately 20% and both standard deviation and skew decreased by approximately 80%. This confirms that de-spiking is important for improving the reliability of statistical measures of the data sets.

Each batch of thirty cells (e.g. $0.00\,m < z < 0.03\,m$) also contains notable variations in values from top to bottom, and obvious discontinuities exist between adjacent batches in both upstream and downstream results. Values at the extreme positions (i.e. closest to and furthest from the ADV probe transmitter) differ the most from those near the centre of each batch. This indicates the quality of data, and level of noise contamination varies with cell position and ideally the de-spiking process would be able to correct this.

The choice of C_λ value has the greatest impact on results in the extreme positions within each batch, where the most variation between post-processed values is generally observed. Values of $C_\lambda = 0.75$ and $C_\lambda = 1.00$ both give similar mean and standard deviation values in the centre of each batch (e.g. $z = 0.018\,m$) but $C_\lambda = 0.75$ gives a greater reduction at the extreme locations. $C_\lambda = 0.5$ gives further reductions at these extreme locations, but also reduces the values in the centre of each batch. This is observed both in the noisy wake data and the relatively clean upstream data, indicating the de-spiking may be

overly selective here. Based on these observations, a value of $C_\lambda = 0.75$ was considered the most appropriate to use for de-spiking of all data series, regardless of level of contamination.

2.6.3.6 Classification of de-spiked time series

The apparent repeated patterns and discontinuities between each batch of adjacent 30 cells indicates a systematic error exists in the raw results. This systematic variation in velocity readings can also be seen in correlation and signal to noise ratio (SNR) data, as shown in Figure 2.6.8. Lower SNR and correlation values are seen at the extreme positions of each measurement batch, with a clear 'sweet-spot' in the approximate cell number range of 10-15 (counting from top of each profile).

The variation in velocity measurements in each batch of 30 cells can be attributed to higher levels of noise (i.e. lower SNR) in cell positions further from the sweet spot (i.e. $z = 18\,mm$). This effect is also seen in phase space plots, as shown in Figure 2.6.9 for both upstream and downstream positions. In the upstream plots, there are no obvious noise 'spokes' but the spread of the data is larger at $z = 0\,mm$ and $z = 30\,mm$ than at $z = 18\,mm$. In the downstream plots, even with the increased levels of noise, the data at $z = 18\,mm$ is also more concentrated. The universal threshold is directly proportional to the spread of the raw data, and therefore if this is higher, the threshold ellipse will be larger and the mPST technique cannot automatically correct this data.

The amount of noise in readings from different cells can also be visualised in frequency space, with series measured at $z = 18\,mm$ containing much less noise, even after de-spiking, especially at the upstream position. By assessing the slope of the PSD in the frequency inertial sub range each de-spiked time series can be objectively assessed as being relatively noise free, or not (see Figure 2.6.10). For the upstream data especially, the relative quality of $z = 18\,mm$ data is clear, with the gradient of the PSD trend approaching -5/3 in the frequency range of 5-20 Hz. For the downstream data, the difference is not as pronounced, but the $z = 18\,mm$ data is again the least contaminated.

In order to further classify the de-spiked data based on the apparent variation in quality seen within each batch, the data has been classified by the gradient of the PSD trend in the estimated inertial sub-range. This is achieved by setting

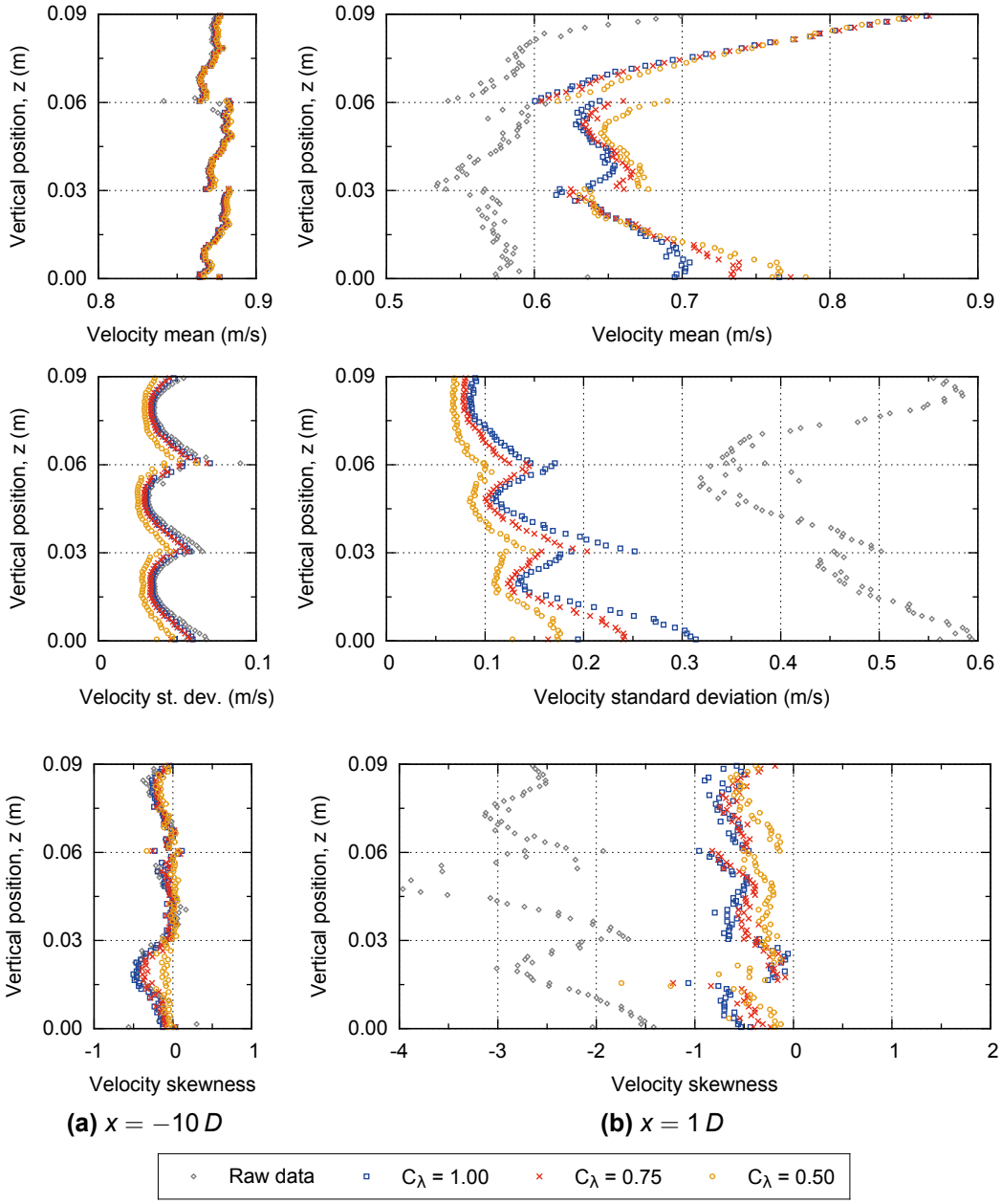

Figure 2.6.7: Profiles showing variation with vertical position of the mean, standard deviation and skewness of individual x-direction velocity series, showing raw data and the effect of various mPST threshold coefficients (C_λ) on despiked data, measured at upstream and downstream positions (both at $y = 0\,m$)

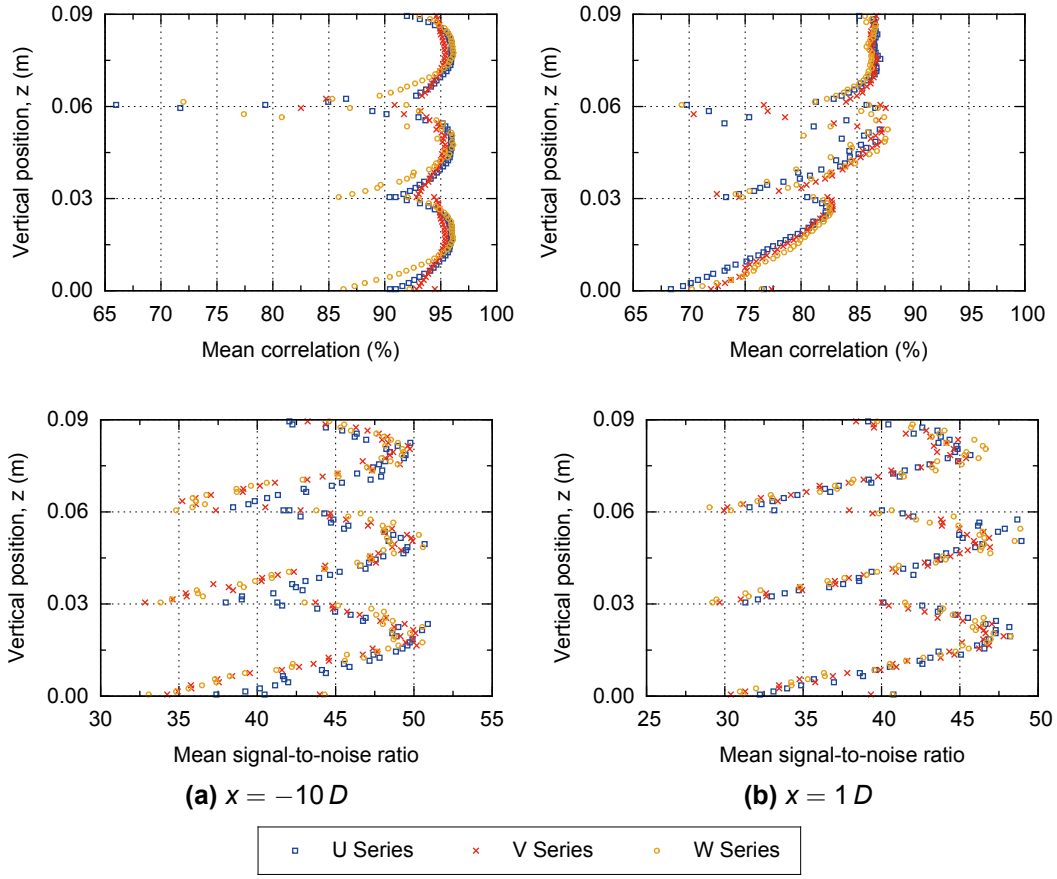

Figure 2.6.8: Profiles showing variation with vertical position of the mean correlation values and signal-to-noise ratios for x, y and z-direction velocity series, measured at upstream and downstream positions (both at $y = 0\,m$)

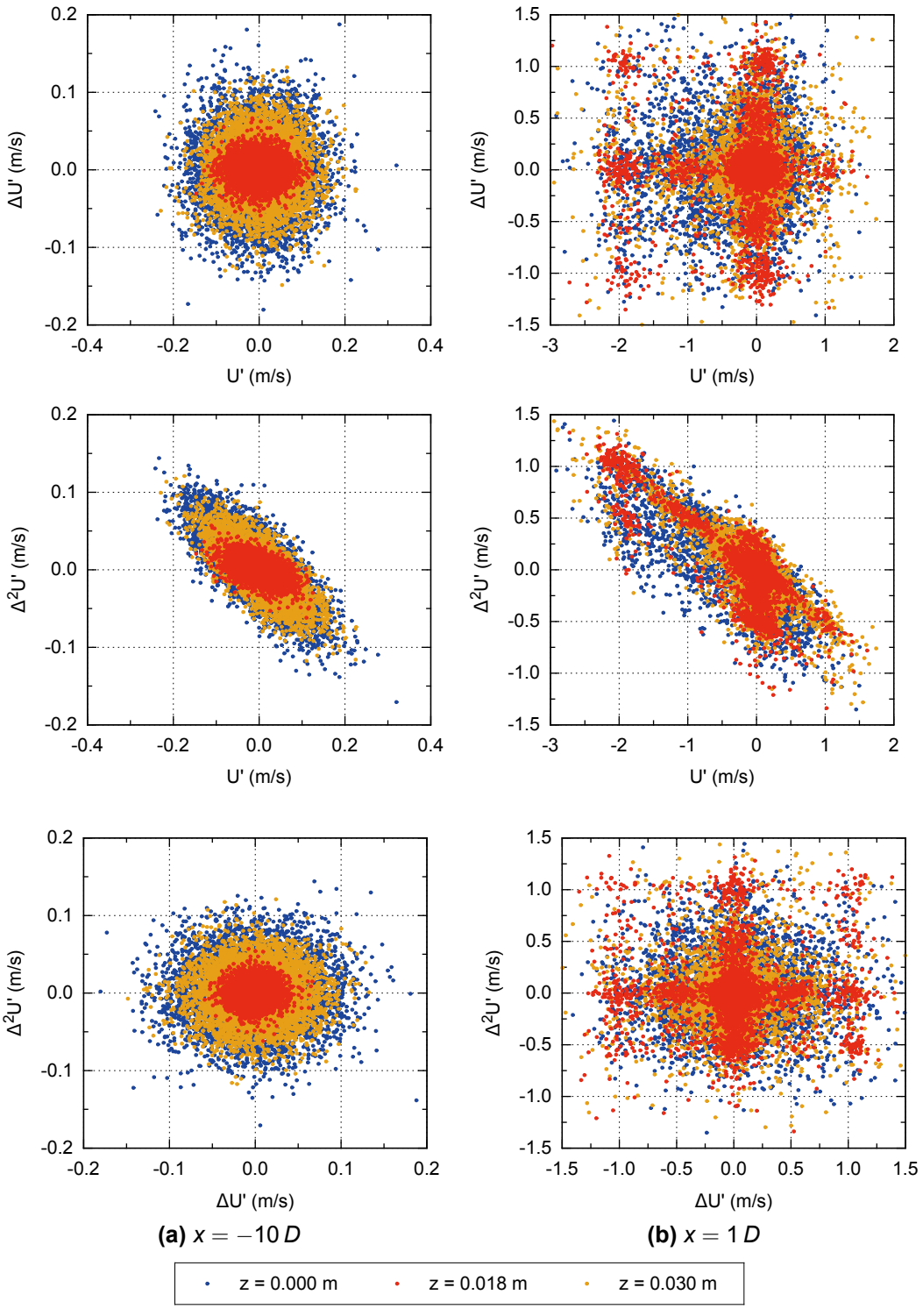

Figure 2.6.9: Phase-space plots for raw x-direction velocity series measured concurrently at upstream and downstream positions (both at $y = 0\,m$)

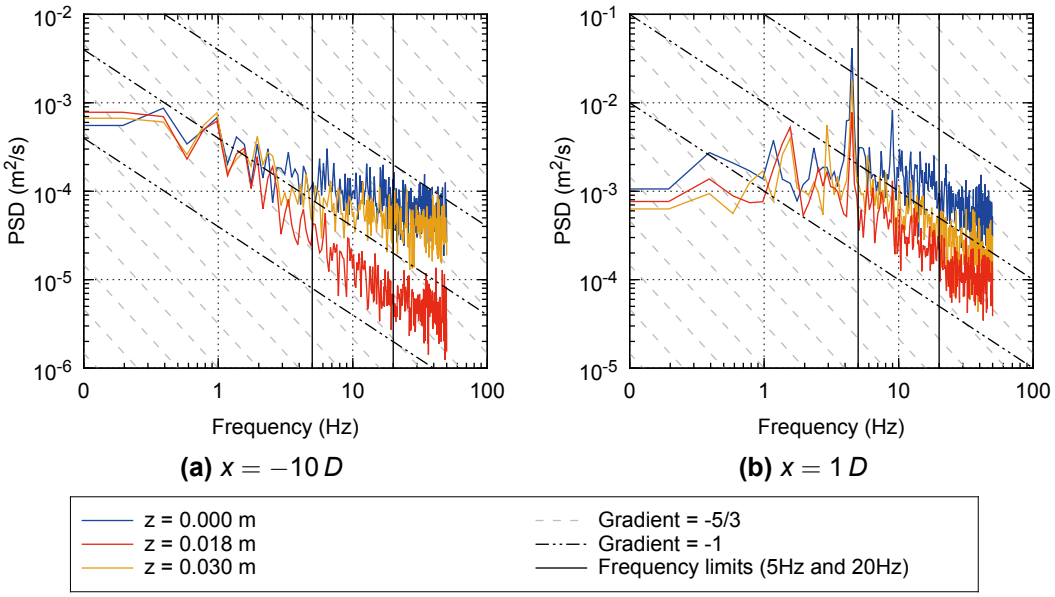

Figure 2.6.10: Estimates of power spectral density for x-direction velocity series measured concurrently, that have been de-spiked using an mPST threshold coefficient of $C_\lambda = 0.75$, measured at upstream and downstream positions (both at $y = 0\,m$)

an upper gradient threshold for a preset frequency range, as enabled by the MITT software of MacVicar.

The selection of the limits for the inertial sub-range presents a challenge; the actual upper limit will extend beyond the frequency limit of the PSD plots (which is 50% of the sampling frequency) but the highest frequencies shown in the plots are more likely to be contaminated with Doppler noise, even after de-spiking. Therefore the upper limit has been set lower than 50Hz; after inspection of a number of results, a value of 20Hz was chosen. A lower limit of 5Hz was also chosen after inspection of a number of results, as this is above the range led to consistent classification for a wide range of data (i.e. upstream and downstream results). The limit on the gradient of the PSD trend was set at -1, as -5/3 was found to exclude too many results. The selected frequency range and gradient limit is also shown in Figure 2.6.10 and indicates that only the data at $z = 18\,mm$ is likely to be accepted when using these criteria.

The effect of both de-spiking and classification on the full depth velocity mean and standard deviation profiles, at upstream and downstream locations, is shown in Figure 2.6.11. The graphs show that in relatively clean locations (e.g. upstream and bypass flow areas), the classification process only accepts a small number of cells in each batch. However, in more noisy locations (e.g. in the

wake) a larger number of cells are accepted. These still present discontinuities in the results and therefore a further sample-averaging step has been used to give a single final value for each batch of 30 cells. Although this reduces the spatial resolution of the results, the final profiles give an overall description of the flow.

In addition to measurements through the depth of the channel, a number of 'centre-line' readings were also taken. The same de-spiking, classification and sample-averaging post-processing sequence was used for these results, with an example shown in Figure 2.6.12. The use of sample averaging here is required, as each batch of readings was taken over the vertical range $-0.15 < z < 0.15\,m$ but only variation of longitudinal position is represented on the graphs.

2.6.4 Experimental results

2.6.4.1 Upstream flow profiles

Figures 2.6.13 and 2.6.14, show the vertical and transverse profiles for mean and standard deviation values of the three velocity components, at the far up-stream position ($x = -10D$). The results show that the velocity mean and standard deviation values are relatively constant in the central portion of the flume corresponding to the turbine position (i.e. $-0.1\,m < z < 0.1\,m$ and $-0.1\,m < y < 0.1\,m$). There is a clear boundary layer region near the base of the flume, where x-direction velocity decreases and standard deviation increases. There are also similar regions near the side walls, as shown in the mid-depth profiles. The y- and z-direction velocity profiles also show there is an amount of flow rotation in the flume. For example, the y-direction velocity is generally positive at the flume bed, and negative at the water surface. Likewise, the z-direction velocity is negative at the front wall and positive at the back wall. However, the maximum magnitudes of these rotating components are approximately 5% of the x-direction velocity and therefore do not adversely affect the experiment.

Note that standard deviation of the velocity series have been presented, and not turbulence intensity or turbulent kinetic energy. The latter values are calculated using all three components of the flow (i.e., x-, y- and z-direction values), but the time series have been analysed and presented as individual components.

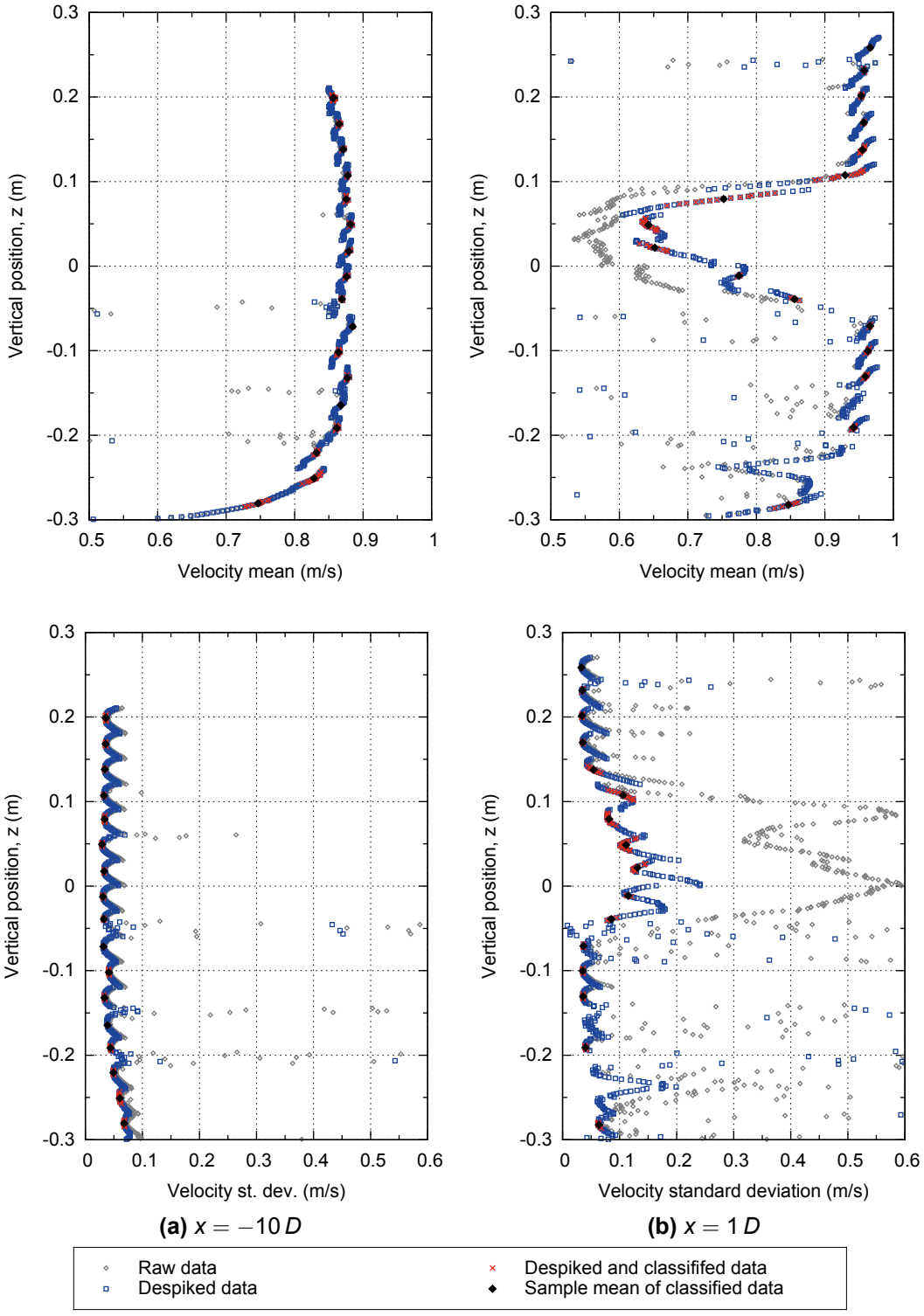

Figure 2.6.11: Profiles showing variation with vertical position of the mean and standard deviation of individual x-direction velocity series, showing results from raw data, data that has been de-spiked, and data that has also been classified by the slope of the PSD estimate, measured at upstream and downstream positions (both at $y = 0\,m$)

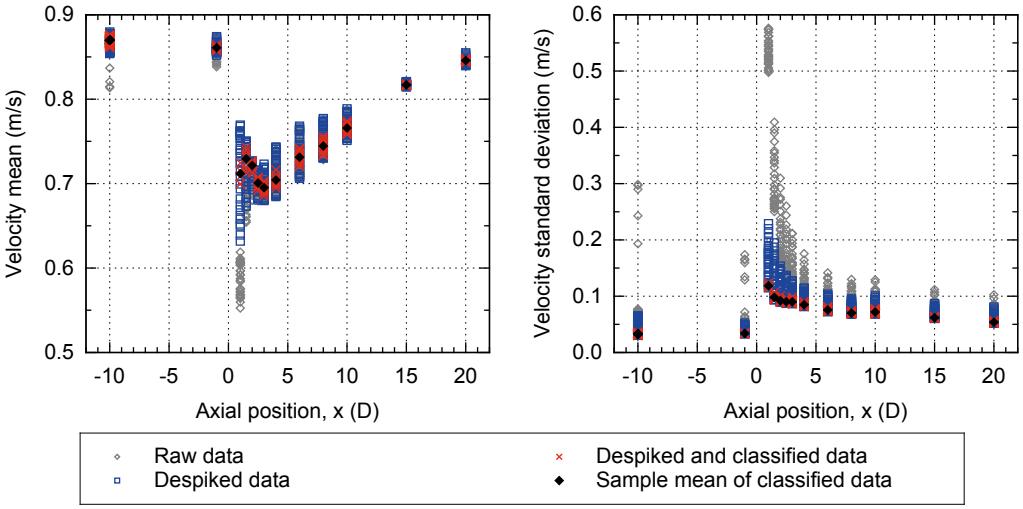

Figure 2.6.12: Profiles showing variation with longitudinal position of the mean and standard deviation of individual x-direction velocity series, showing results from raw data, data that has been de-spiked, and data that has been further classified by the slope of the PSD estimate (at $y = 0\,m$ and $0.00 < z < 0.03\,m$)

The de-spiking and classification process can result in only one or two processed components being presented at a particular cell location, and therefore turbulence values cannot be accurately calculated at all points.

2.6.4.2 Downstream wake profiles

Figures 2.6.15 and 2.6.16 show the full set of mid-span and central-axis depth cross sectional velocity profiles for the turbine operating at $BSR = 0.6$ in a flow of mean inlet velocity $U_0 = 0.87\,m/s$.

The results show a clear wake structure formed directly downstream of the turbine, that extends the height and width of the turbine model. The maximum x-direction velocity deficit does not occur at the central-axis depth, but at approximately $z = 0.05\,m$, corresponding to the position at which the turbine blade creates the maximum blockage to the flow. This peak wake value appears to endure for up to $5\,D$ downstream, before an amount of recovery is seen at $10\,D$. There is a corresponding reduction in standard deviation, or turbulence levels, as longitudinal distance from the turbine increases, which is observed for all three velocity components.

The y- and z-direction results show an amount of disturbance is caused by the turbine and while the latter values tend to decrease towards a uniform profile,

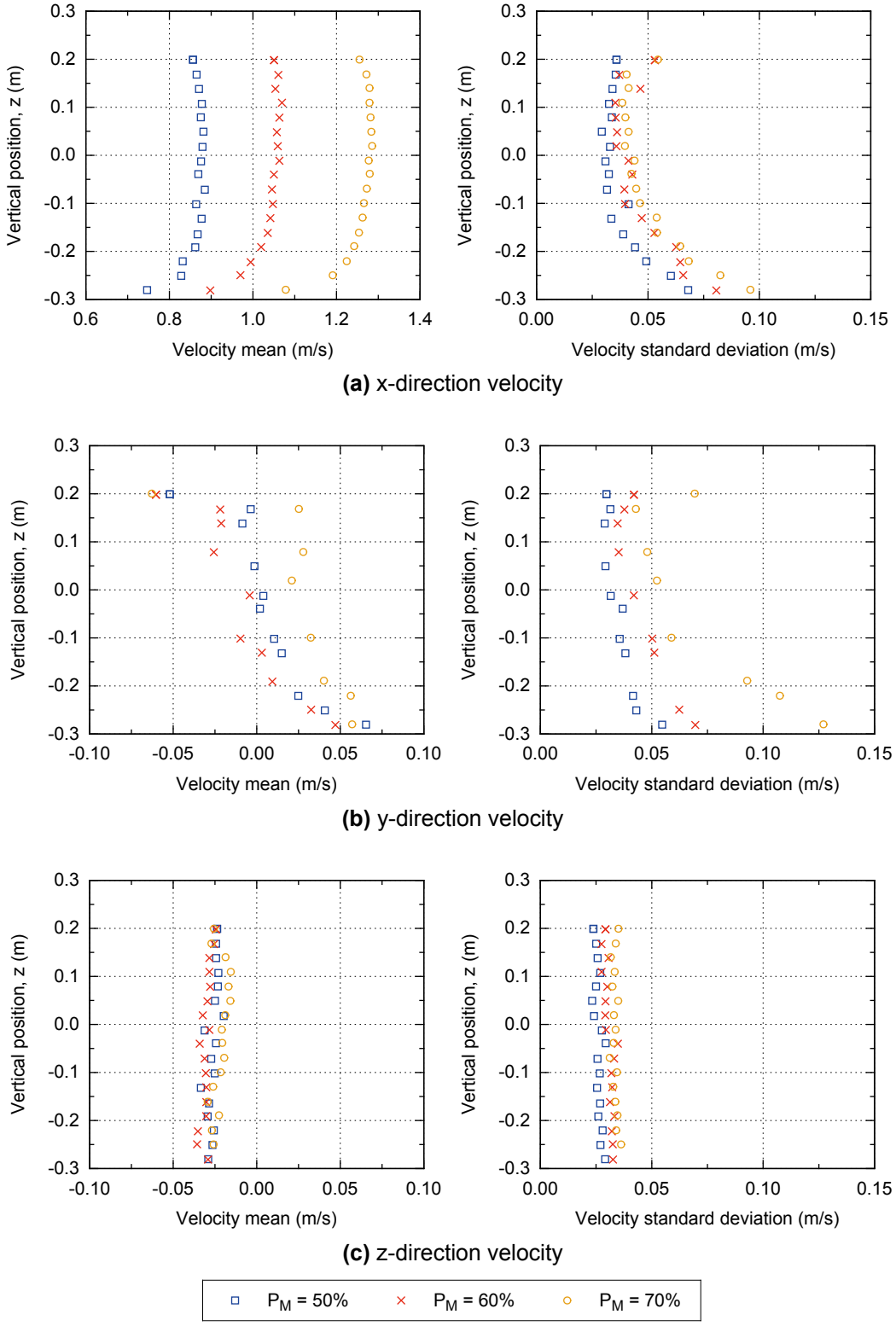

Figure 2.6.13: Profiles showing variation with vertical position of the mean and standard deviation of individual velocity series measured at an upstream position ($x = -10\,D$ and $y = 0\,m$), showing data that has been de-spiked and classified by the slope of the PSD estimate

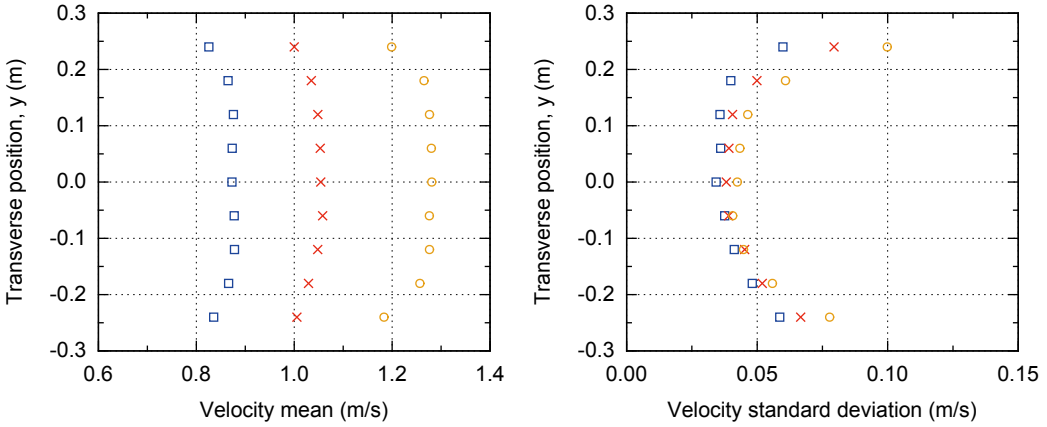

(a) x-direction velocity

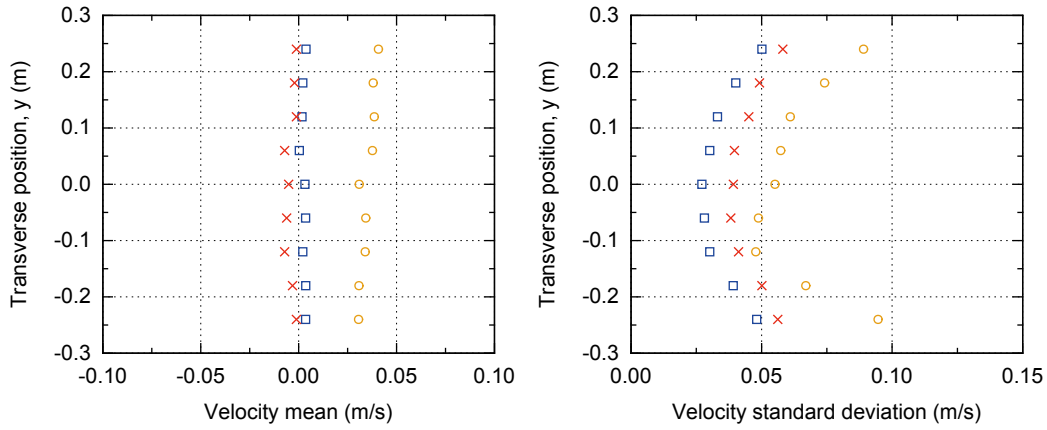

(b) y-direction velocity

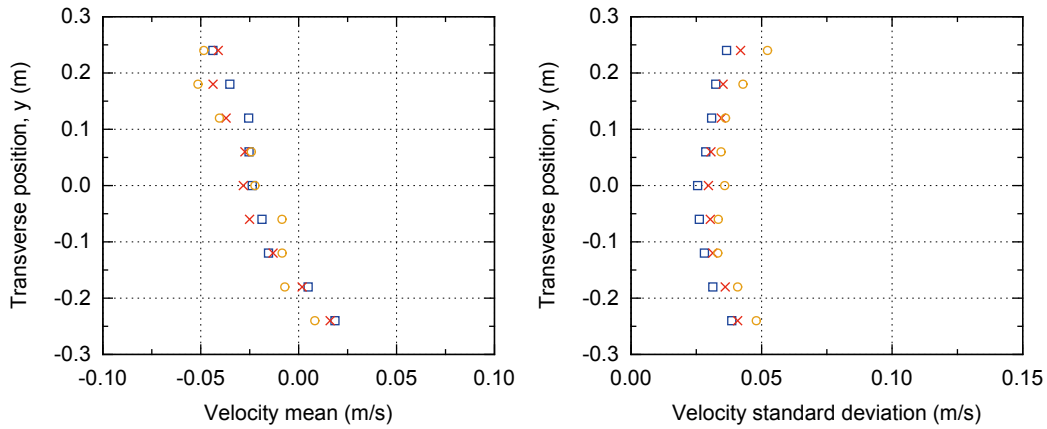

(c) z-direction velocity

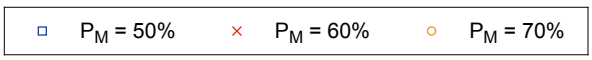

Figure 2.6.14: Profiles showing variation with transverse position of the mean and standard deviation of individual velocity series measured at an upstream position ($x = -10\,D$ and $-0.015 < z < 0.015\,m$), showing data that has been de-spiked, classified and sample-averaged

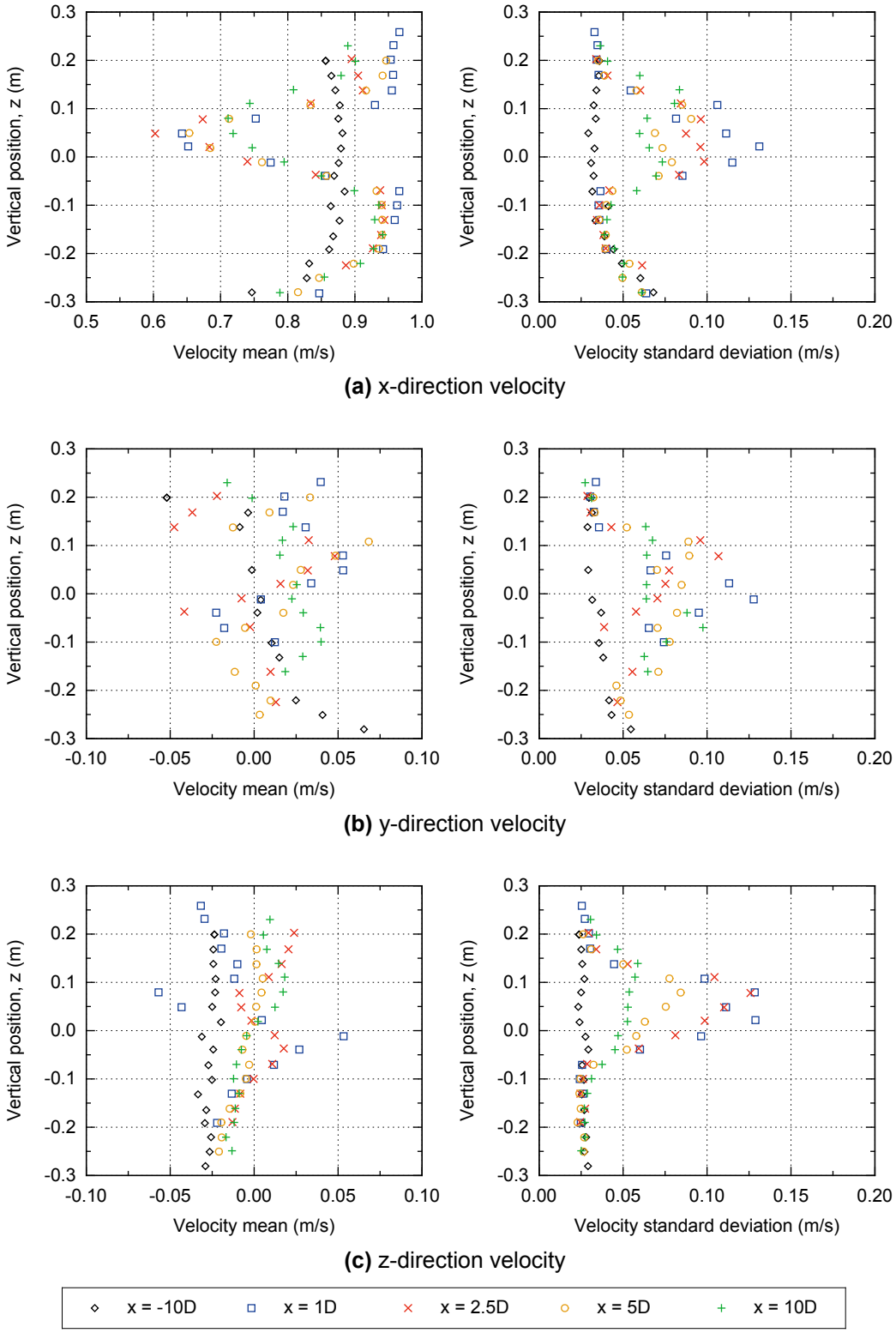

Figure 2.6.15: Profiles showing the variation with vertical position (at $y = 0\,m$) of the mean and standard deviation of individual velocity series measured at various longitudinal positions. The turbine was operating at $BSR = 0.6$ with $\bar{U}_0 = 0.87\,m/s$ and no side plates attached

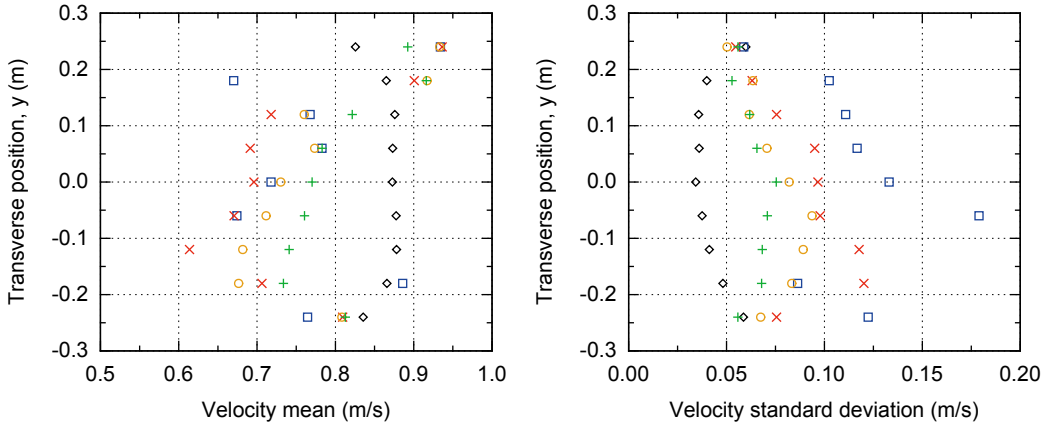

(a) x-direction velocity

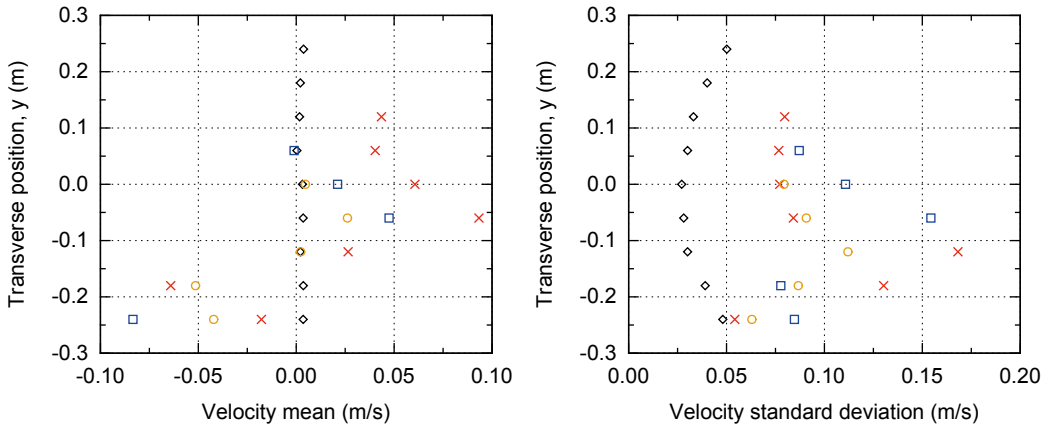

(b) y-direction velocity

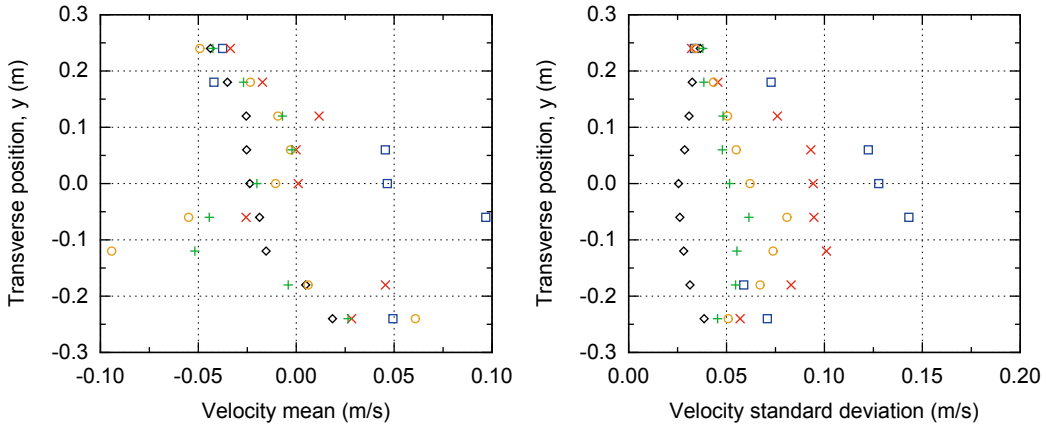

(c) z-direction velocity

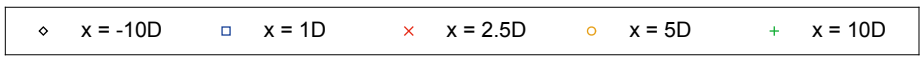

Figure 2.6.16: Profiles showing the variation with transverse position (at $-0.015 < z < 0.015\,m$) of the mean and standard deviation of individual velocity series measured at various longitudinal positions. The turbine was operating at $BSR = 0.6$ with $\bar{U}_0 = 0.87\,m/s$ and no side plates attached

the disturbance in the y-direction component values endures with increasing longitudinal distance. This behaviour was also observed visually, with the wake noticeably meandering from side to side in the flume.

Also notable is the fact the transverse velocity profiles measured at the central-axis depth are not uniform, nor symmetrical about the mid-span position. This indicates the physical structure of the turbine model, which was not symmetrical about the mid-span, had a significant effect on the flow structure downstream of the turbine, and possibly through the turbine swept volume.

Figures 2.6.17, 2.6.18 and 2.6.19 show the centre-line mean and standard deviation velocity profiles, for two resistance torque settings at each of three mean inlet velocity values. Note, a number of data points are missing, particularly in the y-direction graphs, which is a result of high levels of contamination in these time-series, that could not be sufficiently de-spiked in order to meet the classification criteria described previously.

Generally, the velocity deficit downstream of the turbine recovers with longitudinal distance, with approximately 95% recovery of the x-direction velocity at a distance 15 D. The corresponding increase in turbulence seen downstream of the turbine also reduces in line with the velocity recovery.

When comparing the effect of BSR, each graph shows that the higher value (and corresponding lower C_P value) yields a lower near-wake deficit than the lower value. This appears directly linked to the relative power coefficients, with higher degrees of energy conversion corresponding to lower flow velocities directly downstream of the turbine. Also notable is the maximum wake deficits tend to endure for up to a distance of 5 D downstream, which matches the observation of the cross-sectional results discussed previously.

2.6.5 Conclusions of experiment

This section has presented experimental work that was undertaken in order to characterise both the flume inlet flow and wake developed downstream of the experimental MRL turbine model. Although the latter is not the main focus of the wider work, it provides useful data for analysis of CFD simulation results and may be of use to other researchers.

A significant amount of the work presented has focused on the post-processing approach that was developed, based on existing de-spiking and classification

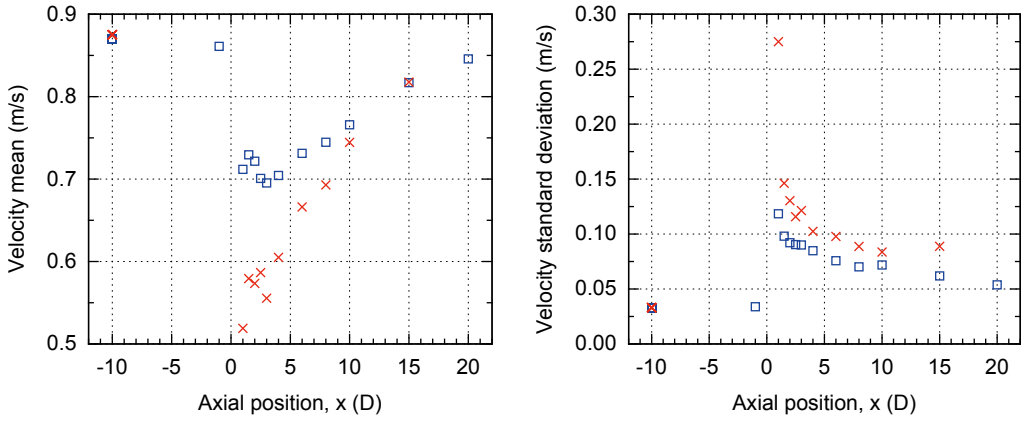

(a) x-direction velocity

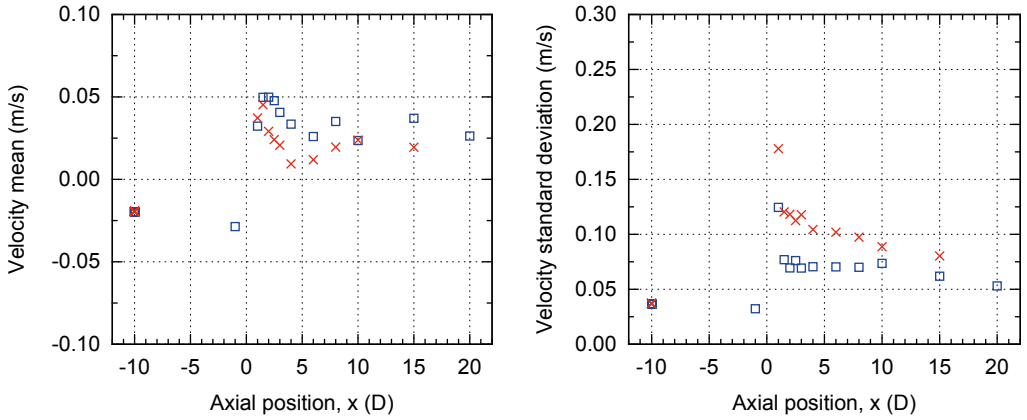

(b) y-direction velocity

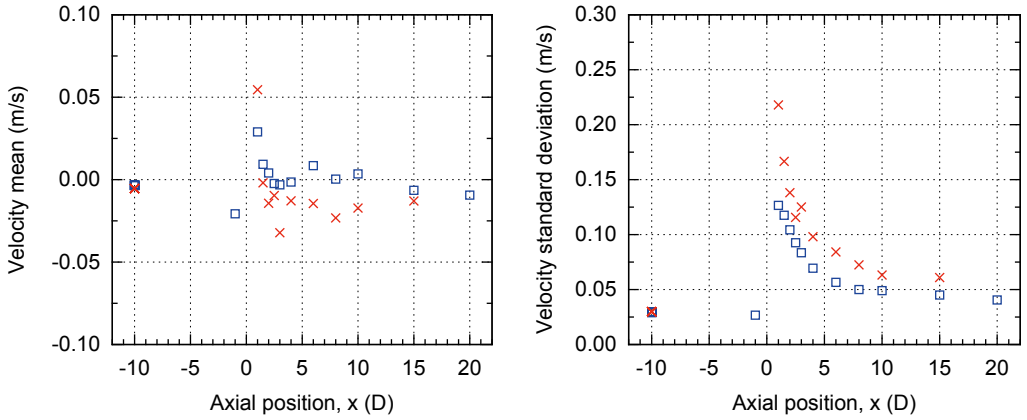

(c) z-direction velocity

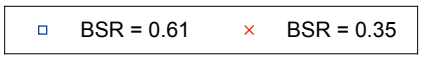

Figure 2.6.17: Profiles showing variation with longitudinal position (at $y = 0\,m$) of the mean (left) and standard deviation (right) of velocity time series. The data points represent the sample-mean values of de-spiked and classified data, measured together in the range $-0.015 < z < 0.015\,m$ at each longitudinal position. The turbine was operating without side plates in a flow of $\bar{U}_0 = 0.87\,m/s$

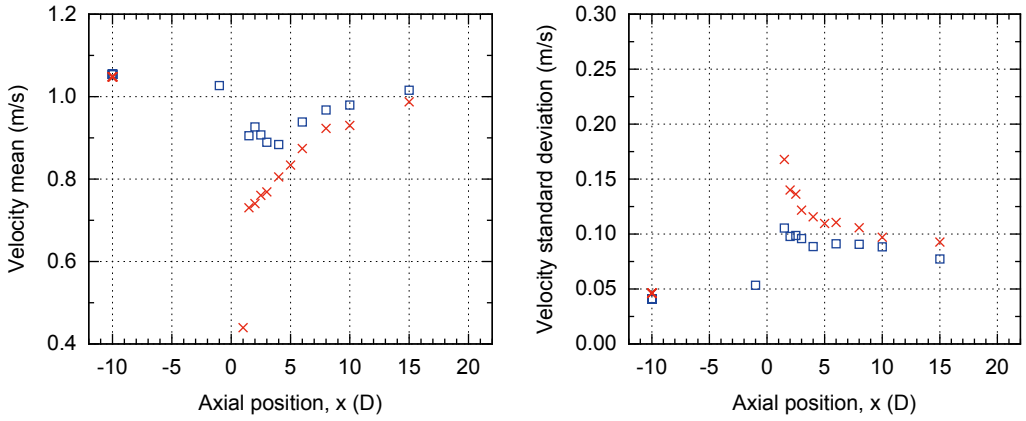

(a) x-direction velocity

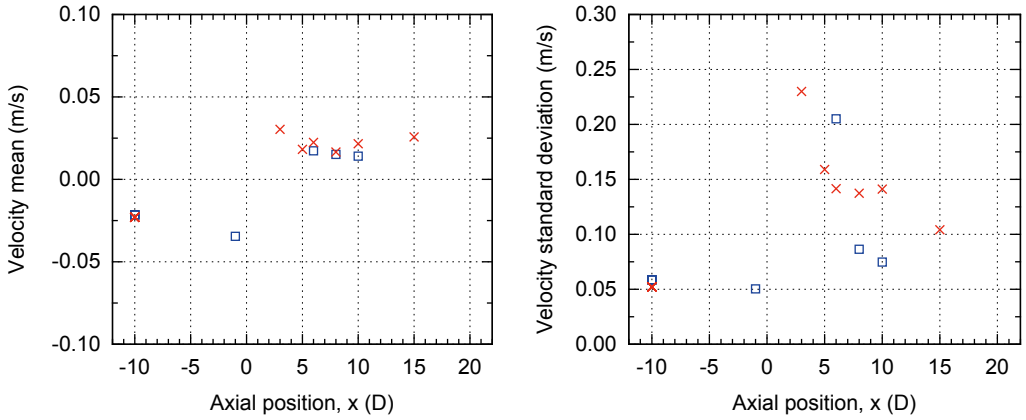

(b) y-direction velocity

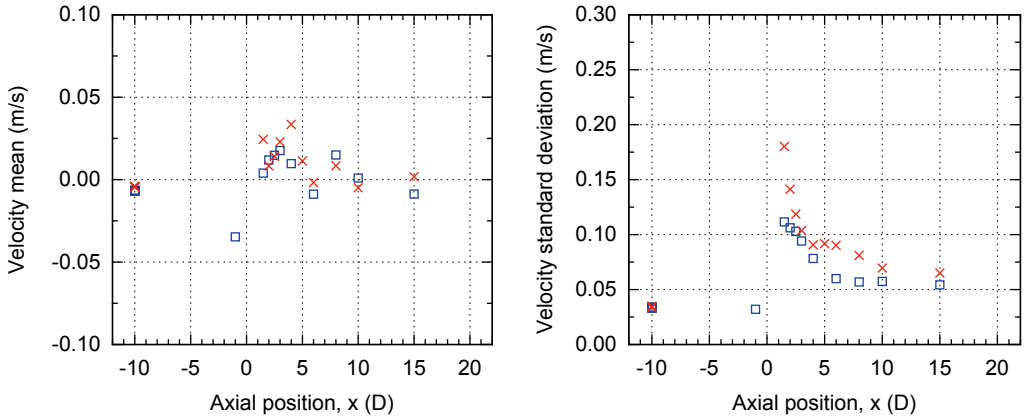

(c) z-direction velocity

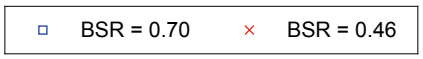

Figure 2.6.18: Profiles showing variation with longitudinal position (at $y = 0\,m$) of the mean (left) and standard deviation (right) of velocity time series. The data points represent the sample-mean values of de-spiked and classified data, measured together in the range $-0.015 < z < 0.015\,m$ at each longitudinal position. The turbine was operating without side plates in a flow of $\bar{U}_0 = 1.05\,m/s$

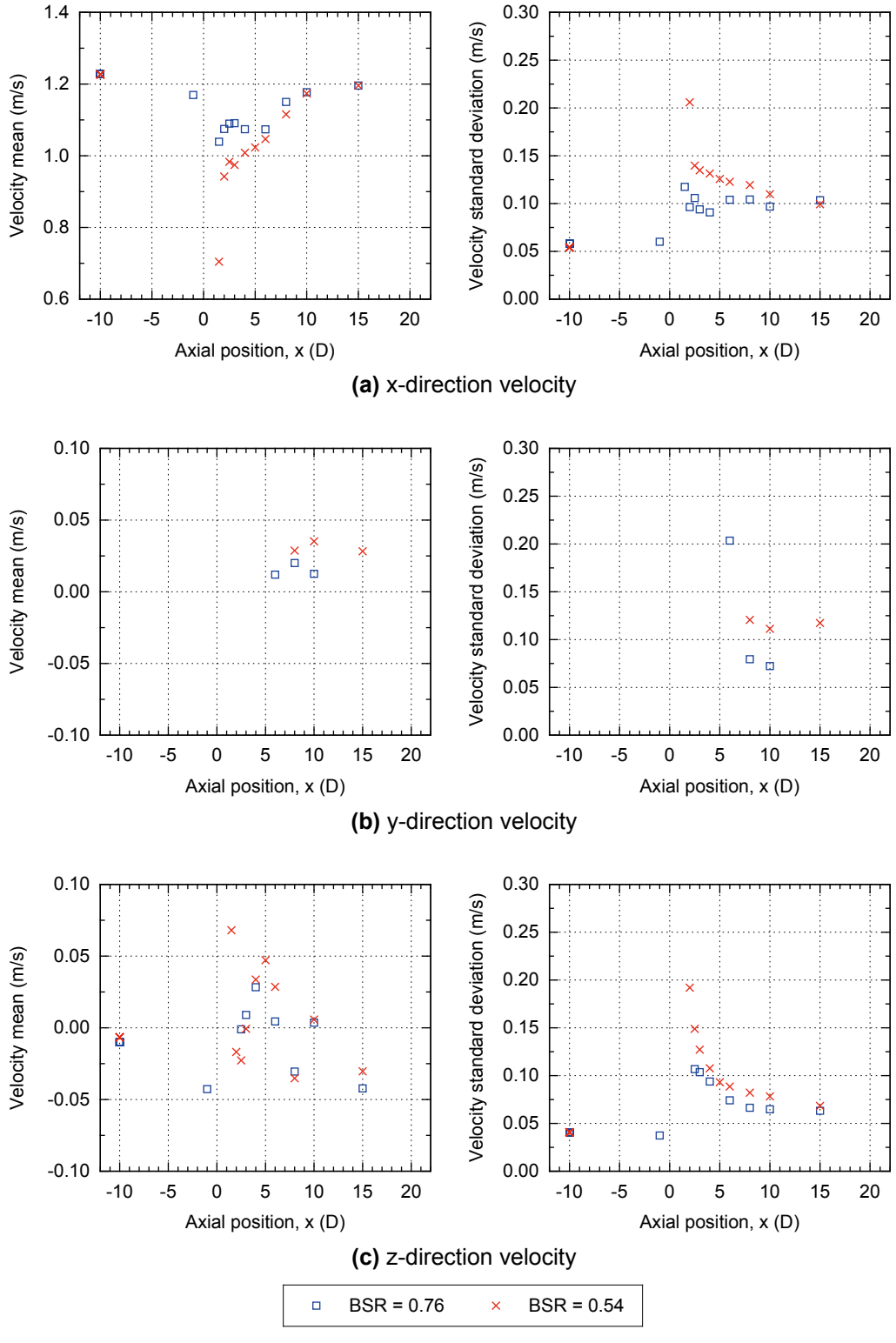

Figure 2.6.19: Profiles showing variation with longitudinal position (at $y = 0\,m$) of the mean (left) and standard deviation (right) of velocity time series. The data points represent the sample-mean values of de-spiked and classified data, measured together in the range $-0.015 < z < 0.015\,m$ at each longitudinal position. The turbine was operating without side plates in a flow of $\bar{U}_0 = 1.22\,m/s$

techniques. The selected procedure improved the reliability of the experimental wake results by reducing the artificial noise levels of the raw data, and selecting the most reliable data from each batch of measurement cells.

The resulting velocity profiles have shown the MRL turbine produces a significant wake, with maximum deficit of the x-direction velocity occurring higher than the central axis position. The maximum wake deficit endures for a distance of approximately 5 D downstream of the turbine before recovery occurs, with 95% recovery by approximately 15 D.

The y- and z-direction velocity profiles show significant disturbance was caused by the turbine model. The near wake values are not uniform with transverse position, which indicates either the incoming flow velocity was not fully aligned with the x-axis or the turbine model (and it's support structure in particular) induced significant three-dimensional flow to occur; either of these may have had an effect on the forces developed by the full span of each blade as it translated through the incoming flow, possibly reducing the torque and power developed, when compared to a hypothetical uniform flow situation.

2.7 Chapter Conclusions

This chapter has presented the experimental hydrodynamic analysis of a single laboratory-scale model of the MRL turbine. A description of the physical characteristics was firstly presented, followed by an analysis of the multiple sources of rotational resistance that exist within the turbine model. A number of relationships that estimate the variation of mechanical and hydrodynamic resistance with turbine rotational speed were developed. Following this a set of experiments were presented that measured the total rotational resistance of the turbine rotating in a tank of stationary water. From these results, and the relationships developed previously, an estimation was made of the total rotational resistance of the turbine when operating in an experimental flume.

The next section presented experimental work with the aim of characterising the turbine model's energy conversion performance at a range of rotational speeds, or blade-speed-ratios. The effect of varying the flow velocity was investigated, as well as the effect of adding of the optional side plates to the model. The results showed a peak torque coefficient occurred at a blade speed ratio in the range of $0.2 < BSR < 0.3$ and a peak power coefficient occurred in the

range $0.35 < BSR < 0.45$. At higher values of BSR both coefficients reduced towards zero at $BSR = 0.9 - 1.0$. The results from different inlet flow velocities were relatively well correlated, although variation and uncertainty in the results increased with BSR value. The use of side plates does not appear to increase the peak torque or power coefficient values, but extends the width of the peak region to higher values of BSR.

The final section of the chapter presented experimental work undertaken with the aim of characterising both the flume inlet flow and wake developed downstream of the turbine model. A post-processing approach, based on existing de-spiking and classification techniques was presented and tuned for use with the gathered data. The selected procedure improved the reliability of the experimental wake results by reducing the artificial noise levels of the raw data, and selecting the most reliable data from each batch of measurement cells. The measured velocity profiles provide an insight into the structure of the downstream wake and show it is not symmetrical about the central-axis depth. The maximum velocity deficit tends to endure for a distance of approximately $5\,D$ downstream of the turbine before recovery occurs, with 95% recovery by approximately $15\,D$. However, the near wake values are not uniform with transverse position, indicating the turbine model structure may have affected the torque and power developed by the turbine.

In order to assess this, it is suggested that further experimental testing is undertaken, but with a higher aspect ratio turbine, possibly in a flume with increased cross-sectional area. The turbine model should be symmetrical about the mid-span plane, and the volume taken up by support structure and pitch control mechanisms should be minimised. A low profile gear system, with consistent rotational resistance would be an improvement on the pulley system used here. Also, the rotational resistance of the turbine should be measured when operating in a flow of water, to allow a more reliable estimation of the developed torque to be made.

This page is intentionally left blank.

CHAPTER 3

COMPUTATIONAL ANALYSIS: THEORY, SETUP AND SENSITIVITY

3.1 Chapter Introduction

This chapter introduces the computational fluid dynamics (CFD) analysis of a single MRL turbine, which was carried out with the open-source CFD toolbox, OpenFOAM. The computational work is focused on the laboratory-scale device described and experimentally analysed in Chapter 2, and seeks to analyse the energy conversion performance of the turbine and the variation of this with operating parameters.

This chapter first gives an overview of the theory underpinning the computational analysis, followed by a description of the CFD model setup, and finally a detailed sensitivity analysis is presented, carried out in order to ensure the results gained were independent of the computational parameters used. The work presented here is furthered in Chapters 4 and 5.

3.2 Computational Theory

The following sections give a brief overview of the theoretical basis of CFD and presents important mathematical definitions. The following information draws from Versteeg and Malalasekera (2007) and other stated sources. Firstly the mathematical basis is presented, focusing on the chosen method for computing turbulent flow fields, followed by a brief overview of the finite volume method.

3.2.1 CFD governing equations

The basis for CFD analysis lies in three equations governing the flow of fluid. These equations are the conservation of mass, conservation of momentum and conservation of energy.

For an incompressible fluid, conservation of mass is given by the continuity equation:

$$\nabla.\mathbf{u} = 0 \tag{3.2.1}$$

where **u** denotes the instantaneous velocity vector, with components *u*, *v* and *w* acting in the x-, y-, and z-directions respectively.

The conservation of momentum is given by the Navier-Stokes (NS) equations (for an incompressible fluid):

$$\frac{\partial \mathbf{u}}{\partial t} + \nabla.\mathbf{u}\,\mathbf{u} = -\frac{1}{\rho}\nabla p + v\nabla^2\mathbf{u} \tag{3.2.2}$$

where p denotes pressure, ρ denotes density and v denotes kinematic viscosity, as given by $v = \mu/\rho$, where μ denotes the dynamic viscosity. Note Equation 3.2.2 represents three equations, one each for the conservation of x-, y- and z-direction momentum.

Changes in temperature (i.e. internal energy) are considered insignificant in this study, and so the third conservation equation is ignored here.

The above system of four equations contain four unknown variables and are able to be solved using the finite volume method, briefly described in Section 3.2.3.

3.2.2 Turbulence modelling

3.2.2.1 Introduction to turbulence

The majority of engineering fluid flows involve turbulence, which can be described as three-dimensional, unsteady, random fluctuations in the flow variables that form coherent rotational structures called eddies. The length and velocity scales of the eddies vary considerably within the same turbulent flow, as kinetic energy is transferred from the largest to smallest scales (termed the turbulent energy cascade). The largest scales are of the same order as those

of the mean flow and here inertia effects dominate, as the mean flow transfers energy to the eddies. At the smallest micro-scale of eddies, named the Kolmogorov scale, viscous effects dominate as the eddy energy is dissipated as heat.

3.2.2.2 Approaches to solving turbulent flows

Whilst the NS and continuity equations given previously can be used to directly solve turbulent fluid flows, this direct numerical simulation (DNS) requires prohibitively large amounts of computational resource in order to solve for all significant scales of motion. Techniques have therefore been developed that aim to reduce the computational cost by either modelling the effect of turbulence on the mean flow (the Reynolds-averaged Navier-Stokes, or RANS, approach), or only directly tracking the behaviour of the larger eddies and modelling the effect of the smaller eddies (the large-eddy simulation, or LES, approach). Although less physically accurate, the first approach is much less computationally expensive (as greater simplifications are made and the simulations can be meaningfully run in two-dimensions) and has therefore been used throughout this study, where the computational cost of directly modelling the MRL turbine blade motion is relatively high and two-dimensional simulations have primarily been used. The RANS approach is described in the following sections.

3.2.2.3 Reynolds decomposition

In order to mathematically describe turbulent flows, instantaneous values of the flow variables can be split with the Reynolds decomposition, as shown below for the velocity vector (and hence also the velocity components u, v and w):

$$\mathbf{u} = \overline{\mathbf{u}} + \mathbf{u}' \tag{3.2.3}$$

and the pressure scalar:

$$p = \overline{p} + p' \tag{3.2.4}$$

where the first term is the instantaneous value (at time t), the second term is the steady mean value and the final term is a time varying fluctuating component (at time t), which has a mean of zero. For flows that are not time dependent (i.e. steady) the mean value of a property at time t is taken to be a time-average. For

unsteady, time dependent flows the mean value is taken to be an ensemble-average which represents the average of the instantaneous values of a property over a large number of repeated identical experiments.

3.2.2.4 Reynolds-averaged Navier-Stokes equations

By substitution of equations 3.2.3 and 3.2.4 into equations 3.2.1 and 3.2.2, the following continuity and momentum equations for the mean flow can be formed:

$$\nabla.\overline{\mathbf{u}} = 0 \tag{3.2.5}$$

$$\frac{\partial \overline{\mathbf{u}}}{\partial t} + \nabla.(\overline{\mathbf{u}}\,\overline{\mathbf{u}}) + \nabla.(\overline{\mathbf{u}'\,\mathbf{u}'}) = -\frac{1}{\rho}\nabla\overline{p} + \nu\nabla^2\overline{\mathbf{u}} \tag{3.2.6}$$

which are known collectively as the Reynolds-averaged Navier-Stokes equations. These mean flow equations are identical in form to the standard equations, except for the additional $\nabla.(\overline{\mathbf{u}'\,\mathbf{u}'})$ term in the momentum equation(s). This term is associated with convective momentum transfer due to turbulent eddies. When rearranged, the RANS momentum equation can be written as:

$$\frac{\partial \overline{\mathbf{u}}}{\partial t} + \nabla.(\overline{\mathbf{u}}\,\overline{\mathbf{u}}) = -\frac{1}{\rho}\nabla\overline{p} + \nu\nabla^2\overline{\mathbf{u}} + \frac{1}{\rho}\nabla.\tau_{ij} \tag{3.2.7}$$

where the final term represents the six (three normal and three shear) Reynolds stresses, of the form:

$$\tau_{ij} = -\rho\,\overline{u'_i\,u'_j} \tag{3.2.8}$$

Here the suffix notation has been used in order to simplify presentation of the equation, with i or $j = 1$ corresponding to the x-direction (i.e. u velocity component), i or $j = 2$ corresponding to the y-direction (i.e. v component), and i or $j = 3$ corresponding to the z-direction (i.e. w component). In order to develop a closed system of equations, the six unknown Reynolds stresses must be treated. This can be done by developing conservation equations for each of the stresses, which is computationally expensive, or making further assumptions in order to reduce the computational cost. The second approach is described in the following sections.

3.2.2.5 Boussinesq approximation

Boussinesq proposed in 1877 that the Reynolds stresses are proportional to the mean rates of deformation, so that:

$$\frac{1}{\rho}\tau_{ij} = -\overline{u'_i u'_j} = 2\nu_t \bar{s}_{ij} - \frac{2}{3}k\delta_{ij} \tag{3.2.9}$$

where the mean rate of strain tensor is given by:

$$\bar{s}_{ij} = \frac{1}{2}\left(\frac{\partial \bar{u}_i}{\partial x_j} + \frac{\partial \bar{u}_j}{\partial x_i}\right) \tag{3.2.10}$$

the turbulent kinetic energy (TKE) per unit mass is given by:

$$k = \frac{1}{2}\left(\overline{u'^2} + \overline{v'^2} + \overline{w'^2}\right) \tag{3.2.11}$$

and δ_{ij} is the Kronecker delta, equal to one if $i = j$ and zero if $i \neq j$, which ensures the correct result is given for the normal Reynolds stresses (when $i = j$)

Also introduced here is ν_t, the turbulent eddy-viscosity, which is not a fluid property, but varies with the flow. In order to close the system of equations, only a solution for the eddy-viscosity is now required. This can be achieved by a simple mixing length model, which is inaccurate where the transport of turbulence is significant, or models where conservation equations for one or more turbulent variables are used. An example of the second approach is described in the following section.

3.2.2.6 $k-\omega$ SST model

The $k-\omega$ shear-stress transport (SST) model is a two-equation eddy-viscosity turbulence model developed and presented by Menter (1994) and revisited in Menter et al. (2003) and Menter (2009). It is based on the classic $k-\varepsilon$ turbulence model (Launder and Spalding, 1974) and the $k-\omega$ model proposed by Wilcox (1988) and blends between the two models based on proximity to wall boundaries. In the following paragraphs the theory and mathematical equations are briefly presented and the benefits of the model are outlined.

An exact transport equation for the turbulent kinetic energy can be formed by firstly multiplying each of the NS momentum equations (equation 3.2.2) by the

corresponding fluctuating velocity component (i.e. the x-direction equation is multiplied by u'), summing the results, repeating the process with the RANS momentum equations (equation 3.2.6), subtracting the two final equations and substantially rearranging to give the following (Tennekes and Lumley, 1972):

$$\frac{\partial k}{\partial t} + \nabla.k\overline{\mathbf{u}} = \nabla.\left(-\frac{1}{\rho}\overline{p'\mathbf{u}'} + 2\nu\overline{\mathbf{u}'s'_{ij}} - \frac{1}{2}\overline{u'_i.u'_i u'_j}\right) - \overline{u'_i u'_j}.\overline{s}_{ij} - 2\nu\overline{s'_{ij}.s'_{ij}} \tag{3.2.12}$$

The equation is of a similar form to the general RANS momentum equation (equation 3.2.7), with the first five terms (from left to right) representing: rate of change of quantity (i.e. TKE or velocity), transport of quantity by convection, transport of quantity by pressure, transport of quantity by viscous stresses and transport of quantity by Reynolds stress. However, the final two terms on the right are new and represent the rate of generation and rate of dissipation of k (per unit mass). Therefore the following quantity can be defined:

$$\varepsilon = 2\nu\overline{s'_{ij}.s'_{ij}} \tag{3.2.13}$$

which is responsible for the destruction of TKE. A transport equation can also be defined for this variable, as used in the $k-\varepsilon$ turbulence model. However, an alternative second transport equation can also be used, based on the turbulent frequency, ω, where:

$$\varepsilon = \beta^* k\omega \tag{3.2.14}$$

where β^* is a dimensionless constant. From dimensional analysis, it can be shown that the turbulent viscosity can be calculated as follows:

$$\nu_t = \beta^* \frac{k^2}{\varepsilon} = \frac{k}{\omega} \tag{3.2.15}$$

Therefore, given transport equations for k and ε or ω, the RANS system of equations can be closed and solved using the finite-volume method.

k transport equation

The exact k transport equation (3.2.12) can be developed into a model k transport equation by use of the gradient diffusion hypothesis to represent the turbulent transport terms (the third, fourth and fifth terms), substitution of the Boussinesq approximation (equation 3.2.9) into the sixth term (generation) and

substitution of equations 3.2.13 and 3.2.14 for the seventh term (dissipation or destruction). This leads to the following transport equation for k used in the $k-\omega$ SST model:

$$\frac{\partial k}{\partial t} + \nabla.k\overline{\mathbf{u}} = \nabla.\left[\left(\nu + \frac{\nu_t}{\sigma_k}\right)\nabla k\right] + \tilde{G}_k - \beta^* k\omega \tag{3.2.16}$$

where σ_k is a turbulent Prandtl number and $\tilde{G}_k$ represents the limited value of k generation, as given by:

$$\tilde{G}_k = min\ (G_k,\ 10\,\beta^* k\omega) \tag{3.2.17}$$

where

$$G_k = 2\,\nu_t \overline{s}_{ij}\overline{s}_{ij} \tag{3.2.18}$$

Note, equation 3.2.16 is identical to the k transport equation used in Wilcox (1988), except for the value taken for σ_k, as discussed later, and the addition of the limiter on the production G_k term. The limiter is introduced to the production term in order to prevent the build up of turbulence in stagnation regions.

ω transport equation

Wilcox (1988) developed a transport equation for ω that proved to have a number of advantages over the ε transport equation of Launder and Spalding (1974). These include the ability to resolve the equation to a wall boundary instead of using wall-functions (see Section 3.2.2.8) and better performance in adverse pressure gradient boundary-layers (Wilcox, 1993). However, the equation also proved overly sensitive to free-stream values of ω (Menter, 1992), a problem not found with the ε equation. Therefore Menter (1994) proposed a model where the Wilcox $k-\omega$ model is used within boundary layers and a transformation of the $k-\varepsilon$ model into a $k-\omega$ formulation is used elsewhere. The transformation was achieved by substituting equation 3.2.14 into the empirical ε transport equation presented by Launder and Spalding (1974). The only difference between the resulting ω transport equation and that of Wilcox are values taken for coefficients and the addition of a cross-diffusion term in the transformed equation. Therefore, to blend between the two, a function F_1 is defined, which varies from one in the viscous sub-layer to zero outside the boundary layer. By multiplying the Wilcox ω equation by F_1 and the trans-

formed ω equation by $(1-F_1)$,and adding the resulting equations, the following ω transport equation was developed for the $k-\omega$ SST model:

$$\frac{\partial \omega}{\partial t} + \nabla.\omega\,\overline{\mathbf{u}} = \nabla.\left[\left(\nu + \frac{\nu_t}{\sigma_\omega}\right)\nabla\omega\right] + \frac{\alpha_\omega}{\mu_t}\tilde{G}_k - \beta_\omega\,\omega^2 + 2\,(1-F_1)\,\frac{1}{\sigma_{\omega,2}\,\omega}\nabla k\nabla\omega \tag{3.2.19}$$

where σ_ω is a turbulent Prandtl number, and α_ω and β_ω are constants. The form of the ω transport equation is similar to that of the k equation, with the terms on the right hand side representing diffusion, generation and destruction from left to right. The final term is the cross-diffusion term modified by the blending function, as defined by:

$$F_1 = tanh\left\langle\left\{min\left[max\left(\frac{\sqrt{k}}{\beta^*\omega\,u}, \frac{500\,\nu}{u^2\,\omega}\right), \frac{4\,k}{CD_{k\omega}\,\sigma_{\omega,2}\,u^2}\right]\right\}^4\right\rangle \tag{3.2.20}$$

where u denotes the distance to the nearest wall and:

$$CD_{k\omega} = max\left(\frac{2}{\sigma_{\omega,2}\,\omega}\nabla k\nabla\omega,\ 10^{-10}\right) \tag{3.2.21}$$

In order to differentiate between the constant values used in the Wilcox equations and the transformed equations, subscripts 1 and 2 are used. To blend between the two values the following equation form is used for the arbitrary constant C:

$$C = C_1 F_1 + C_2(1-F_1) \tag{3.2.22}$$

where C_1 represents the Wilcox equation value and C_2 represents the transformed equation value. C can equal α_ω, β_ω, $1/\sigma_k$ or $1/\sigma_\omega$.

In order to give improved performance in adverse pressure gradient flows, the equation for turbulent viscosity is also modified slightly with a limiter:

$$\nu_t = \frac{a_1\,k}{max(a_1\,\omega,\ S\,F_2)} \tag{3.2.23}$$

where a_1 is a constant, S is the invariant measure of strain rate, given by:

$$S = \sqrt{2\,\overline{s}_{ij}\,\overline{s}_{ij}} \tag{3.2.24}$$

and F_2 is another blending function, given by:

$$F_2 = tanh\left\{\left[max\left(\frac{2\sqrt{k}}{\beta^* \omega u}, \frac{500\nu}{u^2 \omega}\right)\right]^2\right\} \tag{3.2.25}$$

This limiter ensures the standard formulation of $\nu_t = {}^{k}/_{\omega}$ is used outside of boundary layers and the Bradshaw (1967) assumption that shear stress is proportional to TKE is used within boundary layers.

The values for the constants used in the $k-\omega$ SST model are shown below, as updated in Menter et al. (2003):

$$\alpha_{\omega,1} = 0.553,\ \alpha_{\omega,2} = 0.44,\ \beta_{\omega,1} = 0.075,\ \beta_{\omega,2} = 0.0828$$

$$\sigma_{k,1} = 1.176,\ \sigma_{k,2} = 1.0,\ \sigma_{\omega,1} = 2.0,\ \sigma_{\omega,2} = 1.168$$

$$a_1 = 0.31,\ \beta^* = 0.09$$

3.2.2.7 $k-\omega$ SST sustain model

The standard $k-\omega$ SST model, like other two-equation turbulence models, suffers from the problem of prescribed inlet turbulence levels (related to values of k and ω) unrealistically decaying throughout the computational domain. This occurs because the destruction terms in equations 3.2.16 and 3.2.19 are always 'on', even when generation levels are low due to low levels of strain in the flow. Therefore, for external aero- or hydro-dynamic cases (including wind tunnel and flume flows) the turbulence levels encountered by the simulated object (e.g. the foil or turbine device) is not equal to that specified at the domain inlet. Therefore any investigation of the effect of ambient turbulence levels on the device performance is unreliable. To compound the problem, the decay rate is dependant upon both turbulent intensity and eddy viscosity levels in the free-stream, and also coarseness of the computational grid. In order to overcome the decay, either very low levels of free-stream turbulence intensity, or very high levels of turbulent viscosity can be used (Spalart and Rumsey, 2007). Another approach, taken by Gretton et al. (2009) is to calculate the rate of decay and set an increased inlet value for a desired turbulence level at the object of interest. However, a more reliable and less user-dependent solution was suggested by Spalart and Rumsey (2007) and subsequently tested by

Rumsey and Spalart (2008), whereby additional terms are added to the $k-\omega$ SST transport equations, as shown below:

$$\frac{\partial k}{\partial t} + \nabla.k\,\overline{\mathbf{u}} = \nabla.\left[\left(\nu + \frac{\nu_t}{\sigma_k}\right)\nabla k\right] + \tilde{G}_k - \beta^* k\,\omega + \beta^* k_{amb}\,\omega_{amb} \quad (3.2.26)$$

$$\frac{\partial \omega}{\partial t} + \nabla.\omega\,\overline{\mathbf{u}} = \nabla.\left[\left(\nu + \frac{\nu_t}{\sigma_\omega}\right)\nabla \omega\right] + \frac{\alpha_\omega}{\mu_t}\tilde{G}_k - \beta_\omega\,\omega^2 + 2\,(1-F_1)\,\frac{1}{\sigma_{\omega,2}\,\omega}\nabla k \nabla \omega + \beta_\omega\,\omega_{amb}^2 \quad (3.2.27)$$

where k_{amb} and ω_{amb} are constant values, set to equal the ambient, or inlet, values of k and ω. The additional terms in each equation serve to cancel out the destruction terms exactly when $k = k_{amb}$ and $\omega = \omega_{amb}$ and therefore turbulence levels in the free-stream are sustained. Inside boundary layers the new terms are generally several orders of magnitude smaller than the destruction terms and therefore do not significantly effect the solution.

3.2.2.8 Near-wall modelling

The structure and behaviour of turbulent flow near a solid boundary, i.e. a wall, differs considerably from that of free-stream flow. At the wall surface, a no-slip condition exists, where fluid velocity is reduced to zero. The fluid velocity then increases with increasing distance from the wall, until free-stream velocity is reached at distance δ (the boundary layer thickness). The variation in velocity near to the wall (up to approximately $0.2\,\delta$) is described by the 'law of the wall', as shown below (for a wall parallel to the x-direction):

$$u^+ = \frac{u}{u_\tau} = f\left(\frac{u_\tau u}{\nu}\right) = f(y^+) \quad (3.2.28)$$

where u^+ is the dimensionless velocity tangential to the wall, y^+ is the dimensionless perpendicular distance to the wall and u_τ is the friction velocity, given by:

$$u_\tau = \sqrt{\frac{\tau_{wall}}{\rho}} \quad (3.2.29)$$

where τ_{wall} is the wall shear stress.

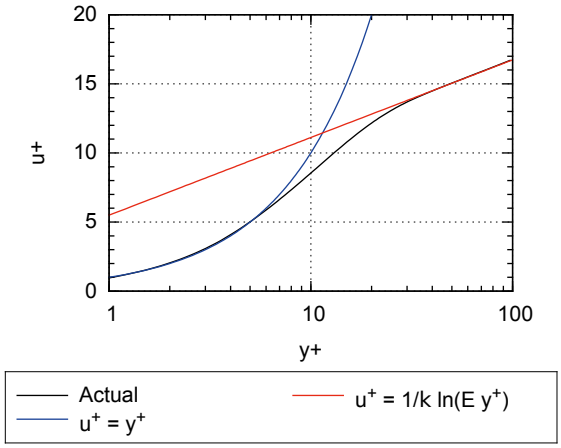

Figure 3.2.1: Variation of dimensionless velocity with dimensionless wall distance in a fluid boundary layer

The actual variation of u^+ with y^+ (found experimentally) is shown in Figure 3.2.1. Also shown are two equations linking the dimensionless values, that closely match the experimental data in different y^+ranges. The first equation, $u^+ = y^+$, is valid for values $y^+ < 5$, and this region is called the linear sub-layer. In this region, where velocity values and turbulent eddy motions are very small, viscous effects dominate and the fluid shear stress throughout the layer is assumed to equal the wall shear stress. The second equation, $u^+ = \frac{1}{\kappa} ln(E y^+)$, is valid for values $30 < y^+ < 500$, and this region is known as the log-law layer, where viscous and turbulent effects are both important, with the latter increasing in importance further from the wall. Here $\kappa \approx 0.4$ is the von Karman constant, and $E \approx 9.8$ is the wall roughness parameter, both of which have been found empirically for high Reynolds number flows past smooth walls. Between these two regions is the buffer layer, where viscous and turbulent stresses are of similar magnitude, and neither of the two equations fit the actual variation of u^+ with y^+.

In the region further than $0.2\,\delta$ from the wall, the flow is free from direct viscous effects due to the wall, and the flow is inertia dominated.

In order to account for the flow behaviour described above, two different approaches exist when using RANS modelling. The first, and most commonly used, is the wall-function or high-Reynolds number approach. Here the first computation point, or cell, next to the wall must satisfy $30 < y^+ < 500$, and the log-law is used to model the fluid behaviour in this cell. The second approach is the wall-resolved or low-Reynolds number approach, where the first wall-

adjacent cell must satisfy $y^+ < 5$, and the $k-\omega$ SST equations can be used to directly model the flow behaviour. The primary advantage of the former approach is reduced computational cost, due to a reduced number of cells in the computational domain. However, the latter approach can give more physically accurate results, especially when boundary layer behaviour is complex (e.g. it involves time-dependent separation).

At wall surfaces, turbulent kinetic energy is zero ($k = 0$) and turbulent frequency tends to infinity ($\omega \to \infty$ as $y \to 0$). It is not possible to accurately specify the latter, so the following relationship is used:

$$\omega_{wall} = \frac{6\,v}{\beta_{\omega,1}\,y^2} \tag{3.2.30}$$

3.2.2.9 Turbulent inlet parameters

At the inlet to the computational domain, it is necessary to prescribe values for the turbulent parameters k_{inlet} and ω_{inlet}. The turbulent kinetic energy can be calculated as:

$$k_{inlet} = \frac{3}{2}\,Ti^2\,\left(\bar{u}_{inlet}^2 + \bar{v}_{inlet}^2 + \bar{w}_{inlet}^2\right) \tag{3.2.31}$$

where Ti is the turbulent intensity (as defined in Equation 2.5.1) and $\bar{u}_{inlet}$, $\bar{v}_{inlet}$ and $\bar{w}_{inlet}$ are the time-averaged x-, y- and z- direction components of the inlet velocity. Also, the turbulent eddy frequency can be calculated as:

$$\omega_{inlet} = \frac{k_{inlet}}{v_t} = \frac{k_{inlet}}{TVR\,v} \tag{3.2.32}$$

where TVR is the turbulent viscosity ratio. Therefore through selection of the turbulent intensity and the turbulent viscosity ratio, values for the inlet turbulence variable can be calculated.

Turbulent intensity for a given flow can be simply calculated, based on the fluctuating components of fluid velocity measurements. It is usually in the order of 1% or below for external aerodynamic problems, although higher values are sometimes found in hydrodynamic situations.

A value for turbulent viscosity ratio is harder to define, and often estimates are made for this, or related variables. For example, Spalart and Rumsey (2007)

suggest the following for the $k-\omega$ SST-sustain model, assuming uniform x-direction inlet flow:

$$\omega_{inlet} = \frac{5\,u_{inlet}}{l_{char}} \tag{3.2.33}$$

where l_{char} is the characteristic length of the body (e.g. aerofoil chord length). This does not actually require selection of a *TVR* value, but it can be calculated using Equation 3.2.32.

An alternative approach, especially for constrained flows (e.g. in wind tunnels or water channels), is to estimate the turbulent mixing length, l_{mix}, which represents the distance travelled by a large eddy before it is destroyed by mixing. For a tunnel or channel, the mixing length can be estimated from the following:

$$l_{mix} = 0.07\,D_H \tag{3.2.34}$$

where D_H is the hydraulic diameter of the tunnel or channel. From this, ω_{inlet} can be calculated as follows:

$$\omega_{inlet} = B^{*\,-\frac{1}{4}}\,\frac{\sqrt{k_{inlet}}}{l_{mix}} \tag{3.2.35}$$

3.2.3 Finite volume method

In order to solve the system of transport equations described in Sections 3.2.1 and 3.2.2, a numerical solution procedure can be used, where the fluid domain is approximated as a series of computational nodes at which the equations are solved. In the vast majority of CFD codes, the finite-volume method (FVM) is used, where the domain is discretised into small control volumes, or cells, surrounding each node in the mesh.

3.2.3.1 Equation discretisation

In order to form the required set of equations to used with the FVM, the governing Navier-Stokes equations (or RANS equations) are integrated over the control volume, and further developed using the Gauss divergence theorem.

For example, the NS conservation of momentum equation (3.2.2) is developed into the following:

$$\int_{CV} \frac{\partial \mathbf{u}}{\partial t}\, dV + \int_{A} \mathbf{n}.\left(\mathbf{u}\,\mathbf{u} - \nu \nabla \mathbf{u}\right)\, dA = -\frac{1}{\rho} \int_{A} \mathbf{n}.\, p\, dA \tag{3.2.36}$$

where *CV* denotes integration over the control volume, *A* denotes integration over the total surface area of the volume, and **n** is the surface normal vector. The second term therefore represents the summation of momentum transport (by convection and diffusion) through each face of the control volume. At each face, the transport flux is assumed to be constant over the surface area and is estimated using values of solution variables stored at grid nodes. Where the cell face coincides with a domain boundary, special conditions are used. The equations are set up for all control volumes in the domain and this gives rise to a system of coupled algebraic equations that are solved using matrix solution techniques.

3.2.3.2 Interpolation schemes

Interpolation schemes are used in order to estimate the transport flux at cell faces. Multiple interpolation schemes exist, based on stored values at one or more adjacent nodes. Successful interpolation schemes meet the following criteria:

1. Conservative: Adjacent cells share a common face and the flux through this should be represented in a consistent manner, i.e., by the same expression in both control volumes

2. Bounded: In the absence of sources, values at nodes should be bounded by the values at the cell boundaries

3. Transportive: The relative importance of diffusion and convection should be reflected

One of the simplest schemes is central differencing, where the face value is estimated to be the average of values at the two adjacent cell nodes. However, this scheme can lead to oscillation of the numerical results and is therefore unbounded. It is also not transportive, as it does not account for flow direction.

However, it is considered second-order accurate in terms of the Taylor series truncation error.

An alternative approach is the upwind scheme, where a convected value at a face is taken to equal the value at the adjacent upwind node. This scheme meets all three criteria given above, but is only considered to be first-order accurate, which may lead to solutions appearing overly diffusive.

More advanced schemes can be used that overcome some of the above problems. An example is the linear-upwind scheme that uses a second-order correction to the standard upwind scheme, thereby ensuring stability with improved accuracy.

3.2.3.3 Solution algorithms

In order to calculate the convection of scalar variables, the local velocity field is required. However, the velocity field is generally a desired output of CFD simulations and is not known beforehand. It must therefore be solved as part of the wider solution process.

The four NS equations governing the transport of momentum, as given in section 3.2.1, are non-linear and closely coupled, and therefore challenging to solve. Also, the main source of momentum transport is the pressure field, and in incompressible flows this is also an unknown. In order to overcome these challenges an iterative solution process must be used.

The most common of these is the Semi-Implicit Method for Pressure-Linked Equations (SIMPLE) developed by Patankar and Spalding (1972). This uses an estimated pressure field to first solve the momentum equations, before the solution is used to calculate corrections to the pressure and velocity fields based on the requirement of the continuity equation. Further transport equations (e.g. for k and ω) are then solved. This process is repeated until the solution for each flow variable satisfies a pre-defined convergence criteria. In order to aid solution stability, under-relaxation techniques are usually used to limit the solution change between each loop.

An alternative method is the Pressure Implicit with Splitting of Operators (PISO) algorithm developed by Issa (1986). This is similar to the SIMPLE algorithm but uses a second pressure corrector step within each loop. This is generally used in time-dependent simulations with one loop per time-step and no use of

under-relaxation. This requires that information from one cell can only pass to adjacent cells in one time-step. This can be achieved by limiting the Courant number, Co, below unity, as defined by:

$$Co = \frac{u_{cell}\,\Delta t}{\Delta S} \tag{3.2.37}$$

where u_{cell} is the local cell velocity, Δt is the size of time-step and ΔS is the size of cell. This criteria must be met at every cell throughout the simulation domain and as fine cells are often required to accurately resolve flow features, this can severely limit the size of time-step and lead to expensive simulations.

An alternative approach for time-dependent simulations is called the PIMPLE algorithm, which combines aspects of PISO and SIMPLE. This introduces multiple outer pressure-momentum correction loops into each time-step and in each of these loops a PISO process is followed (where the number of pressure-correction steps can also be set). This results in stable solutions with time-steps giving $Co >> 1$. Under-relaxation can be used between outer loops (as in the SIMPLE approach) but may not be required. In either case, under-relaxation should not be used at the final outer loop before progressing to the following time-step.

3.3 MRL Turbine Computational Model

This section describes the general setup of the computational models used to simulate the MRL tidal turbine.

3.3.1 Computational fluid dynamics code

OpenFOAM version 2.2.2 was used for all the simulations presented here. This open-source code is free to use, unlike alternative commercial codes such as ANSYS Fluent and Star CCM+. Another advantage is the freedom given to the user to modify the code and develop additional functionality. The code includes pre- and post-processing tools, but unlike many commercial codes, a graphical user interface (GUI) is not included.

OpenFOAM includes the functionality to produce complex simulation meshes with snappyHexMesh, although high quality detailed meshes can be difficult to

build without a GUI. There are also a number of open source packages that add graphical functionality to OpenFOAM pre-processing, such as Engys Helyx-OS, although this was not available at the commencement of the work presented here. A commercial package was therefore used for mesh generation, in order to benefit from use of a GUI. A number of packages are available, such as ICEM or Pointwise, with the latter chosen for this work. This allowed fine control over the mesh generation parameters, as discussed in Section 3.3.5.

3.3.2 Simulation of the MRL blade motion

A sliding-mesh type simulation has been used to accurately model the motion of the MRL turbine blades through a complete turbine rotation. Similar to the simulation of Darrieus type turbines described in Chapter 1, the domain consists of an outer far-field region that remains stationary during the progression of the simulation, and an inner circular mesh region that rotates by a prescribed angular increment at each simulation time-step. However, as the MRL turbine blades each rotate about their own axes as well as the central turbine axis, a further separate mesh region is also required for each blade, resulting in a total of five mesh regions, as shown in Figure 3.3.1.

OpenFOAM 2.2.2 contains code that enables only a single rotor mesh region to rotate within an outer domain region. The source code was therefore developed, in order to combine four rotating zones with the stationary outer domain. In order to accurately recreate the MRL blade motion the following procedure occurs at the beginning of each computational time-step:

1. Each of Rotors 1-3 are rotated by angle $-\Delta\theta/2$ about their own individual axis within the stationary Rotor 0. Note, as the turbine blade axes rotate at half the rate of the turbine axis, and the blades rotate by angle $\Delta\theta$ in step 2, here the code rotates the individual blade regions in the opposite direction to that of the overall turbine rotation.

2. All four Rotor regions 0-3 rotate together by angle $\Delta\theta$ about the central turbine axis.

3. The rotational axis locations of Rotors 1-3 are updated.

The above is achieved by replicating the existing C++ code (for a single rotating mesh region) in a nested structure. Step 1 requires the definition of a local

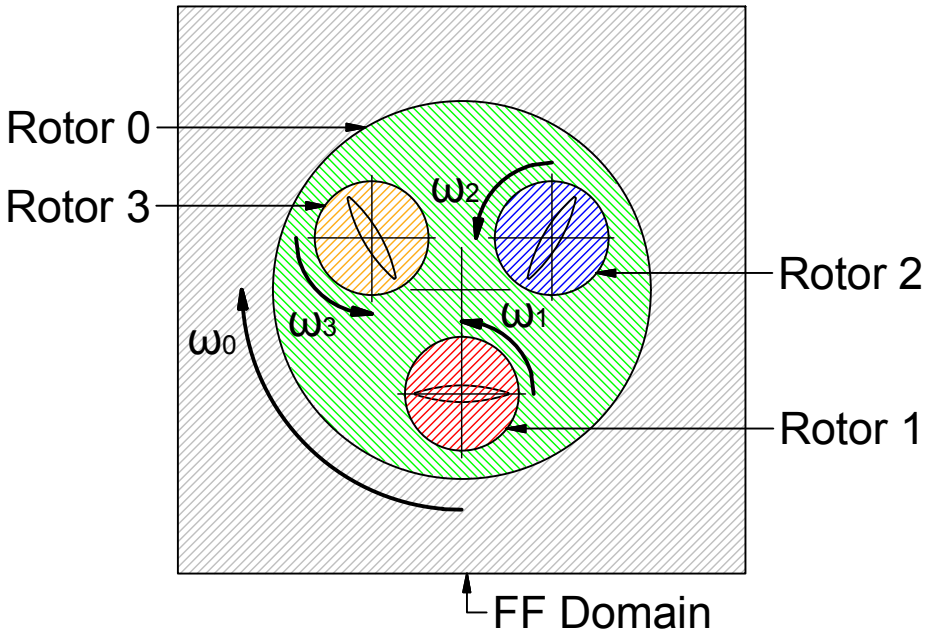

Figure 3.3.1: Diagram showing arrangement of five separate mesh regions that form the computational domain

polar coordinate system for each of Rotors 1-3, so that accurate rotation about the blade axes can be achieved. The initial location of each Rotor axis is therefore defined during the pre-processing stage. During step 2 the global polar coordinate system is used to rotate all Rotor cells about the central turbine axis. In step 3 the location of each blade axis is converted from the local to the global polar coordinate system, and then updated by the appropriate angle of rotation about the turbine axis.

The rotational speed of the turbine, ω_0, is given as an input to each simulation, and is kept constant throughout. The rotation angle per time-step, $\Delta\theta$, is calculated as follows, where Δt is the time-step given in seconds:

$$\Delta\theta = \omega_0 \Delta t \tag{3.3.1}$$

3.3.3 Blade geometry

The blade geometry of the MRL turbine laboratory model was reproduced in the CFD model, each bi-symmetrical blade centred within its circular shaped mesh region. The blade geometry has a maximum thickness of 18% of the chord length and this was maintained when varying the chord length for different

simulations. For the majority of simulations a chord length of 0.05 m has been used, reflecting the experimental model described in Chapter 2.

3.3.4 Computational domain

The domain used was, for the majority of simulations, only one cell deep and therefore simulated two-dimensional flow. This can be understood as the flow at the mid-span plane of a turbine with high aspect ratio blades (i.e. the blade length is large in comparison to the chord). This choice was made in order to minimise the time and computational cost of the simulations. The feasibility of performing fully three-dimensional simulations was also investigated, as presented in Chapter 5.

The cross sectional shape of the domain (i.e. perpendicular to the turbine axis) was square or rectangular, with two different types of domain chosen. Firstly a square 'infinite' domain was used, where the domain was large enough to ensure turbine performance was independent of the proximity of the boundary conditions. Secondly, a finite domain was used, representing the geometry of the experimental flume. Both two-dimensional and three-dimensional versions of this 'flume' domain were created.

Figure 3.3.2 defines the parameters used to describe the domain geometry. These include the height of the domain, upstream and downstream domain lengths, the radius of both Rotor 0 and Rotors 1-3, and the axial length of the blade (used in the three dimensional simulations only). The names of the domain boundaries are also indicated.

3.3.5 Computational mesh

The following sections describe the mesh structure for the three different type of domain regions.

3.3.5.1 Blade region

Rotors 1-3 are identical circular regions of mesh, centred around the blade profile, as shown in Figure 3.3.3. A series of hexahedral inflation-layer cells expand outwards from the blade surface, and then transition into a series of

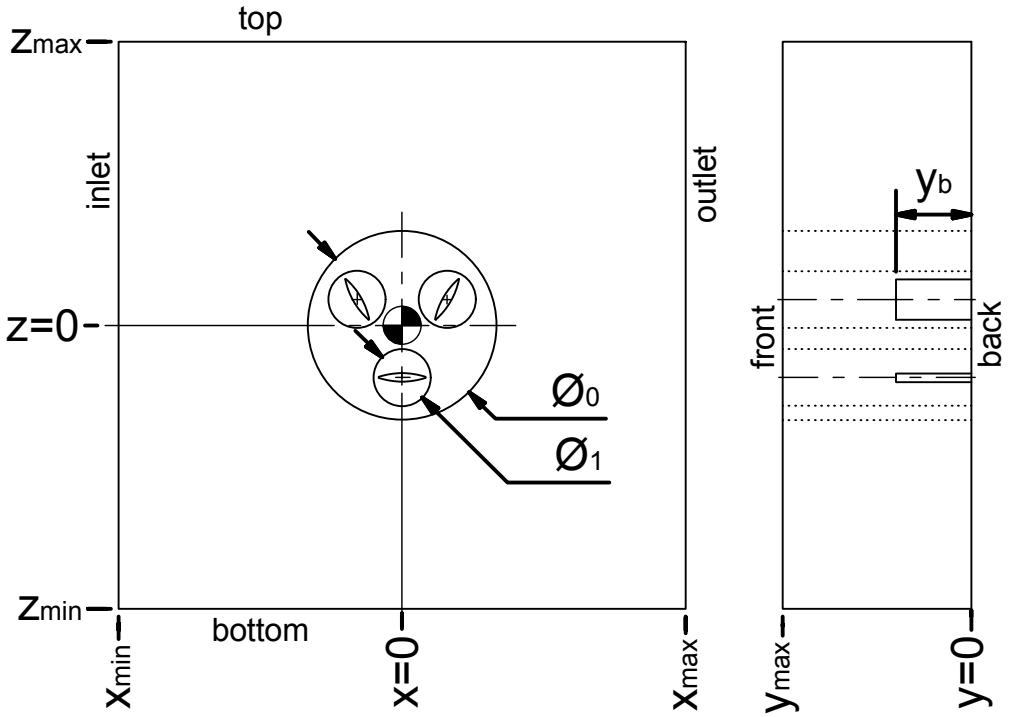

Figure 3.3.2: Diagram defining the computational domain parameters and boundary names

triangular prism cells, arranged in layers. Multiple layers of triangular prism cells also extend inwards from the domain circumference. Between the ordered layers of triangular prisms exist regions of unstructured cells (also triangular prisms).

In order to control the structure of the blade mesh region, a number of parameters have been defined, as shown in Figure 3.3.4. These parameters are:

- ΔS_n: Surface-normal cell spacing at blade wall. The inflation ratio for adjacent layers was set at 1.15.
- ΔS_t: Surface-parallel cell spacing at blade tip.
- ΔS_c: Surface-parallel cell spacing at blade chord-centre.
- ΔS_r: Cell spacing at rotor mesh boundary, i.e., the cell spacing in the rotor region, away from the blade surface.

Values of these parameters are discussed further in Section 3.4. Also defined in Figure 3.3.4 are Walls A and B, which aids in the measurement of time-varying surface values (e.g. y^+), as the position of individual blade walls only repeats once in two turbine cycles.

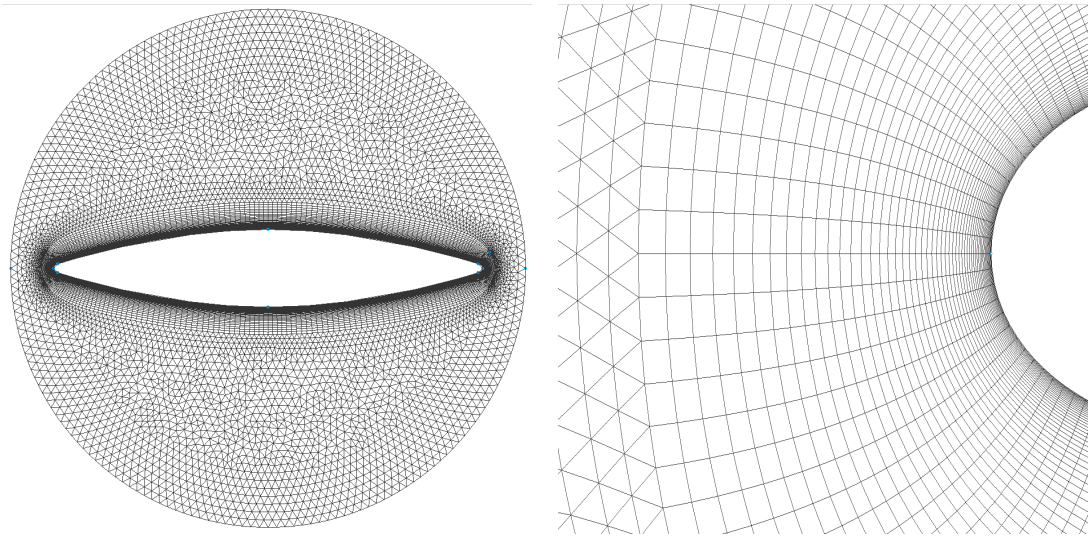

(a) Whole blade region mesh **(b)** Close-up of blade tip mesh

Figure 3.3.3: Typical mesh structure for Rotors 1-3

3.3.5.2 Turbine region

Rotor 0 consists of a circular region of mesh, centred around the turbine axis, with three empty circular regions (for Rotors 1-3 to insert into), as shown in Figure 3.3.5. A series of structured triangular prism cell layers expand from all four surfaces, with the remainder of the region filled by unstructured cells (also triangular prisms).

3.3.5.3 Far-field region

The far-field domain is rectangular or square in shape, centred around the turbine axis, with an empty circular region at the centre for the turbine region to insert into, as shown in Figure 3.3.6. A series of structured triangular prism cell layers expand from all five surfaces, with the remainder of the region filled by unstructured cells (also triangular prisms).

3.3.6 Temporal control

3.3.6.1 Time-step

The time-step for a given simulation is calculated from Equation 3.3.1, given values of turbine rotational speed and rotation angle per time-step. The rotational

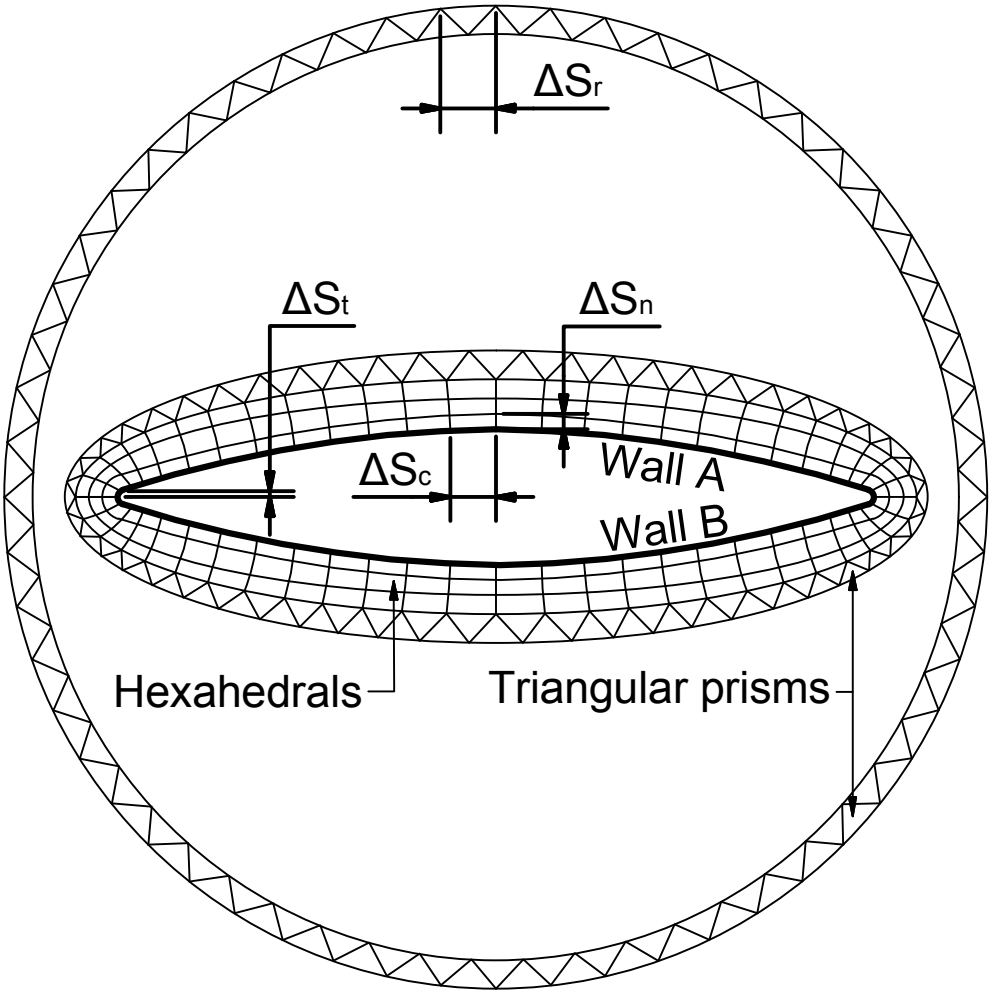

Figure 3.3.4: Diagram defining the computational mesh parameters in Rotors 1-3

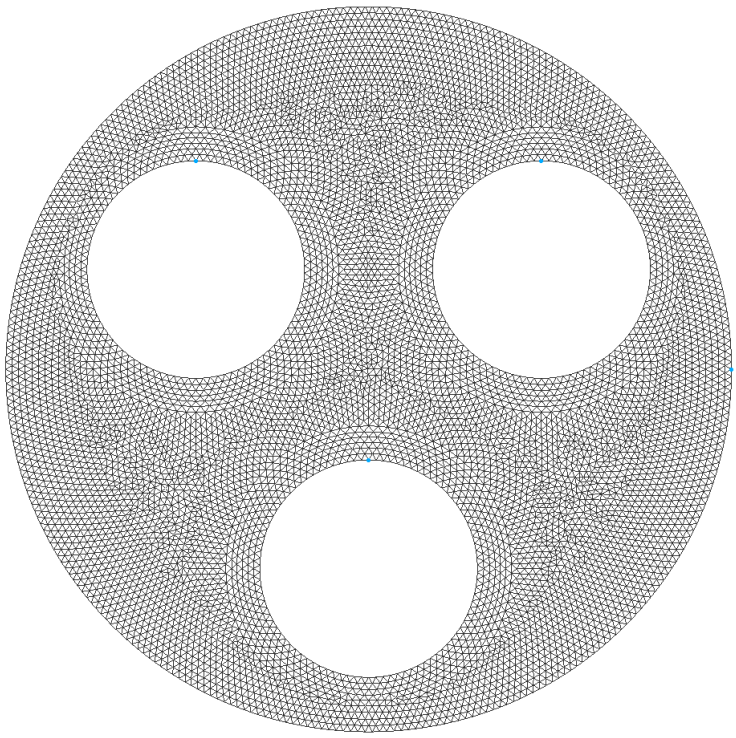

Figure 3.3.5: Typical mesh structure for Rotor 0

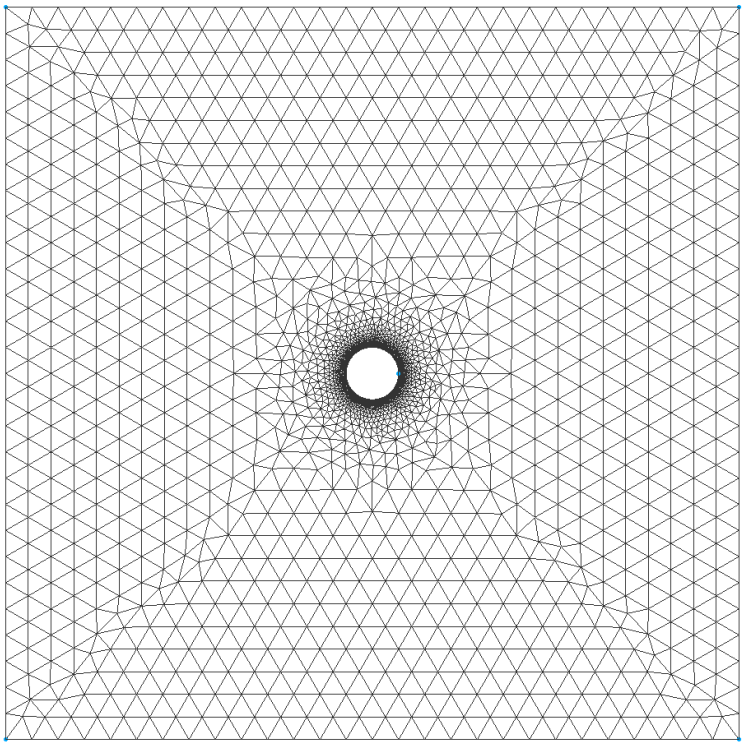

Figure 3.3.6: Typical mesh structure for far-field domain region

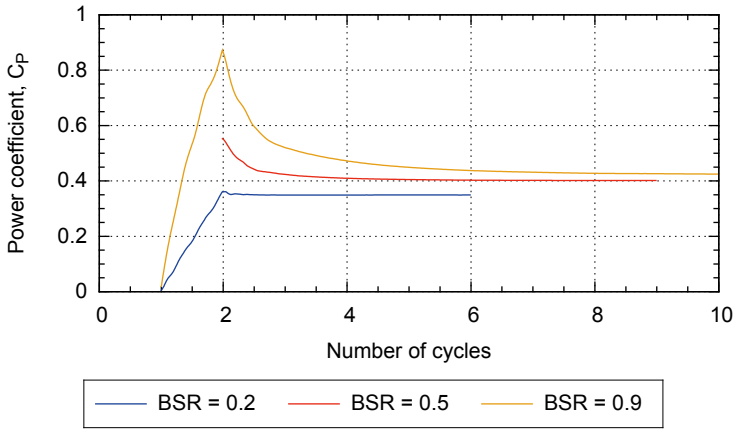

Figure 3.3.7: Graph showing typical development of turbine power coefficient from simulation start-up

speed is calculated from the particular BSR value and inlet flow velocity, and the rotational angle is selected as appropriate (suitable values are investigated in Section 3.4).

3.3.6.2 Simulation time

The total simulated time (i.e. duration of turbine operation that is simulated, rather than the actual duration of the simulation) is chosen so that at least two full turbine rotations are simulated (in order that the blades return to the exact starting position and orientation). However, a fully developed flow field must also be assured, and therefore the simulations were run for a higher number of cycles, until repeating periodic results were obtained. It was found that the required number of cycles varies with BSR value, as shown in Figure 3.3.7, where the development of the turbine power coefficient, averaged over the previous cycle, is presented. It can be seen that the number of cycles required to reach a steady value of power coefficient increases with BSR value. The simulation times have therefore been selected to reflect this, ranging from 5 cycles for $BSR = 0.2$, 8 cycles for $BSR = 0.5$ and 10 cycles for $BSR = 0.9$.

The convergence of results was also checked by inspection of velocity profiles. For example, Figure 3.3.8 shows both the centre-line ($z = 0$) and downstream cross-sectional ($x = 10\,D$) instantaneous velocity profiles from a simulation at $BSR = 0.5$. The graphs show the wake profiles converge as the simulation progresses, and profiles at 6 and 8 cycles cannot be distinguished from one another. This indicates that the simulation has reached a periodically repeating

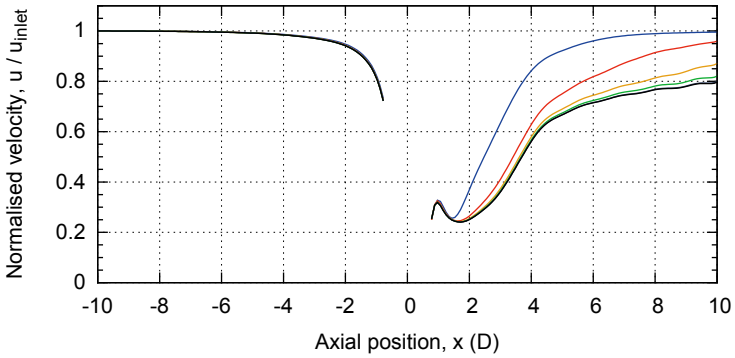

(a) Instantaneous velocity at $z = 0$

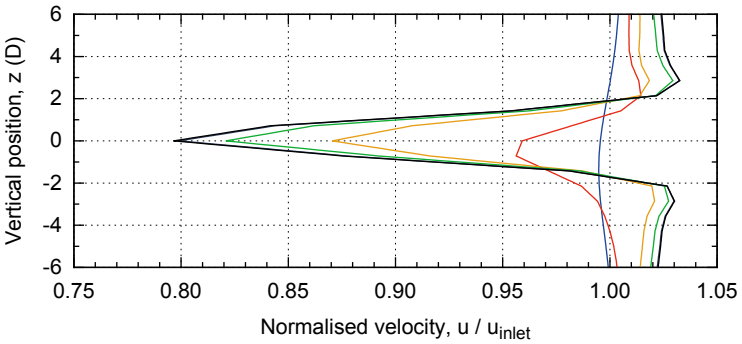

(b) Instantaneous velocity at $x = 10\,D$

Figure 3.3.8: Graphs showing typical development of velocity profiles from simulation start-up ($BSR = 0.5$)

state by 6 cycles, and therefore a maximum simulation time equal to 8 cycles is suitable for this *BSR* value.

3.3.7 Boundary conditions

Table 3.3.1 details the type of boundary condition used for each of the flow variables u, v, w, p, k and ω, at the domain boundaries previously defined in Figure 3.3.2. Of particular interest are the following conditions:

- Blade walls were set with a velocity no-slip condition, by setting $u = v = w = 0\,m/s$, in order to generate boundary layers on these surfaces.
- Turbulent kinetic energy, k, is zero at wall boundaries, but this leads to numerical 'divide by zero' errors. Therefore a very small non-zero value is used at wall boundaries.

- Turbulent frequency, ω, is calculated within the code, using equation 3.2.30 for wall boundary cells.
- The x-direction velocity was set as a constant uniform value across the inlet boundary, with values of the order of $u = 1\,m/s$ used. The y- and z-direction velocity values were set at $0\,m/s$ for all simulations.
- Inlet k and ω values were set as constant uniform values across the boundary, with values calculated as described in Section 3.2.2.9.
- In order to simulate two-dimensional flow, the front and back boundaries are defined as 'empty' (the domain is also one cell wide).
- When simulating 'infinite' domains, the top and bottom boundaries are set as symmetry planes.
- When three-dimensional simulations are run, the back boundary face is set at the mid-span of the blade and a symmetry condition is used, effectively halving the computational requirement. In this case the front boundary is set as a wall, with the same boundary conditions as the blade walls.
- When simulating flume conditions (i.e. in the three-dimensional simulations), the bottom boundary is set as a wall, and the top is set with slip conditions, in order to simply approximate the water surface.
- In addition, all four sliding boundaries between the mesh regions were set with a cyclic arbitrary mesh interface (AMI) condition, which is implemented in OpenFOAM 2.2, based on the work of Farrell and Maddison (2011). This allows flow variable values to be interpolated between adjacent, but separate mesh regions. The continuity of all variables across each AMI boundary was checked in order to confirm the code was performing correctly.

3.3.8 Solution control

3.3.8.1 Schemes

The following schemes have been used for interpolation of flow variables in the discretised transport equations:

Table 3.3.1: Boundary conditions used for each flow variable

Boundary	Flow variable			
	u, v, w	p	k	ω
		All simulations		
Blade walls	Fixed zero	Zero gradient	Fixed zero	Calculated
Inlet	Fixed value	Zero gradient	Fixed value	Fixed value
Outlet	Zero gradient	Fixed zero	Zero gradient	Zero gradient
		Two-dimensional simulations		
Front & back	Empty	Empty	Empty	Empty
		Three-dimensional simulations		
Front	Fixed zero	Zero gradient	Fixed zero	Calculated
Back	Symmetry	Symmetry	Symmetry	Symmetry
		Infinite domain simulations		
Top & bottom	Symmetry	Symmetry	Symmetry	Symmetry
		Flume domain simulations		
Top	Slip	Slip	Slip	Slip
Bottom	Fixed zero	Zero gradient	Fixed zero	Calculated

- u, v, w: Linear upwind
- k, ω: Upwind

In addition, the fully implicit Euler scheme has been used to solve the time derivative term.

3.3.8.2 Solver control

The pimpleDyMFoam solver has been used, which utilises the PIMPLE solution algorithm and dynamic mesh techniques to solve time-dependent incompressible flows. The number of outer PIMPLE loops (i.e. pressure-momentum corrector steps) was generally set at a maximum of 20, with the number of inner loops (i.e. pressure corrector steps) set at 10. No under-relaxation was used between outer loops and the turbulent parameter transport equations were solved at each outer loop.

3.3.8.3 Residual limits

Within each time-step, the residual limits were set at 10^{-5} for all flow variables. If this criteria was reached for all variables within a given outer loop, the solution was judged to be converged and moved onto the next time-step (this was typically achieved after only 5 outer loops). The value of the limit was also changed to 10^{-8} for a number of simulations, in order to ensure the output of the turbine simulation was not affected. The residual values of the final outer loop (per time-step) were observed, confirming convergence was being achieved, and a typical output is shown in Figure 3.3.9.

3.3.9 Measured output

3.3.9.1 Forces and torque

The total force acting upon each blade is calculated at a predefined interval. This is comprised of both pressure forces and viscous forces. The former is due to pressure variation in the surrounding fluid field and the latter is due to viscosity of the fluid acting parallel to the blade surface. These forces are

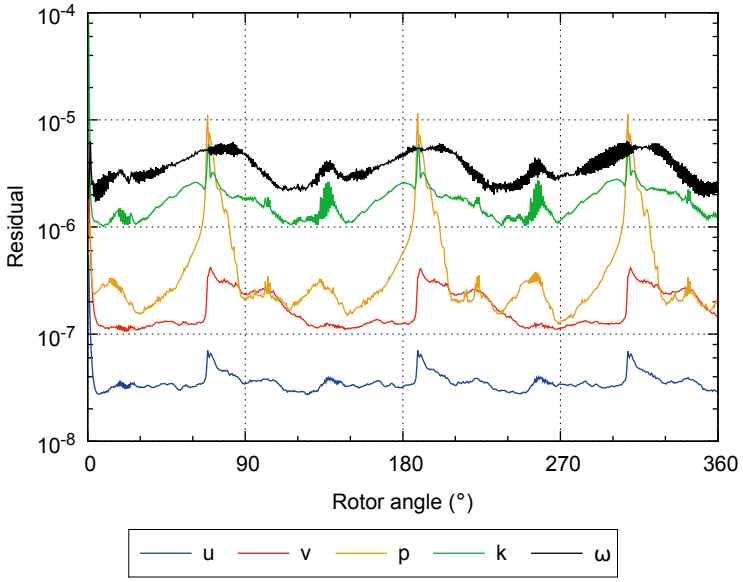

Figure 3.3.9: Plot of residual values in the final outer loop over a full turbine cycle

expressed as acting in both the x- and z-directions, and can be combined to produce the driving torque acting about the turbine central axis, as shown in Equation 3.3.2.

$$T_d = R_b \left(F_z \sin\theta - F_x \cos\theta \right) \tag{3.3.2}$$

In order to obtain a fine resolution of measurement, the output interval was set at 5° of turbine rotation. For convenience, the two-dimensional simulations results are converted and expressed in units per metre span of blade (as the simulated cell thickness is only 5mm). In the three-dimensional simulations, the values are directly related to the simulated turbine blade length.

3.3.9.2 Torque, power and thrust coefficients

The mean driving torque acting over a single cycle, $\overline{T_d}$ can be converted into a torque coefficient, as shown in Equation 3.3.3:

$$C_Q = \frac{\overline{T_d}}{{}^1\!/_2 \rho D l_b R_b u_{inlet}^2} \tag{3.3.3}$$

where $D l_b$ is the swept frontal area of turbine.

Mean power is calculated as the product of cycle-mean torque and the constant turbine rotational speed (in rad/s). The power coefficient is calculated as the mean power divided by the available power of the flow through the turbine frontal area, as shown in Equation 3.3.4:

$$C_P = \frac{\omega_0 \overline{T_d}}{1/2 \rho D l_b u_{inlet}^3} = C_Q BSR \tag{3.3.4}$$

The cycle-mean forces acting on the blades can also be expressed as thrust coefficients acting in the x- and z-directions, as shown in Equations 3.3.5 and 3.3.6:

$$C_{T,x} = \frac{\overline{F_x}}{1/2 \rho D l_b u_{inlet}^2} \tag{3.3.5}$$

$$C_{T,z} = \frac{\overline{F_z}}{1/2 \rho D l_b u_{inlet}^2} \tag{3.3.6}$$

3.4 Sensitivity Analysis

3.4.1 Aim of section

The aim of the sensitivity analysis was to optimise the computational mesh and time-step selection, i.e., find a computational setup that minimises the computational cost and time requirement, whilst yielding reliable results that are independent of the setup.

3.4.2 Approach

A number of simulation parameters have been varied independently, with the torque output and computational duration recorded. Table 3.4.1 gives an overview of the simulations undertaken, with results presented in the following sections. Values of $BSR = 0.2$, 0.5 and 0.9 were simulated, in order to confirm independence is achieved across the full range of blade speed ratios to be investigated. All other geometry and operating condition parameters were kept constant throughout, as detailed in Table 3.4.2.

Please note the following:

- The square, infinite domain type was used throughout the sensitivity analysis and therefore $x_{max}/D = -x_{min}/D = z_{max}/D = -z_{min}/D$.

- Unless otherwise stated, turbulent intensity was kept constant at $Ti = 1\%$ and $TVR = 1.5$ was selected, which corresponds to the boundary condition suggested by Equation 3.2.33, when using the blade chord as characteristic length (i.e. $l_{char} = 0.05\,m$). The effects of varying these values are also investigated at the end of the sensitivity analysis.

- The simulations were ran on a computational node consisting of 32 Intel Xeon 2.3 GHz processors, with 4 GB of RAM available per processor.

3.4.3 Results

Table 3.4.3 details the total number of cells in the domains created for tests 01-24, the number of processors used to run each simulation in parallel, along with the simulation duration of a single cycle at *BSR* values of 0.2, 0.5 and 0.9. Times for both the final cycle and the mean of all cycles are presented. In the following sections, the torque results for each set of tests are discussed further, with reference to these values.

3.4.3.1 Blade wall-normal cell spacing

The height of the initial cell adjacent to the blade surface, ΔS_n, was varied with all other mesh and computational parameters kept constant (test no. 01-04). The output torque, due to pressure and viscous forces acting on a single blade ($T_{b,p}$ and $T_{b,v}$ respectively), over a single turbine rotation are presented in Figure 3.4.1, for *BSR* values of 0.2 and 0.9. (Graphs for $BSR = 0.5$ results are omitted throughout this section, as the characteristics are very similar to those of $BSR = 0.9$).

The graphs show negligible visible variation between results at $BSR = 0.9$, but some variation can be seen at $BSR = 0.2$. In particular, although the overall trend is very similar, the results for $\Delta S_n = 8x10^{-6}m$ (pressure torque) visibly vary from the finer mesh results in the range $135° < \theta < 330°$. This indicates the wall-normal cell height has an influence on the flow field around

Table 3.4.1: Sensitivity analysis simulation parameter values

Test No.	Parameter values					
	ΔS_n	ΔS_t	ΔS_c	ΔS_r	$\Delta\theta$	x_{max}/D
	(m)	(m)	(m)	(m)	(°)	(-)
	$x10^{-6}$	$x10^{-5}$	$x10^{-4}$	$x10^{-4}$		
01	1					
02	2	5	4	10	0.25	10
03	4					
04	8					
05		5				
06	1	10	4	10	0.25	10
07		20				
08			1			
09	1	10	2	10	0.25	10
10			4			
11				5		
12	2	5	4	10	0.25	10
13				20		
14					0.125	
15					0.25	
16	2	5	4	10	0.5	10
17					1	
18					2	
19					4	
20						40
21						20
22	4	10	4	20	0.5	10
23						5
24						2.5

Table 3.4.2: Sensitivity analysis geometry and operating condition values

Parameter	n	c	R_b	u_{inlet}	Ti	TVR
	(-)	(m)	(m)	(m/s)	(%)	(-)
Value	3	0.05	0.055	1.0	1.0	1.5

Table 3.4.3: Sensitivity analysis cell number and simulation duration results

Test No.	No. Proc.	No. Cells	Simulation duration, 1 cycle					
			$BSR = 0.2$		$BSR = 0.5$		$BSR = 0.9$	
			(hours)		(hours)		(hours)	
		$x10^5$	Final	Mean	Final	Mean	Final	Mean
01	4	1.97	14.28	14.19	6.27	6.50	4.83	5.97
02	4	1.86	10.02	10.27	6.42	6.17	6.62	6.26
03	4	1.75	9.28	10.66	4.92	5.79	5.13	5.37
04	4	1.64	6.81	8.23	5.22	5.11	4.18	4.71
05	4	1.97	14.28	14.19	6.27	6.50	4.83	5.97
06	4	1.88	13.65	13.87	6.73	7.12	4.44	6.23
07	4	1.82	10.93	13.25	6.32	6.50	4.48	6.11
08	4	4.34	22.9	34.8	15.66	17.30	12.49	15.94
09	4	2.72	19.55	18.41	10.24	10.08	9.87	10.40
10	4	1.88	13.65	13.87	6.73	7.12	4.44	6.23
11	8	4.76	13.67	24.29	10.05	10.03	9.46	9.36
12	4	1.86	10.02	10.27	6.42	6.17	6.62	6.26
13	2	1.03	12.74	13.16	2.42	2.38	4.77	5.01
14	4	1.86	12.14	10.26	9.22	9.21	7.01	7.66
15	4	1.86	10.02	10.27	6.42	6.17	6.62	6.26
16	4	1.86	8.97	10.78	2.79	3.32	1.53	1.72
17	4	1.86	3.18	3.29	1.76	2.62	1.27	1.83
18	4	1.86	N/A	N/A	2.98	3.55	0.84	0.77
19	4	1.86	N/A	N/A	1.93	2.11	0.95	0.83
20	2	1.00	1.72	1.76	0.62	0.62	0.61	0.73
21	2	0.78	1.03	1.05	0.52	0.55	0.45	0.49
22	2	0.69	0.94	0.97	0.47	0.51	0.38	0.40
23	2	0.71	1.97	2.05	0.62	0.60	0.42	0.42
24	2	0.70	2.58	2.65	1.22	1.15	0.92	0.93

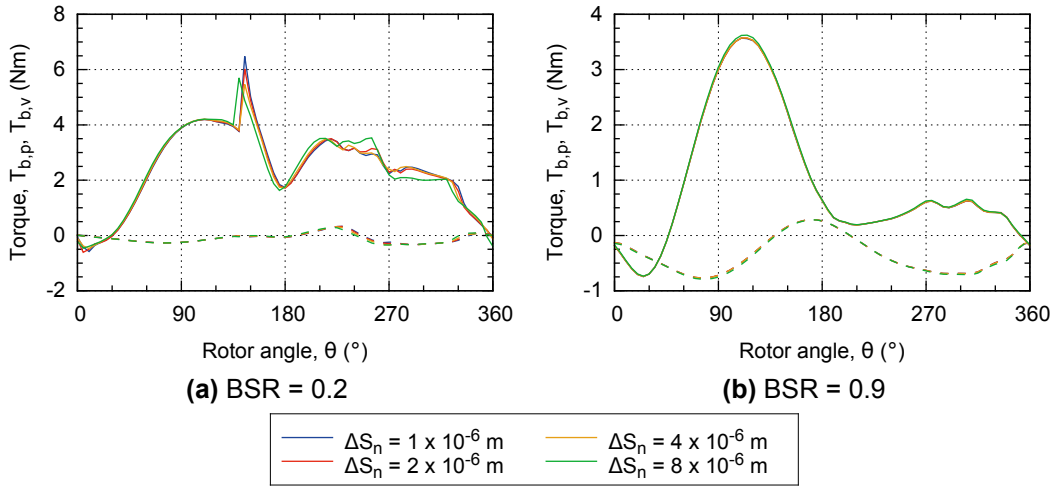

Figure 3.4.1: Effect of blade wall-normal cell height on output torque, per metre span of blade, generated due to forces acting on a single blade in a single cycle (n=3 turbine simulation). Solid lines represent torque due to pressure forces and dashed lines represent torque due to viscous forces.

the turbine blade and the coarsest value tested here does not yield mesh-independent results. The remaining three sets of results show minor variations throughout the cycle; therefore $\Delta S_n = 4x10^{-6}m$ has been selected as the most appropriate, as Test 03 gave a reduction in mean cycle duration of between 6% and 14%, when compared to Test 02.

In addition to the unsteady torque results, the time-varying y^+ values for both surfaces of a single blade have been recorded, as shown in Figure 3.4.2. The maximum cellular value on each surface, and the mean value across all cells on each surface are presented. Both sets of results show a pronounced variation in y^+ throughout the turbine cycle, with a similar profile to the torque curves (i.e. two major peaks per cycle). The surface-mean results for Wall A are significantly higher than those for Wall B, as Wall A was the downstream face throughout the particular cycle analysed here (during the next cycle Wall B would be the downstream face). The highest velocities and y^+ values occur on the downstream face, due to the acceleration of flow and build up of vortices, as discussed in Chapter 4. In contrast, the surface-maximum values on Wall A and Wall B are often similar during particular stages of the cycle. This indicates the maximum values are occurring at a blade tip, where the break between Wall A and B is defined, and the maximum acceleration of flow likely occurs.

The $BSR = 0.2$ results show the three finest meshes give a maximum y^+ below

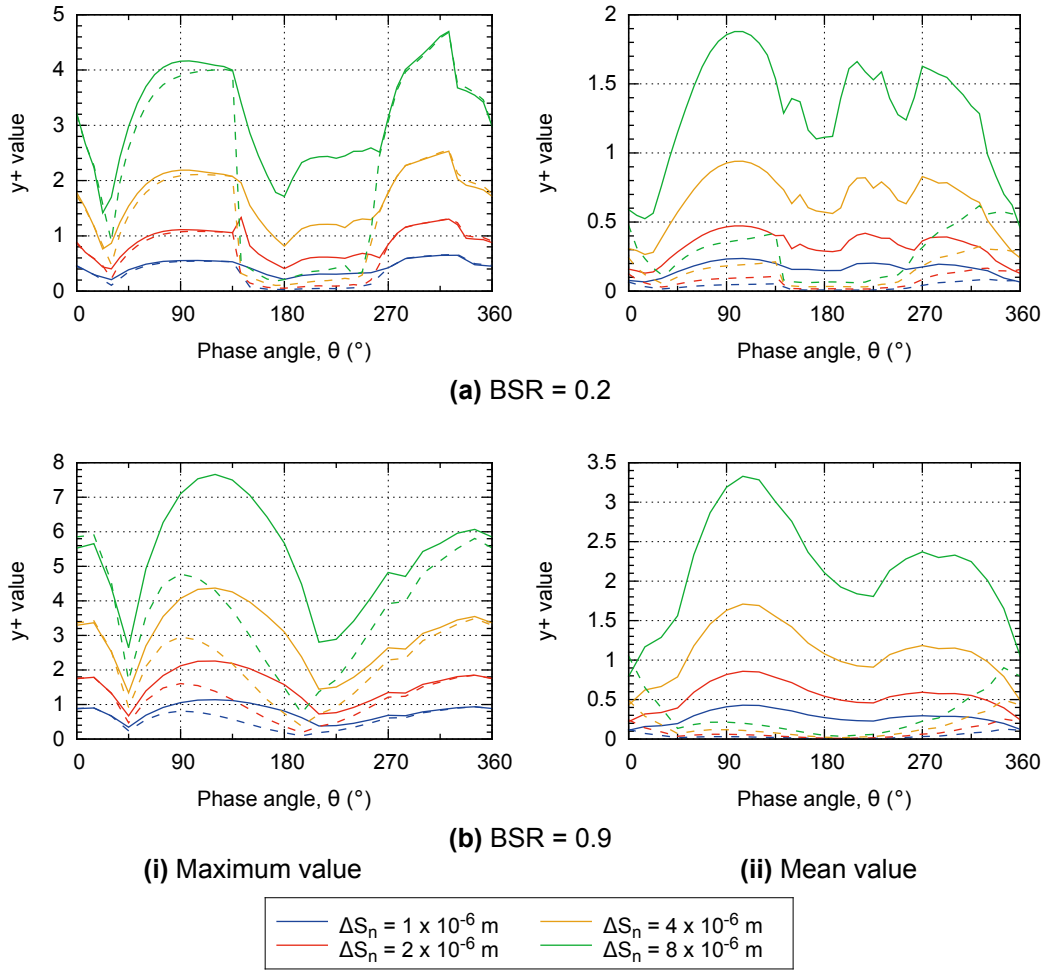

Figure 3.4.2: Effect of blade wall-normal cell height on maximum and mean y^+ values for a single blade in a single turbine cycle (n=3 turbine simulation). Solid lines represent Wall A values and dashed lines represent Wall B values.

2.0, and a mean value below 1.0 throughout the majority of the turbine rotation. In contrast, the coarsest mesh yields maximum and mean values above 2.0 and 1.0 respectively, for the majority of the turbine rotation. As discussed in Section 3.2.2.8, the wall-resolved RANS method of modelling boundary-layer flow generally requires $y^+ < 5$. Therefore, the results show this approach is appropriate for the near-wall cell heights tested here. However, other sources state that the approach is most accurate when $y^+ \approx 1$. Therefore, whilst the coarsest mesh yields valid results, they are less reliable than the finer mesh results, as observed in Figure 3.4.1.

Results at *BSR*=0.9 also show the maximum and mean y^+ values increasing significantly with increasing value of ΔS_n. Here, the two coarsest meshes yield maximum and mean y^+values in excess of 2.0 and 1.0 for the majority of a

turbine cycle. However, in contrast to *BSR*=0.2 results, no visible difference in torque output was seen in Figure 3.4.2. This shows that accurate boundary layer modelling is more important at lower rotational speeds, at least in terms of gaining mesh independent torque results. This may also indicate that vortex separation plays a more significant role in the process of torque generation at lower *BSR* values, or that the modelling approach used here does not successfully model vortex separation at higher *BSR* values. This is discussed in more depth in Chapter 4, when further analysing the simulated torque results.

3.4.3.2 Blade tip cell spacing

The width of the cells at the blade tips, ΔS_t, was varied with all other mesh and computational parameters kept constant (test no. 05-07). The output torque, due to pressure and viscous forces acting on a single blade, over a single turbine rotation are presented in Figure 3.4.3 for *BSR* values of 0.2 and 0.9.

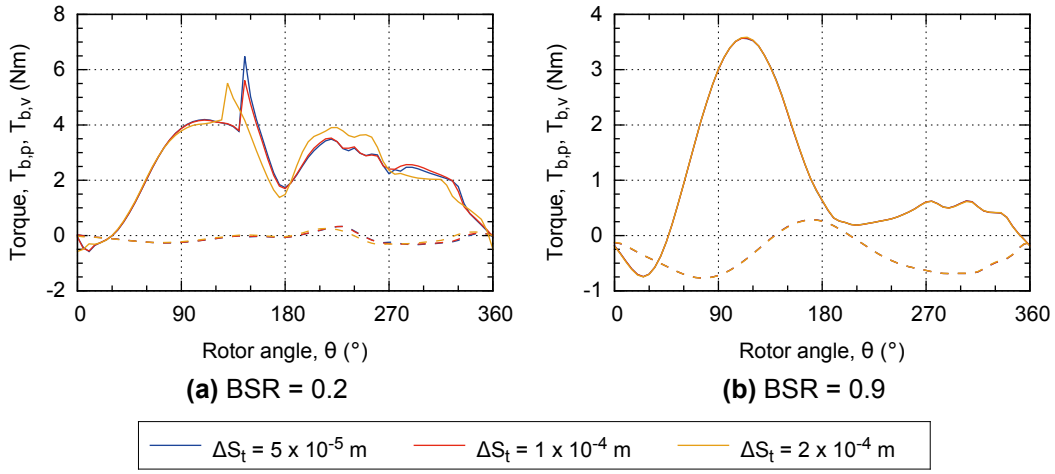

Figure 3.4.3: Effect of blade tip cell width on output torque, per metre span of blade, generated due to forces acting on a single blade in a single cycle (n=3 turbine simulation). Solid lines represent torque due to pressure forces and dashed lines represent torque due to viscous forces

The *BSR*=0.9 test results again show negligible variation from each other throughout the turbine cycle. However, variation between test results can be clearly seen at $BSR = 0.2$. In particular, the results for $\Delta S_t = 2x10^{-4}m$ (pressure torque) visibly vary from the finer mesh results in the approximate range of

$135° < \theta < 330°$. The sharp peak in pressure torque that occurs at approximately $\theta = 135°$ is due to a sudden vortex formation and shedding event at the leading edge tip (as discussed further in Chapter 4). The coarsest mesh results show this occurring earlier in the turbine cycle, indicating the cell resolution in the tip region has a strong influence on the simulation of this behaviour. The pressure torque results throughout the remainder of the cycle also appear to be directly affected by the timing of this event, and therefore the coarsest mesh cannot be used to gain independent results at low *BSR* values.

The remaining two sets of results show minor variations throughout the cycle and both values are considered appropriate for use in further turbine simulations. The simulation duration was similar for all simulations, as the overall cell count was not strongly affected by this localised parameter.

3.4.3.3 Blade mid-chord cell spacing

The width of the cells at the blade mid-chord, ΔS_c, was varied with all other mesh and computational parameters kept constant (test no. 08-10). The output torque, due to pressure and viscous forces acting on a single blade, over a single turbine rotation are presented in Figure 3.4.4 for *BSR* values of 0.2 and 0.9.

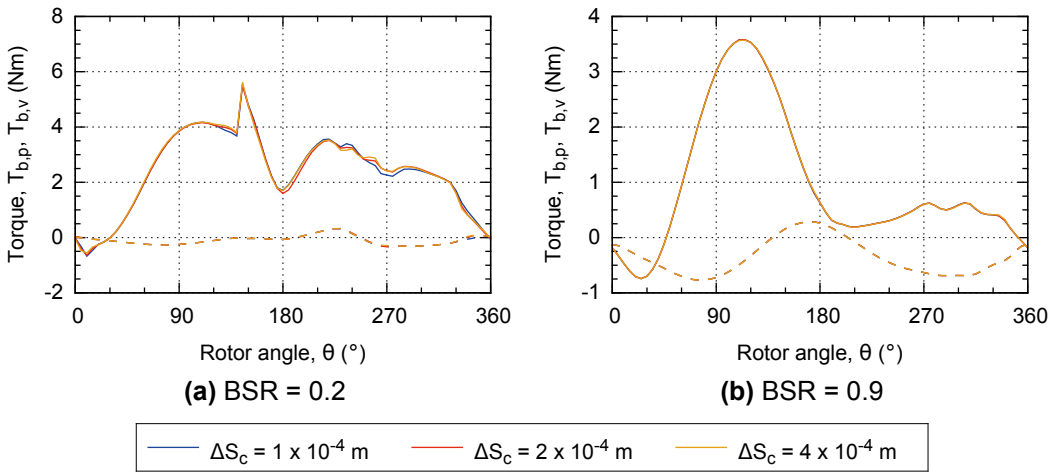

Figure 3.4.4: Effect of blade mid-chord cell width on output torque, per metre span of blade, generated due to forces acting on a single blade in a single cycle (n=3 turbine simulation). Solid lines represent torque due to pressure forces and dashed lines represent torque due to viscous forces

The *BSR*=0.9 test results again show negligible variation from each other throughout the turbine cycle, indicating all three values of ΔS_c tested are suitable throughout the range of *BSR* values to be investigated.

In contrast to the previous two sets of results, there is also minimal variation between test results at *BSR*=0.2, especially when comparing the location and magnitude of the sudden torque spike. There is some variation between results in the region $225° < \theta < 300°$, with the finest mesh results departing most visibly from the other two curves. However, the shape of the curves in this region are very similar and the maximum variation is less than 10% of the absolute torque value (at $\theta = 270°$). A reduction of 57% in cell number is seen between Tests 08 and 10 and this corresponds to a reduction of 60% in mean cycle duration. Therefore the coarsest value tested, $\Delta S_c = 4x10^{-4}m$, was selected as the most suitable value for further simulations.

It would have been pertinent to also test a mesh with a higher value of ΔS_c than this, but it was found that higher values made it more difficult to achieve a good cell quality throughout the blade mesh region. This was mainly due to the transition from hexahedral cells to triangular prism cells, away from the blade surface. As the value of ΔS_c increases, so does the width of the triangular prisms; this necessitates either low aspect ratio triangular prisms, or a high volume ratio between the adjacent hexahedral and triangular prism cells. Both of these options are not considered good for simulation accuracy. Also, with the tip spacing set at a maximum of $\Delta S_t = 1x10^{-4}m$, a ratio of at least 1:4 must be achieved between the cell spacing at the tip and the chord centre. It was found that increasing this ratio generally reduced mesh quality.

3.4.3.4 Rotor zone cell spacing

The spacing of the cells in the rotor zone, ΔS_r, was varied with all other mesh and computational parameters kept constant (test no. 11-13). The output torque, due to pressure and viscous forces acting on a single blade, over a single turbine rotation are presented in Figure 3.4.5, for *BSR* values of 0.2 and 0.9.

The graphs again show negligible visible variation between results at $BSR = 0.9$, but some notable variation can be seen at $BSR = 0.2$. In particular, the results for $\Delta S_r = 2x10^{-3}m$ (pressure torque) visibly vary from the finer mesh

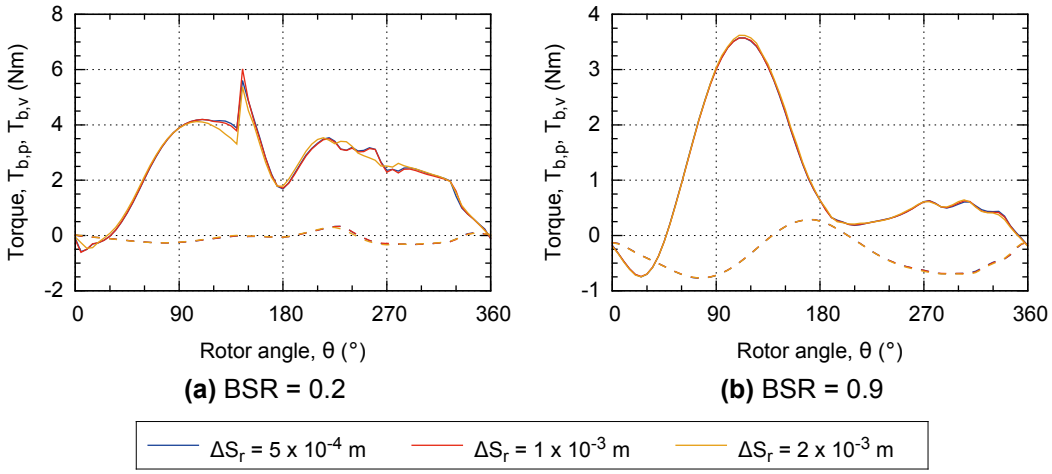

Figure 3.4.5: Effect of rotor boundary cell spacing on output torque, per metre span of blade, generated due to forces acting on a single blade in a single cycle (n=3 turbine simulation). Solid lines represent torque due to pressure forces and dashed lines represent torque due to viscous forces

results in the ranges $100° < \theta < 140°$ and $210° < \theta < 290°$. Whilst the profiles of the curves are generally well matched throughout, there is a difference of approximately 13% in torque magnitude at $\theta = 140°$, directly preceding the sudden torque spike. In the second half of the cycle, where the blade passes through the wake of the upstream blades, there is also some variation in torque values between tests, with a 13% difference in torque magnitude at $\theta = 260°$. This indicates the rotor zone cell spacing does have an influence on the flow field around the turbine blade and the coarsest value tested here does not yield results that are completely independent of the mesh selection, at least at this low BSR value.

However, the value of ΔS_r has the greatest influence on total cell number, as it effects the number of cells in the whole turbine region. A reduction of 45% in cell number is seen between Tests 12 and 13 and this corresponds to a large reduction in simulation duration. The results cannot be directly compared, as different numbers of processors were used, but Test 13 at $BSR = 0.5$ completed in 60% less time than Test 12, with half the number of processors. This represented a significant increase in the amount of simulations that could be run concurrently with finite computational resources. After further investigation into the effect of the parameter value at other BSR values, $\Delta S_r = 2x10^{-3}m$ was chosen as the most suitable value for all simulations between $BSR = 0.3 - 0.9$. For $BSR = 0.2$ simulations, $\Delta S_r = 1x10^{-3}m$ was used.

3.4.3.5 Time-step

The angular displacement per time-step, $\Delta\theta$, was varied with all other mesh and computational parameters kept constant (test no. 14-19). The output torque, due to pressure and viscous forces acting on a single blade, over a single turbine rotation are presented in Figure 3.4.6, for *BSR* values of 0.2 and 0.9.

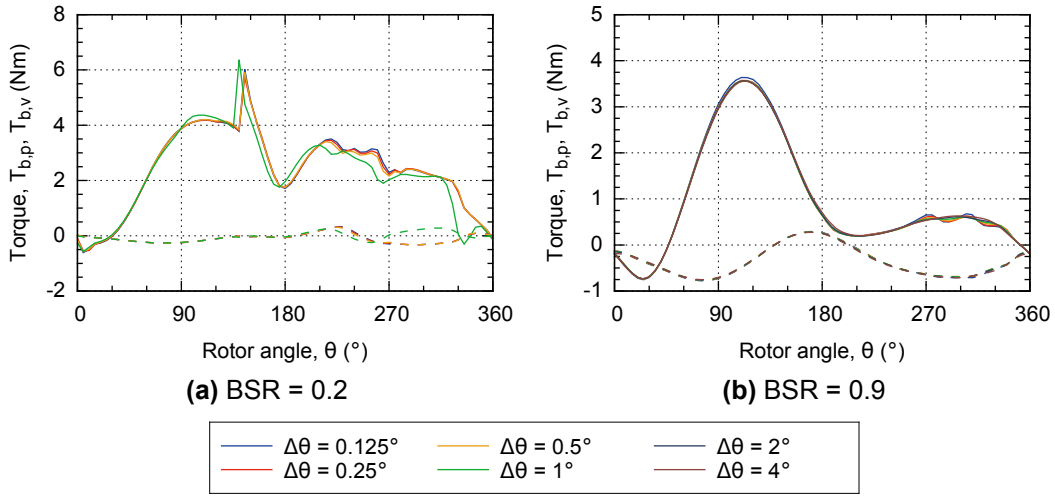

Figure 3.4.6: Effect of time-step on output torque, per metre span of blade, generated due to forces acting on a single blade in a single cycle (n=3 turbine simulation). Solid lines represent torque due to pressure forces and dashed lines represent torque due to viscous forces

For simulations at $BSR = 0.2$, values of $\Delta\theta = 2°$ and $\Delta\theta = 4°$ were not stable and could not be run successfully. For simulations that did complete, it can be seen that values of $\Delta\theta \leq 0.5°$ yield very similar results throughout the turbine cycle, with a maximum difference of approximately 8% in torque magnitude at $\theta = 260°$. However, $\Delta\theta = 1°$ results clearly depart from the others, indicating this magnitude of angular increment does not produce reliable results.

In contrast, all simulations at *BSR*=0.9 ran successfully and gave near identical torque results. However, there is visible variation between results in the region $240° < \theta < 360°$, where finer angular increments yield a more highly fluctuating torque profile, although results for $\Delta\theta \leq 0.5°$are very similar.

When compared to Test 15, Tests 16 gave a reduction in mean cycle duration of 46% for $BSR = 0.5$ and 72% for $BSR = 0.9$. In contrast, $BSR = 0.2$ gave an increase of 5% for the same tests, although the final cycle time was reduced by

10%. Therefore a value of $\Delta\theta = 0.5°$ was selected as the most suitable value for further simulations.

3.4.3.6 Domain size

The size of the domain, x_{max}/D (measured in all four directions from the turbine axis), was varied with all other mesh and computational parameters kept constant (test no. 20-24). The output torque, due to pressure and viscous forces acting on a single blade, over a single turbine rotation are presented in Figure 3.4.7, for *BSR* values of 0.2 and 0.9.

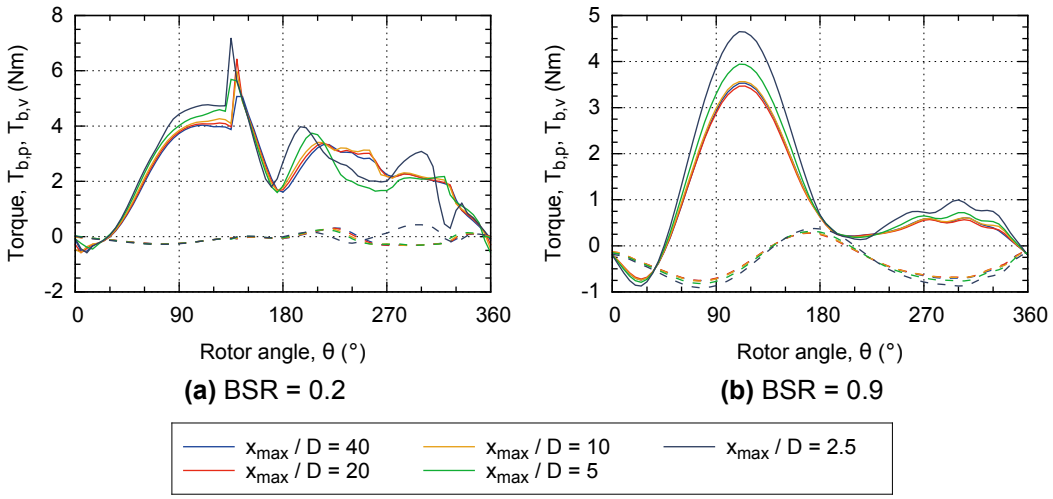

Figure 3.4.7: Effect of domain size on output torque, per metre span of blade, generated due to forces acting on a single blade in a single cycle (n=3 turbine simulation). Solid lines represent torque due to pressure forces and dashed lines represent torque due to viscous forces

The graphs show highly visible variation between results, at both *BSR* values. Generally the profiles of the curves are well matched throughout the turbine cycle, but decreasing domain size to $x_{max}/D = 5$ or below leads to increased peak torques in both halves of the turbine cycle. In addition, a significantly different profile can be seen during the downstream half of the $BSR = 0.2$ simulation. These variations are likely due to increased flow velocity encountered by the turbine blades, due to higher blockage ratios accelerating the inlet flow. Therefore, when investigating the behaviour of the turbine in an 'infinite' domain, a value of $x_{max}/D = 10$ has been used, as this gives a decrease in mean cycle duration of between 7% and 18%, when compared to $x_{max}/D = 20$.

It should also be noted that this set of tests (20-24) are the first to combine all the optimised values of ΔS_n, ΔS_t, ΔS_c, ΔS_r and $\Delta\theta$. The results of Test 22 gave a mean cycle duration in the range of 0.4-1.0 hours, with simulations ran on two processors. This represents a marked improvement from Test 01, when cycle durations were in the range of 6.0-14.2 hours with four processors used, representing a reduction in time of 93% with half the computational resource.

3.4.3.7 Turbulent parameters

Investigation of the sensitivity of simulation results to inlet turbulent parameters has also been undertaken. This concerns both the turbulent viscosity ratio (*TVR*) and turbulent intensity, which are used to define inlet values of k and ω.

The *TVR* value has so far been set according to the suggestion of Equation 3.2.33. However, as 'flume' domain conditions are to be simulated, it is important to also trial values more appropriate to that situation. Therefore, using a hydraulic diameter of $D_H = 0.8\,m$ (for the exposed-surface $0.6\,m$ x $0.6\,m$ width x depth flume), Equation 3.2.34 gives a mixing length of $l_{mix} = 0.056m$. From Equation 3.2.35, a value for ω can be calculated that leads to a value of $TVR = 375$. Therefore, *TVR* values two orders of magnitude greater than initially trialled are more appropriate when simulating flume conditions.

Figure 3.4.8 shows the output torque, due to pressure and viscous forces acting on a single blade, over a single turbine rotation , for *BSR* values of 0.2 and 0.5, with three *TVR* values. It can be seen that increasing the ambient *TVR* value by two orders of magnitude has a minor effect on torque results at $BSR = 0.2$ and negligible effect at higher *BSR* values. This shows that the selection of *TVR* value is not critical for obtaining reliable results.

In addition, the ambient turbulent intensity has also been varied, whilst using a *TVR* value corresponding to $l_{mix} = 0.056m$. Figure 3.4.9 shows the output torque, due to pressure and viscous forces acting on a single blade, over a single turbine rotation , for *BSR* values of 0.2, 0.5 and 0.9, with four *Ti* values in the range of $1 - 20\,\%$.

Overall it can be seen that *Ti* values of 1, 5 and 10 % give similar results for all three *BSR* values, except in the range of $200° < \theta < 330°$ for $BSR = 0.2$, where a marked reduction in torque occurs at $Ti = 5$ and $Ti = 10\,\%$. Higher ambient turbulence values result in further variations in torque profile, although

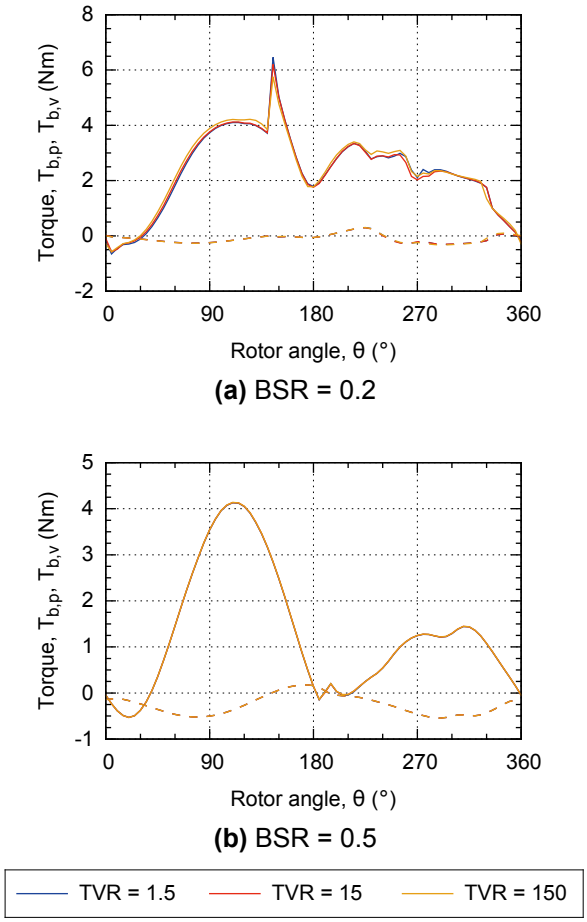

Figure 3.4.8: Effect of ambient turbulence viscosity ratio on output torque, per metre span of blade, generated due to forces acting on a single blade in a single cycle (n=3 turbine simulation). Solid lines represent torque due to pressure forces and dashed lines represent torque due to viscous forces

the overall shape remains similar. Results for $Ti = 20\,\%$ are most significantly different from other results, for all three *BSR* values tested. This indicates that turbulent intensity needs to be defined accurately, although values in the range of $1 - 10\,\%$ give similar results throughout.

3.5 Chapter Conclusions

This chapter has firstly presented the theory underpinning the computational fluid dynamics analysis of the MRL tidal turbine, with a focus on the $k - \omega$ SST sustain RANS approach to modelling turbulent flow.

Following this a description of the general computational setup was given, focusing on the sliding mesh approach and defining parameters used to describe the domain, mesh and time-step.

Finally, a sensitivity analysis was presented. The results of this show that the mesh and simulation parameter values used in Test 22 are most suitable for use in CFD simulations of the laboratory-scale MRL turbine. These yield results that are largely independent of the chosen value, whilst enabling a relatively short simulation duration to be achieved, for the full range of *BSR* values to be investigated. Unless otherwise stated, these parameter values are used in simulations presented in Chapters 4 and 5. Also, ambient turbulent intensity (and therefore k) must be defined appropriately for a given simulation but the selected value of turbulent viscosity ratio (and therefore ω) is not critical.

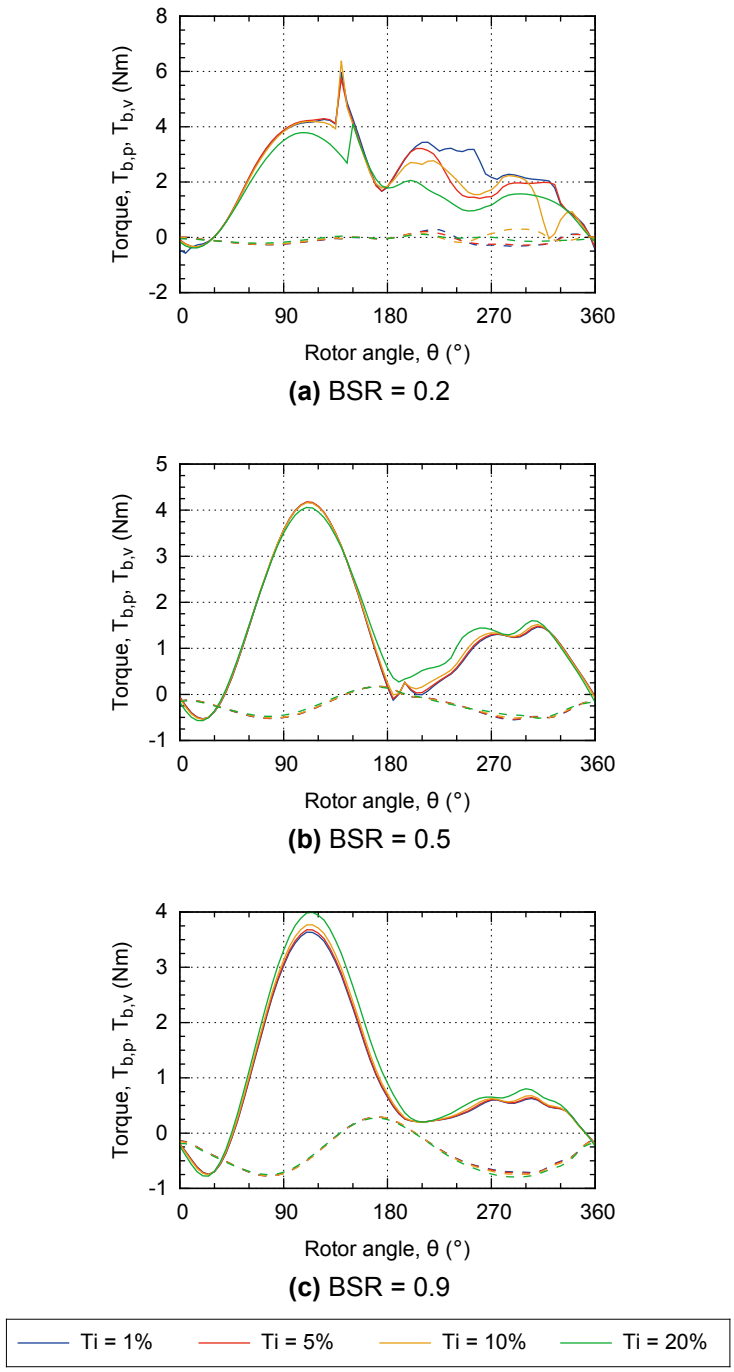

Figure 3.4.9: Effect of ambient turbulence intensity on output torque, per metre span of blade, generated due to forces acting on a single blade in a single cycle (n=3 turbine simulation). Solid lines represent torque due to pressure forces and dashed lines represent torque due to viscous forces

This page is intentionally left blank.

CHAPTER 4

COMPUTATIONAL ANALYSIS: SINGLE BLADE

4.1 Introduction

This chapter firstly presents an analysis of the MRL turbine blade motion, predicting how the relative velocity, effective angle of attack and pitching rate varies with rotor angle. The results are used to highlight the range of conditions a single blade encounters as it rotates about the central axis, and how these conditions vary with blade speed ratio (*BSR*).

Secondly, a CFD study of a flat plate pitching about its mid-chord axis, at various reduced frequencies, is presented and compared to existing experimental results. The aim is to validate the CFD modelling technique and give an insight into the flow structure formed at different angles of attack and reduced frequencies.

Further simulations of a blade undergoing MRL motion are also presented, with the blade geometry matching both that of the physical turbine model and a flat plate. The aim is to give an insight into the simulated flow structure formed by the MRL motion, in comparison to simple, steady rotation.

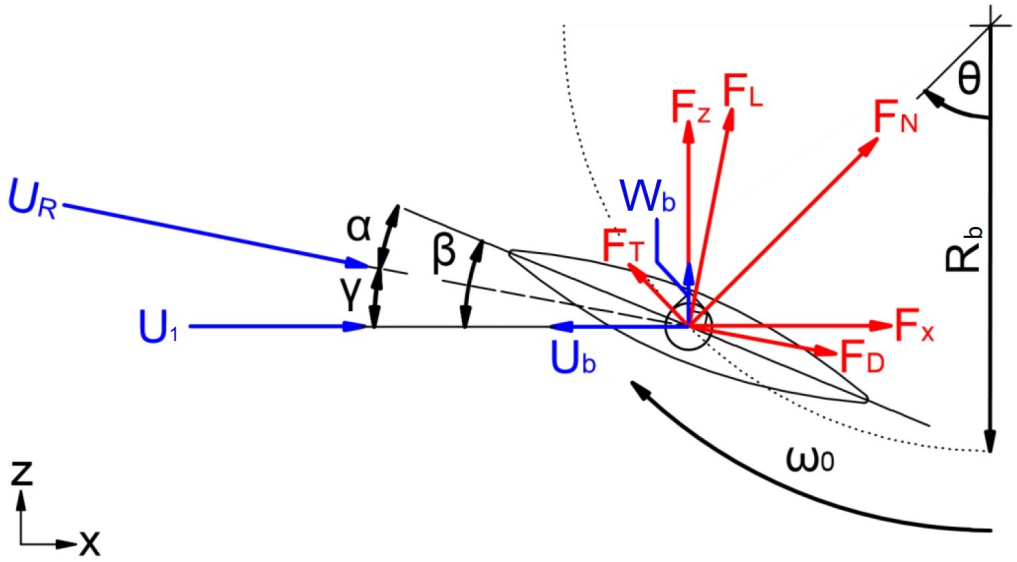

Figure 4.2.1: Diagram showing the orientation of velocity vectors (blue) and force vectors (red) acting on the blade at rotor angle *θ*

4.2 Analysis of Effective Blade Conditions

4.2.1 Aim of section

The magnitude and direction of forces acting on a single blade, as it undergoes MRL turbine motion, can be predicted at any instantaneous position (if lift and drag coefficients are known for a particular blade profile). To achieve this, it is important to know the angle of attack of the blade compared to the relative incoming flow and the relative magnitude of the flow velocity. Also pertinent to a continuously pitching plate is the rate of pitch change, or reduced frequency.

This section defines these parameters, and presents the theoretical variation of these with turbine rotor angle and blade speed ratio. Values are also compared to those representing the Darrieus turbine, in order to highlight the different operating conditions of the two designs.

4.2.2 Definition of parameters

Figure 4.2.1 shows a number of velocities, forces and angles used in this analysis, as defined in the following sub-sections.

4.2.2.1 Velocities

U_b and W_b are the velocities of the blade centre in the x- and z-directions respectively, due to the motion of the blade about the turbine central axis. These are defined as positive in the positive x- and z-directions; therefore U_b shown in Figure 4.2.1 is negative in sign. These are resolved components of the blade tangential velocity, which is the product of turbine rotational speed, ω_0, and radius, R_b, or alternatively the upstream flow velocity, U_0, and blade speed ratio, as shown below:

$$U_b = -\omega_0 R_b \cos\theta = -U_0 BSR \cos\theta \tag{4.2.1}$$

$$W_b = \omega_0 R_b \sin\theta = U_0 BSR \sin\theta \tag{4.2.2}$$

U_1 is the incoming flow velocity local to the blade, acting in the positive x-direction (flow velocity in the z-direction is taken to be zero). The relative velocity, U_R, is the sum of these three vectors, calculated as follows:

$$U_R = \sqrt{(U_1 - U_b)^2 + W_b^2} \tag{4.2.3}$$

Note that although the symbol U_R is used for relative velocity, it is a vector rather than x-direction component.

The induced flow velocity local to the blade, U_1, will be lower in magnitude than the flow velocity upstream of the turbine, U_0. This is due to the transfer of kinetic energy from the flow to the rotor blades that results in a reduction in velocity through the turbine. This reduction in velocity cannot happen instantaneously across the blades, otherwise unlimited acceleration and forces would occur (Sharpe, 2004). Therefore the velocity reduction begins upstream of the turbine and is accompanied by a steady increase in static pressure above the free-stream value (maintaining total pressure). The extraction of energy from the flow results in a sudden drop in static pressure through the turbine. The pressure then gradually increases back towards the free-stream value downstream of the turbine, which results in a further decrease in flow velocity until the wake is fully developed.

The upstream reduction in flow velocity can be quantified with the following:

$$U_1 = U_0 (1 - a) \tag{4.2.4}$$

where a is called the induction factor (the value $(1 - a)$ is called an interference factor in some texts). Momentum theory (originating from Rankine (1865) and Froude (1889)) states that when an energy conversion device (i.e. a turbine) is modelled as an actuator disk, the induced reduction in velocity upstream of the disk is half of the total reduction from far upstream to the fully developed wake boundary. Therefore, the velocity in the fully developed wake, U_2, is given by:

$$U_2 = U_0 (1 - 2a) \tag{4.2.5}$$

The mass of fluid that flows through a given area of turbine can be modelled as bound within a stream-tube. As the mass flow is conserved and the velocity gradually deceases in the stream-wise direction, the cross-sectional area of the stream tube must gradually increase. This theory forms part of the basis for blade-element and momentum (BEM) analysis, as first developed for cross-flow turbines by Templin (1974), who modelled the rotor as enclosed within a single stream-tube. The theory was further developed with the use of multiple stream-tubes (Strickland, 1975), which allows the induction factor to be varied across the turbine section.

Paraschivoiu (1988) further developed this approach by separately modelling each interaction of the blades with the stream-tubes, i.e., an actuator disk was used in both the upstream and downstream half-cycles for each stream-tube. This approach assumes the flow velocity has reduced to the far wake value of the first stream-tube within the turbine region. This velocity value is then used for the inlet of the second stream-tube. This modelling assumption may not be valid, as it is unlikely that there is time for the velocity to reach the first stream-tube wake value within the turbine region. This is especially true for high solidity machines such as the MRL turbine, where the blades are relatively large compared to the rotor diameter. However, it should be recognised that in reality the cycle-averaged flow velocity within the turbine region will be of lower magnitude than directly upstream of the turbine, as energy has already been extracted by the passage of blades in the upwind half-cycle. It is therefore likely the torque producing performance of the blades in the downwind half-cycle will be significantly different to the first half-cycle.

Generally the momentum theory approach is valid for values of $a < 0.5$, as otherwise the fully developed wake velocity is less than zero, requiring a reversal of the flow. In reality this cannot occur and instead the wake becomes turbulent and mixes in fluid from outside of the wake (Burton et al., 2011).

4.2.2.2 Angles

The angle of attack, α, is the angle between the blade chord-line and direction of the relative flow velocity, and can be calculated as shown:

$$\alpha = \beta - \gamma \tag{4.2.6}$$

Here β is the angle between the blade chord-line and the x-axis. For a standard Darrieus turbine, $\beta = \theta$, but for the MRL turbine, where the blades rotate about their own axes once per two turbine rotations, the value is given by:

$$\beta = \theta/2 \tag{4.2.7}$$

Also, γ is the angle between the relative velocity direction and the x-axis. This is calculated from the relative velocity components in the x- and z-directions, as shown:

$$\gamma = tan^{-1}\left(\frac{W_b}{U_1 - U_b}\right) = tan^{-1}\left(\frac{BSR\,sin\,\theta}{1 - a + BSR\,cos\,\theta}\right) \tag{4.2.8}$$

Note that the angle γ is a function of BSR, θ and a only, and is independent of the type of blade motion, i.e, the value is the same for MRL and Darrieus turbines. Also note that BSR is used throughout this discussion, and this is equivalent to TSR when discussing Darrieus turbines.

Related to the angle of attack and relative velocity is the reduced frequency, K, which is calculated with the following equation:

$$K = \frac{d\,\alpha}{dt}\,\frac{c}{2\,U_R} \tag{4.2.9}$$

where $\frac{d\,\alpha}{dt}$ is the rate of change of angle of attack measured in rad/s, and c is the blade chord length. This can be seen as the ratio between the blade tip velocity (due to rotation about its axis), and the incoming relative flow velocity.

4.2.2.3 Forces

Figure 4.2.1 shows the total force acting on the blade centre can be resolved into any one of three pairs of perpendicular components. These are:

- F_x and F_z: Forces resolved the x- and z-directions.

- F_L and F_D: Lift force (acting in the direction perpendicular to the relative velocity) and drag force (acting in the direction parallel to the relative velocity).
- F_T and F_N : Tangential force (acting in the direction of blade motion) and normal force (acting towards the turbine central axis).

The first two pairs can be related with the angle γ, as shown:

$$F_x = F_L \sin\gamma + F_D \cos\gamma \tag{4.2.10}$$

$$F_z = F_L \cos\gamma - F_D \sin\gamma \tag{4.2.11}$$

The lift and drag forces are related to the lift coefficient, C_L, and drag coefficient, C_D, as follows:

$$C_L = \frac{F_L}{1/2\,\rho\, c\, l_b\, U_R^2} \tag{4.2.12}$$

$$C_D = \frac{F_D}{1/2\,\rho\, c\, l_b\, U_R^2} \tag{4.2.13}$$

where l_b represents the blade length and ρ is the fluid density.

The third pair of forces can also be related to the first with the angle θ, as shown:

$$F_T = F_z \sin\theta - F_x \cos\theta \tag{4.2.14}$$

$$F_N = F_z \cos\theta + F_x \sin\theta \tag{4.2.15}$$

Now the torque acting about the turbine central axis due to the tangential component of the force can be calculated as follows:

$$T_d = F_T R_b = T_{F_L} + T_{F_D} \tag{4.2.16}$$

Here the total torque has also been separated into torque generated due to lift forces, T_{F_L}, and torque generated due to drag forces, T_{F_D}. These can be directly related to the lift and drag forces with the following:

$$T_{F_L} = A_{F_L} F_L R_b \tag{4.2.17}$$

$$T_{F_D} = A_{F_D} F_D R_b \tag{4.2.18}$$

Here A_{F_L} and A_{F_D} are defined as the 'coefficient of lift torque' and 'coefficient of drag torque' respectively. These can be directly calculated from the angles θ and γ as shown:

$$A_{F_L} = \sin\theta\cos\gamma - \cos\theta\sin\gamma \tag{4.2.19}$$

$$A_{F_D} = -(\sin\theta\sin + \cos\theta\cos\gamma) \tag{4.2.20}$$

This allows the relative contribution of lift and drag forces to torque to be assessed at a given blade position, regardless of actual force magnitude. Note that these coefficients are functions of θ and γ and are therefore independent of blade pitch motion, i.e., the variation with θ is equal for MRL and Darrieus turbines at given *BSR* (or *TSR*) value. The blade pitch motion affects the angle of attack, which in turn affects lift and drag coefficients and the magnitude of developed forces.

4.2.3 Analysis of parameter variation

4.2.3.1 Comparison of MRL and Darrieus blade motion

Before exploring the effective operating conditions of MRL turbine blades in more detail, it is pertinent to compare operating conditions of the MRL and Darrieus turbine designs. The equations set out in Section 4.2.2 have been used to produce Figures 4.2.2 and 4.2.3, which explore the variation of key parameters in the first half cycle of blade motion (assuming an induction value of $a = 0$).

Figure 4.2.2a shows the variation of flow angle relative to the x-axis, γ, with rotor angle, θ, for a wide range of *BSR* values. This shows that for values of $BSR < 1$, the relative flow angle is contained within a window with a maximum of $\gamma = 90°$. In this range the x-direction component of relative flow is always acting positively. Conversely, for value of $BSR > 1$, the maximum value increases to $\gamma = 180°$, where the x-direction component is acting negatively.

Figure 4.2.2b presents the resulting angle of attack variations when two of these γ curves (for $BSR = 0.5$ and $BSR = 5.0$) are combined with the blade motion of the Darrieus and MRL turbine designs (i.e., $\beta = \theta$ and $\beta = \theta/2$).

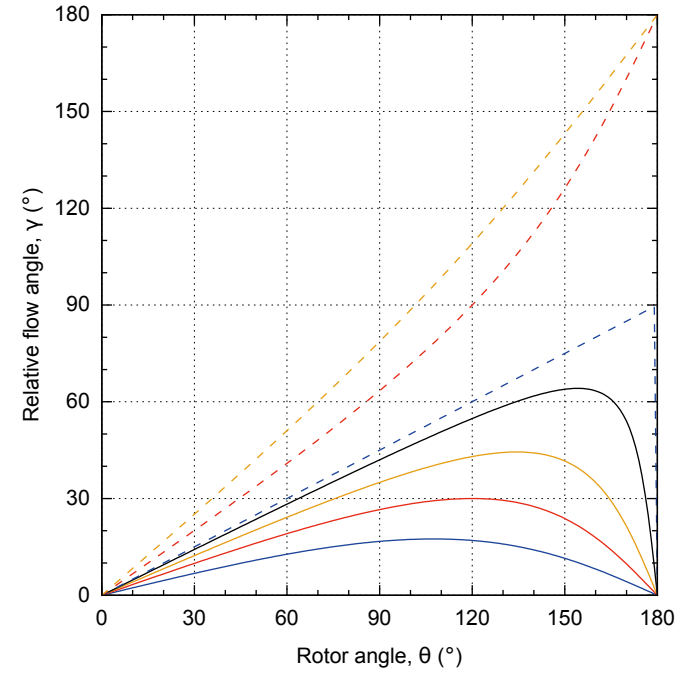

(a) Relative flow angle vs rotor angle

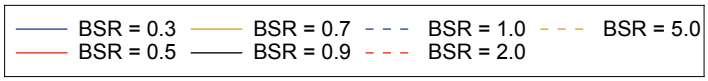

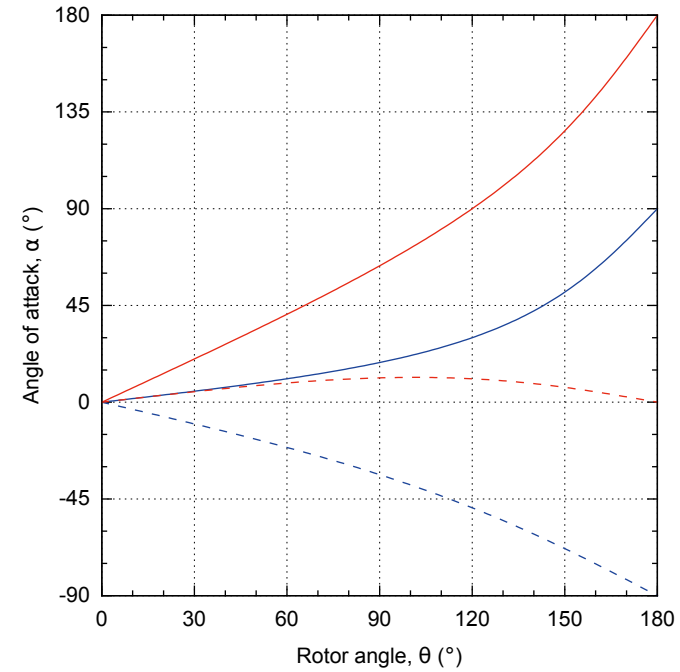

(b) Angle of attack vs rotor angle

Figure 4.2.2: Variation with rotor angle of relative flow angle and angle of attack, for both MRL and Darrieus motions at two *BSR* values

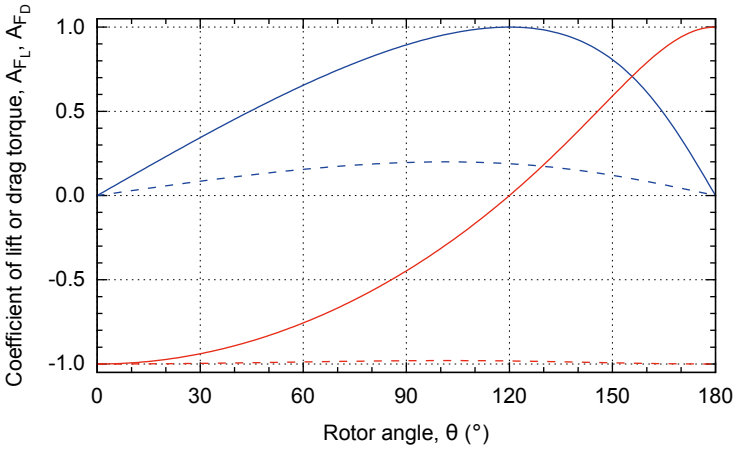

(a) Coefficients of torque vs rotor angle

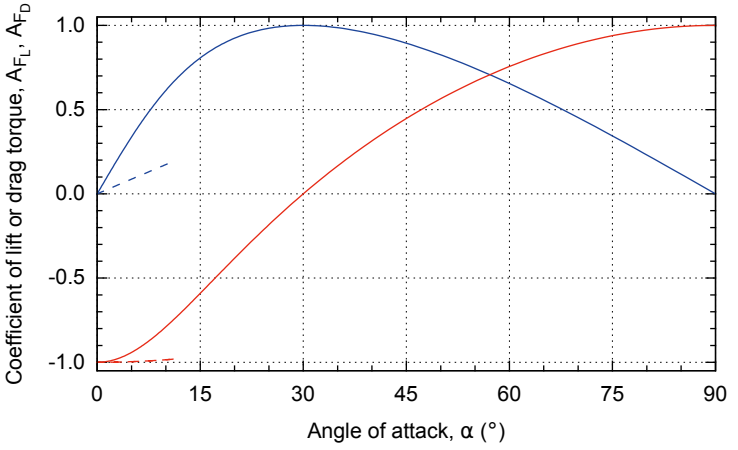

(b) Coefficients of torque vs angle of attack

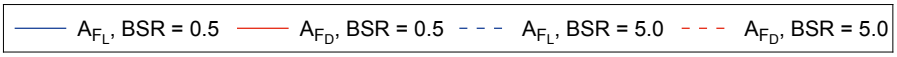

Figure 4.2.3: Variation with rotor angle of coefficients of lift and drag forces at two *BSR* values (*α* relates to MRL motion at $BSR = 0.5$ and Darrieus motion at $BSR = 5.0$)

Darrieus motion The results show how Darrieus turbines operating at low *BSR* values (less than unity) theoretically develop angles of attack that continuously increase from $\alpha = 0°$ to $\alpha = 180°$. Alternatively, Darrieus turbines operating at values of $BSR > 1$ develop relatively low maximum angles of attack of $\alpha \approx 10 - 15°$, and return to $\alpha = 0°$ at $\theta = 180°$.

The latter case is the optimum operating condition of the Darrieus turbine, and related coefficients of lift and drag torque are presented in Figure 4.2.3. The results for $BSR = 5.0$ show how the coefficient of lift force reaches a maximum of approximately $A_{F_L} = 0.2$, whilst the coefficient of drag force is relatively constant at $A_{F_D} = -1.0$. This indicates that due to the relative flow direction, only a maximum 20% of any generated lift force contributes to positive driving torque and approximately 100% of any generated drag force contributes to parasitic, negative driving torque.

The significance of this behaviour can be explained with reference to Figure 4.2.4, where the typical variation of lift and drag coefficients with angle of attack are presented for a static NACA profile foil. The graphs show that at low angles of attack (approximately $\alpha < 18°$) the lift coefficient reaches a pre-stall maximum and the drag coefficient remains near zero. By operating at relatively high *BSR* values, the Darrieus turbine therefore harnesses the generation of useful lift forces and minimises the generation of parasitic drag forces.

Alternatively, if the Darrieus turbine operates at $BSR = 0.5$, maximum A_{F_L} occurs at $\theta = 120°$ where $\alpha = 90°$ and $C_L \approx 0$, and maximum positive A_{F_D} occurs at $\theta = 180°$ where $\alpha = 180°$ and $C_D \approx 0$. The turbine is therefore unable to effectively operate at these speeds, resulting in poor start-up behaviour for fixed blade Darrieus designs.

MRL motion Figure 4.2.2b shows how the theoretical angle of attack for the MRL turbine consistently varies from the Darrieus turbine equivalent by $\alpha = -\theta/2°$, when operating at the same *BSR* value. This results in maximum angle of attack magnitudes of $\alpha = 90°$ and $\alpha = -90°$ for $BSR < 1$ and $BSR > 1$ respectively.

Figure 4.2.3a shows that at $BSR = 5.0$, the coefficients of lift and drag force reach a maximum (of approximately $A_{F_L} = 0.2$ and $A_{F_D} = -1.0$) at approximately $\theta = 110°$, where $\alpha = -45°$ for MRL motion. At this negative angle of attack, the lift coefficient reaches a maximum negative value of approximately

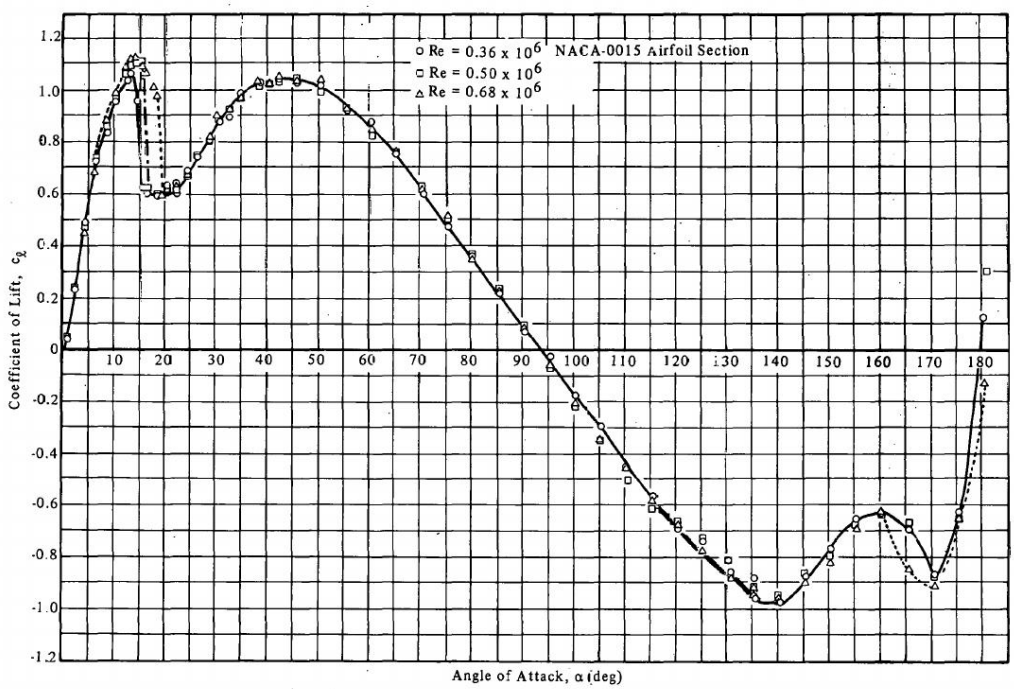

(a) Lift coefficient vs. angle of attack

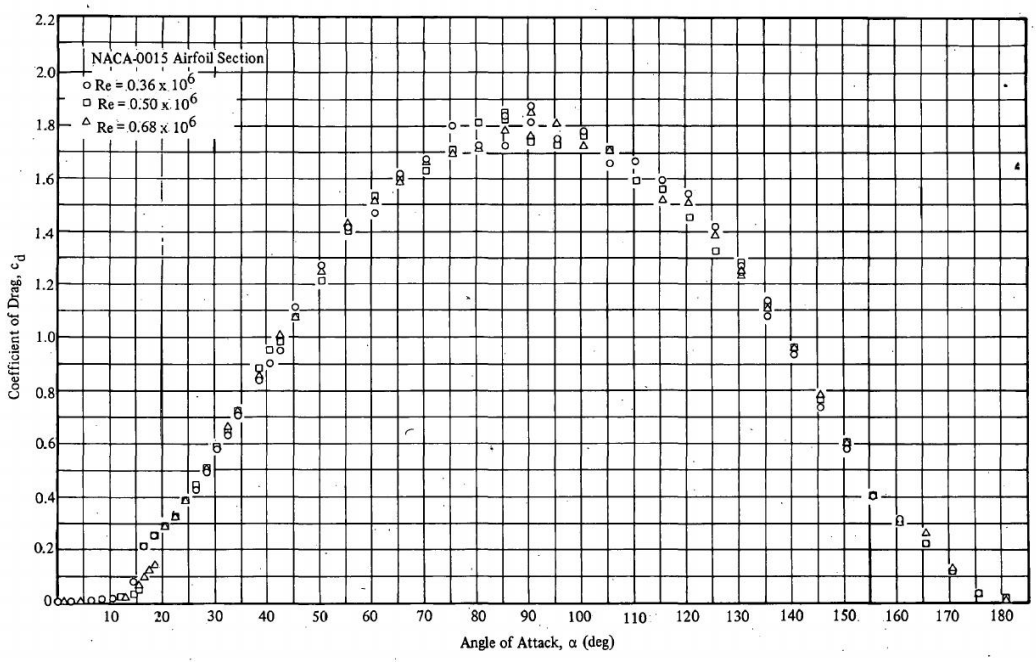

(b) Drag coefficient vs. angle of attack

Figure 4.2.4: Variation of lift and drag coefficients with angle of attack, for a static NACA0015 aerofoil (Sheldahl and Klimas, 1981)

$C_L = -1.0$ and drag force also reaches $C_D = +1.0$. Therefore a high magnitude of negative-direction acting torque would be developed if the MRL turbine was to operate at this rotational speed. In fact, these results suggest it is not feasible for the MRL turbine to operate at $BSR > 1$.

In contrast, Figure 4.2.3b shows that at $BSR = 0.5$, maximum values of $A_{F_L} = 1.0$ and $A_{F_D} = 1.0$ are reached at $\alpha = 30°$ and $\alpha = 90°$ respectively. These angles of attack correspond to near maximum lift and maximum drag for static aerofoils, suggesting the contribution of developed lift and drag forces to useful torque are near optimised by the MRL turbine operating at this *BSR* value.

Whilst these results suggest the MRL turbine has a distinct benefit over the Darrieus turbine in terms of proportion of developed lift and drag forces translated into positive torque, it should be noted that the magnitude of the forces depend not only on the lift or drag coefficient, but also on the square of relative flow velocity. As the Darrieus turbine operates at significantly higher *BSR* values, the relative flow velocities are also higher ($U_R \approx BSR\,U_0$ compared to $U_R \approx U_0$), resulting in greater lift and drag force magnitudes. This serves to offset the relatively low translation of lift into torque, but is also a disadvantage when considering generation of parasitic drag forces. This reinforces the importance of Darrieus turbine angles of attack remaining low (pre-stall), where the ratio of lift to drag is high.

4.2.3.2 MRL motion with induction factor of zero

This section further presents the variation of effective MRL turbine blade parameters with rotor angle. The relationships are presented for a blade of chord length $c = 0.05\,m$, rotating at a radius of $R_b = 0.055\,m$ and *BSR* values in the range of $0.2 - 0.9$. The values presented are calculated using an induction factor of $a = 0$, i.e., the inflow velocity local to the blade is equal to the far upstream value. As induction factor cannot be known at this point, $a = 0$ is used as a base case in order to investigate the relationship between the presented parameters and *BSR* value.

Firstly, Figure 4.2.5a shows the variation of effective angle of attack with rotor angle θ, for one half of a turbine cycle. The graphs show the angle of attack increases with rotor angle from $\alpha = 0°$ at $\theta = 0°$, to $\alpha = 90°$ at $\theta = 180°$, for all *BSR* values from 0.2-0.9. All curves also increase in gradient with increasing θ.

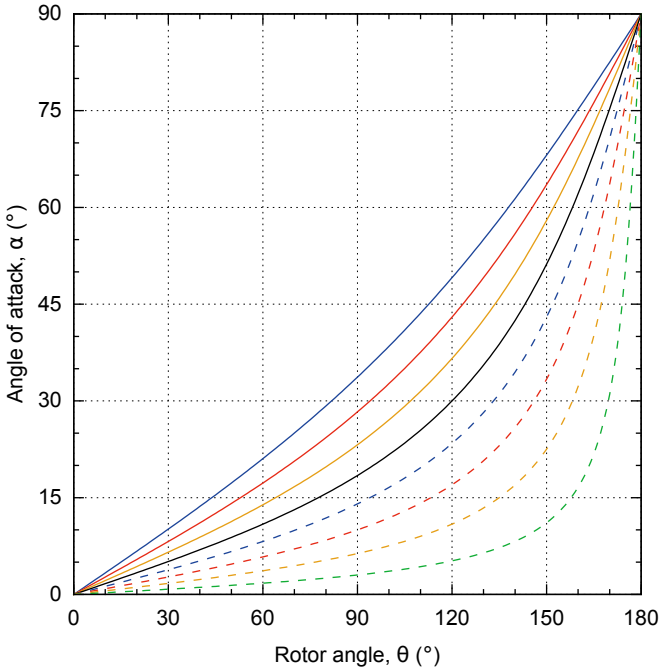

(a) Angle of attack vs rotor angle

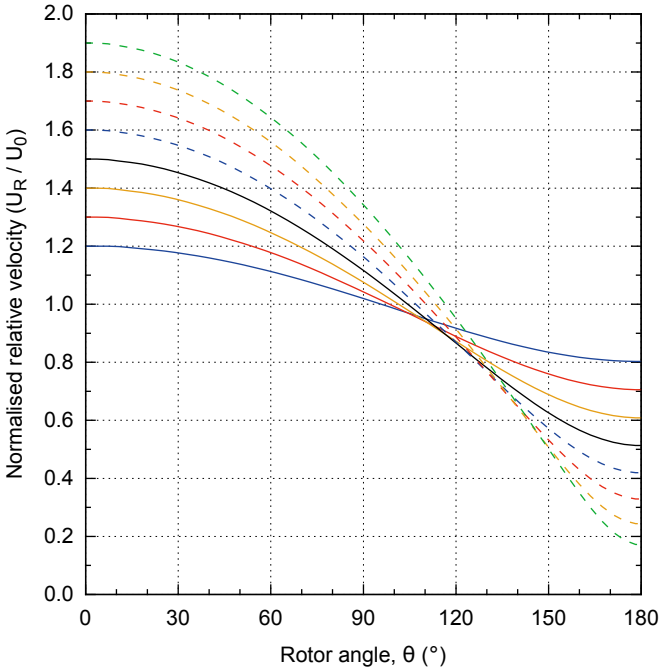

(b) Normalised relative velocity vs rotor angle

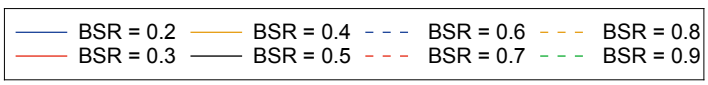

Figure 4.2.5: Variation with rotor angle of key parameters defining the relative flow over a single MRL turbine blade, for various values of blade speed ratio (a=0)

The curve for $BSR = 0.2$ has the most consistent gradient throughout, whilst $BSR = 0.9$ first experiences the slowest rate of change of α before transitioning to the fastest rate of change. This is because higher BSR values represent higher ratios of tangential velocity to inlet velocity, which leads to higher angles of γ, and for a given angle θ (and therefore β) this results in lower values of α.

Figure 4.2.5b shows the variation of relative velocity (normalised to U_0) with rotor angle θ, for one half of a turbine cycle. At $\theta = 0°$, all curves begin at $U_R/U_0 = 1 + BSR$, as here the blades are moving directly towards the incoming flow velocity. All BSR curves then decrease with increasing values of θ, before reaching values of $U_R/U_0 = 1 - BSR$ at $\alpha = 180°$, where the blades are moving directly away from the incoming flow velocity. Higher BSR values lead to higher variations in relative velocity though the cycle, with all curves lying in the range of $U_R/U_0 = 0.85 - 0.95$ at $\alpha = 120°$.

Figure 4.2.6 presents the theoretical variation of reduced frequency through a turbine half cycle, with reference to both the rotor angle θ and angle of attack α. These show the reduced frequency generally increases as the blade progresses through a turbine cycle, which corresponds to the increasing rate of α discussed previously.

At $\theta = 0°$, BSR values in the range of $0.2 - 0.5$ begin with similar values of $K = 0.025 - 0.030$, whilst higher BSR values begin with lower values ($BSR = 0.9$ starting as low as 0.006). However, at $\theta = 180°$, the values are more evenly spaced (on a logarithmic scale), with $BSR = 0.2$ reaching $K = 0.085$ and $BSR = 0.9$ reaching $K = 40$. Overall this highlights how the variation of effective blade conditions greatly differs depending on BSR value, with the most consistent values occurring at lower BSR values.

Figures 4.2.7 and 4.2.8 show the variation of the coefficients of lift and drag torque, with reference to rotor angle, angle of attack and reduced frequency.

The coefficient of lift torque (Figure 4.2.7) increases from zero at $\theta = 0°$, to unity in the region of $\theta = 110°$-$160°$, before decreasing back to zero at $\theta = 180°$. Increasing the BSR value shifts the maximum point to higher rotor angles. When plotted against angle of attack, the results give a similar profile, with peaks occurring in the range of $\alpha = 10°$-$40°$. However, increasing BSR value shifts the peak to lower angles of attack. The plot of A_{F_L} against reduced frequency effectively combines Figures 4.2.6a and 4.2.7a, and again highlights the varying range of pitch rates that are encountered at different BSR values.

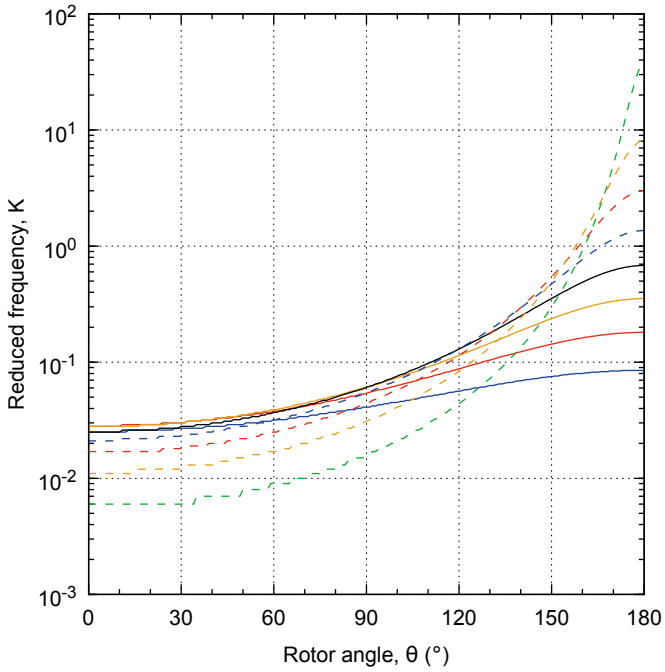

(a) Reduced frequency vs rotor angle

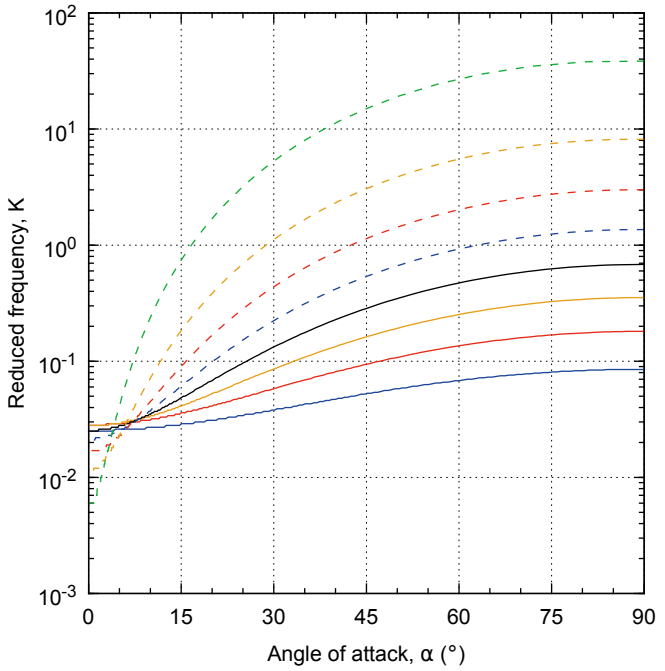

(b) Reduced frequency vs angle of attack

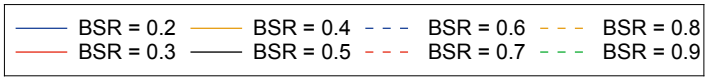

Figure 4.2.6: Variation of the reduced frequency of a single MRL turbine blade, for various values of blade speed ratio (a=0)

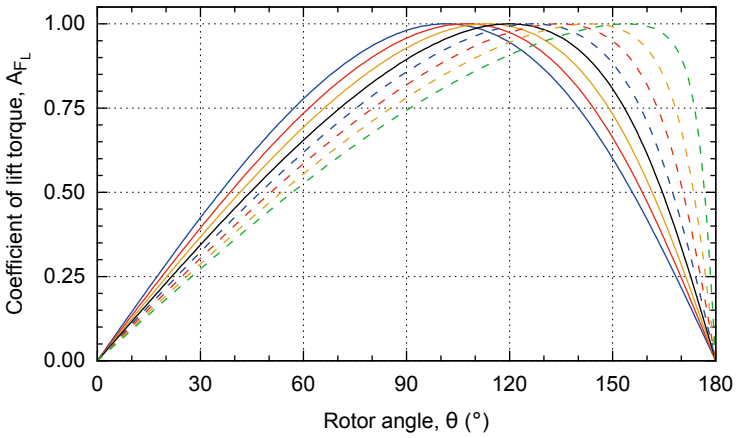

(a) Coefficient of lift torque vs rotor angle

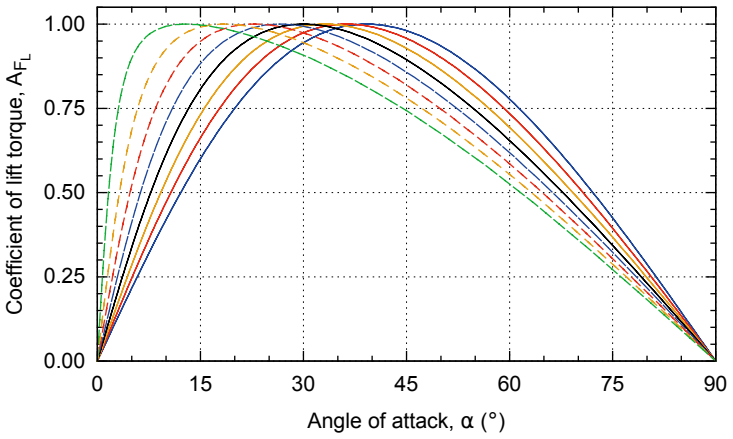

(b) Coefficient of lift torque vs angle of attack

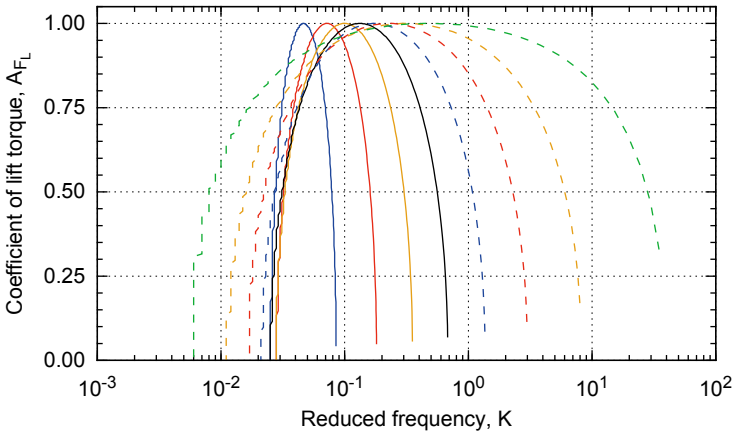

(c) Coefficient of lift torque vs reduced frequency

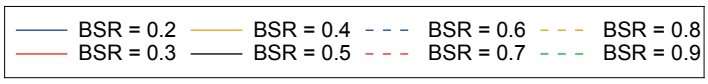

Figure 4.2.7: Variation of the coefficient of lift force with key blade parameters, for various values of blade speed ratio (a=0)

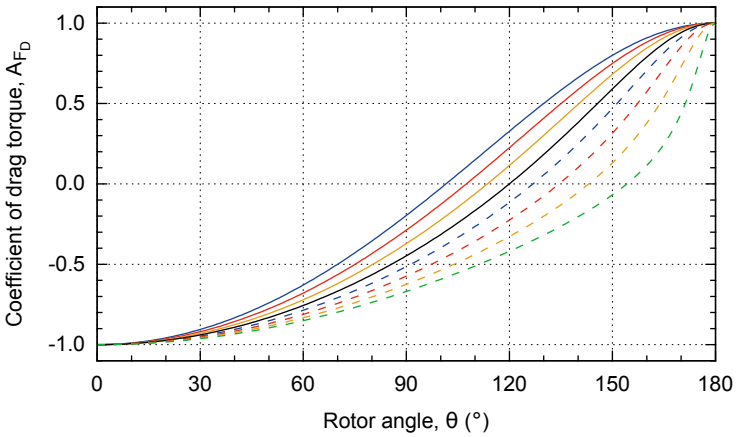

(a) Coefficient of drag torque vs rotor angle

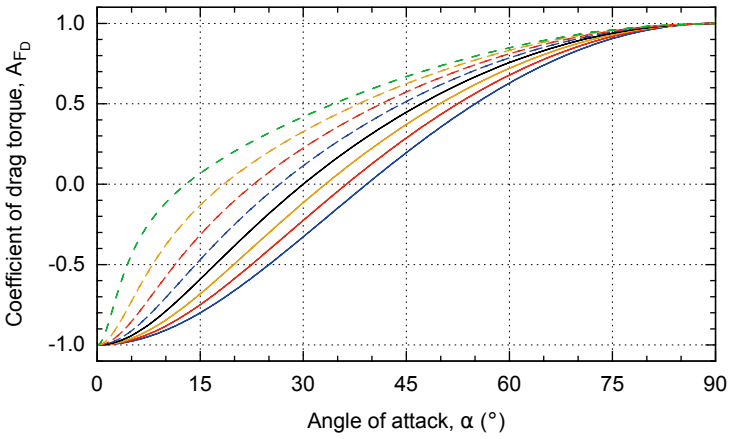

(b) Coefficient of drag torque vs angle of attack

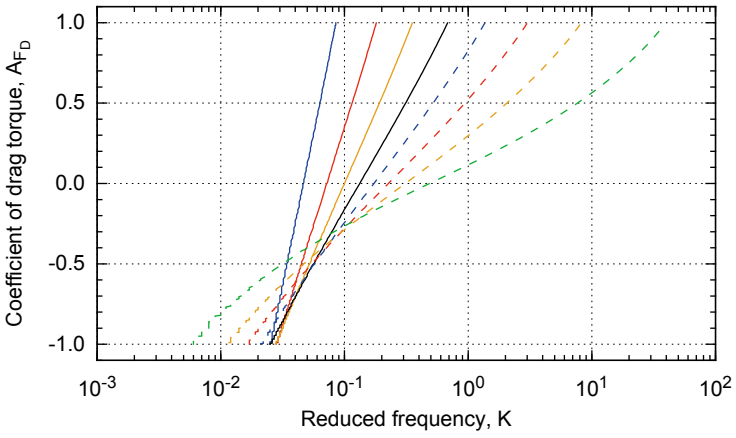

(c) Coefficient of drag torque vs reduced frequency

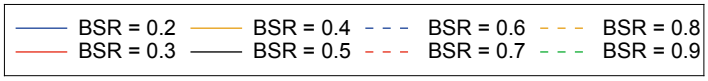

Figure 4.2.8: Variation of the coefficient of drag force with key blade parameters, for various values of blade speed ratio (a=0)

It also shows the pitch rates at which lift forces give the highest contribution to rotor torque.

The coefficient of drag torque (Figure 4.2.8) increases from negative unity at $\theta = 0°$, to zero in the region of $\theta = 100°$-$155°$, and on to positive unity at $\theta = 180°$. Increasing the *BSR* value gives a lower gradient initially, before transitioning to a higher gradient later on in the cycle. When plotted against angle of attack, the results again give a similar profile, but increasing *BSR* values leads to a higher gradients at lower angles of attack and vice versa. Negative values of A_{F_D} contribute to parasitic torque, and the graphs shows that at as *BSR* increases, so does the range of rotor angles in which this occurs.

4.2.3.3 MRL motion with induction factor greater than zero

The previous sub-section presented results for an induction factor of $a = 0$, i.e., the incoming velocity local to the blade is equal to the far upstream value U_0. However, as discussed in section 4.2.2.1, in reality the induced velocity magnitude will be lower than this value, i.e., $a > 0$. The induced velocity is also likely to vary throughout the rotor cycle, both across the frontal section and from upstream to downstream half-cycle. It is therefore not possible to predict the induced velocity magnitude without further modelling (e.g. a BEM or CFD model). However, the general effect of increasing induction factor on the effective blade conditions can be investigated. Therefore, Figure 4.2.9 shows the variation of angle of attack and reduced frequency with rotor angle, for a single value of $BSR = 0.3$ and multiple values of a.

In general, increasing values of induction factor has the same effect of increasing blade speed ratio. This is because the relative magnitude of the tangential blade velocity increases with decreasing inflow velocity. Therefore, as the value of a increases, the angle of attack firstly increases with a shallower gradient before transitioning to a higher gradient towards $\theta = 180°$. This is reflected in Figure 4.2.9b, where the initial value of K decreases, and final value increases, with increasing a. However, only values of $a > 0.4$ result in largely different initial K values, although all results visibly diverge at $\theta = 90°$.

Results for $a = 0.8$ clearly differ from the four lower values presented. The initial angle of attack is negative and increases in magnitude with rotor angle, before rapidly reducing in magnitude, becoming positive and increasing to $\alpha = 90°$.

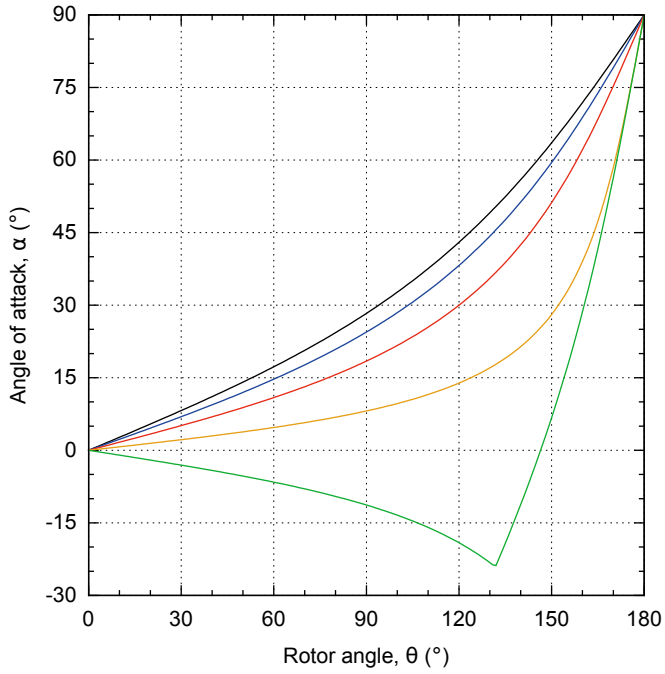

(a) Angle of attack vs rotor angle

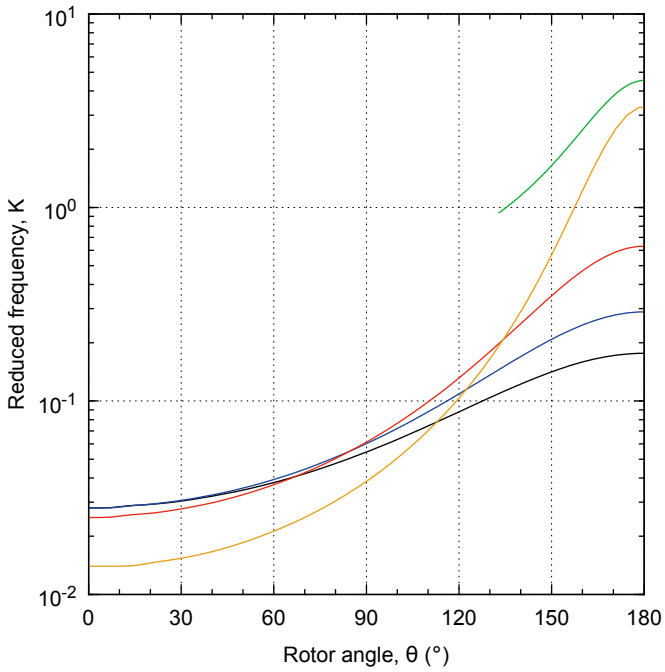

(b) Reduced frequency vs rotor angle

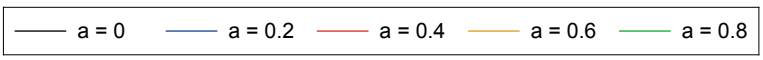

Figure 4.2.9: Variation with rotor angle of angle of attack and reduced frequency, for $BSR = 0.3$ and various values of induction factor

Correspondingly, K is negative until the angle of attack begins to increase, and therefore only the positive portion of the cycle is shown on the log scale graph of reduced frequency.

The effect of negative angle of attack in the first part of the cycle is likely the reduction of torque, or even development of negative, parasitic torque, as lift forces generally act in the negative z-direction. This state occurs when $BSR > (1 - a)$, as the tangential blade velocity magnitude is greater than the local inflow velocity magnitude. For the presented case of $BSR = 0.3$, the threshold is $a = 0.7$ and so only one presented curve displays this behaviour. However, at higher values of BSR (approaching 1) even moderate values of a will result in this state occurring. This behaviour is also more likely to occur in the second half-cycle of rotation, where the inflow velocity local to the blade will already be reduced in comparison to the upstream value. Note that the above condition is also equivalent to values of $BSR > 1$ for $a = 0$ and suggests that the turbine may not operate effectively at speed ratios greater than unity, as shown by the experimental results in Chapter 2.

4.2.4 Conclusion of analysis

This section has defined a number of parameters that can be used to describe the conditions effectively encountered by a single MRL turbine blade at a given position in the turbine rotation. This analysis assumes uniform inlet flow velocity and ignores the effects of any secondary flow features, such as vortices or flow deflection that may significantly affect the localised conditions.

The analysis has yielded a set of graphs that describe the variation of these parameters through a turbine half cycle, and how these relationships vary with blade speed ratio. Generally the graphs have highlighted the large variation in resultant velocity, angle of attack and reduced frequency that occur both throughout a cycle, and between different BSR values.

The majority of results are presented for an induction factor of zero, which will not be achievable in reality. However, these results do allow the comparisons described above. A set of results for higher induction factors has also been presented, that highlights the effect of increasing induction factor is the same as increasing blade speed ratio.

The variation of key parameters has also been presented for the Darrieus turbine, and compared to those of the MRL turbine. This aids understanding of the different blade operating conditions for the two turbine designs.

Although the parameters have only been presented for the first half of the turbine cycle, the second half of the cycle can be represented by a mirror image of the first. However, during the second half of the cycle, the blade will more likely pass through disturbed flow, and therefore the conditions are less likely to be as predicted here.

4.3 Simulation of Pitching Flat Plates

4.3.1 Aim of section

The previous section identified the various ranges of effective blade conditions a MRL turbine blade encounters as it travels through a cycle. Based on this information, this section aims to perform CFD simulations of suitable simple test cases that can be compared to data found in the literature. The purpose is two-fold; firstly the CFD code and set-up can be validated using time-dependent data, and secondly the CFD results can provide an insight into the characteristics of the flow structure formed. This information can then be used when analysing the behaviour of flow around the more complex case of a blade undergoing MRL motion.

4.3.2 Selected data-set

No time-dependent data is available for a blade undergoing MRL motion and therefore a simpler test case must be selected for validation modelling. The next most appropriate choice would be a MRL blade pitching about its mid axis; however, the MRL turbine blade profile is bespoke to the experimental model being investigated, and there is no specific data available. Therefore a flat plate has been selected, as this retains the characteristic symmetry about both the chord and mid point, and is a classic case study in fluid dynamics.

Ideally, data would be available that describes lift and drag coefficient variation with both continuously changing angle of attack and reduced frequency. Also,

pitch amplitudes of 180° and K values in the range of $0.006 - 40$ would be covered. However, most data available in the literature concerns relatively low pitch amplitudes, even when described as 'high angle of attack' studies. For example, Visbal and Shang (1989) investigate a flow structure around a pitching foil, but with pitch amplitudes of 50°, Ol (2009) analyses the flow around plates pitching up to 40° and Lu et al. (2013) perform numerical studies with pitch amplitudes up to 30°. A classic set of data exists for NACA foils pitched up to 180° (Sheldahl and Klimas (1981)), but these relate to a foil held at steady state, not undergoing constant pitching.

Two sets of data have been identified for plates / foils pitching up to 90° with various constant pitch rates. These are presented in Strickland and Graham (1987) and Granlund et al. (2013). The former concerns NACA-0015 aerofoils and values of K from $0.09 - 1.0$. In contrast, the latter is a much more recent study, and investigates a flat plate pitching with K values from $0.03 - 0.5$. The study also investigates the effect of pitch axis location and proposes correlations for lift and drag coefficients that are dependent on angle of attack, reduced frequency and pitch axis location.

These correlations are based on those proposed by Strickland and Graham (1987), which are shown below:

$$C_L = 2 A_L \sin\alpha \cos\alpha \tag{4.3.1}$$

$$C_D = A_D \sin^2\alpha \tag{4.3.2}$$

where A_L and A_D are constants that can be empirically related to reduced frequency. Note, the above equations are based on Prandtl's lifting line theory that can be used to predict lift and drag for static foils at high angles of attack. In that case A_L and A_D are equal to the maximum coefficient values that occur in the range $0° < \theta < 180°$. These are generally taken as 1.0 and 2.0 respectively.

Granlund et al. (2013) further developed the above correlations to take account of pitch axis location (x_p/c), resulting in the following:

$$C_L = 2 B_L \sin\alpha \cos\alpha + 4 \pi K \left(0.75 - x_p/c\right) \cos\alpha \tag{4.3.3}$$

$$C_D = 2 B_D \sin^2\alpha + 4 \pi K \left(0.75 - x_p/c\right) \sin\alpha \tag{4.3.4}$$

Table 4.3.1: Case parameters for pitching flat plate simulations

Inlet velocity	Reynolds number	Turbulent intensity	Chord length	Thickness ratio	Blockage ratio	Reduced frequency
u_{inlet}	Re_c	Ti	c	h/c	B	K
(m/s)	$(-)$	(%)	(m)	(%)	(%)	-
1.0	2x10^4	1.0	0.05	2, 0.4	12.5	0.03, 0.05, 0.1, 0.2, 0.3, 0.5, 0.7, 1.0, 2.0

Here B_L and B_D are constants, with proposed values of 2.1 and 2.0 respectively. The correlations were shown to be well matched to experimental data for $K >$ 0.1, especially for lift coefficient. These correlations are presented as part of the validation data in the following sections.

4.3.3 Simulation setup

Two-dimensional CFD simulations of a flat plate pitching about a mid-chord axis in a uniform flow, with various constant pitch rates, have been undertaken. Two full revolutions were simulated (i.e. $0° < \alpha < 720°$), although only the first 90° are compared to the available data. Further physical characteristics of the set up are given in Table 4.3.1, which match to the experiments of Granlund et al. (2013). As well as the first six reduced frequency values, which match the validation data, three further values (0.7-2.0) have been simulated, in order to gain an insight of the effect of higher pitch rates.

Two values of plate thickness have been simulated: 2% and 0.4%. The former 'thick plate' matches the experimental setup and the latter 'thin plate' was trialled for reasons discussed later. The Reynolds number of $2x10^4$ is of the same order of the MRL turbine experimental work ($5x10^4$ based on blade chord and inlet flow velocity), ensuring the applicability of this validation study to the wider context of the work. The chord length and inlet flow velocity has been kept constant throughout, with kinematic viscosity varied to achieve the desired Reynolds number.

The computational mesh was based on the suitable parameter values identified in Chapter 3. However, a significantly finer mesh was also trialled, which confirmed mesh independent results were obtained. The chosen mesh, for both flat plate thicknesses (and also the MRL turbine blade) are shown in Figure 4.3.1. Two time steps, representing $\Delta\alpha = 0.1°$ and $\Delta\alpha = 0.025°$ were trialled; both gave identical results at a number of pitch rates, and therefore the former was used throughout the analysis.

4.3.4 Results

4.3.4.1 Comparison of force coefficients

The lift and drag forces, acting in the z- and x-directions respectively, were recorded and converted into coefficients using Equations 4.2.12 and 4.2.13. These are compared to the experimental and correlation results in Figures 4.3.2, 4.3.3 and 4.3.4, for pitch amplitudes up to $\alpha = 90°$. Figure 4.3.5 shows the same CFD results through to $\alpha = 180°$.

The figures show that in general, the CFD simulation results are similar in profile and magnitude to the experimental results, for both lift and drag forces. However, the success of the simulations does vary considerably with angle of attack and reduced frequency, and also thickness of plate. Following is a brief discussion of the key observations:

K=0.03-0.1

Figure 4.3.2 shows the simulation and experimental results are well matched at these lower reduced frequency values, with similar trends observed through the range of $0° < \alpha < 90°$. This is particularly true for lift coefficient, where the CFD results follow a similar initial gradient. It also captures the fluctuating behaviour at $K = 0.03 - 0.05$ and the single peaked profile at $K = 0.1$. However, the peak lift is over-predicted in each case, by approximately 23%, 10% and 7% respectively (for the thick plate). The location of the initial peak also lags the experimental results by approximately 5°. The behaviour after the initial peak location is generally well predicted, with secondary lift peaks occurring for $K = 0.03 - 0.05$ (although the magnitudes are significantly over-predicted) and a steady decrease for $K = 0.1$.

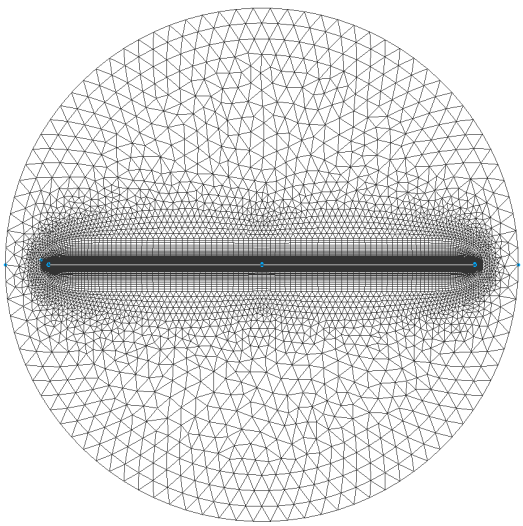

(a) Thin flat plate

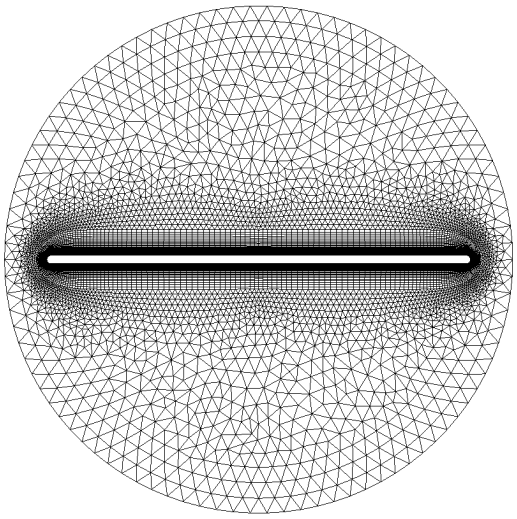

(b) Thick flat plate

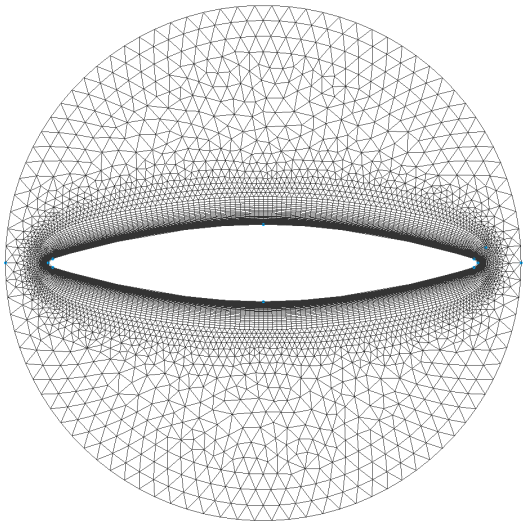

(c) MRL blade

Figure 4.3.1: Mesh regions for three profiles used in the simulation of a single plate/blade

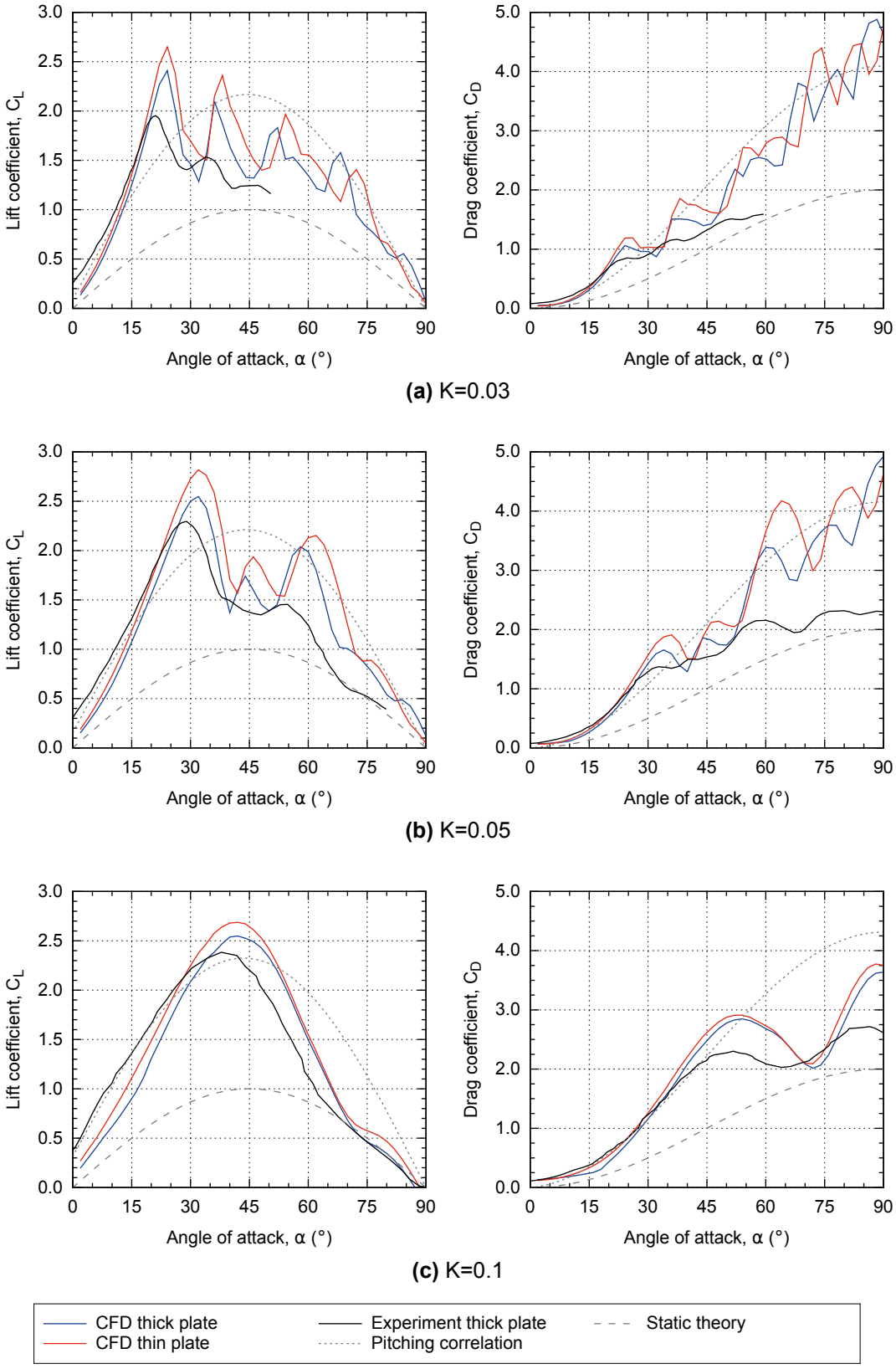

Figure 4.3.2: Comparison of CFD, experimental and correlation results (from Granlund et al. (2013)) for the variation of lift and drag coefficients with angle of attack for a pitching flat plate ($K = 0.03 - 0.1$)

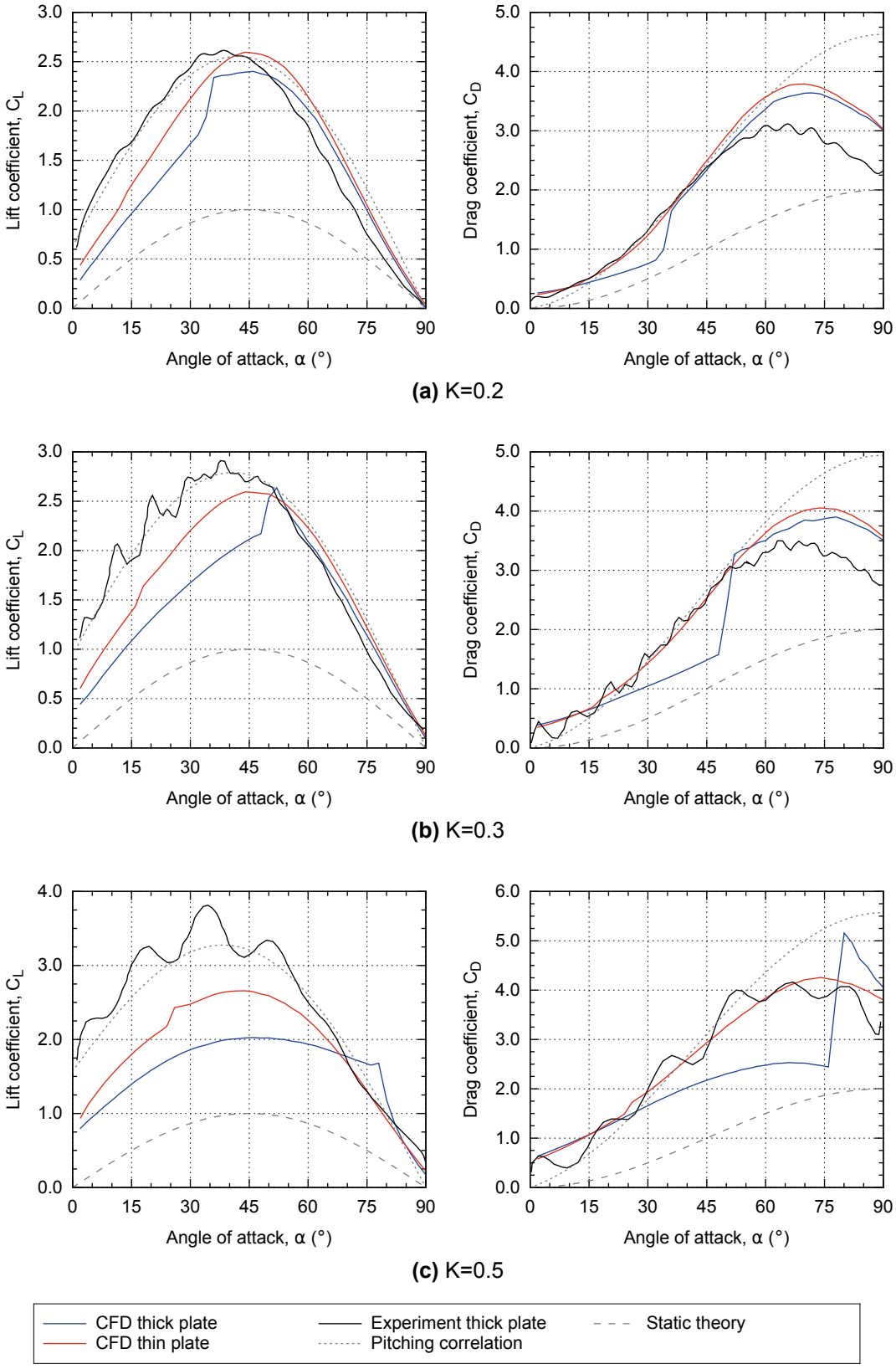

Figure 4.3.3: Comparison of CFD, experimental and correlation results (from Granlund et al. (2013)) for the variation of lift and drag coefficients with angle of attack for a pitching flat plate ($K = 0.2 - 0.5$)

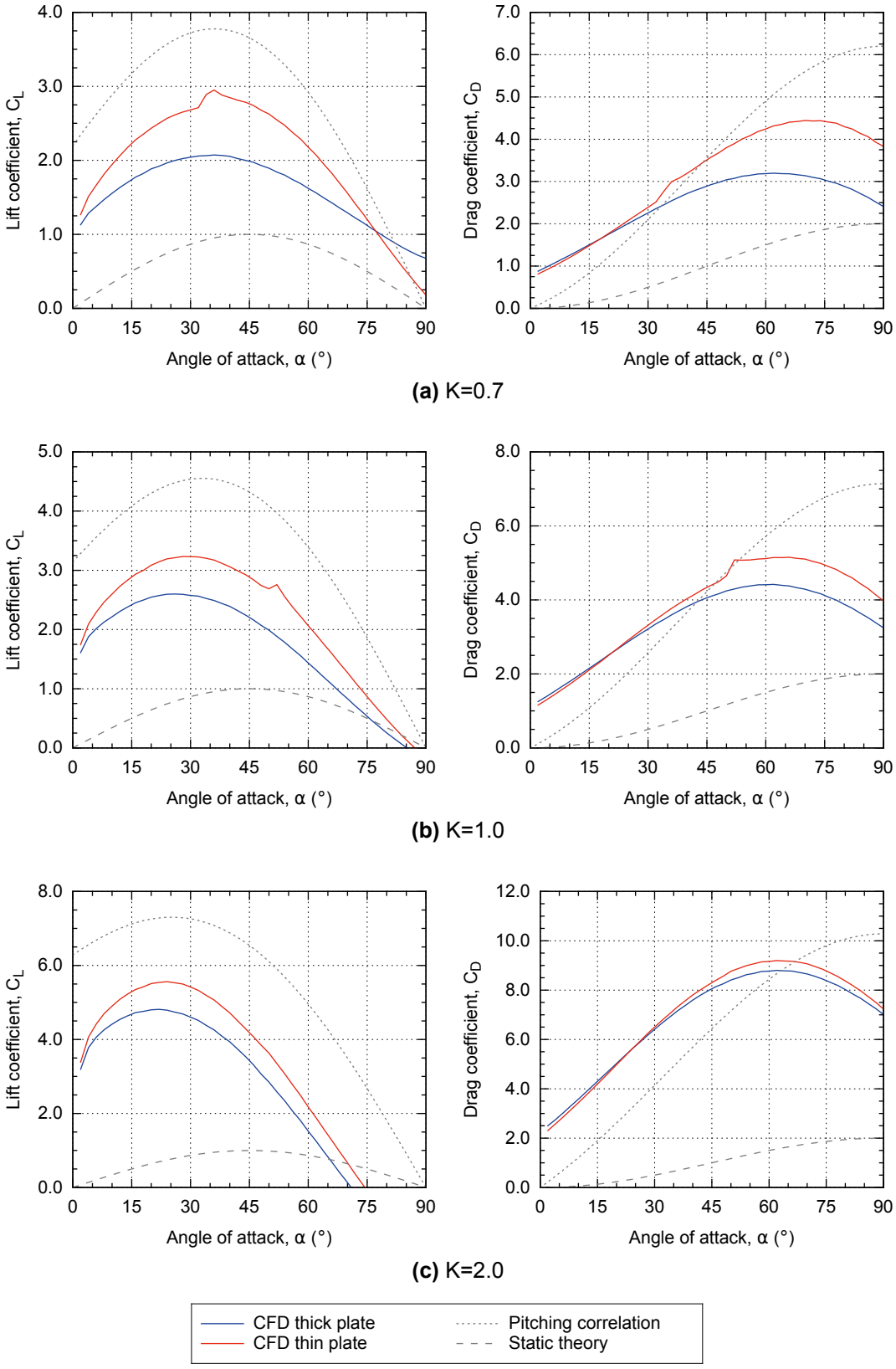

Figure 4.3.4: Comparison of CFD, experimental and correlation results (from Granlund et al. (2013)) for the variation of lift and drag coefficients with angle of attack for a pitching flat plate ($K = 0.7 - 2.0$)

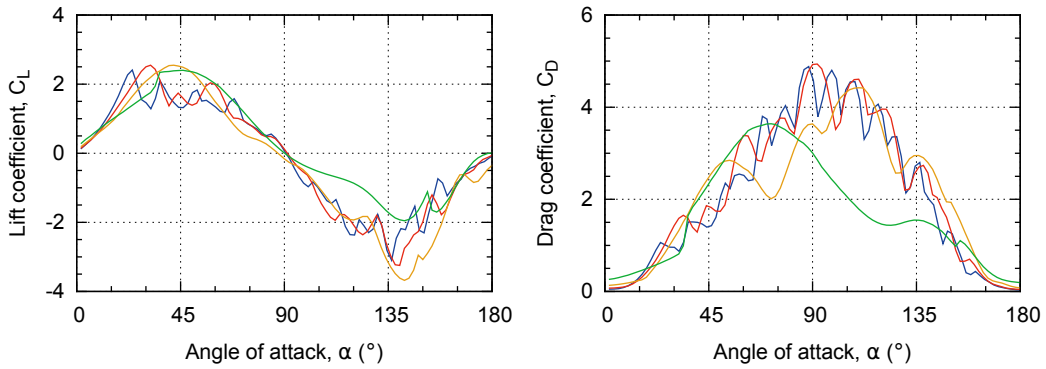

(a) $K = 0.03 - 0.2$

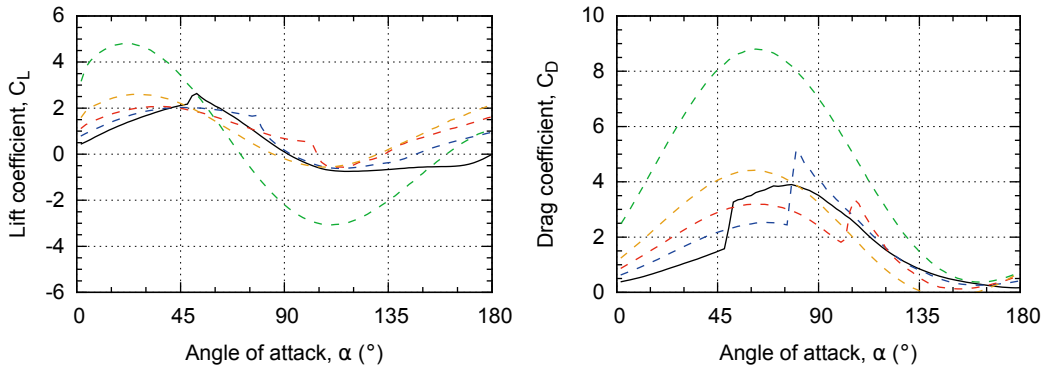

(b) $K = 0.3 - 2.0$

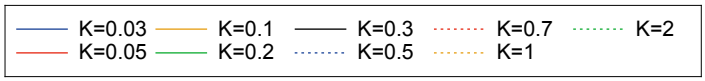

Figure 4.3.5: Comparison of CFD results showing the variation of lift and drag coefficients with angle of attack

The drag coefficient results are well matched up to approximately $\alpha = 45°$, with a well predicted initial gradient before fluctuating behaviour occurs. Results for $K = 0.1$ capture the two peaks that occur at higher pitch angles, although the drag coefficient at the initial peak is over predicted by approximately 24%, and the drag at $\alpha = 90°$ by 38%. At the two lower values of K, the CFD results diverge to an even greater extent at higher angles of attack, with a final over prediction of approximately 120% for $K = 0.05$. The trend at $K = 0.03$ appears to be similar, although experimental results are only available up to $\alpha = 60°$.

At these values of K, the CFD results are similar for both simulated plate thicknesses, indicating the thickness is not having a large effect on the flow mechanisms that are responsible for the behaviour discussed above. However, the thin plate initial peak values are approximately 10% higher than the corresponding thick plate values, although the angle of attack of peak lift and drag remains the same. Secondary peaks are further affected, with both higher magnitudes and angles of attack for the thin plate results.

K=0.2-0.5

Figure 4.3.3 shows the profiles of the thin plate CFD results generally match well to the experimental results for both lift and drag coefficients, whilst the thick plate CFD results show major deviations. This effect becomes more pronounced as K increases, with sudden jumps or spikes appearing at progressively higher angles of attack. Before these jumps appear, the lift and drag values are suppressed, but then return to similar values as the thin plate results. The flow structure underpinning these observations are discussed in section 4.3.4.2.

Focusing on the thin plate results only, it can be seen that the CFD and experimental lift results become less well matched as K increases. The opposite is true for the drag coefficient results. The CFD lift results are consistently lower than experimental results through the initial 45° of rotation, but tend to be better matched in the second 45°. At $K = 0.2$ the peak lift coefficients are equal, although the CFD results lag by approximately 7°, and the drag coefficient peak and final values are over predicted by approximately 33%. In contrast, at $K = 0.5$ the peak lift is under predicted by 40%, whilst the peak drag coefficient is within 9% of the experimental result.

K=0.7-2.0

At the final three K values simulated, there were no available experimental results, although the computational results can still be compared to correlation predictions. For values of $K = 0.03 - 0.5$ discussed above, it can be seen that the correlations are able to predict the experimental results with varying degrees of success. In general, as K has increased, the reliability of both the lift and drag coefficient correlations has improved. This includes the increase in initial lift coefficient observed at $\alpha = 0°$, although the drag correlation always fails to match the reduction seen in experimental results at higher angles of attack ($\alpha > 60°$). If the same trend continues, it can be assumed that the correlations would be well matched to experimental results in the range $K = 0.7 - 2.0$, apart from an over prediction of drag at $\alpha > 60°$.

Figure 4.3.4 therefore shows that the CFD results continue to under predict the lift coefficient with increasing values of K. The drag coefficient results also appear to be over predicted at lower angles of attack, but this may not be the case; Figure 4.3.3 also shows the drag coefficient value at $\alpha = 0°$ increases with increasing values of K, for both CFD and experimental results. Therefore the CFD results are considered more reliable than the correlation curve in this situation.

When comparing the two thicknesses of plate, the results again show a significant difference for both lift and drag magnitudes. The thick plate results are lower in value than the thin plate results, but there are no sharp jumps or spikes, and the profiles are similar in shape throughout. As K increases the two sets of results become more similar in magnitude.

4.3.4.2 Visualisation of flow

To aid understanding of the flow structure around the pitching plates, the vorticity has been calculated from the simulation results, as shown in Figures 4.3.6, 4.3.7, 4.3.8 and 4.3.9. The results are shown for pitch angles increments of 15° in the range $15° \leq \alpha \leq 180°$ and at eight values of constant reduced frequency.

The vorticity is calculated as the curl of the velocity vector and describes the local rotating motion at a point in the fluid. This can be understood as the motion that is superimposed onto the steady velocity field, in order to describe

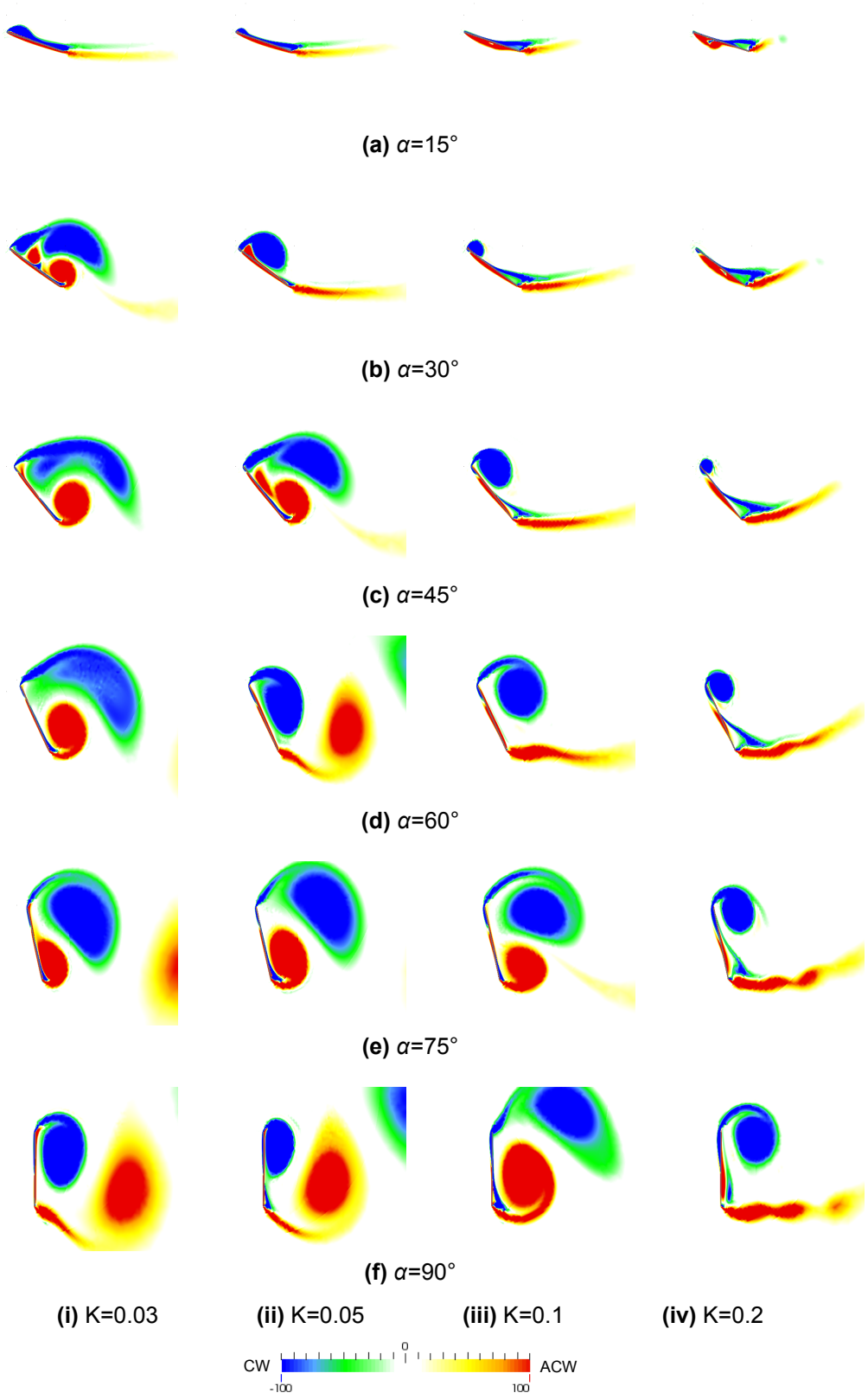

Figure 4.3.6: Contour plots showing vorticity about y-axis for a flat plate (2% thickness ratio) pitching about its mid chord ($0.03 \leq K \leq 0.2$, $15° \leq \alpha \leq 90°$)

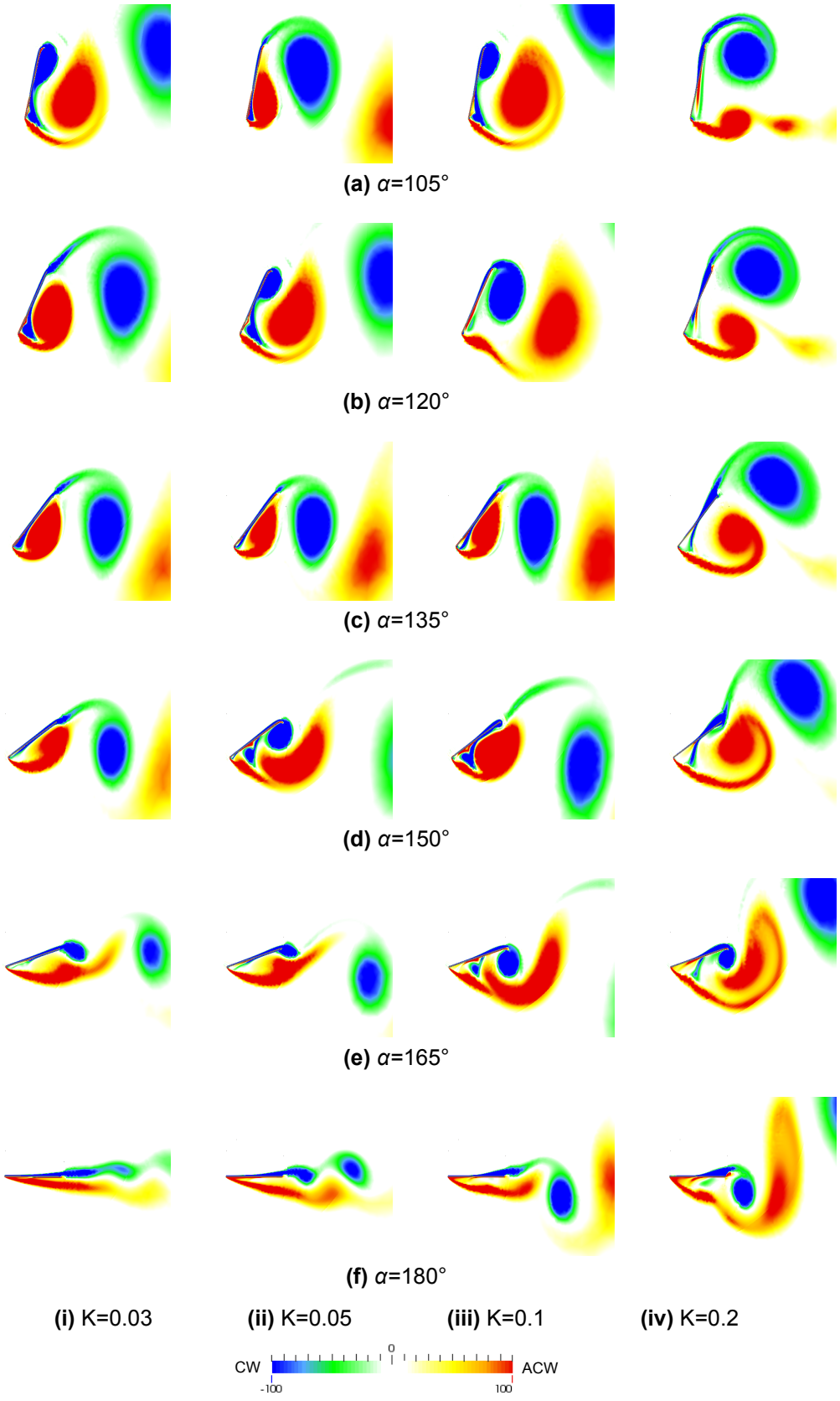

Figure 4.3.7: Contour plots showing vorticity about y-axis for a flat plate (2% thickness ratio) pitching about its mid chord ($0.03 \leq K \leq 0.2$, $105° \leq \alpha \leq 180°$)

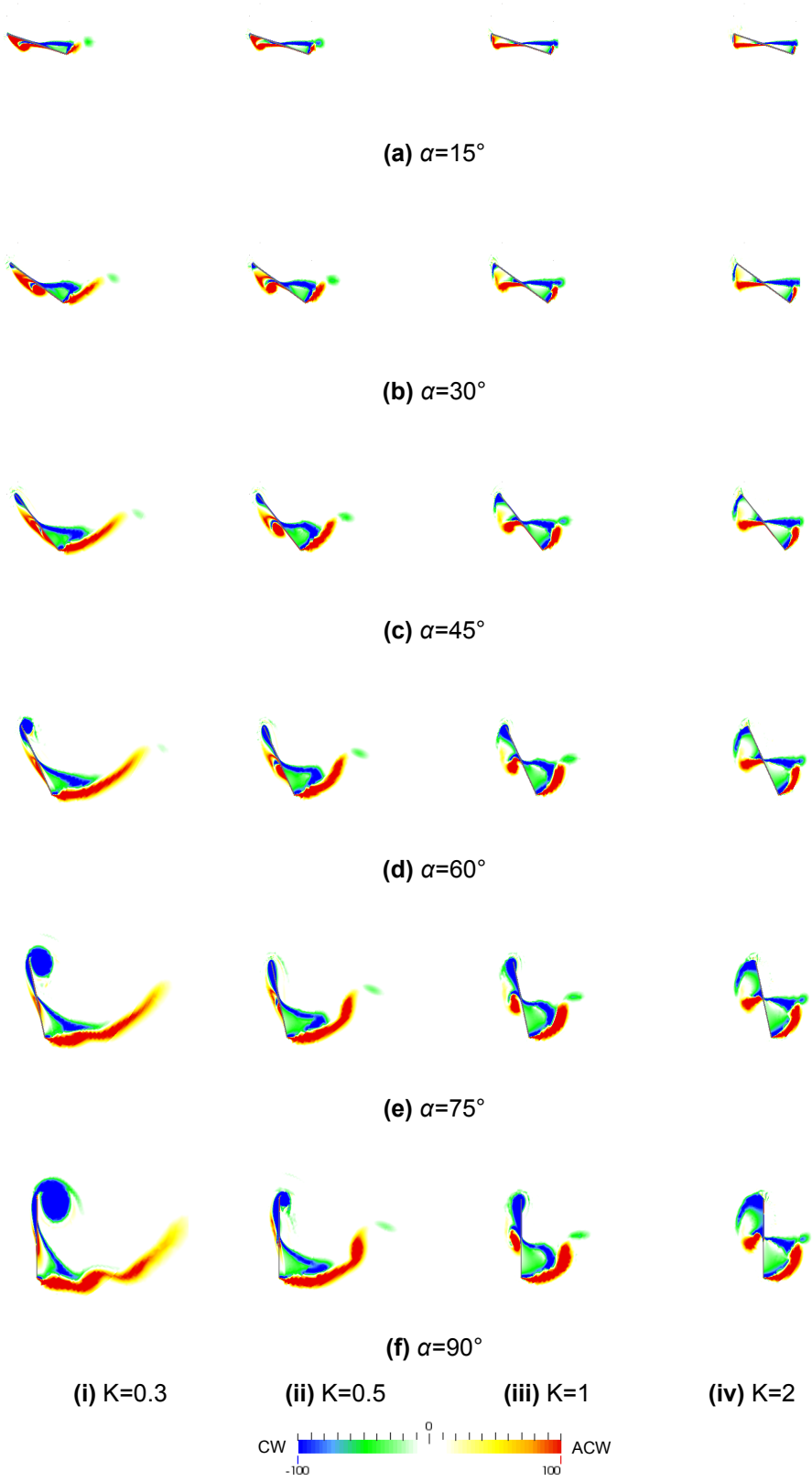

Figure 4.3.8: Contour plots showing vorticity about y-axis for a flat plate (2% thickness ratio) pitching about its mid chord ($0.3 \leq K \leq 2$, $15° \leq \alpha \leq 90°$)

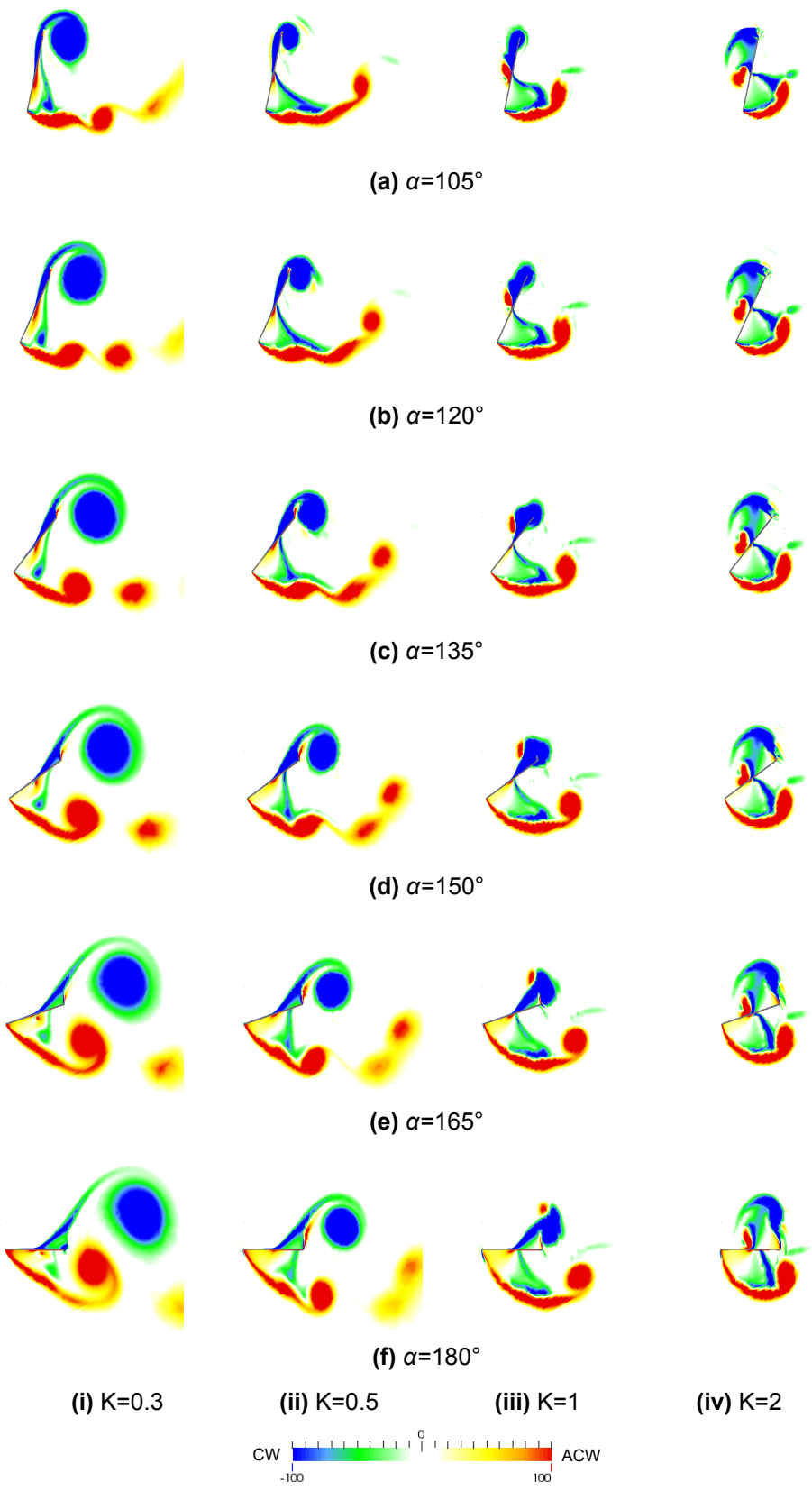

Figure 4.3.9: Contour plots showing vorticity about y-axis for a flat plate (2% thickness ratio) pitching about its mid chord ($0.3 \leq K \leq 2$, $105° \leq \alpha \leq 180°$)

the acceleration of flow about the tips of plate or foil. The highest velocity, and therefore lowest static pressure occurs at the core. If a region of vorticity is closely attached to the downstream face of a pitching plate, the pressure differential across the plate creates a strong lift and/or drag force, depending on the angle of attack. When the vorticity no longer remains attached to the surface, it is 'shed', and a corresponding reduction in force occurs.

The results show a series of leading edge vorticity (LEV) and trailing edge vorticity (TEV) regions being formed and shed from the plate as it rotates. Note, the leading edge is taken as the upwind tip (with an acute angle of attack) in each quarter cycle, and the trailing edge is the downwind tip. The leading and trailing edges therefore swap position at $\alpha = 90°$. In the first half cycle, LEV regions rotate in a clockwise (CW) direction, as shown in blue and TEV regions are anti-clockwise (ACW), as shown in red. In the second half cycle, the rotational directions of LEV and TEV regions are reversed. Below is a discussion of some key observations drawn from the results:

$0° < \alpha < 90°$

As the plates pitch from $\alpha = 0°$, an area of LEV forms, which accounts for the initial increase in lift and drag. When this vorticity is shed, a sudden reduction in force occurs. For example, this occurs in the region of $15° < \alpha < 30°$ at $K = 0.03$, $30° < \alpha < 45°$ at $K = 0.05$ and $45° < \alpha < 60°$ at $K = 0.1$. These values correspond to the initial peaks in lift and drag shown in Figure 4.3.2. At these low values of K an attached region of TEV then forms, which contributes to second peaks in lift and drag force. At $K = 0.03$ and 0.05, further regions of LEV and TEV also form before $\alpha = 90°$. However, as discussed previously, the drag forces at these high angles of attack are greatly over-predicted, indicated the predicted intensity of these vorticity regions is too high.

Lower pitch rates tends to produce larger, more intense regions of shed vorticity at the leading edge tip, in the range $0° < \alpha < 90°$. Here the relative flow velocity past the tip is greater than at higher K values, as the tangential tip speed is lower (the tip is moving away from the incoming flow). Also, the size of attached LEV and TEV regions is similar at lower values of K, as the relative flow velocities at the leading and trailing tips are close in magnitude.

As K increases to $0.2-0.5$, the relative velocity past the leading edge decreases in magnitude, and the relative velocity increases at the trailing tip (which is

moving towards the flow). This tends to produce attached LEV regions with slower growth and continuous streams of TEV that are not attached to the plate. This results in a single shed vortex in the first quarter rotation, and a single peak in the lift and drag curves.

At $K \geq 1$, the plate tangential tip speed is at least equal to the incoming flow velocity. The LEV regions are left as a wake trail upstream of the leading tip, and a trail of TEV is continuously shed from the opposite tip.

The sudden jumps observed in some force curves can be explained by comparing the vorticity visualisation for 0.4% and 2% thick plates. For example, Figure 4.3.10 shows the plates at $\alpha = 45°$ and 60° when pitching at $K = 0.3$. At the earlier pitch angle an area of attached LEV has visibly formed downstream of the thinner plate and continues to grow gradually as α increases. However, for the thicker plate the downstream LEV region is not apparent, although the flow around the remainder of the plate appears identical. This has the effect of suppressing the lift and drag forces acting on the plate. The LEV region then forms very suddenly at approximately $\alpha = 50°$ and continues to grow gradually. This suddenly brings the lift and drag forces to approximately the same values for both plates at $\alpha = 60°$. As this behaviour does not match well to the experimental validation data, it is not considered to be an accurate representation of physical behaviour.

$90° < \alpha < 180°$

As the plate continues to pitch from $\alpha = 90°$, all simulations with $K \leq 0.5$ show a large area of vorticity being shed from the uppermost tip (which has now swapped to become the trailing edge). From this point on-wards, a series of attached LEV and TEV regions form and shed downstream. At $K = 0.03 - 0.05$ this leads to lift and drag profiles that are approximately the reverse of the first quarter rotation, with similar magnitude peaks (see Figure 4.3.5).

However, as K increases, the force profiles vary to an increasing extent in comparison to the first 90° of rotation. The relative velocity at the leading edge is no longer similar to that of the first quarter rotation and therefore the flow field is no longer similar. The relative leading edge velocity is greater in magnitude (as it is now moving towards the incoming flow) and this generally leads to a stream of LEV shed from the tip, rather than formation of a surface-attached region. Therefore the maximum force magnitudes in the second quarter of

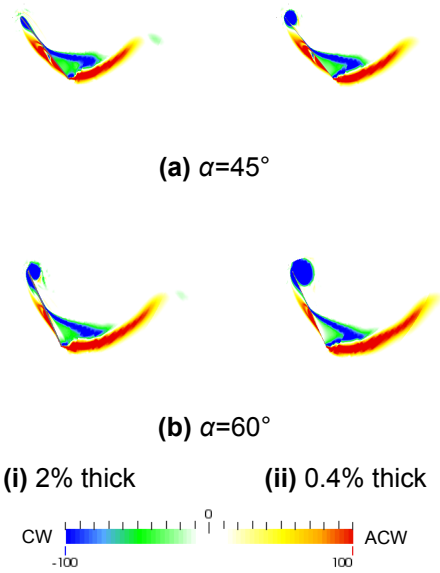

Figure 4.3.10: Contour plots showing vorticity about y-axis for a flat plate (2% and 0.4% thickness ratio) pitching about its mid chord ($K = 0.3$, $45° \leq \alpha \leq 60°$)

rotation are reduced in comparison to the first. For example, at $K = 0.3$ the maximum lift coefficient is $|C_L| = 2.7$ in the first quarter, but only $|C_L| = 0.7$ in the second.

4.3.5 Conclusion of section

This section has identified a suitable pitching plate test case for which CFD simulations have been presented and compared to published experimental results. The results have been compared quantitatively using force coefficient profiles, and vorticity plots have also provided a qualitative insight into the flow structure formed. The key observations are as follows:

- A series of leading and trailing edge vorticity regions form as the plate angle of attack increases. Attached vorticity regions correspond to increasing lift and drag forces. When the vorticity sheds, sudden reductions in lift and drag occur.
- The CFD simulations are more successful at predicting physically accurate behaviour at lower values of K, when focusing on lower angles of attack (where lift is dominant). In contrast, the behaviour at higher

angles of attack (approaching $\alpha = 90°$, where drag is dominant) is better predicted as values of K increase.

- The simulations of 2% thick plates (matching the published experimental setup) introduce sudden jumps or spikes in the force coefficient profiles when $0.2 \leq K \leq 0.5$. This behaviour does not appear in the simulation of a 0.4% thick plate. In the latter case the results are better matched to experimental data and the vorticity plots show this behaviour is the results of sudden, rather than gradual, leading edge vorticity formation. The former is not considered to be physically accurate behaviour.
- The peak magnitudes of lift coefficient are similar, or greater, in the second quarter of rotation for $K \leq 0.1$. At higher reduced frequencies the second quarter peak magnitudes are lower. This is because of the difference in relative velocity at the leading edge tip, from the first quarter rotation to the second, and the effect increases in strength with increasing reduced frequency.

4.4 Simulation of a Single Plate and Blade

4.4.1 Aim of section

This section presents a CFD study of the flow about a single blade undergoing MRL motion. The results are analysed quantitatively with time-dependent force and torque values and qualitatively with visualisation of the flow structure. Both a flat plate and the MRL blade profile are investigated. The objective is to gain an understanding of the flow formed around the blades, how this varies with rotor angle and BSR value, and compare the results to those of a simply pitching plate.

4.4.2 Approach

The parameters presented in Table 4.4.1 have been used to simulate a single flat plate and MRL blade profile. To achieve this, rotors 2 and 3 (as described in Chapter 3) were replaced with simple mesh regions of consistent cell size, with no blade profiles included. The domain size, mesh and angular time-step

Table 4.4.1: Single blade simulation parameter values

Parameter	n	c	R_b	u_{inlet}	Ti	TVR	Mesh	$\Delta\theta$	x_{max}/D
	(-)	(m)	(m)	(m/s)	(%)	(-)	(-)	(°)	(-)
Value	1	0.05	0.055	1.0	1.0	150	As Test 22	0.5	10

used were those previously selected in section 3.4. The simulations were run for a range of BSR values from 0.2 to 0.9, in increments of 0.1.

Two variations of the flat plate were simulated. Firstly the thin flat plate with a thickness ratio of 0.4% and secondly the thick flat plate with thickness ratio of 2%. The width of the latter is also equal to the MRL model blade tip ($1\,mm$). Thirdly, the MRL blade was simulated with a maximum thickness ratio of 18%, giving a centre-chord thickness of $9\,mm$. The purpose of this choice was to allow separate analysis of thickness and profile effects. Note, the mesh regions for the three profiles were previously shown in Figure 4.3.1.

The simulations were run for a number of turbine cycles until periodically repeating results were obtained. The forces acting on the blade, due to pressure and viscous effects, have been converted into torque acting about the turbine central axis. The presented results represent the final cycle of the simulation, and are qualitatively identical to the previous cycle (the cycle-mean torque typically varied by less then 0.05% between cycles).

4.4.3 Results

4.4.3.1 Torque variation

Figure 4.4.1 shows the variation, over a single cycle, of torque acting about the turbine central axis due to the forces acting on a single MRL blade, at various values of BSR.

Generally the graphs show the profile of torque variation through a turbine rotation is similar for all *BSR* values and blade profiles, with a major peak torque occurring in each half cycle. At $\theta = 0°$ the torque is approximately negative 0.3-0.5 Nm at all *BSR* values, due to parasitic drag acting against the direction of the blade motion. The torque begins to increase with increasing turbine angle, following a consistent gradient until peak torque of approximately 6.5-7.0 Nm

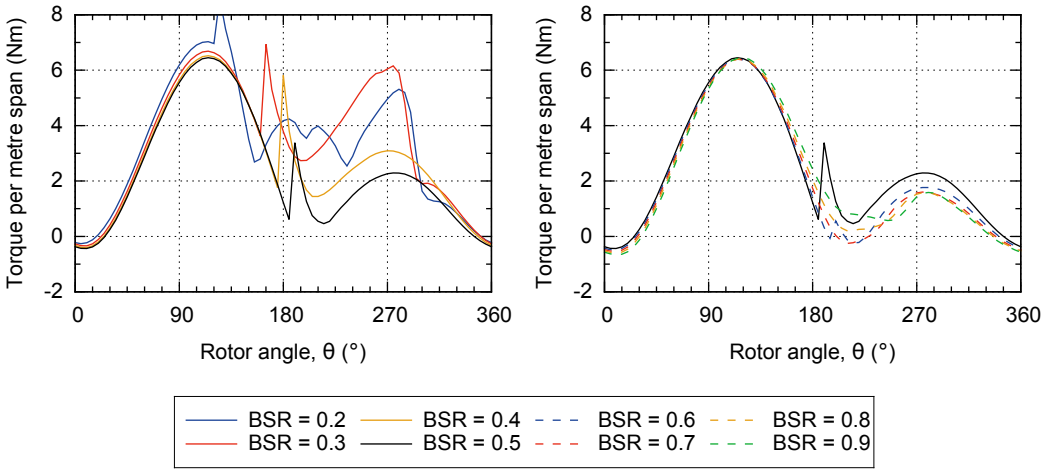

Figure 4.4.1: Variation of output torque generated by a single MRL blade, comparing the effect of BSR value

occurs in the range of $\theta = 105 - 120°$. Following this the torque decreases to a mid-cycle minimum; this varies in value and angular position depending upon *BSR* value. For example, at $BSR = 0.2$ a minimum of approximately 2.7 Nm occurs at $\theta = 155°$, and at $BSR = 0.5$ a minimum of approximately 0.4 Nm occurs at $\theta = 215°$. At higher values of *BSR* the minimum occurs at approximately the same angular position, with values in the range of $-0.25 - 0.7\,Nm$.

The torque profiles up to this point are further complicated by the appearance of sharp spikes that occur for *BSR* values in the range of 0.2-0.6. At lower *BSR* values the spike appears earlier in the cycle and vice versa, from $\theta = 120°$ at $BSR = 0.2$ to $\theta = 190°$ at $BSR = 0.6$. These appear to be similar to the sudden jumps in force observed in the thick plate results of section 4.3.4; this is discussed further in section 4.4.3.3.

Following the mid-cycle minimum, the torque increases to a second maximum that occurs in the range of $\theta = 270° - 285°$ at all BSR values. Unlike the first peak, the magnitude of the second peak varies greatly depending upon *BSR* value, with lower peak torque occurring as *BSR* is increased (this also corresponds to the lower mid-cycle minimum values at higher *BSR* values). For example, at $BSR = 0.3$ the second peak is approximately 6.0 Nm and at $BSR = 0.7$ it is 1.6 Nm.

The exception to the general profile shape described above is $BSR = 0.2$, which shows an extra two smaller-amplitude peaks centred at $\theta = 200°$. The final peak then has a lower magnitude than that of $BSR = 0.3$. Following the

Table 4.4.2: Percentage difference in single blade mean torque, in comparison to 0.4% thickness flat plate simulation

BSR	2% thick plate	MRL blade
$(-)$	$(\%)$	
0.2	+5.9	+5.6
0.3	-3.9	-3.4
0.4	-20.0	-16.7
0.5	-10.0	-9.0
0.6	-4.7	-6.4
0.7	-3.4	-1.6
0.8	+0.4	+2.5
0.9	+2.0	+3.6

final torque peak, the curves all follow a similar gradient from $\theta = 300°$ onwards, back to the initial value.

Figure 4.4.2 presents the same results as described above, but additionally compares the effect of plate thickness and profile, at six different *BSR* values. This allows a more direct comparison to the work undertaken in Section 4.3. Figure 4.4.3 also presents the variation of cycle-average torque with BSR, for the three plate/blade profiles. Table 4.4.2 gives the percentage variation between these results at each BSR value.

The results show that at the majority of BSR values, the average torque between blade profiles varies by less than 10%. The exception is $BSR = 0.4$, where the results differ by up to 20%. The time varying torque profiles are also very similar, although notable variation exists at $BSR = 0.2$ and 0.4, as discussed in the following paragraphs.

$BSR = 0.7$ and 0.9: At these *BSR* values the three profiles are very similar throughout the full turbine cycle. One relatively minor variation is the thin plate produces a lower-magnitude parasitic torque at $\theta = 0°$; this is due to the decreased frontal area of the blade compared to the thick plate and blade.

$BSR = 0.5$: The profiles follow the same general shape, although the sudden torque spikes are only present for the thick plate and blade. This is consistent with the pitching flat plate CFD results, and suggests the spikes are not phys-

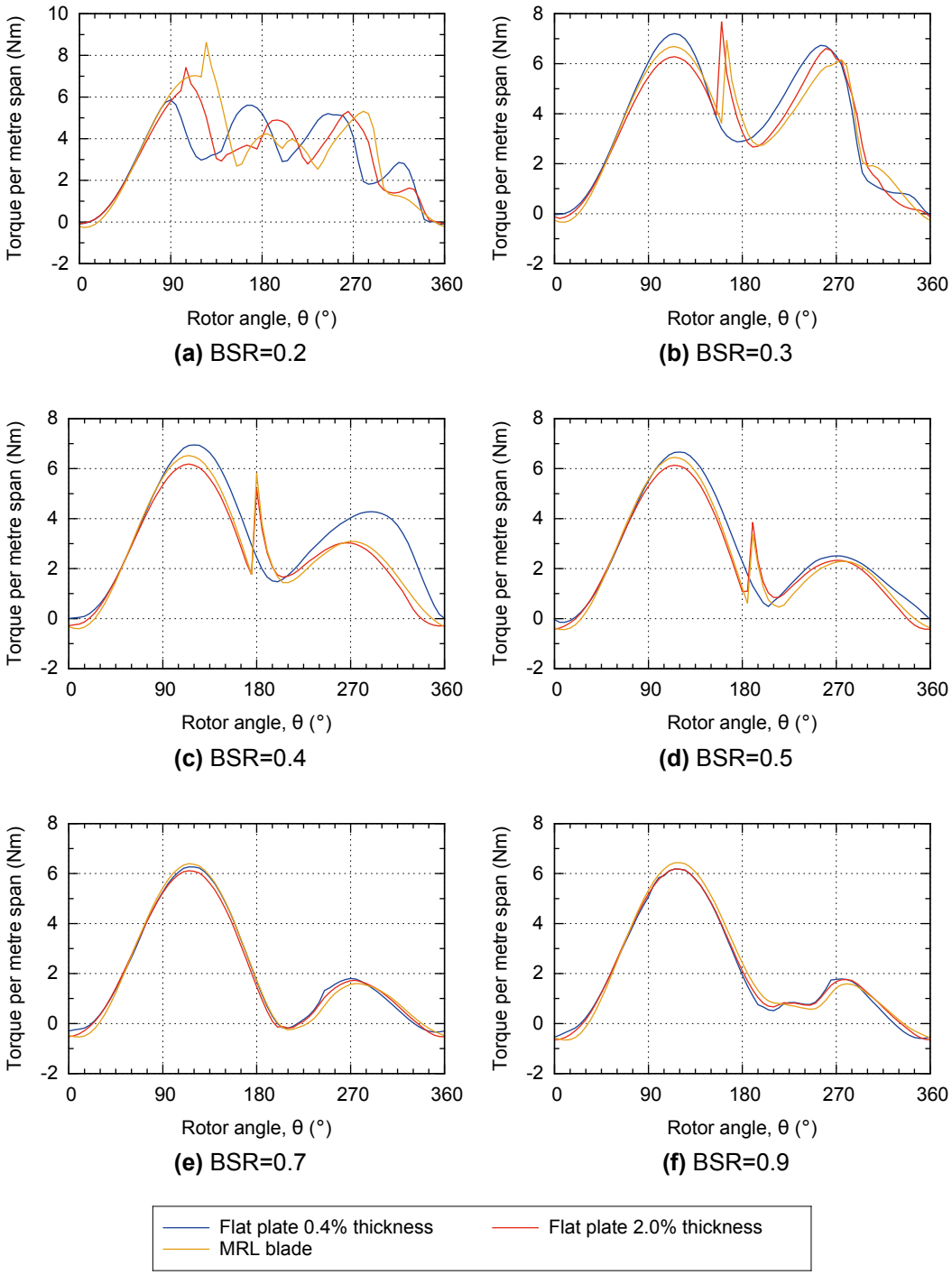

Figure 4.4.2: Variation of output torque over a single MRL cycle, comparing the effect of blade profile at specific BSR values

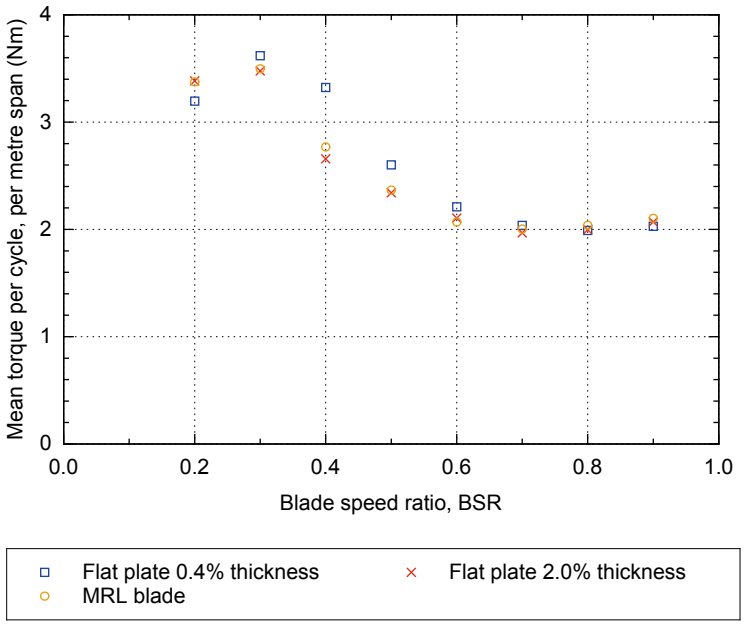

Figure 4.4.3: Variation of mean output torque with BSR value, comparing three blade profiles

ically accurate. The thin flat plate peak is 10% and 5% higher than the thick plate and blade results respectively, and also lags by approximately 10°.

$BSR = 0.4$: Similar to discussed above, the profiles follow the same general shape, although the sudden torque spikes are only present for the thick plate and blade. The thin flat plate initial peak is 13% higher than the thick plate result and the corresponding second peak is 40% higher. This accounts for the 20% difference in average torque seen at this *BSR* value.

$BSR = 0.3$: The magnitudes of both peaks differ by up to 16% and the thin plate results lead the blade results by up to 15° in the second half cycle.

$BSR = 0.2$: The results for the three plate/blade profiles are the most varied from each other. They all produce five main torque peaks through the full turbine cycle, but with significant differences in magnitude and angular position. The initial peak moves to higher magnitudes and angular position as the profile changes from thin plate to MRL blade, and the small sharp peak also appears. From this position on-wards the MRL blade results lag the flat plate results by approximately 5-10°.

4.4.3.2 Force variation

Figure 4.4.4 shows the variation, over a single cycle, of forces acting in both the x- and z-directions, at various values of BSR.

The graphs show how force acting in the x-direction, F_x, and z-direction, F_z, follow a similar profile of a single peak (in terms of magnitude) in each half-cycle. However, F_x acts in the positive direction throughout the cycle, whereas F_z swaps from positive to negative direction. This means that F_x negatively contributes to torque in the first and fourth quarter-cycles, and positively contributes in the second and third quarter-cycles. In contrast, F_z generally positively contributes to torque throughout the complete cycle.

As with the torque results, the simulated force results are significantly affected by the blade profile. The variations between curves is generally more significant for F_x than F_z, with greater magnitude of variation at lower values of *BSR*. The largest discrepancies in F_x generally occur near $\theta = 90 - 120°$, where the contribution to torque is relatively low (e.g. the contribution is zero at $\theta = 90°$). However, at this angular location, F_z is at or near a maximum with values well matched for all profiles. For this reason the large variations in x-direction force do not entirely translate into large variations in driving torque.

In one case, $BSR = 0.4$, there is a large discrepancy between the thin flat plate results and the other two profiles, for both F_x and F_z in the second half-cycle. This corresponds to the large difference in torque seen in the torque results for this *BSR* value. The reasons for these variations, between profiles and BSR values, are discussed in the following sub-section.

4.4.3.3 Vorticity visualisation

Visualisation of vorticity contour plots give an insight into the simulated flow structure formed as the blade position progresses, and aids further analysis of the associated force and torque profiles. The following is a discussion of the results, for a number of key *BSR* values, with reference to flow visualisation and analysis presented previously in sections 4.2 and 4.3.

BSR=0.2: Comparison between plate and blade results

The torque profiles at $BSR = 0.2$ (see Figure 4.4.2a) are the most varied

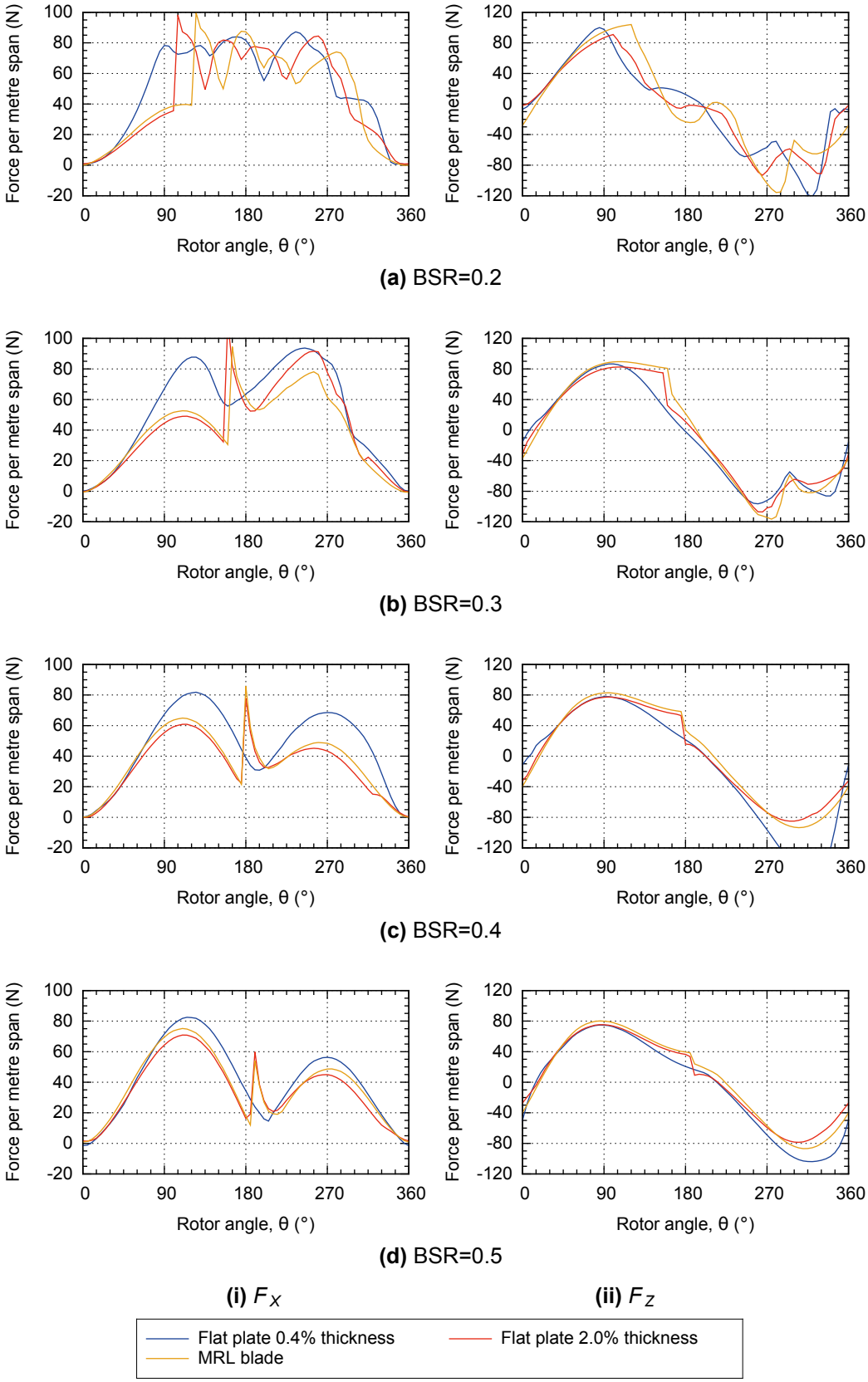

Figure 4.4.4: Variation of x- and z-direction forces acting on a single blade over a single MRL cycle, comparing the effect of blade profile at specific BSR values

from each other; therefore, vorticity contours for both the flat plate and MRL blade are of particular interest, as shown in Figure 4.4.5. Comparison of these results gives further insight into the differences between the respective torque profiles.

The thin flat plate torque reaches a first maximum of 5.8 Nm at $\theta = 90°$, after which the torque decreases to a local minimum of 3.0 Nm at approximately $\theta = 120°$. A gradual increase in torque follows until $\theta = 140°$, before a higher gradient rise until a peak of 5.6 Nm at $\theta = 170°$.

In comparison, the MRL blade torque reaches a first peak of 7.0 Nm at $\theta = 120°$, after which the torque decreases to a local minimum of 1.8 Nm at approximately $\theta = 150°$. A second peak of 4.2 Nm occurs at $\theta = 180°$ and a third peak of 4.0 Nm occurs at $\theta = 210°$.

The vorticity visualisations show the above behaviour correlates to the same series of LEV and TEV formation and shedding, but at different angular positions. For example, the flat plate results show the first peak coincides with the shedding of a LEV region that gradually grows from $\theta = 0°$. In contrast, the blade results show the LEV region does not grow gradually, but suddenly forms and sheds in the region of $120° < \alpha < 150°$, which corresponds to the sharp spike in the torque curve. The slight increase in torque at $\theta = 140°$ for the flat plate, and the peak at $\theta = 180°$ for the blade, both correspond to the formation and shedding of a TEV region. Likewise, the third peaks correspond to LEV formation (at $\theta = 170°$ for the flat plate and $\theta = 210°$ for the blade). In comparison to the flat plate, the blade results show this forms and is shed over a shorter timescale and contributes less to torque production.

In the remainder of the turbine cycle, additional peaks are seen in both the flat plate and blade results. The first peak occurs at $\theta = 240°$ for the flat plate and $\theta = 280°$ for the blade. These correspond to the formation and shedding of LEV regions (now anti-clockwise). The flat plate then shows formation of TEV (now clockwise), which contributes to the flat peak until $\theta = 260°$. The blade results do not show the formation of this TEV, or any further LEV regions, and the torque gradually reduces to approximately zero at $\theta = 360°$. In contrast, a further peak occurs at $\theta = 320°$ in the flat plate results, due to the formation of a final LEV region. This makes a less pronounced contribution to torque than the previous LEV, as force acting in the x-direction produces a negative turbine torque at this angular position.

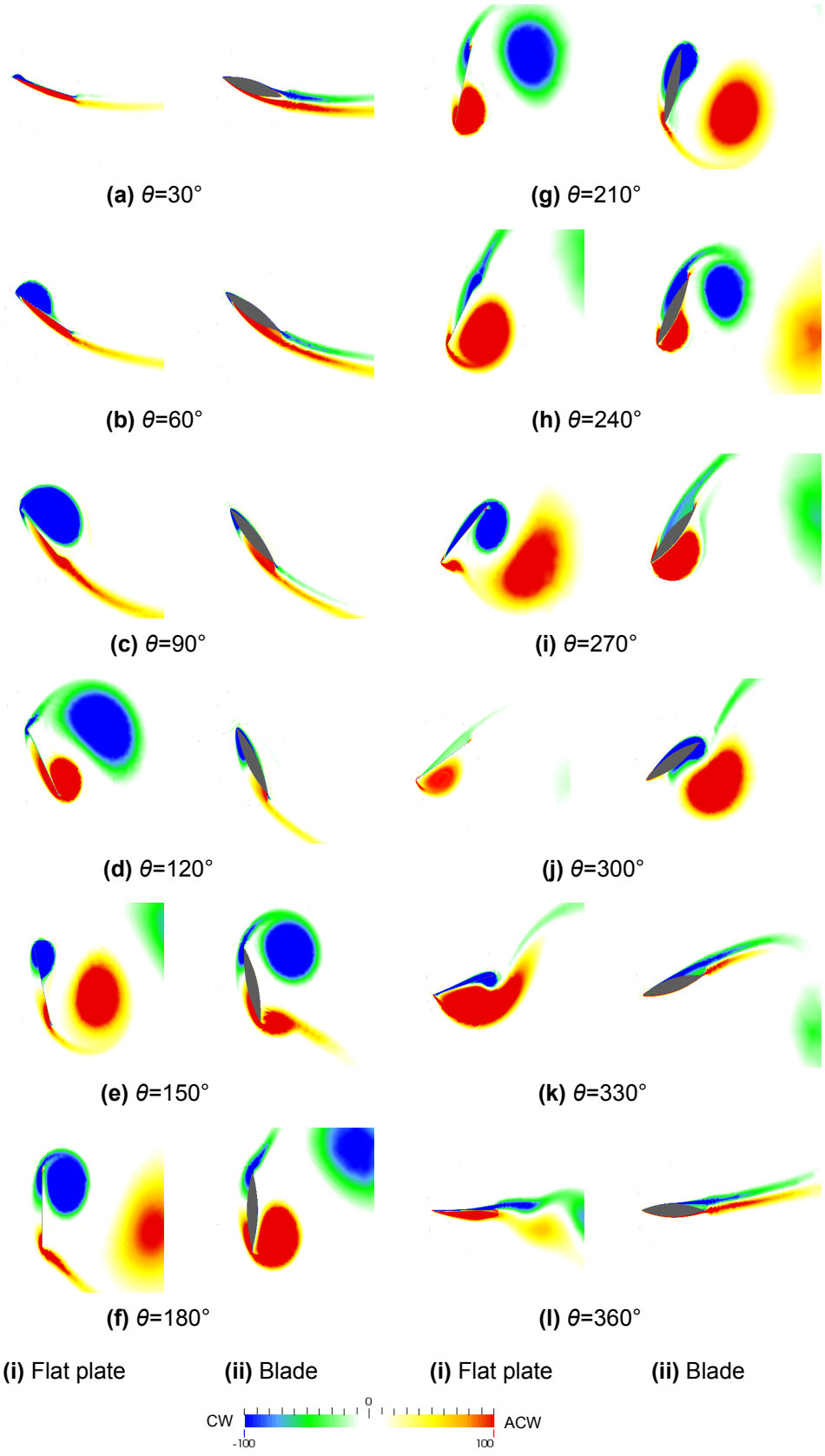

Figure 4.4.5: Contour plots showing vorticity about y-axis for a flat plate (0.4% thickness) and blade undergoing MRL turbine motion ($BSR = 0.2$, $30° \leq \theta \leq 360°$)

BSR=0.2: Comparison to simple pitching plate results

With reference to Figure 4.2.5a ($BSR = 0.2$ curve), the theoretical angle of attack of the turbine blade at $\theta = 90°$ is approximately $\alpha = 35°$, and theoretical reduced frequency is approximately $K = 0.04$ (for an induction factor of $a = 0$). The CFD results for a simply pitching flat plate at $K = 0.05$ (Figure 4.3.2b) shows a peak lift coefficient occurring at approximately $\alpha = 32°$, which suggests that at this BSR value, the flow around the MRL-motion plate is qualitatively similar to a simply pitching plate, for corresponding effective pitch rate and angle of attack. Also note that Figures 4.2.7 and 4.2.8 indicate the relative importance of lift force is $A_{F_L} = 0.98$ at $\theta = 90°$, whilst the relative importance of drag force is only $A_{F_D} = 0.2$. Therefore the sudden reduction in lift strongly affects the torque production at this point.

The flat plate vorticity visualisation results show a flow structure that is qualitatively similar to that of the pitching flat plate (Figure 4.3.6ii), up to $\alpha = 45°$, where a LEV region is formed and shed in the same manner. At the third flat plate peak torque ($\theta = 170°$), the theoretical effective angle of attack is $\alpha = 82°$ and the reduced frequency has reached $K = 0.08$. Figures 4.2.7 and 4.2.8 indicate the relative importance of lift force is $A_{F_L} = 0.2$ at $\theta = 170°$, whilst the relative importance of drag force has reached $A_{F_D} = 0.99$. The drag coefficient is approaching a maximum at $\alpha = 82°$, for both reduced frequencies of $K = 0.05$ and $K = 0.1$, as large TEV regions form and then shed in the range $75° < \alpha < 90°$. However, in contrast to this, Figure 4.4.5 shows a LEV region forms in the range of $150° < \theta < 180°$ for the turbine-motion flat plate. Therefore, although both the MRL-motion plate and the simply pitching flat plate encounter an increase in drag force at this set of effective conditions, the vorticity history cannot be directly compared. This is understandable, given that the theoretical reduced frequency has increased from $K = 0.025$ to 0.08 through the turbine half-cycle.

Following the above observations, an estimation of the accuracy of the turbine torque magnitudes can be made. For example, at $K = 0.05$ the simulated peak lift of the simply pitching plate was overestimated by 10%, in comparison to the validation data. At $K = 0.1$, the drag coefficient was overestimated by 38% at $\alpha = 90°$. It is therefore likely the torque for a single blade in MRL turbine motion is also over predicted by a similar degree at corresponding positions.

In the second half-cycle, the turbine blade angle of attack can be compared to the simply pitching plate in the range of $90° < \alpha < 180°$. At values of $K = 0.03 -$

0.1, the CFD simulations for the pitching plate gave torque results that are very similar to the first quarter rotation (although reversed). This corresponded to similar strength vorticity regions shown in both the up-stroke and down-stroke. This behaviour can also be seen in the $BSR = 0.2$ plate and blade results, where peak torques are relatively even in magnitude throughout the full cycle.

Overall it has been shown that the flow structure around a blade undergoing MRL turbine motion, at $BSR = 0.2$, is complex; the continuously changing angle of attack and reduced frequency lead to a series of vorticity formation and shedding events that contribute to a highly fluctuating torque profile. It has also been shown that the growth and shedding location of the initial vortex is qualitatively comparable to that of a simply pitching flat plate with the same effective angle of attack and reduced frequency conditions. This suggests the induction factor is relatively low at this BSR value, as $a = 0$ predictions are applicable. However, after the first shedding event, and as the reduced frequency of the flat plate increases through the cycle, it is more difficult to find direct comparisons of vortex formation in the simply pitching plate results.

BSR=0.3

Figures 4.4.6 and 4.4.7 show the vorticity contours for flow about a single blade undergoing MRL motion, at increments of $\theta = 30°$, for BSR values in the range 0.3-0.7.

Figure 4.4.2 showed the torque curve for a thin flat plate rotating at $BSR = 0.3$ differs significantly from the $BSR = 0.2$ results, with only two peaks appearing through the cycle, distributed approximately symmetrically about $\theta = 180°$. The results for the two plate thicknesses and blade are also similar throughout, except for the addition of a sharp torque spike at $\theta = 165°$.

Focusing on the MRL blade, the first peak torque of $6.5\,Nm$ is reached at $\theta = 115°$, before a gradual reduction in torque occurs, up to the location of the sharp spike. The flow visualisation in Figure 4.4.6i shows the initial LEV formation is not significant until separation suddenly occurs in the range $150° < \alpha < 180°$.

Figure 4.2.5a ($BSR = 0.3$ curve) indicates that at $\theta = 115°$, the theoretical angle of attack is approximately $\alpha = 40°$, and theoretical reduced frequency is approximately $K = 0.08$. Figures 4.2.7 and 4.2.8 indicate the relative importance of lift force is $A_{F_L} = 1.0$ and the relative importance of drag force is $A_{F_D} = 0.1$. The simply pitching flat plate results (Figure 4.3.2c) show that

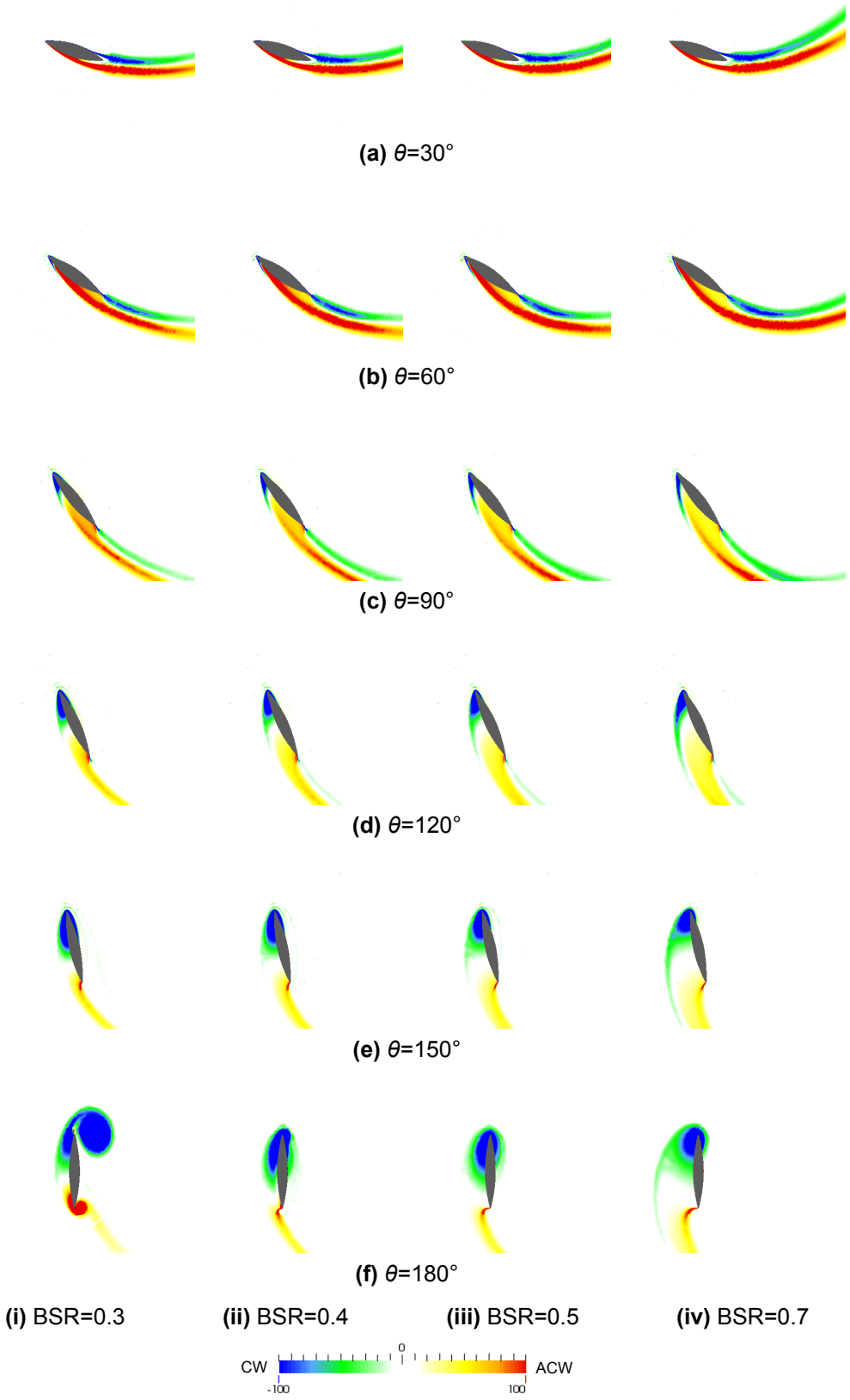

Figure 4.4.6: Contour plots showing vorticity about y-axis for a single blade undergoing MRL turbine motion ($0.3 \leq BSR \leq 0.7$, $30° \leq \theta \leq 180°$)

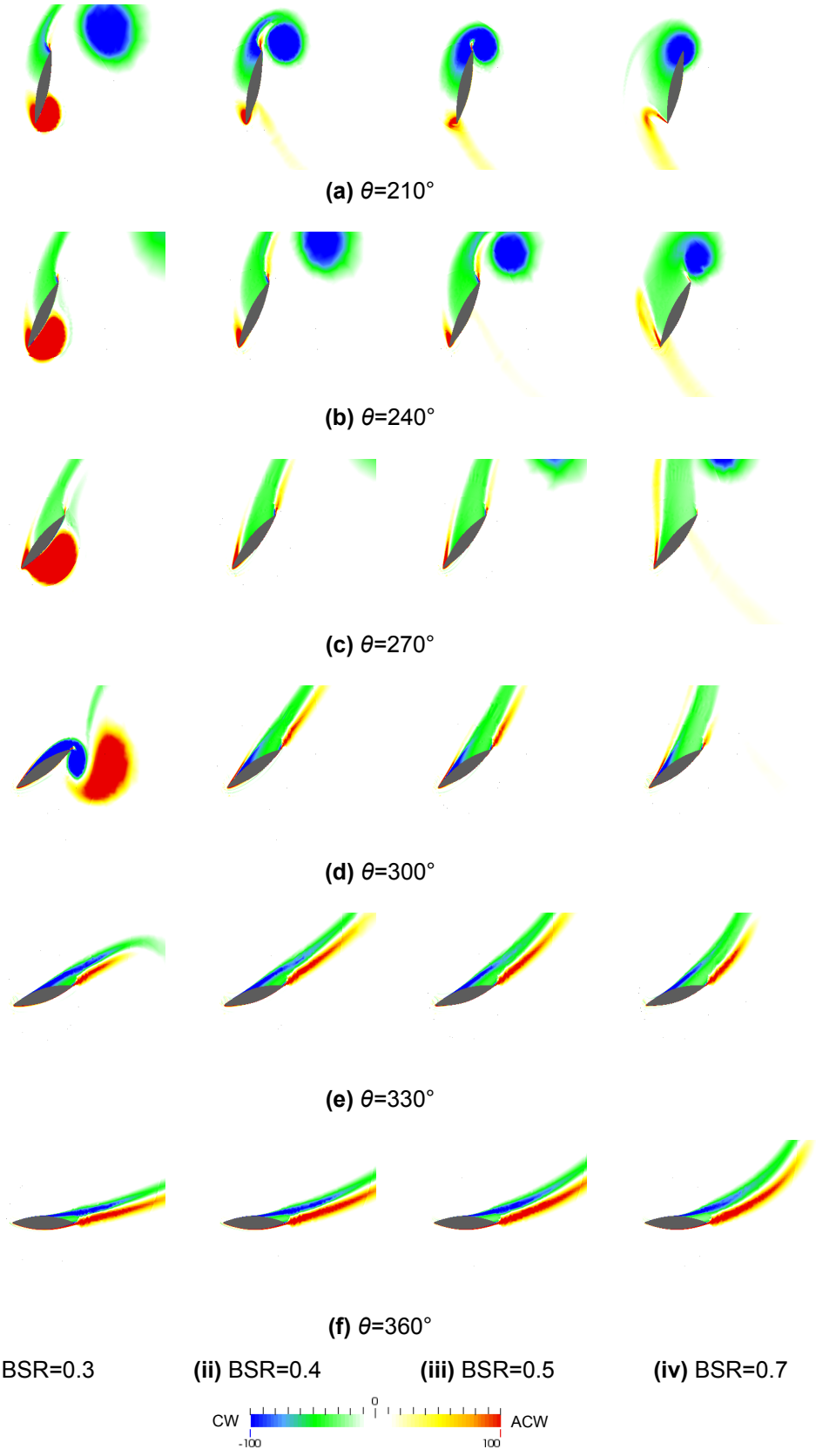

Figure 4.4.7: Contour plots showing vorticity about y-axis for a flat plate undergoing MRL turbine motion ($0.3 \leq BSR \leq 0.7$, $210° \leq \theta \leq 360°$)

at $K = 0.1$ a peak lift coefficient occurs at approximately $\alpha = 42°$, and this corresponds to the location of peak turbine torque. This again indicates that, up to this angular position, the flow around the MRL-motion blade is qualitatively similar to a simply pitching plate, for corresponding effective pitch rate and angle of attack.

As θ increases towards 180°, the torque reduces significantly to a local minimum of approximately 3.0 Nm. At this point the theoretical angle of attack is $\alpha = 90°$ and the reduced frequency has reached approximately $K = 0.2$ (for $a = 0$). Figure 4.3.6iv.f shows that at $K = 0.2$, an attached TEV region (ACW) fails to form, and this leads to the significant reduction in drag in the range $70° < \alpha < 90°$, as seen in Figure 4.3.2. This is in contrast to the results for $K = 0.1$, where the formation of a large attached TEV gives rise to an increase in drag at this point (which leads to the torque increase in this region of the cycle for $BSR = 0.2$).

In the second half of the cycle the torque curve is very similar to the first half, with a peak of 6.0 Nm is reached at $\theta = 270°$. Figure 4.4.7i shows this corresponds to the formation and shedding of a LEV region. At this location the theoretical reduced frequency has reduced back to approximately $K = 0.06$. The CFD results for a pitching plate showed that at $K = 0.05$ the forces produced in the down stroke were of similar magnitude to the up-stroke; this explains why the torque peaks are also of similar magnitudes.

BSR=0.4-0.9: Comparison between plate and blade results

Figure 4.4.1 showed that the torque profiles in this BSR range are very similar throughout the turbine cycle. The only key variations are the location and magnitude of the sudden torque spikes at $BSR = 0.4 - 0.6$ and the variation in magnitude of the peak at $\theta = 270°$.

Observation of the vorticity plots for the MRL blade show the flow field is also very similar for all simulations in this BSR range. In contrast to the results of $BSR = 0.2$ and 0.3, there is only one vorticity shedding event through the complete cycle, which occurs in the range $180° < \theta < 210°$ and leads to the sudden torque spikes in this range.

The difference in magnitude of the second peak at $BSR = 0.4$ is likely due to the formation of a LEV region for the thin plate results, when compared to the blade results. The vorticity plots for the latter (Figure 4.4.7ii) shows no

significant formation of LEV in the second half of the cycle, although the flat plate results do.

The results can again be compared with those of a simply pitching flat plate at theoretically equal conditions. At $\theta = 115°$ (where peak torque occurs for all *BSR* values), the effective angle of attack varies between $\alpha = 32°$ and $\alpha = 5°$ for $BSR = 0.4$ and 0.9 respectively. Likewise, the reduced frequency varies between $K = 0.15$ and $K = 0.03$, although the relative velocities are similar, in the range of $U_R = 0.9 - 1.1$. These values suggest that a wide range of lift and drag forces would be contributing to torque at this position, and therefore the torque peaks would be expected to vary in magnitude. However, this is not the case, suggesting the theoretical steady state analysis presented in section 4.2 is not valid at higher *BSR* values. One reason may be related to the induction factor, i.e. the reduction in flow velocity from free-stream to the blade locality. This will likely change with *BSR* value and will would strongly affect the blade forces developed. Therefore, comparing results for $a = 0$ for all cases is not fully valid.

4.4.4 Conclusions of section

This section has presented CFD simulations of a single blade (and two thicknesses of flat plate) undergoing MRL turbine motion at a range of *BSR* values. Both the torque developed through a single cycle and vorticity visualisations have been used to analyse the results. The conclusions to the section are discussed in more detail in the following chapter conclusions.

4.5 Chapter Conclusions

This chapter has consisted of three main sections. Firstly, the motion of a single blade relative to the incoming flow has been analysed at a given MRL rotor position. From this a number of parameters were defined that describe effective conditions encountered by a blade. The analysis yielded a set of graphs that describe the variation of these parameters through a turbine cycle, and how these relationships vary with blade speed ratio. Generally the graphs highlighted the large variation in resultant velocity, angle of attack, α, and reduced frequency, K, that occur both throughout a cycle, and between different *BSR* values.

Secondly, a suitable pitching plate test case was identified and corresponding CFD simulations were carried out. The presented lift and drag coefficient profiles generally compared well to published experimental results. Vorticity plots have also provided a qualitative insight into the flow structure formed. These show a series of leading and trailing edge vorticity regions form as the plate angle of attack increases. This leads to increasing lift and drag forces, but when the vorticity sheds, sudden reductions in lift and drag occur. The CFD simulations were more successful at predicting physically accurate behaviour at lower values of K, when focusing on lower angles of attack (where lift is dominant). In contrast, the behaviour at higher angles of attack is better predicted at higher values of K.

Significantly, the simulations of 2% thick plates (matching the published experimental setup) introduced sudden jumps or spikes in the force coefficient that did not appear in the simulation of a 0.4% thick plate. In the latter case the results are better matched to experimental data and the vorticity plots show the behaviour is the result of physically inaccurate sudden vorticity formation. The CFD simulations therefore appear unable to simulate the accurate development of vorticity without a sharp leading edge.

The final section presented further simulations of a blade undergoing MRL motion, with the blade geometry matching both that of the physical turbine model and a flat plate. The aim was to give an insight into the simulated flow structure formed by the MRL motion and where appropriate, compare this to simple, steady rotation.

All values of BSR greater than 0.2 yielded a torque curve with two major peaks per cycle. The first peak torque is approximately equal in magnitude and angular location for all BSR values. It is also generally higher than the second peak magnitude, which reduces in magnitude with increasing BSR value. The torque profiles are generally very similar regardless of blade/plate profile, except for the occurrence of a sudden spike near the mid cycle point, for thick plate and blade profiles. This sudden spike occurs in the same way as for a simple pitching plate, where the simulated leading edge vorticity region suddenly forms and sheds. It is therefore not considered an accurate representation of physical flow behaviour. Regardless of this spike, the mean values of cycle torque for the different blade profiles lie within 10% of each other at each BSR value, apart from $BSR = 0.4$. Here the thick plate and blade results are 20% lower than the thin plate result, which is primarily due to a significantly lower magnitude of the

second torque peak. This occurs due to the lack of a leading edge vorticity region that is formed when simulating the thin plate. The results also show the maximum mean torque is developed when a blade/plate travels at a *BSR* value of 0.3; at higher values the mean developed torque reduces significantly, although the values level off at $BSR \geq 0.7$.

The torque generation behaviour has been linked to the formation and shedding of leading and trailing edge vorticity regions, which occur more frequently at lower values of *BSR*. At $BSR = 0.2$ and $BSR = 0.3$, the initial development of torque has been successfully compared to the flow field around a simply pitching flat plate at equivalent values of angle of attack and reduced frequency. However, the flow field responsible for subsequent torque peaks are more difficult to directly compare, which may be due to the continuous increase in reduced frequency through a cycle. At higher *BSR* values, only a single vorticity shedding event occurs per cycle, near $\theta = 180°$. This is qualitatively similar to behaviour observed for plates pitching at reduced frequencies of $K \geq 0.2$, which is theoretically reached for all *BSR* values greater than 0.3.

An estimation of the accuracy of the turbine torque magnitudes can be made, particularly for $BSR = 0.2$ and 0.3, where the reduced frequency theoretically stays below $K = 0.2$. In these cases the maximum contribution of lift forces to torque theoretically occurs at approximately $\theta = 105°$, where reduced frequencies between $K = 0.05$ and 1.0 are predicted. At these pitch rates the simulated peak lift of the simply pitching plate was overestimated by approximately 10%, in comparison to the validation data. The initial peak torque can also be expected to be overestimated by a similar degree. In addition, at $K = 0.1$ and 0.2, the drag coefficient was overestimated by approximately 35% at $\alpha = 90°$ and it is therefore likely the torque for a single blade in MRL turbine motion is also over predicted by a similar degree at approximately $\theta = 180°$ (where drag force contribution to torque is maximised). If both of these predictions are correct, the mean cycle torque at $BSR = 0.3$ can be expected to be approximately 20% lower than predicted by the simulation.

Overall, this chapter has thoroughly investigated the flow developed around a single MRL blade and flat plate, when simply pitching and in MRL turbine motion. The following chapter builds upon this work with simulation of a full three-blade turbine.

CHAPTER 5

COMPUTATIONAL ANALYSIS: MRL TURBINE PERFORMANCE

5.1 Chapter Introduction

This chapter builds on the work presented in Chapters 3 and 4, presenting results from CFD simulations of the MRL turbine.

Firstly, two-dimensional simulations of a three-blade turbine are presented, with the torque produced by multiple blades compared to the single blade results presented previously.

Further turbine simulations are presented, with domain size and inlet conditions representing the experimental flume conditions outlined in Chapter 2. The magnitude of torque and power coefficients, and their relationship with operating conditions, are compared to the physical experimental results.

Finally, a number of simulation results are presented that explore varying turbine geometries not tested during the physical experiments.

5.2 Simulation of a Three-Blade MRL Turbine

5.2.1 Aim of section

This section presents results of two-dimensional (2D) CFD simulations of three-blade MRL turbines, analysing the time-varying torque and power output, and

Table 5.2.1: Turbine simulation geometry and operating condition values

Parameter	n	c	R_b	u_{inlet}	Ti	TVR	Mesh	$\Delta\theta$	x_{max}/D	B
	(-)	(m)	(m)	(m/s)	(%)	(-)	(-)	(°)	(-)	(%)
Value	3	0.05	0.055	1.0	1.0	150	Test 22	0.5	10	5

the associated flow structure within the turbine region. The first aim is to compare the results from an individual blade in a three-blade turbine to those of a single blade presented in Chapter 4. Both MRL blade profiles and 0.4% thick flat plates have been simulated, in order to further analyse the effect these have on the simulations results. Following this, the aim is to analyse the effect of *BSR* value on torque and power.

5.2.2 Approach

CFD simulations have been run using the general set-up presented in Chapter 3, including the mesh parameters selected from the sensitivity analysis. Further turbine geometry and operating conditions are presented in Table 5.2.1. Except for total number of blades, the parameters are identical to those of simulations presented in Chapter 4. Simulations have been run with *BSR* values in the range $0.2 - 0.9$, in increments of 0.1.

5.2.3 Results

5.2.3.1 Visualisation of typical flow-field

Figures 5.2.1 and 5.2.2 present visualisations of instantaneous velocity magnitude, relative pressure and turbulence intensity flow-fields for a single case of a thin flat plate, three blade turbine operating at $BSR = 0.5$. The two figures show the turbine at two instantaneous rotational positions of $\theta = 0\,°$and $\theta = 180\,°$.

The results show the turbine significantly affecting both the downstream flow (i.e., the wake) and to a lesser extent, the upstream flow. Although only a single blade-speed-ratio value is presented, the general characteristics of the flow field is typical of all simulated cases.

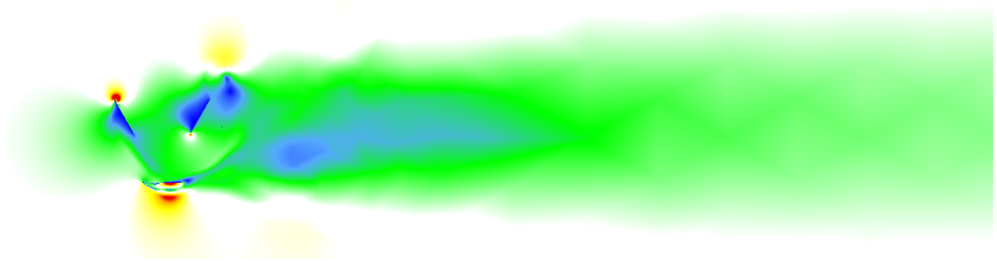

(a) Velocity magnitude

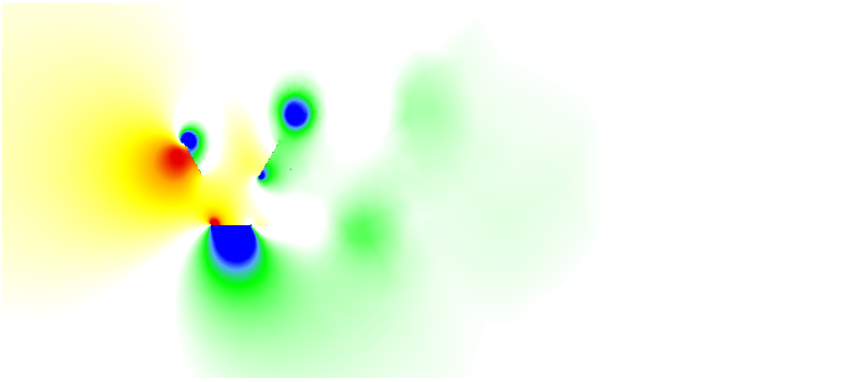

(b) Relative pressure

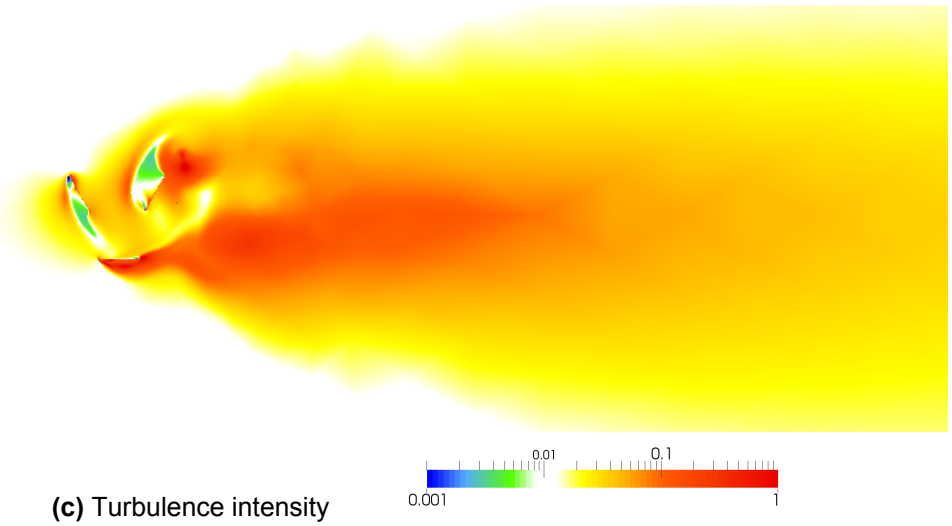

(c) Turbulence intensity

Figure 5.2.1: Visualisation of simulated flow field around three-blade turbine (0.4% thick flat plate, BSR=0.5, $\theta = 0°$)

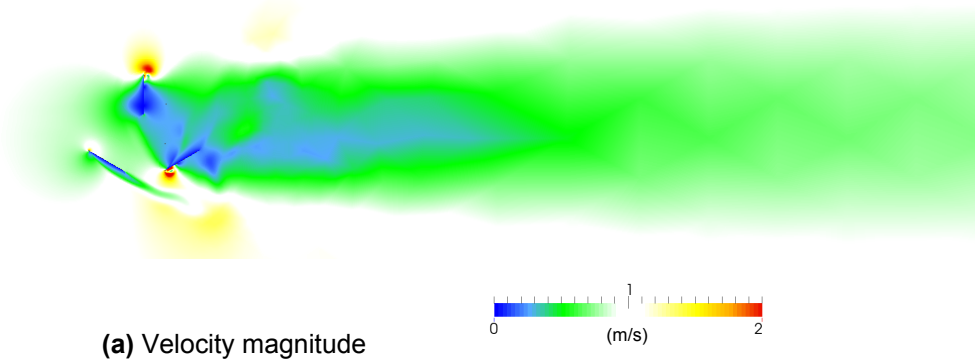

(a) Velocity magnitude

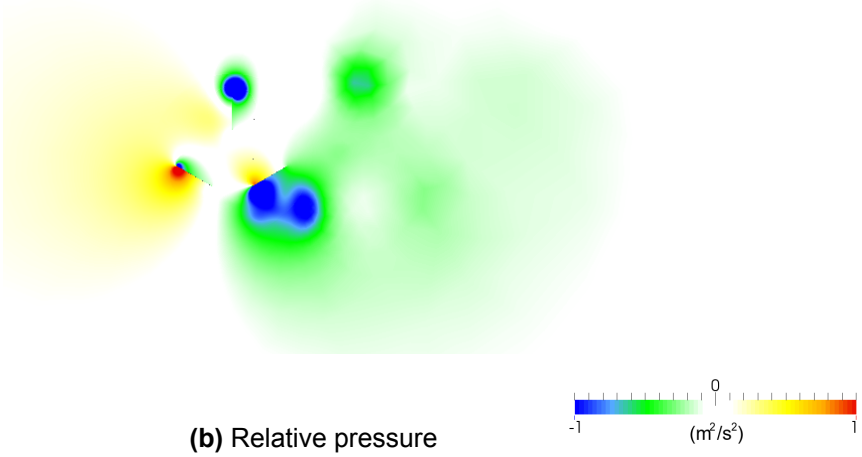

(b) Relative pressure

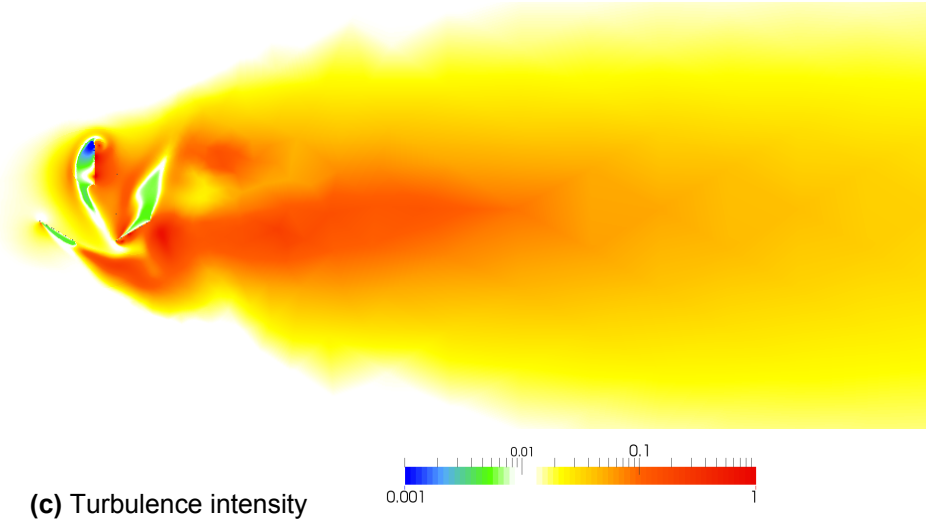

(c) Turbulence intensity

Figure 5.2.2: Visualisation of simulated flow field around three-blade turbine (0.4% thick flat plate, BSR=0.5, $\theta = 180°$)

The flow velocity gradually reduces from the free-stream value as it approaches the turbine, before interacting with the moving blades. The velocity is significantly reduced immediately downstream of the turbine, before gradually recovering towards the free-stream value. However, full recovery does not occur before the outlet boundary of the computational domain, with a value of approximately 80% of the free-stream observed in this region.

The gradual decrease in velocity upstream of the turbine also corresponds to a gradual increase in pressure as the flow approaches the turbine. As the blades interact with the incoming flow the highest values of pressure occur at the upstream faces, and the lowest values at the downstream face, contributing to generation of forces and torque acting on the turbine. The extraction of energy from the flow corresponds to a general reduction in pressure across the turbine region. The resulting low pressure regions in the near wake gradually recover towards the free-stream value as the flow travels downstream.

The turbulence intensity flow-field shows how the volume of flow affected by the turbine operation significantly expands downstream of the turbine. This is typical of energy extraction devices, as the reduction in velocity occurring in the near wake necessitates an increase in flow area, in order to satisfy conservation of mass. This flow has passed through the turbine region where interaction with the blades causes an increase in turbulence. The highest turbulence intensities are observed in the immediate wake of the blades, where strong vortices are shed, and in the central area of the near wake, where velocity is lowest. As the flow progresses, the turbulence intensity gradually reduces in the central wake region, due to the recovery of flow velocity. However, the wake also continues to increase in width, as mixing with the free-stream occurs. At the domain outlet, the wake turbulence intensity is approximately 200-300% of the inlet free-stream value.

Although near and far wake results have been presented here, it should be noted that the mesh in these regions was relatively coarse, as the computational setup was primarily designed for analysis of forces and torque generation. The visualisations of flow-fields in the wake region therefore only give a general indication of characteristics and further sensitivity analysis of the wake region mesh and time-step would be required in order to increase confidence in the results.

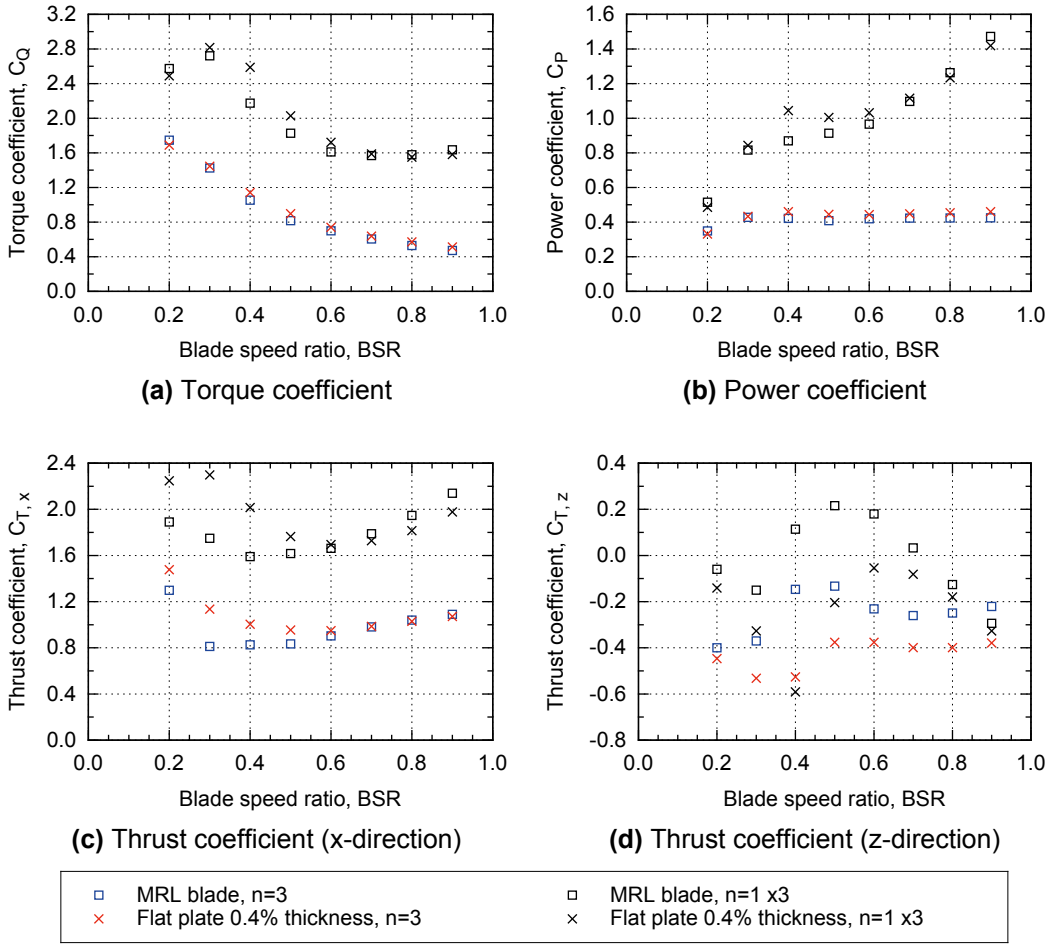

Figure 5.2.3: Variation of performance coefficients with BSR value, comparing two blade profiles for a single-blade and three-blade turbine. Single-blade results are multiplied by three in order to allow direct comparison to three-blade results ($B = 5\,\%$)

5.2.3.2 Variation of torque, power and thrust coefficients

Torque, power and thrust coefficients have been calculated for each *BSR* value simulated, for both MRL blade and flat plate profiles, as presented in Figure 5.2.3. Also presented are coefficients calculated from the single blade simulation results presented in Chapter 4 (Section 4.4). These results have been multiplied by three in order to allow direct comparison to the three-blade results. This therefore represents the torque, power and thrust that would be generated by three blades acting independently of each other.

Variation with BSR (MRL blade, n=3) The following refers to the results for a three-blade turbine with MRL blade profiles. Generally, torque coefficient

shows an inverse correlation with BSR, and varies between $C_Q = 1.75$ at $BSR = 0.2$ to $C_Q = 0.45$ at $BSR = 0.9$. The trend appears linear in the range $0.2 \leq BSR \leq 0.5$ and also in the range $0.5 \leq BSR \leq 0.9$, albeit with a lower gradient in the latter range.

The power coefficient is calculated as torque coefficient multiplied by BSR and therefore shows a different overall trend. In the range $0.2 \leq BSR \leq 0.5$ results generally follow a peaked-curve type relationship, with maximum values of $C_P = 0.43$ at $BSR = 0.3$. However, in the range $0.5 \leq BSR \leq 0.9$, the power coefficients begin to increase in magnitude with increasing BSR value, albeit with a shallow gradient. This is directly related to the different torque coefficient gradients in the two BSR ranges, as discussed above.

The x-direction thrust coefficient follows a similar initial trend to torque coefficient, with a negative gradient section occurring at lower values of BSR. This runs from a peak of $C_{T,x} = 1.3$ at $BSR = 0.2$ to a minimum of $C_{T,x} = 0.85$ at $BSR = 0.5$. In contrast to torque coefficient, the results then follow a positive gradient at higher values of BSR, reaching $C_{T,x} = 1.1$ at $BSR = 0.9$.

In comparison to x-direction values, the z-direction thrust coefficient magnitudes are significantly lower throughout the BSR range. This is a result of x-direction forces acting in the same (positive) direction throughout a cycle, whilst z-direction forces act in opposite directions in each half-cycle (as presented in Section 4.4.3.2). However, the magnitude of z-direction thrust does follow a similar profile of reducing from $C_{T,z} = -0.4$ at $BSR = 0.2$ to $C_{T,z} = -0.13$ at $BSR = 0.5$, before increasing to $C_{T,z} = -0.22$ at $BSR = 0.9$. The coefficient (derived from cycle-mean force) is negative throughout the BSR range, indicating the negative z-direction force that occurs through the second half-cycle is greater in magnitude than the positive force acting throughout the first half-cycle.

Comparison of blade profile The results of simulating a 0.4% thick flat plate are also presented alongside those of an MRL blade profile. There are observable variations between the sets of results, particularly in the range of $BSR = 0.2 - 0.6$. These variations are a result of the differences in strength of simulated vortex strength, as discussed for a single blade and plate in Section 4.4.

The greatest difference in torque coefficient occurs at $BSR = 0.4$, with blade results 7.8% lower than flat plate results. This compares to 16.7% for the single blade simulation, indicating the three-blade simulations yield lower variation between the two sets of results.

The power coefficient results also show a difference in magnitude between sets of results, with a maximum variation of 8.7% at $BSR = 0.4$, although the trend with BSR is similar throughout for both sets of results.

There is more significant variation between sets of thrust coefficient results, especially at lower values of BSR. The maximum differences are 28% at $BSR = 0.3$ for x-direction and 72% at $BSR = 0.4$ for z-direction thrust (for the three-blade results). The magnitude of the variations are again greater for a single-blade, indicating the interaction of the three blades affects the strength of the simulated vortex generation for flat plates more than the blade profile.

Comparison of total number of blades Generally the single-blade results are increased by a significant amount in comparison to the three-blade counterparts (i.e. MRL blade or flat plate results), throughout the BSR range. This suggests that the flow through the turbine and over each blade is significantly affected by the presence of additional blades. The reason for this is discussed in detail in the following section.

The trend with BSR value is generally similar for both single and three-blade results, for all coefficients presented. One exception is that the peak torque coefficient occurs at $BSR = 0.2$, rather than $BSR = 0.3$ and the reduction in gradient at higher BSR values is greater for the single blade results. This also corresponds to a higher gradient of power coefficient trend at higher BSR values.

The z-direction thrust coefficient follows a similar trend for both sets of results, but the three blade results have a more negative bias. This suggests that the presence of additional blades increases the relative magnitude of negative z-direction forces acting in the second half-cycle. This is likely, as the presence of upwind blades will affect the flow over blades in downwind positions.

5.2.3.3 Time-varying blade torque

In this section the time-varying torque results are presented using polar plots, in order to show how torque varies with angular location. The plots are aligned with the simulated turbine axis, so that the turbine rotates in a clockwise direction, with $\theta = 0°$ at the bottom of the plot, and the flow direction is from left to right. Therefore $\theta = 90°$ is the most upstream blade location and $\theta = 270°$ is the most downstream. The magnitude of torque varies along the radial axis, regardless of angular location and values represent Newton-metres. Also note that a negative value, rather than zero torque is often located at the centre of the plot, with zero located at a radial distance from this point. Any torque results with a negative magnitude are therefore acting in the direction opposite to the turbine rotation.

Figure 5.2.4 shows the variation of torque due to forces acting on an individual blade (in a three-blade turbine) as it rotates through the turbine cycle, for six discrete *BSR* values. Results for a single-blade are also presented, as well as comparison between an MRL blade profile and a 0.4% thick flat plate.

Comparison of total number of blades

For all results except $BSR = 0.2$, the general shape of the n=1 and n=3 profiles are similar, with a maximum torque value occurring in the upstream half of rotation, and generally a smaller magnitude maximum occurring in the second half of rotation. This is the same behaviour as previously discussed in Chapter 4, and is repeated when moving from a single-blade simulation to a three-blade simulation.

However, there is a clearly significant difference between the magnitude of peak torque for single- and three-blade turbines. The former has initial peak magnitudes of approximately $6 - 7\,Nm$, whilst the three-blade turbine peaks at approximately $3 - 4\,Nm$ for each blade, giving an average reduction of approximately 45%. The peaks in the second half of rotation are also reduced by a similar magnitude. This indicates that although the flow structure may be similar, the addition of multiple blades in close proximity has a pronounced effect on the magnitude of pressure differences across the blades. This may be due to lower flow velocities acting on the blade upstream faces, due to an increased local blockage effect (i.e., an increased induction factor).

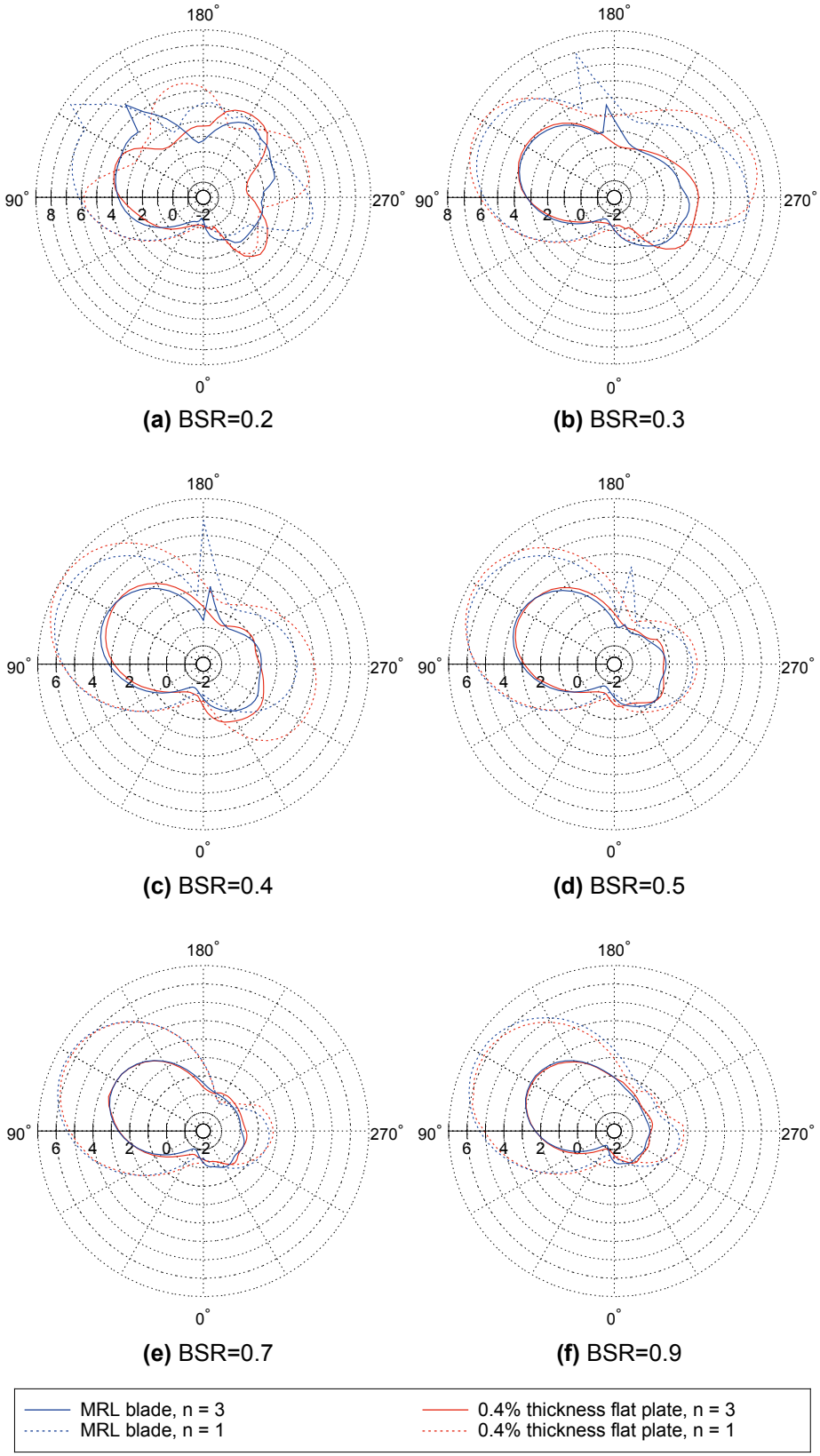

Figure 5.2.4: Variation of single blade torque (Nm per metre span) with rotor angle, comparing the effect of blade profile and total number of blades

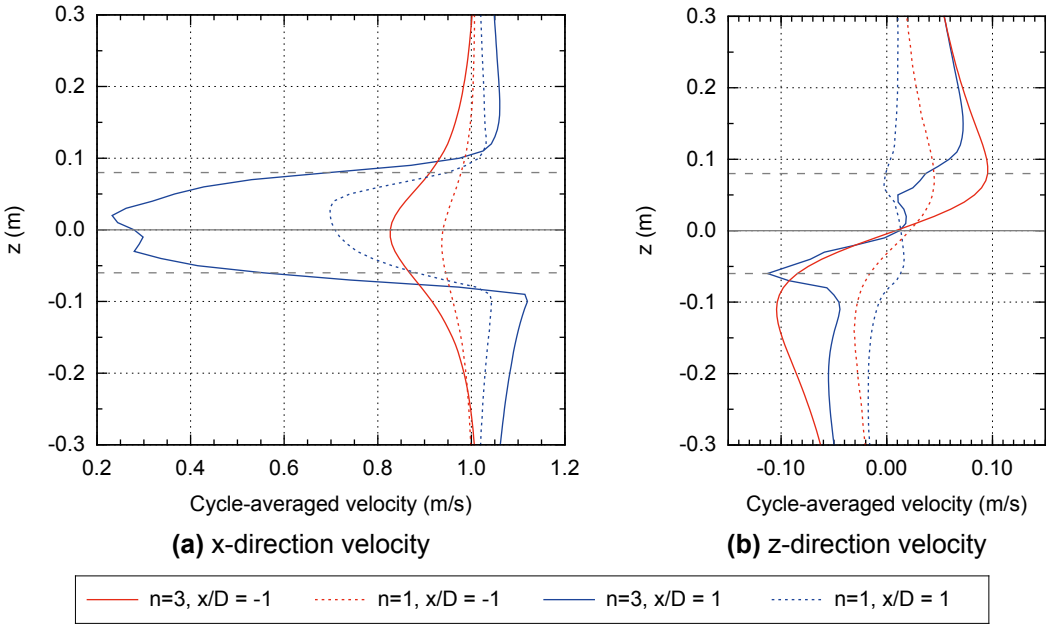

Figure 5.2.5: Cycle-averaged velocity profiles comparing single blade and three-blade simulation results (BSR=0.5)

This effect is quantified as shown in Figure 5.2.5, where cross-sectional profiles of cycle-averaged velocity are shown both directly upstream and downstream of a single blade and three-blade turbine at $BSR = 0.5$. The profiles vary with z-direction, with the turbine axis located at $z = 0\,m$, and dashed grey lines indicating the extent of the turbine blade sweep.

Directly upstream of the turbine ($x = -1\,D$) the x- and z-direction velocity components are significantly changed from the inlet conditions of $1\,m/s$ and $0\,m/s$ respectively. The x-direction values are reduced across the vertical section, with the minimum velocity value occurring in line with the turbine axis. The z-direction velocity graph shows the flow being deflected around the turbine region (i.e. below the turbine axis there is a negative z-direction velocity component and vice versa).

Directly downstream of the turbine ($x = 1\,D$) a significant wake region has formed in the x-direction velocity, and the bypass flow (above and below the turbine) has accelerated to velocities greater than the inlet value. This behaviour ensures that conservation of mass flow is satisfied throughout the domain. The z-direction velocity deflection is still apparent, but with a lower magnitude.

By comparing the velocity profiles for the single blade and three-blade turbine, it can be seen that the former causes less upstream flow deceleration and

deflection around the turbine (i.e., a reduced induction factor). At the turbine central axis line, the single blade reduces the cycle-averaged velocity to 94% of the inlet value (induction factor, $a = 0.06$), while the three-blade turbine reduces this to 83% ($a = 0.17$). This is understandable, as within a given time (e.g. one cycle), three times as many blades pass through the incoming flow and the cycle-mean induction factor is increased by approximately a factor of three.

This effect of multiple blades is visualised in Figure 5.2.6, comparing a single- and three-blade turbine operating at $BSR = 0.4$. Both velocity and pressure fields are shown at the peak torque position of $\theta = 120°$, as well as $\theta = 240°$. Also shown are velocity streamlines that represent the paths followed by particles in the flow.

The velocity streamlines show the direction of the flow field around the upstream and downstream blades are similar for a single blade and three-blade turbine. In both cases, the velocity and pressure fields also appear very similar at the upstream face of the upstream blade ($\theta = 120°$).

However, the magnitude of the velocity downstream of the upstream blade and upstream of the downstream blade ($\theta = 240°$), is significantly reduced in the three-blade simulation, compared to the single-blade simulation. This is due to the close proximity of the blades (i.e., high solidity of the turbine), which impedes acceleration of the flow at the downstream face of the upstream blade. The magnitude of relative negative pressure is therefore reduced at this location, meaning the pressure difference across the blade is reduced.

This also has a direct effect on the downstream blade, where the velocity of flow onto the upstream face is reduced, especially around the leading edge. This causes a reduction in both the magnitudes of relative positive pressure at the upstream face, and relative negative pressure at the downstream face. Again, this leads to a reduced pressure difference, and therefore a reduced force acting upon the blade.

Figures 5.2.7, 5.2.8, 5.2.9 and 5.2.10 present velocity contour plots at a number of stages in a full cycle, at a further four *BSR* values.

The plots show the flow through the turbine is complex at all values of *BSR*, and the wake from blades in the upstream half cycle has a strong effect on the flow at the downstream positions, as discussed for $BSR = 0.4$. Also, as *BSR* increases, the average flow velocity within the turbine region appears

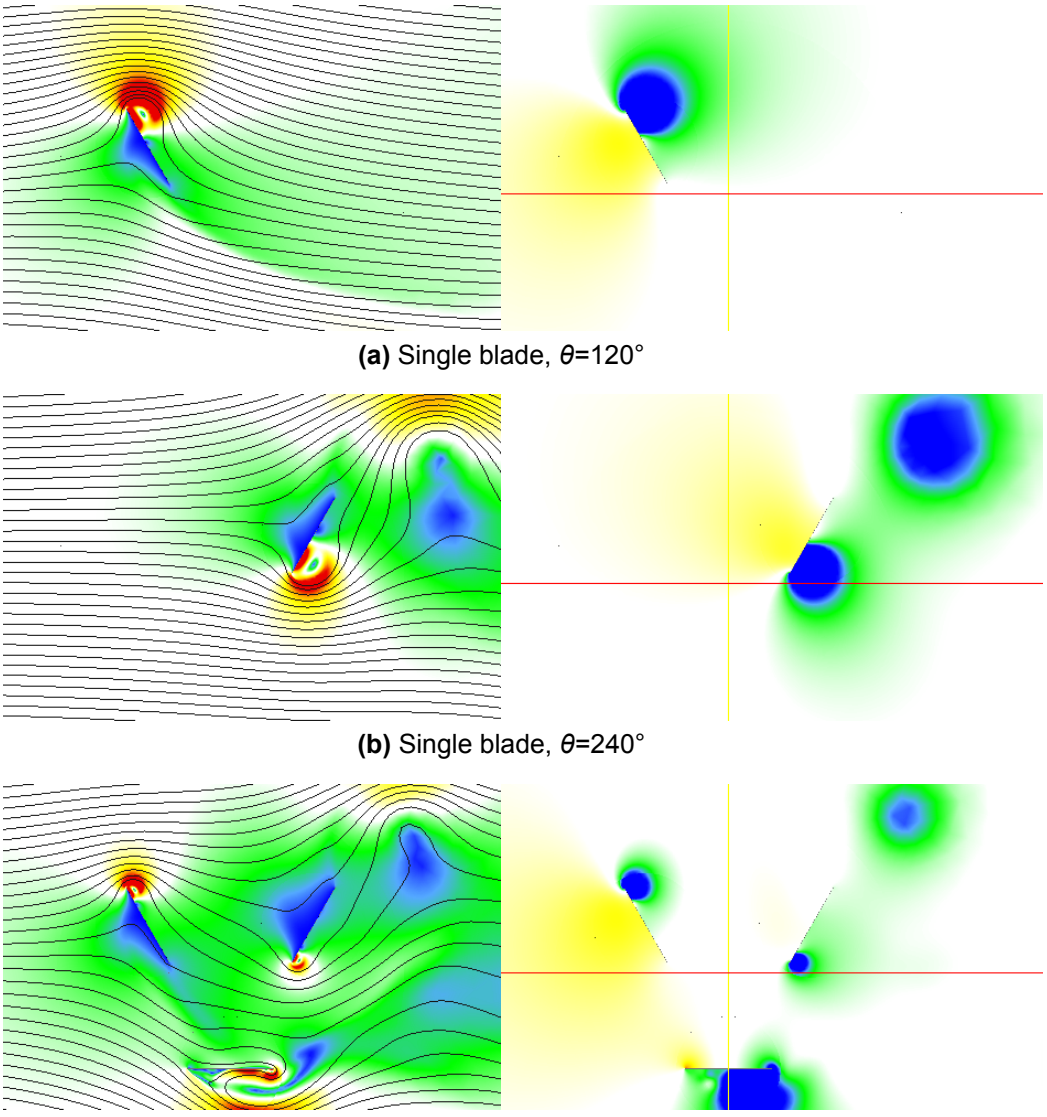

Figure 5.2.6: Comparison of flow velocity streamlines and pressure field around a single blade and a three-blade turbine (0.4% thick flat plate, BSR=0.4)

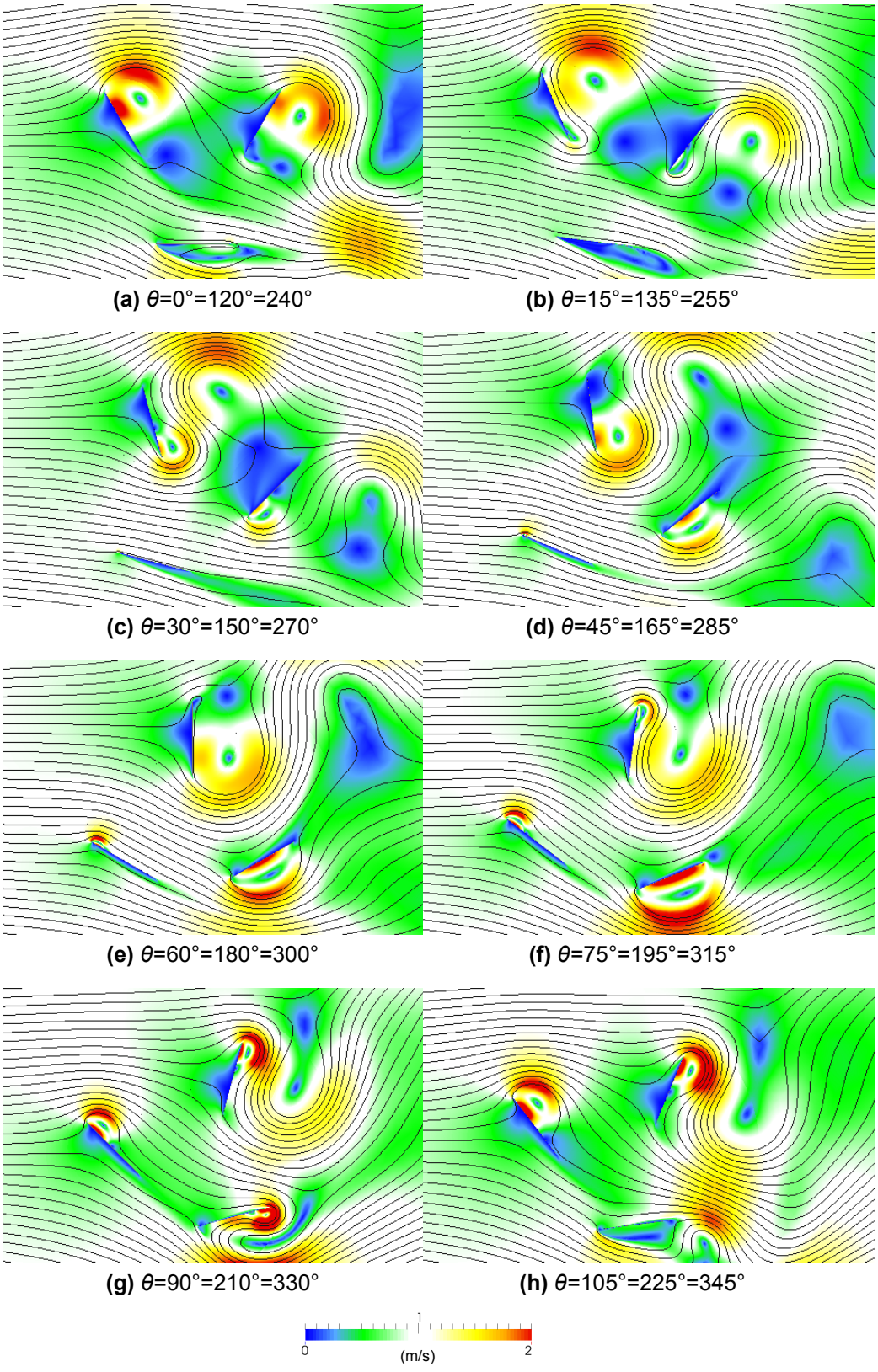

Figure 5.2.7: Variation with rotor angle of flow velocity streamlines around a three-blade turbine (0.4% thick flat plate, BSR=0.2)

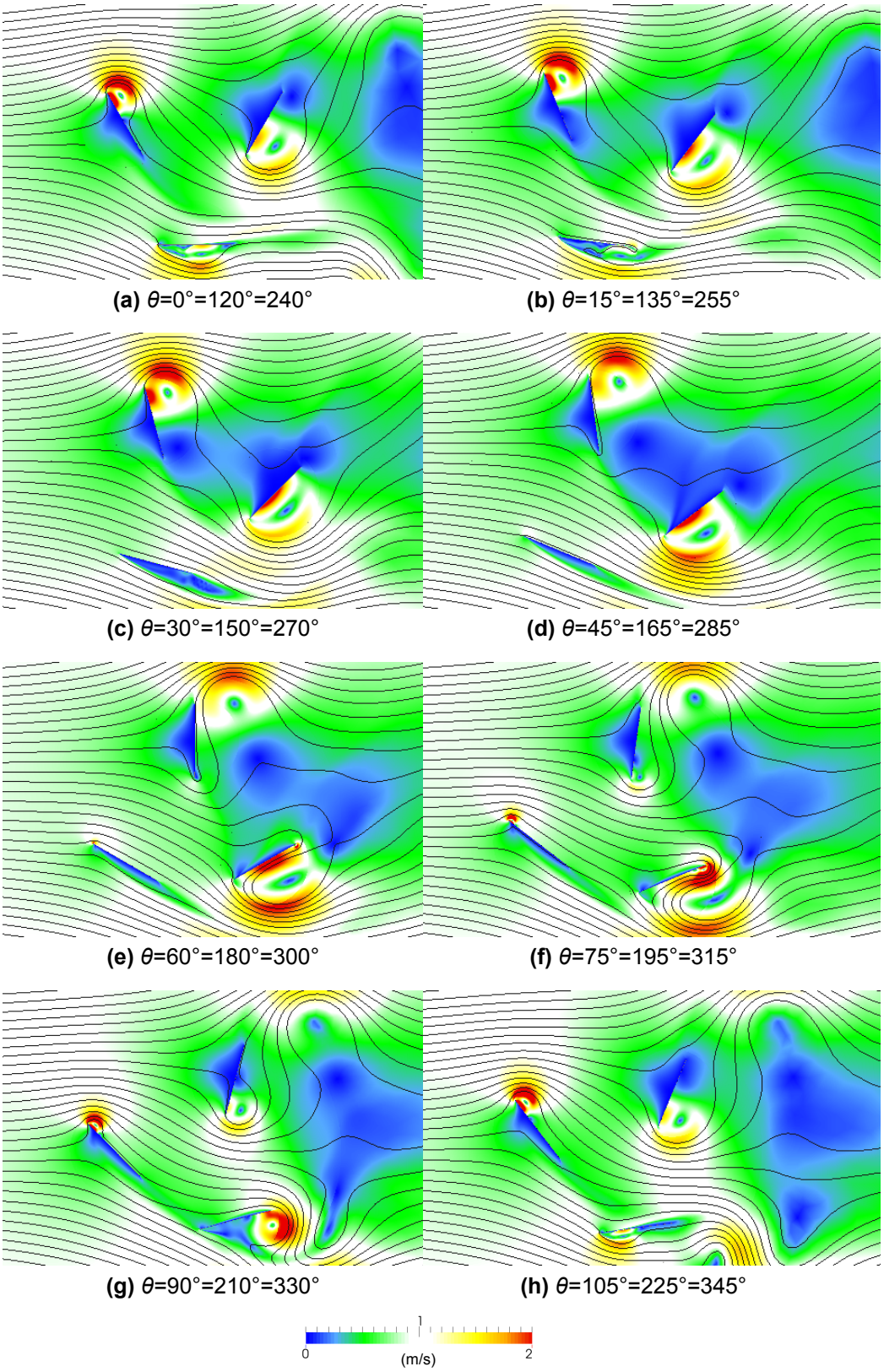

(a) θ=0°=120°=240° **(b)** θ=15°=135°=255°

(c) θ=30°=150°=270° **(d)** θ=45°=165°=285°

(e) θ=60°=180°=300° **(f)** θ=75°=195°=315°

(g) θ=90°=210°=330° **(h)** θ=105°=225°=345°

Figure 5.2.8: Variation with rotor angle of flow velocity streamlines around a three-blade turbine (0.4% thick flat plate, BSR=0.3)

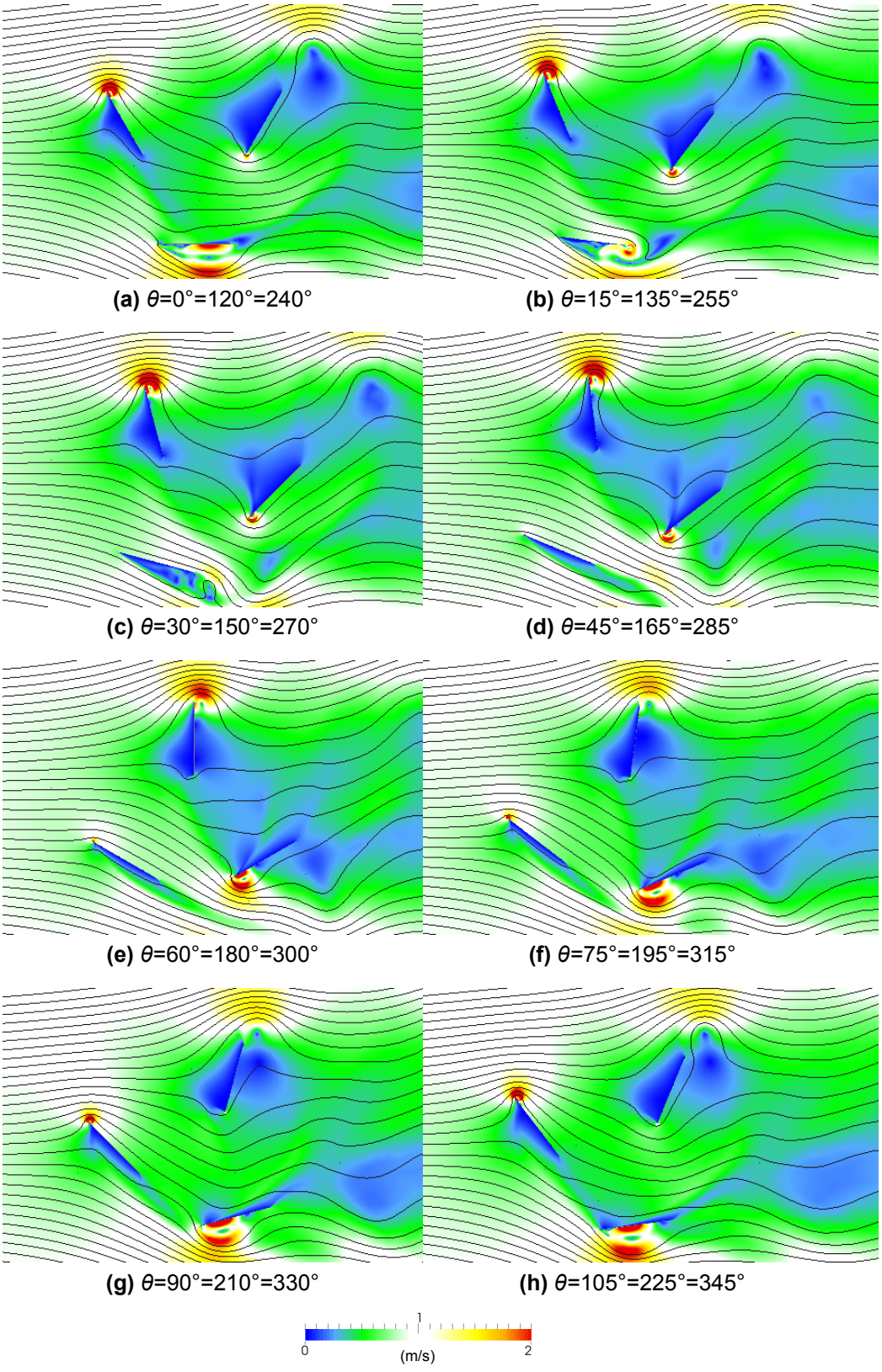

Figure 5.2.9: Variation with rotor angle of flow velocity streamlines around a three-blade turbine (0.4% thick flat plate, BSR=0.5)

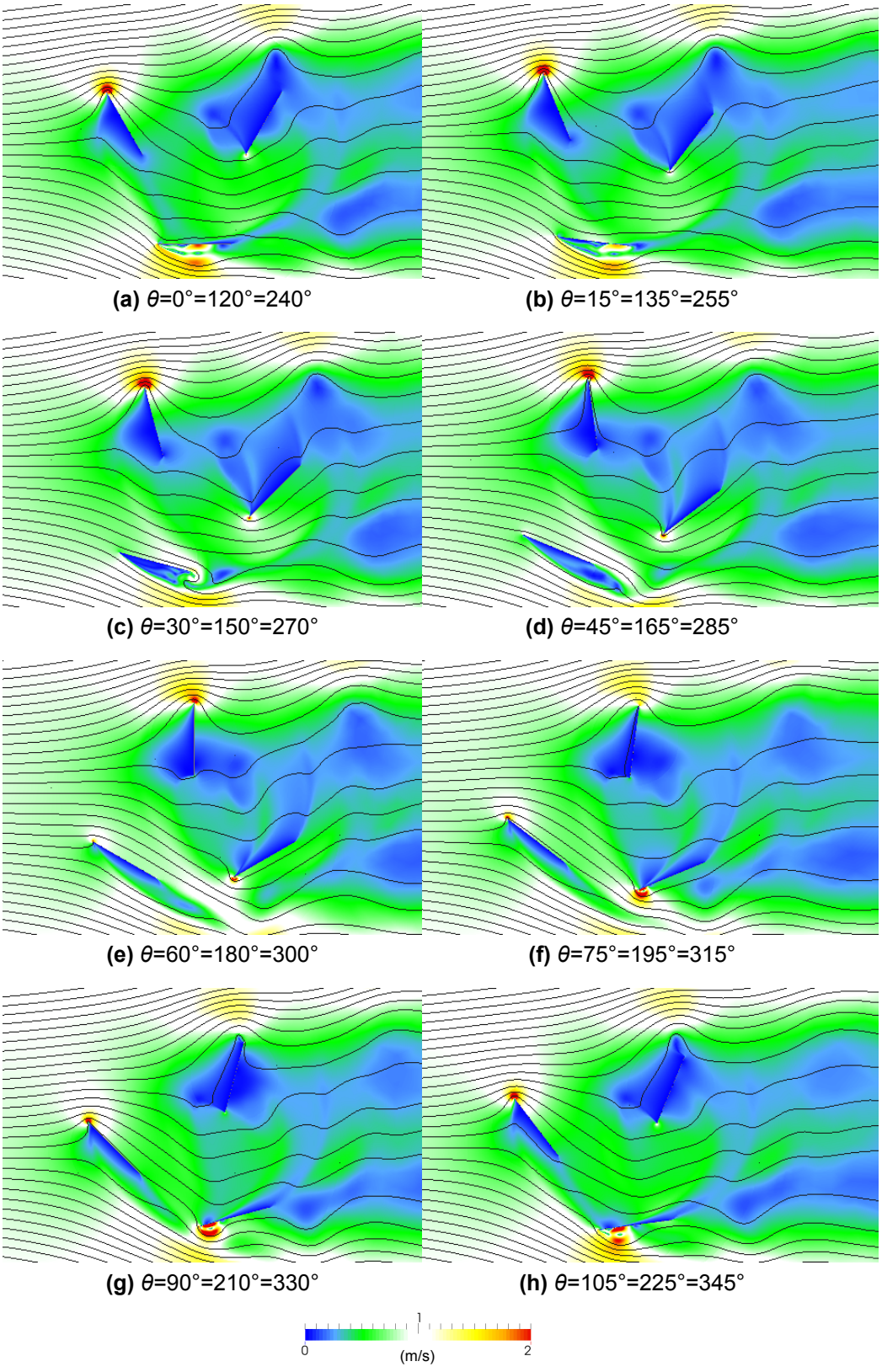

Figure 5.2.10: Variation with rotor angle of flow velocity streamlines around a three-blade turbine (0.4% thick flat plate, BSR=0.7)

to be reduced, corresponding to an overall increase in pressure in this area. This effectively increases the local blockage, causing a greater amount of flow deflection around the turbine, as indicated by the streamlines.

Figure 5.2.4 showed that in addition to the significant difference in torque magnitude, the three-blade results appears to be delayed by up to 30° at $BSR = 0.2$. For example, for a single flat plate, the initial peak occurs at $\theta = 90°$, while in the $n = 3$ flat plate turbine the event occurs at $\theta = 120°$. A similar effect is observed at $BSR = 0.3$, where results are delayed by approximately 15°. This occurs because formation of the upstream leading edge vorticity (LEV) region is delayed in the three-blade turbine, due to flow deflection from the preceding blade. This is shown in Figure 5.2.7, where this flow is directly impinging on the leading edge of the blade at $\theta = 330°$. This causes the incoming flow angle of attack to be negative at $\theta = 0°$, and does not reach zero until $\theta = 30°$. Only after this point does the flow accelerate in a clockwise direction around the leading edge, forming the LEV region.

5.2.3.4 Time-varying total torque

Figure 5.2.11 shows how the torque generated by forces acting on each blade/plate combine to give the total torque acting about the turbine central axis. The results are shown at individual *BSR* values and show the torque generated by each blade set at intervals of $\theta = 120°$. The angular position for blades 2 and 3 curves actually refer to the rotor angle of blade 1; for example, when the blade 2 result peaks at $\theta = 240°$ (at $BSR = 0.3$), this refers to the angle of blade 1. As blade 2 lags blade 1 by 120°, the former is actually located at $\theta = 120°$ (where peak torque is generated for each blade). Therefore the total torque at any angular position is the sum total of torque produced by each blade at that point in time.

The results show the simulated torque generated by the 0.4% thick flat plates, rather than the MRL blade, as these do not include the non-physical sudden torque spikes (and therefore model a more physically accurate build up of leading edge vorticity). Apart from at $BSR = 0.2$, this does not have a significant effect on the total torque variation, apart from removal of the spikes. In the

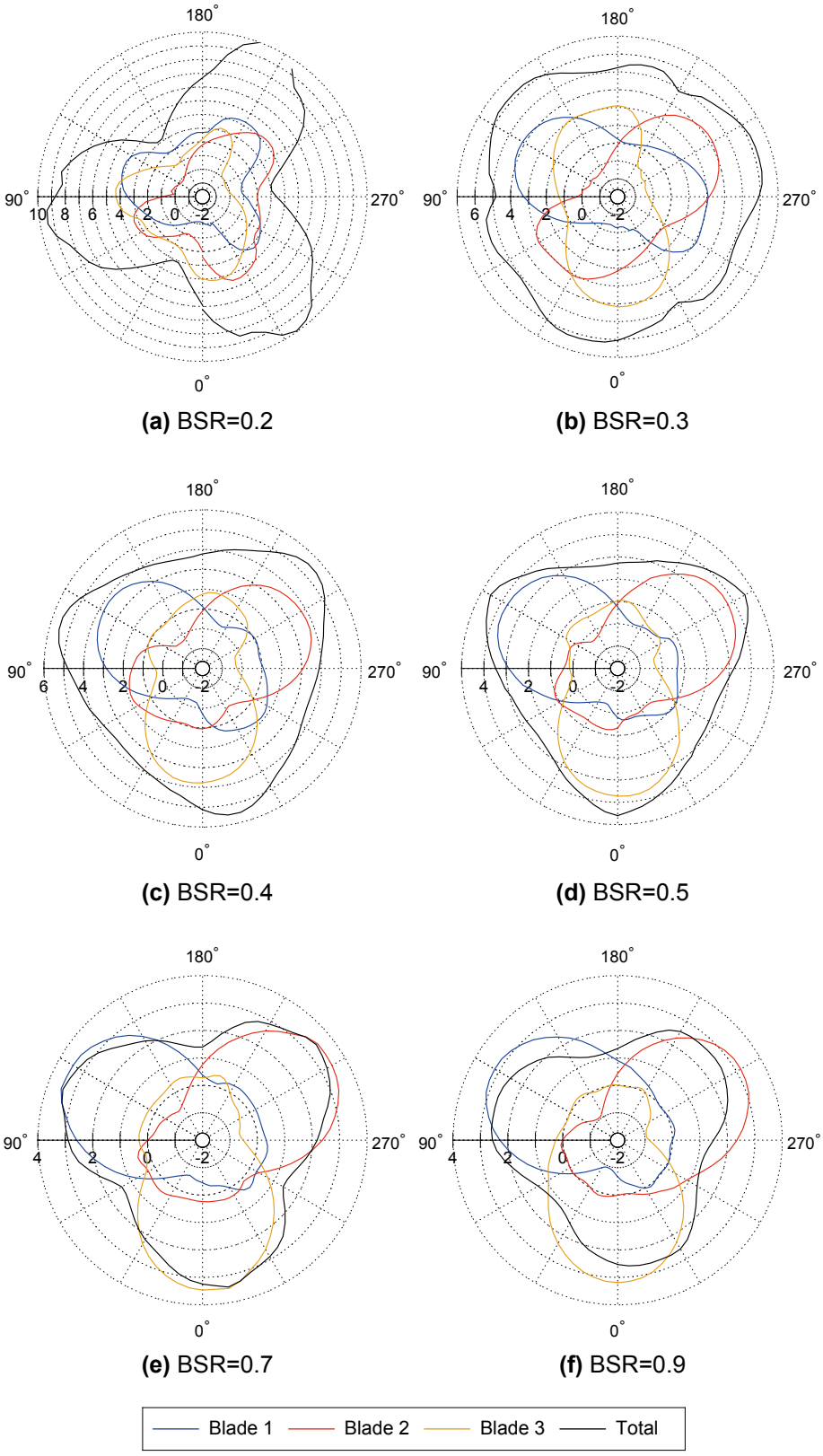

(a) BSR=0.2 **(b)** BSR=0.3

(c) BSR=0.4 **(d)** BSR=0.5

(e) BSR=0.7 **(f)** BSR=0.9

Figure 5.2.11: Variation of torque (Nm per metre span) with rotor angle, showing individual blade and total values (0.4% thick flat plate)

following discussion, the term "blade" is used to refer to the plates, regardless of profile.

At $BSR = 0.2$ the individual torque curves for each blade yield three major peaks throughout the cycle, which are spaced at approximate intervals of 100°, 100° and 160° from each other. When combined, these peaks tend to coincide, giving a highly fluctuating total torque. The peak values are over 100% greater than the peak value generated by each blade, and the total torque is never less than the torque of a single blade at any given angular location. This is because there is negligible negative torque produced by a single blade, at any point in the cycle, unlike at higher *BSR* values.

$BSR = 0.3$ gives the most consistent total torque throughout a cycle. This is because, for each individual blade, peak torques of similar magnitude occur in each half cycle, approximately $\theta = 180°$ apart. This results in similar magnitude peaks occurring every 60° of rotation when all three plates are combined. In addition, the negative, parasitic torque that occurs at $\theta = 0°$ is of lower magnitude than at higher *BSR* values. This is due to the lower relative flow speed and associated drag force acting against the direction of blade motion.

As *BSR* increases in the range $0.4 \leq BSR \leq 0.9$, total torque shows progressively more variation during an individual cycle. Each of the curves has three main peaks, which generally coincide with the upstream peak of a single blade (at approximately $\theta = 120°$), although this varies with *BSR* value. At this location in the turbine cycle, the following blade (at approximately $\theta = 0°$) is producing near-zero or negative torque, and the final blade (at approximately $\theta = 240°$) is also producing a significant, but lower magnitude positive torque.

The total torque peak values vary in magnitude to the peak of each blade, between +42% at $BSR = 0.4$ and -22% at $BSR = 0.9$. This is because the parasitic torque reaches lower negative values as *BSR* increases, as well as the downstream peak values decreasing in magnitude. When combined, this leads to a reduction in peak and local minimum values as *BSR* increases. This relationship is shown in Figure 5.2.12, where torque produced by each individual blade (in a three-blade turbine), as well as the three-blade total, are directly compared at various values of *BSR*.

The results clearly show the negative correlation of total torque with *BSR* value, for the three-blade turbine results. The reduction in torque that occurs from one *BSR* value to the next generally applies over the complete cycle, at both

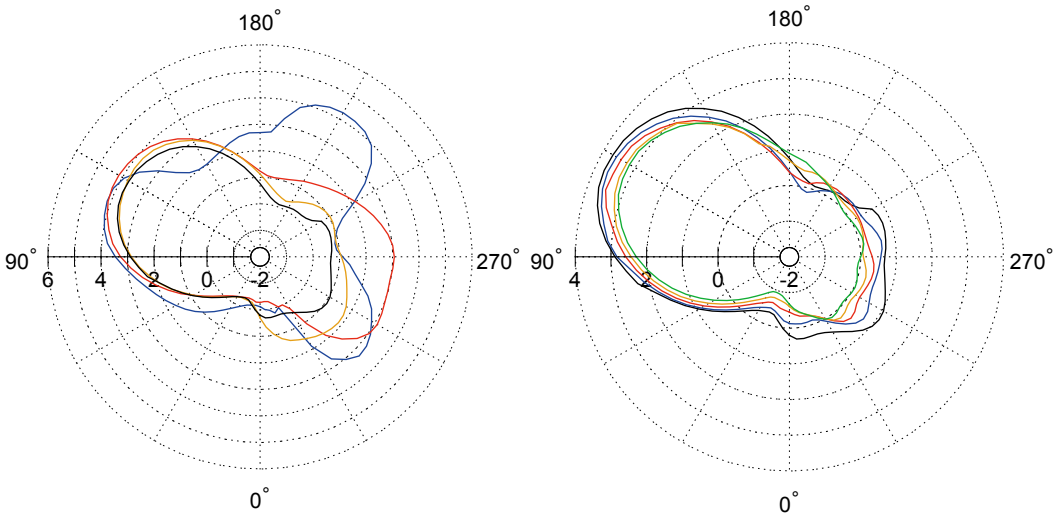

(a) One blade

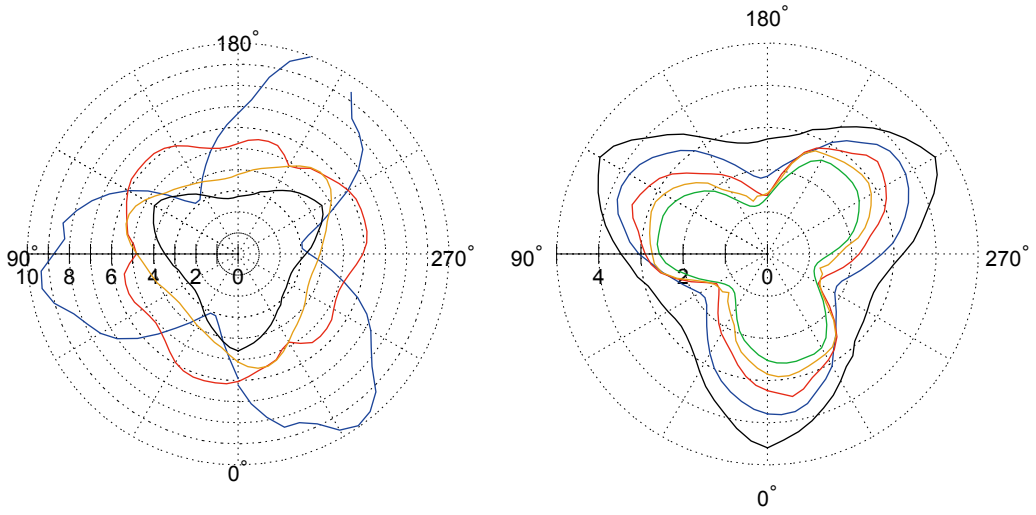

(b) Total (Three blades)

i) $0.2 \leq BSR \leq 0.5$ ii) $0.5 \leq BSR \leq 0.9$

Figure 5.2.12: Variation of individual blade and total torque (Nm per metre span) with rotor angle, comparing the effect of blade speed ratio (0.4% thick flat plates)

minimum and maximum values. The torque results for individual blades also show a reduction in peak values as *BSR* increases, but to a smaller degree, especially in the first half of rotation. In the second half of rotation the reduction in peak torque is more pronounced as *BSR* increases, especially in the range $0.3 \leq BSR \leq 0.5$. This highlights the importance of torque generation through the whole cycle, and the strong influence that torque reduction in the second half of rotation has on total torque. In the range $0.5 \leq BSR \leq 0.9$ there is a similar magnitude of reduction in both upstream and downstream peaks, as *BSR* increases. There is also a decrease in magnitude (towards negative values) of the local minimum that occurs at approximately $\theta = 20°$. As this occurs approximately 100° from the peak value, the maximum and minimum torque values for separate blades occur at approximately the same time. This has a strong influence on the reduction of peak total torque.

5.2.4 Conclusion of section

This section has presented results of two-dimensional CFD simulations of a three-blade MRL turbine operating in an effectively infinite sized domain. The analysis compared torque, power and thrust coefficients, time varying torque profiles and flow visualisations to results from simulations of a single-blade turbine, as previously presented in Chapter 4. The majority of presented results are from simulations involving thin flat plates, rather than thick blades, as the simulated flow structure is considered to be more physically accurate.

The time-varying torque curves show that at each *BSR* value, the torque developed by each blade in a three-blade turbine is similar in profile to that developed by a single blade in MRL motion. However, the magnitude of both the upstream and downstream peaks is significantly reduced, which is likely a result of decreased velocity and increased pressure within the turbine region. The downstream peaks at $BSR = 0.3$ and 0.4 are reduced to a greater extent than other *BSR* values, which in turn reduces the cycle mean torque to a greater extent.

Therefore, the simulated maximum torque coefficient of $C_Q = 1.75$ occurs at $BSR = 0.2$ rather than $BSR = 0.3$ (as was the case for single blades). The torque coefficient curve also continues to reduce through the full *BSR* range, rather than levelling off. The associated power coefficient curve shows a peaked curve relationship at *BSR* values up to $BSR = 0.5$, although the

power values level off or even increase at higher *BSR* values. A peak value of approximately $C_P = 0.46$ occurs at $BSR = 0.4$ for the thin flat plate simulations.

The MRL blade simulations give similar torque and power coefficient values to the thin flat plate simulations, with a maximum variation of less than 8% occurring at $BSR = 0.4$. The time-varying plate/blade torque profiles are also very similar at all *BSR* values except $BSR = 0.2$, where equivalent vorticity shedding events take place at different angular positions. This indicates the simulation of MRL blades, rather than flat plates, does not have a significantly adverse effect on the reliability of cycle-averaged torque and power results, although care should be taken when analysing time varying results of $BSR = 0.2$ simulations.

However, there is a more significant variation between MRL blade and flat plate thrust coefficients, with maximum variations of 28% and 72% for x- and z-direction values respectively. This is due to the differences in simulated vortex strength that affects thrust at all angular locations. This is in comparison to torque that is less sensitive to vortex strength at some angular locations, as discussed in Chapter 4.

5.3 Comparison to Experimental Results

5.3.1 Aim of section

This section presents results from simulations of the MRL turbine operating in equivalent conditions to the experimental work presented in Chapter 2. Two-dimensional results are firstly presented, followed by a number of three- dimensional results. The aim is to compare the magnitude and trends of simulated performance coefficients to those from the experimental work, in order to assess the reliability of the CFD model.

5.3.2 Approach

5.3.2.1 Two-dimensional simulations

MRL turbine simulations have been run with parameter values matched to the experimental flume. Compared to previously presented simulations, the inlet

Table 5.3.1: 2D flume geometry, operating condition and simulation parameter values

Parameter	n	c	R_b	u_{inlet}	Ti	TVR	Mesh	$\Delta\theta$	B
	(-)	(m)	(m)	(m/s)	(%)	(-)	(-)	(°)	(%)
Value	3	0.05	0.055	0.87 1.05 1.22 1.40	4.0	1243 1503 1763 2023	Test 22	0.5	23

Table 5.3.2: 2D domain dimensions for experimental flume simulations

Dimension	x_{max}	x_{min}	z_{max}	z_{min}
Value (m)	2.8	-2.8	0.3	-0.3

conditions are changed; four inlet velocities are simulated, with turbulence intensity and viscosity ratio matched to the flume flow, as shown in Table 5.3.1. A range of BSR values have been simulated as before, but in smaller increments of $BSR = 0.05$.

The domain dimensions were also matched to the experimental flume, as shown in Table 5.3.2. The two-dimensional simulation domain remained one cell thick, which effectively modelled an infinite span turbine. However, all results were converted to represent the torque or power generated by $0.22\,m$ of blade span, in order to directly compare to the experimental results.

All simulations use a domain height matched to the flume (i.e. 0.6 m), with the turbine axis located at mid-height. Note, a number of boundary conditions were also changed in comparison to previous simulations, as set out in Chapter 3. For example, the bottom boundary represented the flume bed, and was set with no-slip conditions. The mesh was therefore adjusted to incorporate inflation layers at this face, as shown in Figure 5.3.1. The top boundary represented the water surface boundary, and in order to simplify the simulation, slip conditions were used. This ensured the flow was constrained by this surface but not affected in any other way, allowing a relatively coarse mesh to be used in this area. The upstream and downstream distances were set at $20\,D$, in order to ensure fully developed inlet flow at the turbine location.

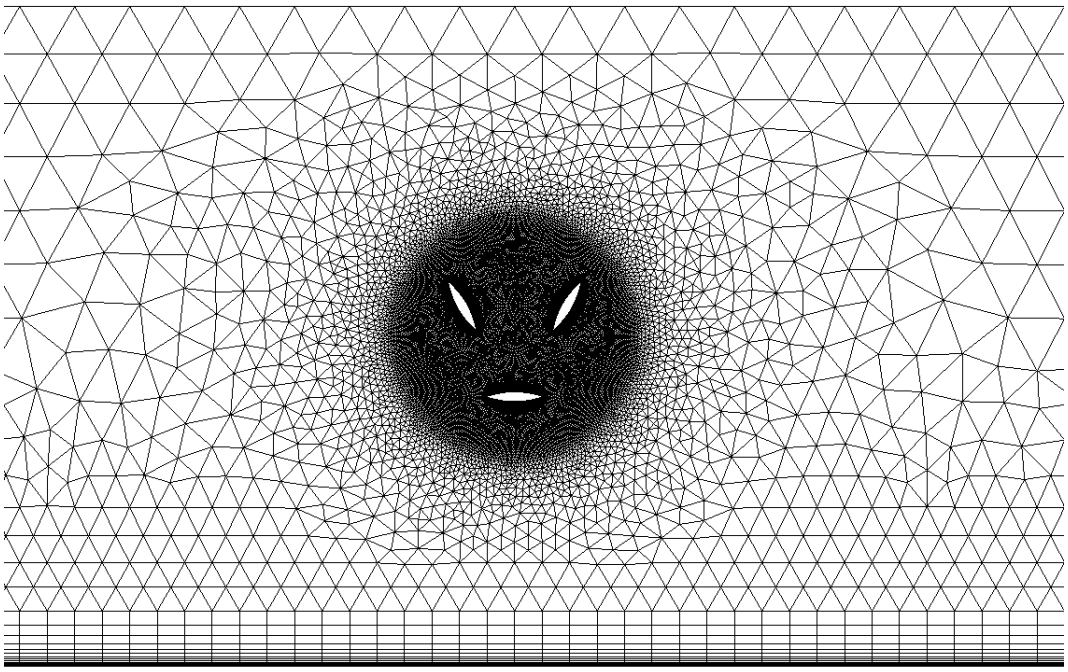

Figure 5.3.1: View of the computational mesh in the two-dimensional flume domain

Table 5.3.3: 3D flume geometry, operating condition and simulation parameter values

Parameter	n	c	R_b	u_{inlet}	Ti	TVR	Mesh	$\Delta\theta$	B
	(-)	(m)	(m)	(m/s)	(%)	(-)	(-)	(°)	(%)
Value	3	0.05	0.055	0.87 1.04	4.0	1243 1503	Test 22	0.25	9

5.3.2.2 Three-dimensional simulation

The three-dimensional simulations were primarily run with one set of inlet conditions ($u_{inlet} = 1.04\,m/s$), at a range of BSR values. A second inlet velocity ($u_{inlet} = 0.87\,m/s$) was simulated at $BSR = 0.6$ only, in order to allow direct comparison of simulation and experimental velocity profiles. The time-step was reduced in comparison to the two-dimensional simulations; this was required in order to improve simulation stability. The general setup is shown in Table 5.3.3.

The three-dimensional domain was identical in the x-z plane (at $y = 0$) to the two-dimensional domain discussed above. However, it modelled a finite y-direction distance, with $y_{max} = 0.3\,m$ matching the experimental flume. One half of the experimental model blade span ($y_b = 0.11\,m$) was simulated, with

a symmetry plane located at $y = 0$. Therefore, the total flume width was effectively modelled with 50% of the required computational expense. Again, all results were converted to represent the torque or power generated by 0.22 m of blade span, in order to directly compare to the experimental results.

In order to create the mesh, the two-dimensional blade and turbine mesh regions (i.e. Rotors 0-3) were extruded along the y-axis in increments of 5mm, as shown in Figure 5.3.2a. However, at the blade tip the increments were gradually reduced in size, in order to successfully blend into the inflation layers that extend from the blade end surface. In order to link these inflation layers to the remainder of the extruded mesh, a small region of unstructured tetrahedral cells were used, as shown in Figures 5.3.2b and c. This type of cell was also used in the majority of the domain region (i.e. outside of the extruded Rotors 0-3 and away from non-slip boundary faces), in order to minimise the total cell count. The resulting total cell count for both two- and three-dimensional domains are given in section 5.3.3.1.

5.3.2.3 Choice of turbine geometry

In all simulations presented previously in this chapter, the turbine blade chord and radius dimensions have matched the experimental model presented in Chapter 2. However, only the blades themselves have been modelled, and no support structure.

To allow the most reliable comparison of simulation and experimental results, the support structure would be incorporated into the simulations. The two-dimensional flume simulations represent only the mid span of the turbine, and therefore a central shaft (diameter 6 mm) has been incorporated into the mesh, in order to assess its effect on torque production.

In addition, the three-dimensional simulations would ideally incorporate the end plates, pulley housing and other supporting framework. This would require the full span of the flume to be modelled, as the experimental model was not symmetrical about the mid plane (due to the pulley housing). It would also greatly increase the complexity of the mesh, and increase the cell count and computation time. Therefore, only the turbine blades have been modelled in the three-dimensional simulations presented here. This also allows a more direct comparison to be made between the two- and three-dimensional results.

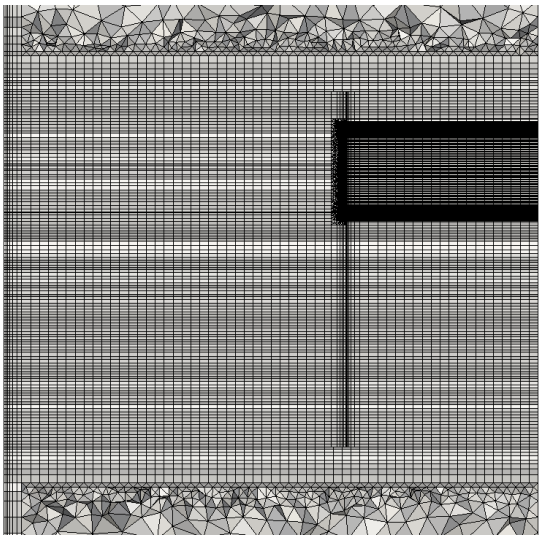

(a) Cross-section through turbine region (showing one blade region)

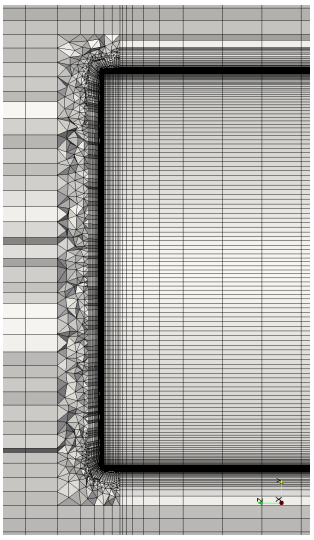

(b) Cross-section through blade tip region

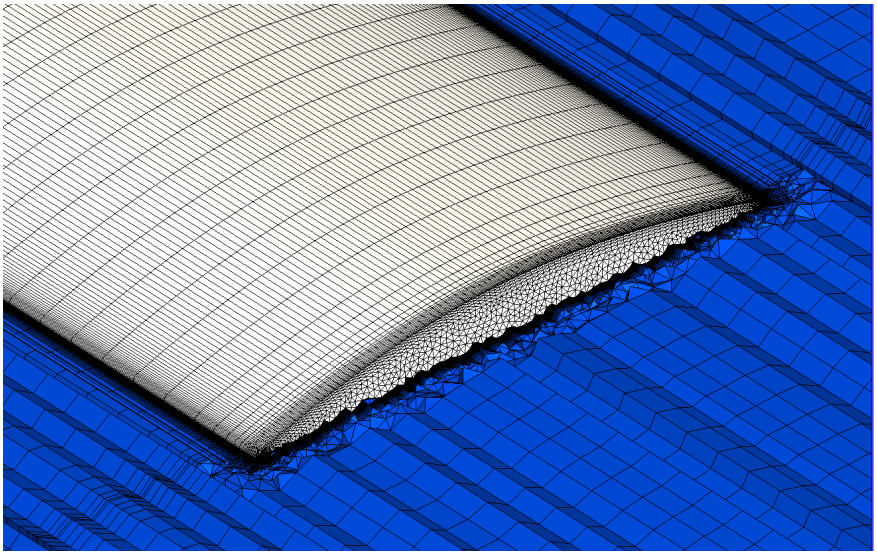

(c) View of blade tip surface mesh

Figure 5.3.2: Views of the computational mesh in the three-dimensional flume domain

Table 5.3.4: 2D and 3D flume domain total number of cells and simulation duration

Domain	No. Proc.	No. Cells	Simulation duration, 1 cycle		
			BSR=0.2	*BSR*=0.5	*BSR*=0.9
			(hours)	(hours)	(hours)
		$x10^5$	Final	Final	Final
2D	1	0.84	16.6	3.7	6.0
3D	60	43.8	91.4	30.0	27.8

Only simulations involving MRL blade profiles, rather than flat plates, are presented in this section. Whilst this has been shown to introduce non-physical spikes in torque, the cycle-averaged blade torque results varied by less than 9% in comparison to the flat plate results (as presented in section 5.2) and are considered sufficiently representative.

5.3.3 Results

5.3.3.1 Simulation times

The total cell count for both two- and three-dimensional simulations are shown in Table 5.3.4, along with the number of parallel processors used and the time taken to simulate one turbine cycle, for three values of *BSR*.

The results show the three-dimensional mesh contains approximately 52 times as many cells as the two-dimensional mesh and therefore required a much greater amount of computational resource. Although the former simulations were ran on 60 times the number of processors, it took between 4.6 and 8.1 times as long to compute one turbine cycle and are therefore much less practical as a design development tool.

5.3.3.2 Overview of results

Figure 5.3.3 shows the torque and power coefficient results for the two- and three-dimensional flume domain results, with comparison to the experimental results presented in Chapter 2.

The following observations are immediately apparent:

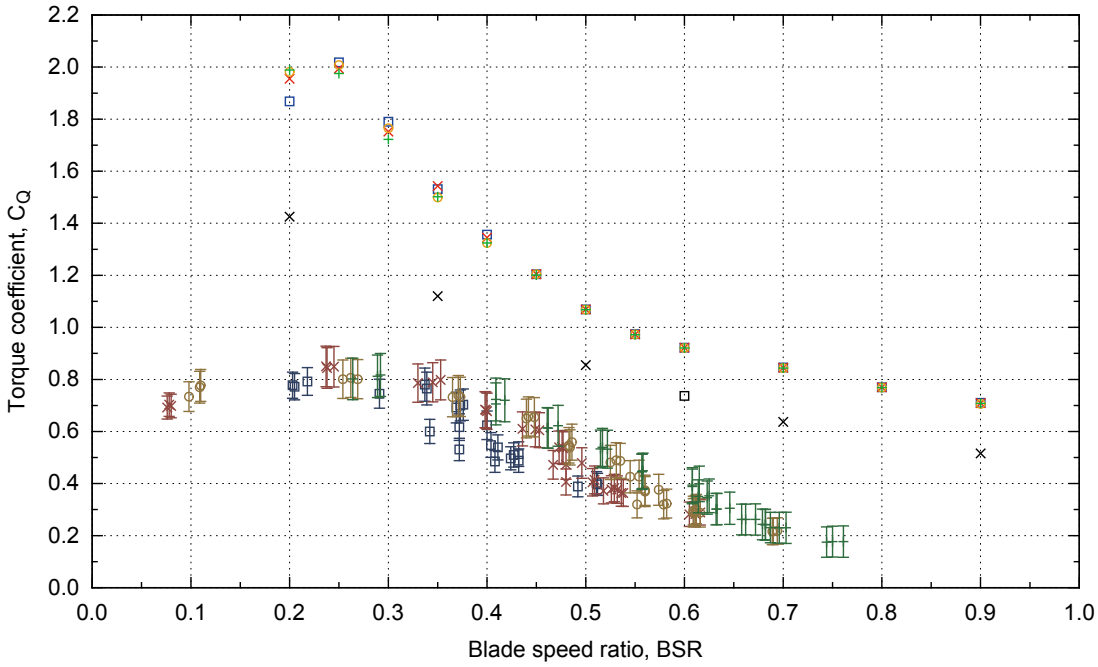

(a) Torque coefficient

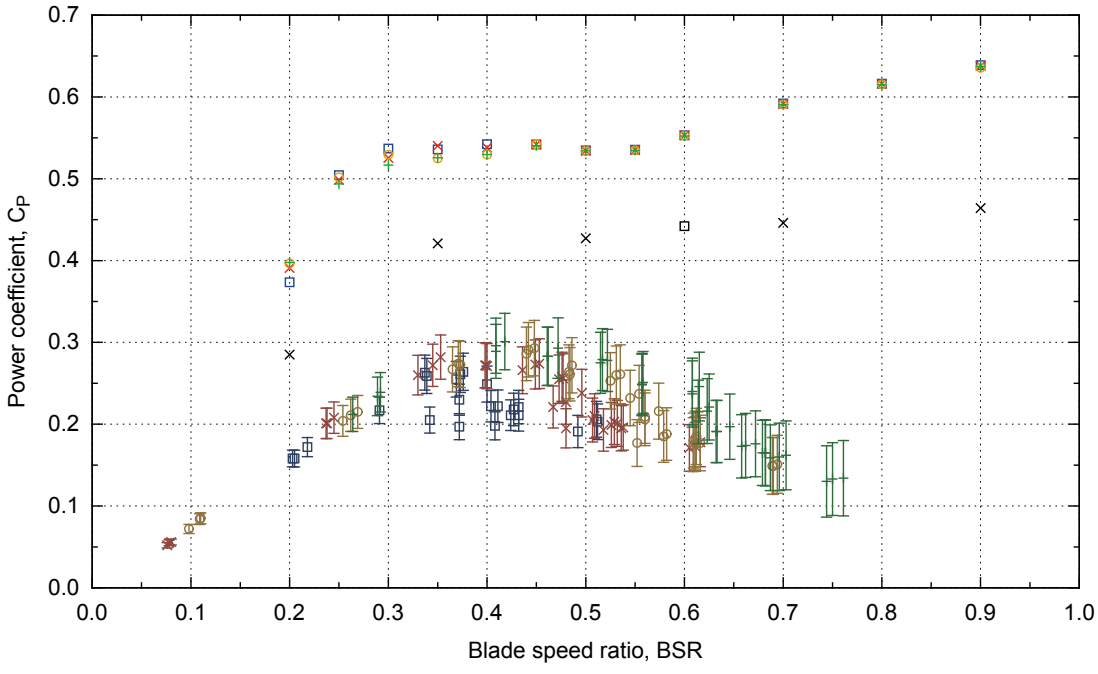

(b) Power coefficient

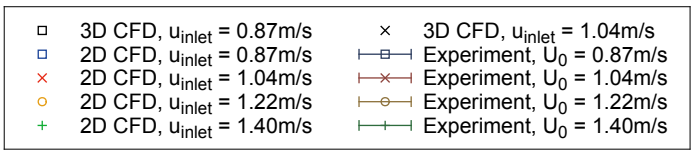

Figure 5.3.3: Variation of performance coefficients with BSR value, comparing experimental results with 2D and 3D simulation results

1. The torque coefficient results show a similar trend with *BSR* in all sets of simulation and experimental results
2. The power coefficient results show a similar trend at lower values of *BSR* but there is a divergence at values above $BSR = 0.5$
3. Changing the value of inlet flow velocity has minimal impact on the magnitude of simulation performance coefficients
4. The three-dimensional simulation results yield a significant reduction in torque and power compared to the two-dimensional simulation results
5. There is a significant difference in magnitude between all simulation results and the experimental results

The above points are discussed in more detail in the following sections.

5.3.3.3 Effect of two-dimensional domain height and central shaft

In order to understand the effect of decreasing the two-dimensional domain height, one set of results from Figure 5.3.3 are also shown in Figure 5.3.4. The latter shows the variation of torque, power and thrust coefficients with BSR, for two-dimensional flume and infinite domain CFD simulations ($u_{inlet} = 1.04\,m/s$ and $u_{inlet} = 1.00\,m/s$ respectively). In addition, the flume domain results are shown for cases both including and excluding the central turbine shaft.

All three sets of results show a trend of decreasing torque coefficient with increasing *BSR* value, with the exception of the increase seen from $BSR = 0.20$ to $BSR = 0.25$ in the flume-domain results.

The central shaft causes a minor reduction in torque at lower values of *BSR*, with a maximum variation of 4.7% at $BSR = 0.25$. This is likely due to interaction between shaft wake and the downstream blade. At higher values of *BSR* the shaft has negligible impact, which is likely due to the reduced magnitude of useful torque generated in the downstream half-cycle.

The variation between results in the two different domains is more pronounced, with the flume domain yielding an increase in torque coefficient of approximately 18% of the peak value, consistently throughout the *BSR* range. This is likely due to an increase in incoming flow velocity at the turbine, due to an increased blockage ratio, although the domain inlet velocities were approximately equal.

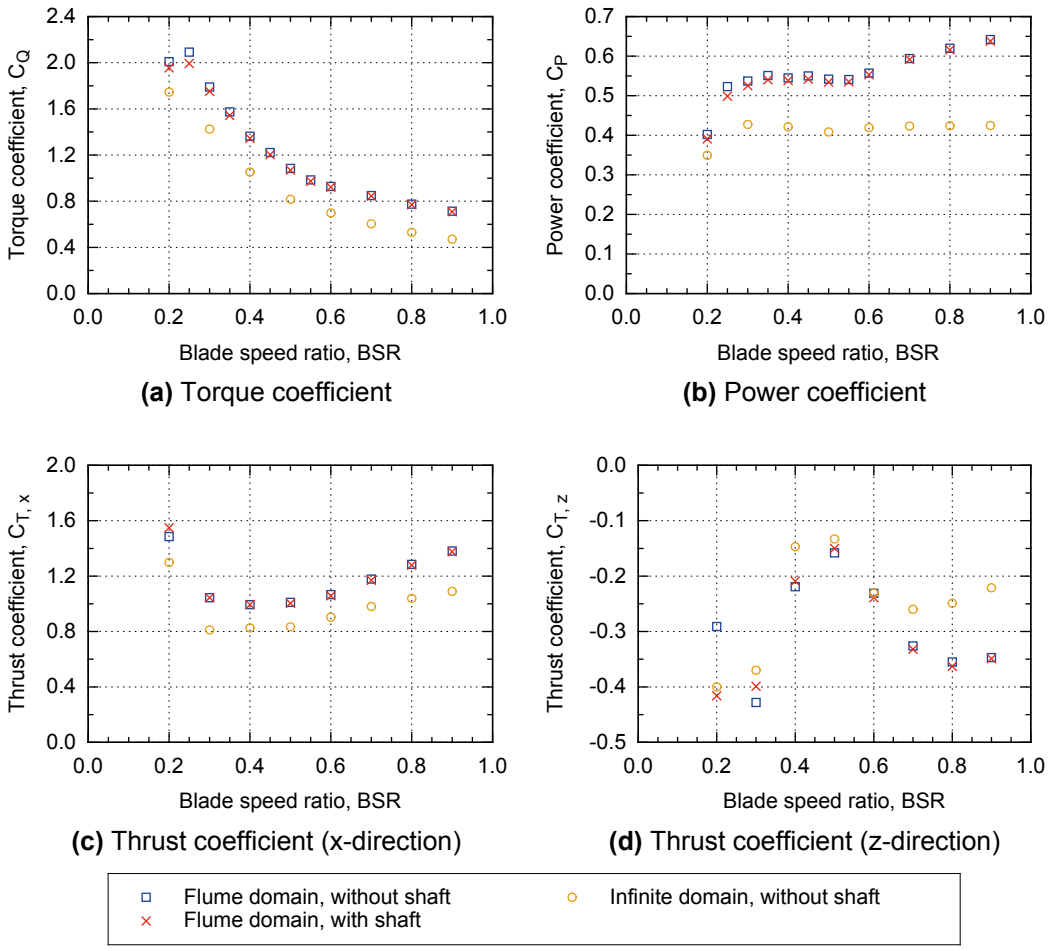

Figure 5.3.4: Variation of performance coefficients with BSR value, comparing 2D infinite domain ($B = 5\,\%$) and flume domain ($B = 23\,\%$) results

Both of these trends are also repeated in the power coefficient graphs, although as *BSR* increases, the magnitude of variation between the infinite and flume domain results is magnified. This is because the increasing rotational velocity has a greater influence on power at higher *BSR* values. This serves to highlight how sensitive the shape of the C_P vs *BSR* curve is to magnitude of torque coefficient; even though the absolute variation in torque coefficient is approximately equal throughout the *BSR* range, the power coefficient curve diverges strongly as *BSR* increases.

The relationship between flume and infinite domain results is also repeated for thrust coefficient results. The x-direction flume domain results are increased by a similar magnitude throughout the BSR range, in comparison to the infinite domain results. The z-direction results show greater variation at low and high BSR values, while results are similar at $BSR = 0.5$ and 0.6. An outlier to this trend occurs at $BSR = 0.2$, where the magnitude of the flume domain (without shaft) result is lower than the infinite domain result.

Overall these results show that increasing the blockage ratio of the domain, and therefore increasing the flow velocity at the turbine will increase useful power output but also increase the forces acting on the turbine in both the flow and perpendicular directions.

Regardless of domain, optimal hydrodynamic performance is achieved at $BSR = 0.4-0.5$ where the power coefficient is near maximum and the x- and z-direction thrust coefficient magnitudes are minimised. At this operating point the useful energy extracted will be maximised and the forces acting on the mooring system will be minimised. However, if the turbine operates at higher rotational speed, the torque transferred through the drive-train will be reduced, while the CFD results show power output remains near maximum or may even increase. This may be beneficial to the life of the components of the drive train, such as gear box. However, the thrust acting on the turbine mooring system would also increase and therefore would need to be designed accordingly.

5.3.3.4 Effect of inlet flow velocity

As discussed previously, the simulation torque coefficient results shown in Figure 5.3.3 show a decreasing trend with increasing *BSR* value. This trend is repeated at all inlet flow velocities used in the simulations. In addition, the

results vary little with inlet flow velocity; a typical difference of less than 2% is seen between $u_{inlet} = 0.87\,m/s$ and $u_{inlet} = 1.40\,m/s$ results at $BSR \leq 0.45$, although this does increase to 12% in one case ($BSR = 0.20$). This shows the proportion of energy in the flow that is converted into rotational energy of the turbine central shaft is generally independent of inlet velocity, at the values investigated here.

5.3.3.5 Effect of three-dimensional simulation

In comparison to the two-dimensional simulation results, the three-dimensional simulations yield a significant reduction in torque and power coefficient throughout the *BSR* range. The magnitude of torque coefficient reduction varies with *BSR* value, although the percentage reduction is approximately constant at 20-25% throughout. The magnitude of reduction is therefore greater at lower values of *BSR*.

Figure 5.3.5 shows comparison of the time-varying total torque (acting on a 0.22 m span turbine) for two- and three-dimensional simulations at four values of *BSR*. Also shown is the effect of including the central shaft, as discussed previously.

The results show the three-dimensional results generally follow the same variation with rotor angle as the two-dimensional results, at all values of *BSR*. This shows that the time-varying behaviour of two-dimensional simulations is generally representative of three-dimensional simulations, except in magnitude of the forces produced at any point in a cycle.

This overall reduction in force and torque could be attributed to two factors:

1. Reduced area blockage resulting in a reduced mean flow velocity along the total blade span
2. Additional vorticity formation at the blade ends reducing the total force acting on the blades

The reduced blockage is a result of the increased width of domain and finite blade span used in the three-dimensional simulation. Therefore, as the domain height was unchanged from the two-dimensional domain, the area blockage ratio was decreased from 23% to 9%. The effect of this on velocity immediately

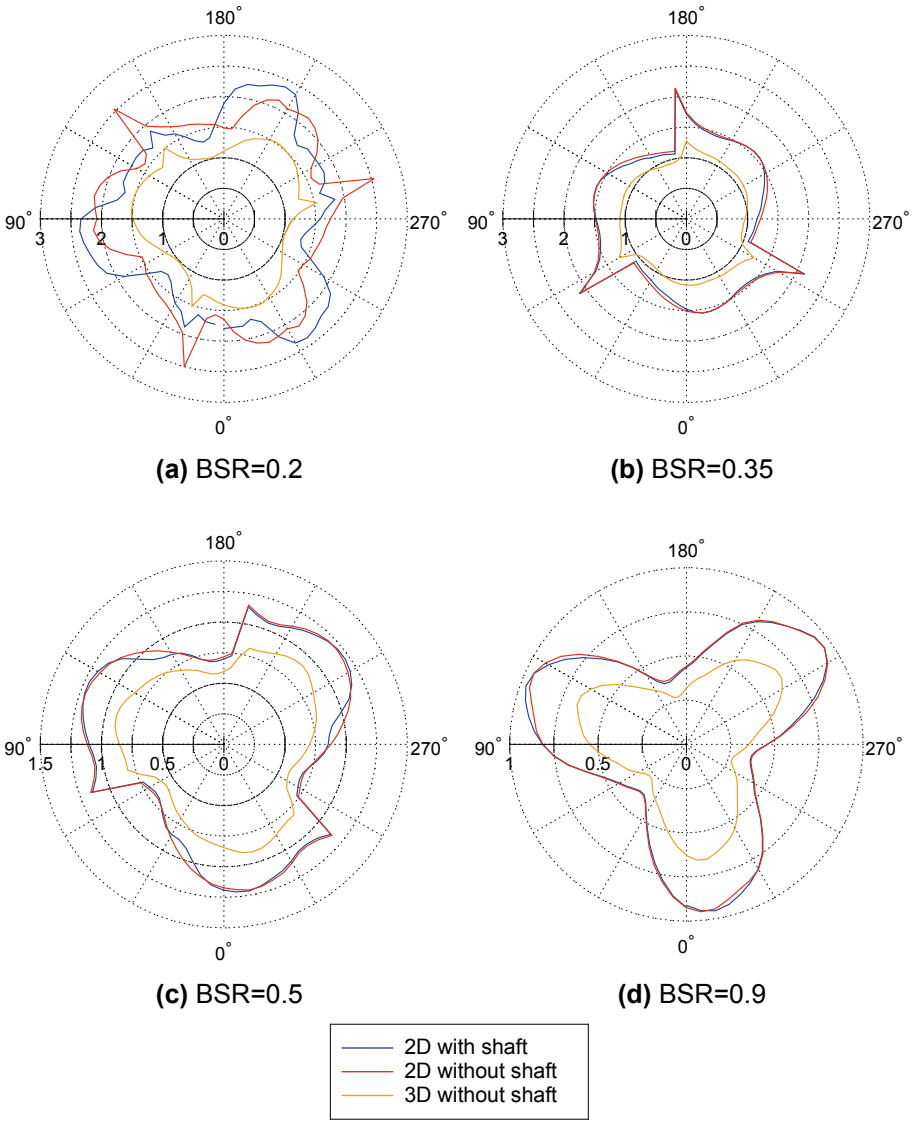

(a) BSR=0.2 **(b)** BSR=0.35

(c) BSR=0.5 **(d)** BSR=0.9

Figure 5.3.5: Variation of total turbine torque (Nm per 0.22m span) with rotor angle, comparing 2D and 3D flume domain results

upstream and downstream of the turbine, at both the blade mid-span and axis-depth locations, is shown in Figures 5.3.6 and 5.3.7. Also shown are processed experimental results at the $x = 1\,D$ location; note the mid-depth results show two sets of results, representing both sides of the turbine blade span (i.e. in the positive and negative y direction). The positive y-direction represents the side of the turbine where the pulley housing was located and the negative y-direction represents the end of the turbine with only an end plate present.

The mid-span graphs (Figure 5.3.6) show the three-dimensional, upstream, x-direction velocity at $z = 0\,m$ is approximately unchanged from the two- dimensional simulations. There is a greater change above and below the turbine swept area, where the velocity is decreased by up to 3.5%. There is also a greater reduction, of up to 11%, in these bypass areas $1\,D$ downstream of the turbine axis. Here the simulated velocity profile also matches well to the experimental results, although there is a large discrepancy directly downstream of the turbine, in the wake area. However, the bypass flow velocity likely has little effect on the torque production, as it does not interact with the turbine blades. The upstream, z-direction flow velocity in the two- and three-dimensional simulations is also well-matched through the turbine swept frontal area (at the mid-span location) and therefore it is unlikely to account for the significant variation in total torque.

The mid-depth results (Figure 5.3.7) show that in the three-dimensional simulations the flow does direct along the blade span, with the span-wise y-direction velocity gradually increasing in magnitude towards the blade tip, before decreasing to zero at the flume wall. Note however, the upstream peak y-direction velocity component is only 5.6% of the upstream x-direction component at the blade tip (i.e. $y = 0.11\,m$). The graph also shows the upstream x-direction velocity is relatively constant along the blade span, with an increase of approximately 7% near the blade tip, compared to the mid-span value. The two-dimensional simulations effectively simulate an unchanged x-direction velocity component along the blade span (i.e. equal to the mid span value) and therefore the three-dimensional velocity profile results do not indicate that the significant reduction in torque and power is due to a decrease in inlet flow velocity at the turbine location.

In order to gain further insight into the variation of torque with blade span, the time-varying results from discrete 0.01 m segments of an individual blade span are shown in Figure 5.3.8, for four values of *BSR*. Only four segments are

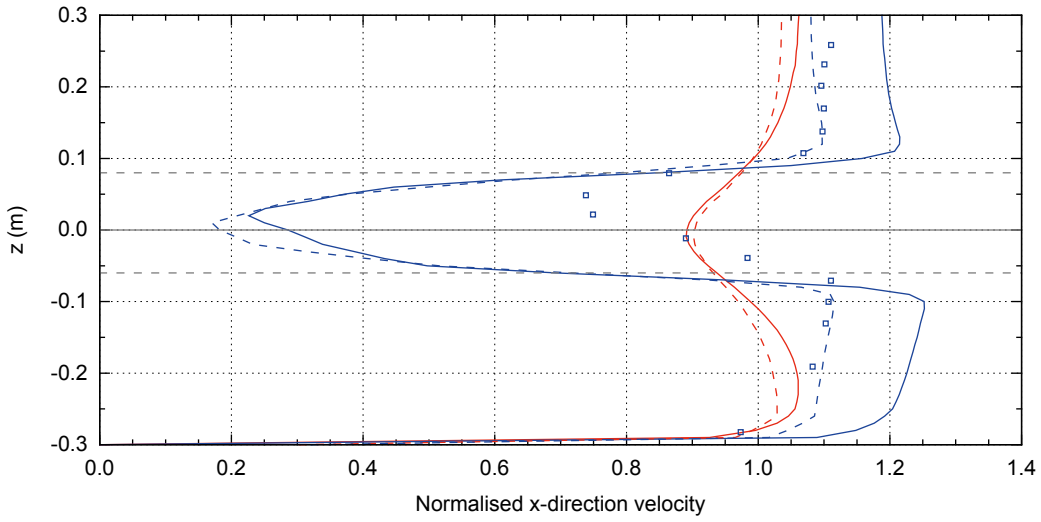

(a) x-direction velocity

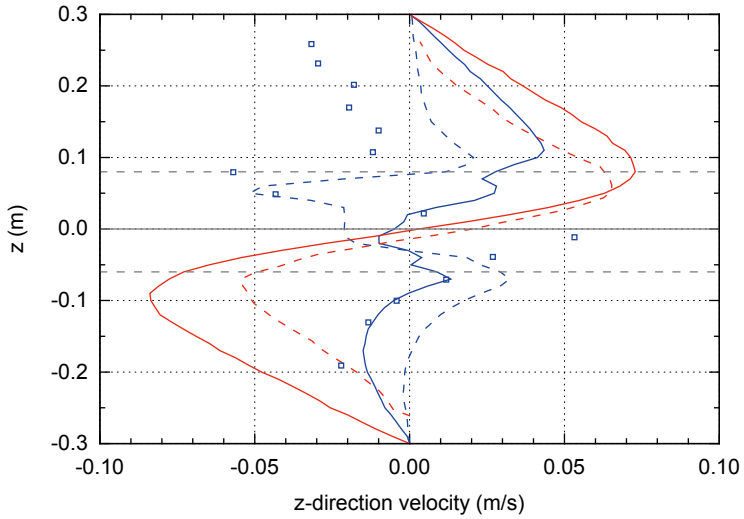

(b) z-direction velocity

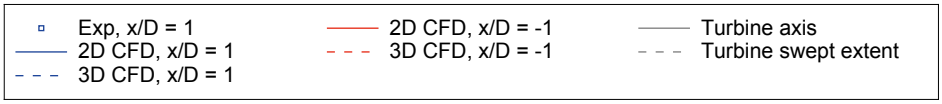

Figure 5.3.6: Cycle-average velocity profiles at blade mid-span, comparing experimental results with 2D and 3D simulation results ($\bar{U}_0 = u_{inlet} = 0.87\,m/s$, $BSR = 0.6$)

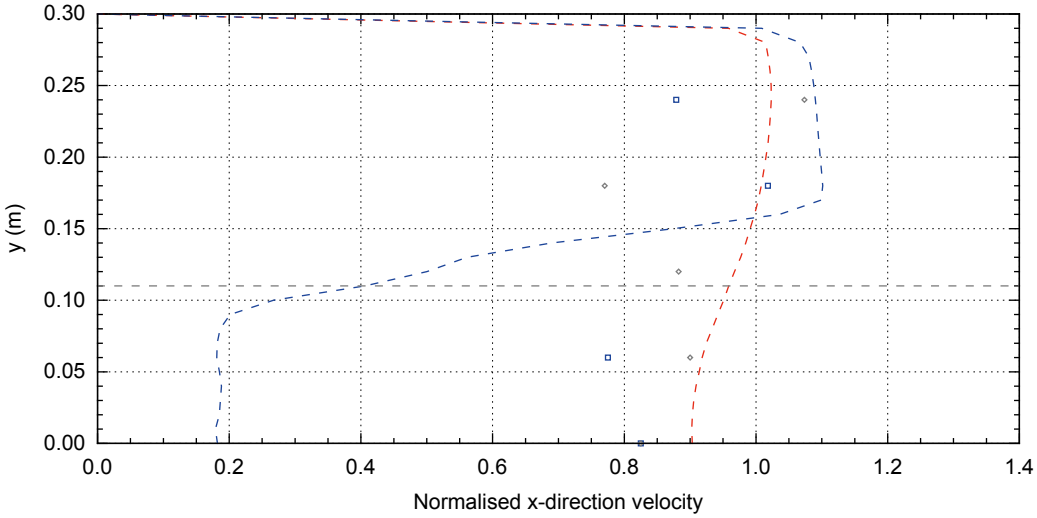

(a) x-direction velocity

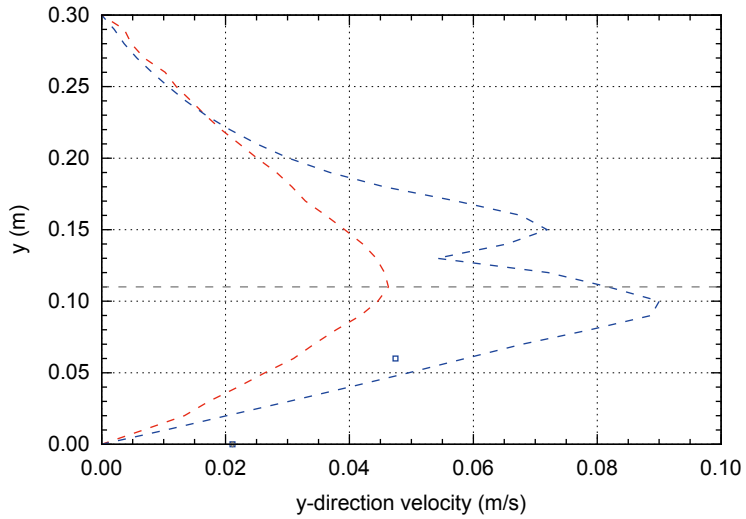

(b) y-direction velocity

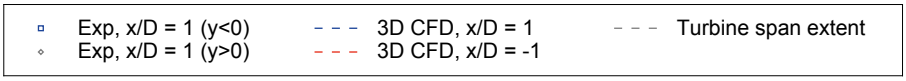

Figure 5.3.7: Cycle-average velocity profiles at blade axis-depth ($\bar{U}_0 = u_{inlet} = 0.87\,m/s$, $BSR = 0.6$)

shown, along with the two-dimensional results, in order to aid clarity. The results have all been converted to torque per metre span, in order to allow direct comparison.

The results firstly show that at the mid-span ($0.00 < y < 0.01\,m$), the three-dimensional peak values are reduced in comparison to the two-dimensional results, in both the upstream and downstream half-cycles for all values of *BSR*. At $BSR = 0.5$ the magnitude of reduction is approximately equal at both the upstream and downstream peaks. At higher values of *BSR* the peak reduction in upstream torque is greater than the reduction in downstream torque, and the opposite is true at lower values of *BSR*. In fact, the reduction in magnitude is significantly larger in the second half-cycle at $BSR = 0.2$, which indicates three-dimensional flow patterns produced by the upstream blade is having a marked impact on the forces produced by the downstream blade. This is likely a result of the relatively large influence the second half cycle has on torque production at lower *BSR* values.

The second and third torque curves shown are due to forces acting in the ranges $0.08 < y < 0.09\,m$ and $0.09 < y < 0.10\,m$. Here the upstream torque magnitudes are progressively reduced in comparison to the mid-span values, at all values of *BSR*. The downstream values are also reduced, but generally to a lesser extent. However, there are significant increases in torque observed in the approximate range of $150° < \theta < 240°$. This indicates the flow structure changes significantly with blade span in this stage of a cycle. Also notable is the absence of the sudden torque spikes at these span positions, indicating the growth of leading edge vorticity and associated torque has occurred gradually in the upstream half-cycle.

The three curves discussed above represent the torque produced along 91% of the total blade span. However, it can be observed that the upstream peak values reduce by similar amounts in the first 82% of span, compared to the next 9% of span. A further significant, and similar magnitude, reduction is also seen in the final 9% of span ($0.10 < y < 0.11\,m$). This indicates the torque produced by forces acting on the upstream blade is relatively constant with span position, but reduces greatly near the blade tip.

This behaviour is visualised in Figures 5.3.9 and 5.3.10, where the iso-surfaces of vorticity magnitude are shown at a range of blade rotor positions, for two values of *BSR* (the behaviour at higher values is very similar and therefore

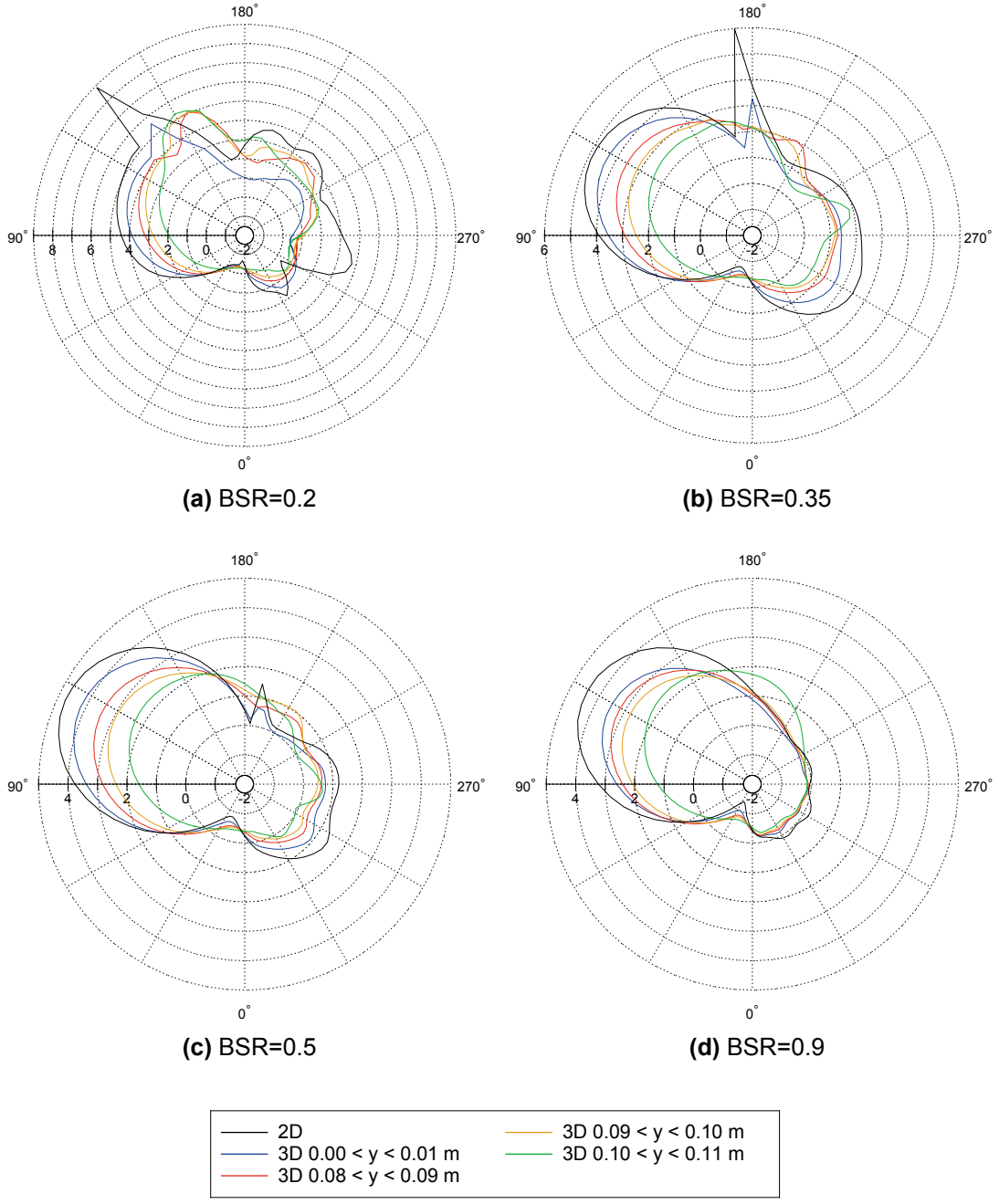

Figure 5.3.8: Variation of individual blade torque (Nm per metre span) with rotor angle, showing variation along blade span ($u_{inlet} = 1.04\,m/s$)

not shown here). Note, in contrast to vorticity contours shown previously for two-dimensional simulations, the different colour extremes of blue and red only represent magnitude of vorticity, and do not convey the rotational direction of the vorticity.

Both sets of results show that a significant amount of three dimensional vorticity is formed at the tip of the upstream blade at approximately $\theta = 60°$. This forms a trailing stream of rotating wake that stays attached as the blade angular position increases. At approximately $\theta = 180°$ the stream of wake moves away from the tip, towards the mid-span of the blade. It stays attached to the underside of the blade until approximately $\theta = 240°$, which would greatly affect the forces produced at this position, comparison to two-dimensional flow. This corresponds well to the significant variation in torque produced in the range $180° < \theta < 240°$, as shown previously in Figure 5.3.8.

Furthermore, in the range $270° < \theta < 300°$, the blade tip passes through and interacts with the tip wake trailing from the upstream blade. This may account for the significant reduction in torque observed at this position, in comparison to two-dimensional results, for both $BSR = 0.20$ and $BSR = 0.35$.

Overall, both the torque curves at discrete span-wise positions and the vorticity visualisations show the three-dimensional simulations allow a much more complex flow structure to form, in comparison to the two-dimensional simulations. In particular, the forces acting on the blade in the upstream half-cycle are markedly reduced near the tip, and in the downstream half-cycle the torque is strongly reduced across the blade span. This appears to be due to complex flow structures that form at the tips of upstream blades and interact with blades in downstream positions.

5.3.3.6 Comparison to experimental results

Trend with BSR

As previously shown in Figure 5.3.3, the simulation and experimental torque coefficient results follow the same trend with *BSR*, with peak values occurring in the range of $0.2 < BSR < 0.3$ and decreasing as *BSR* increases. However, at lower values of *BSR* the two-dimensional simulation results appear to follow a steeper gradient than the experimental results, and the opposite is true at higher *BSR* values.

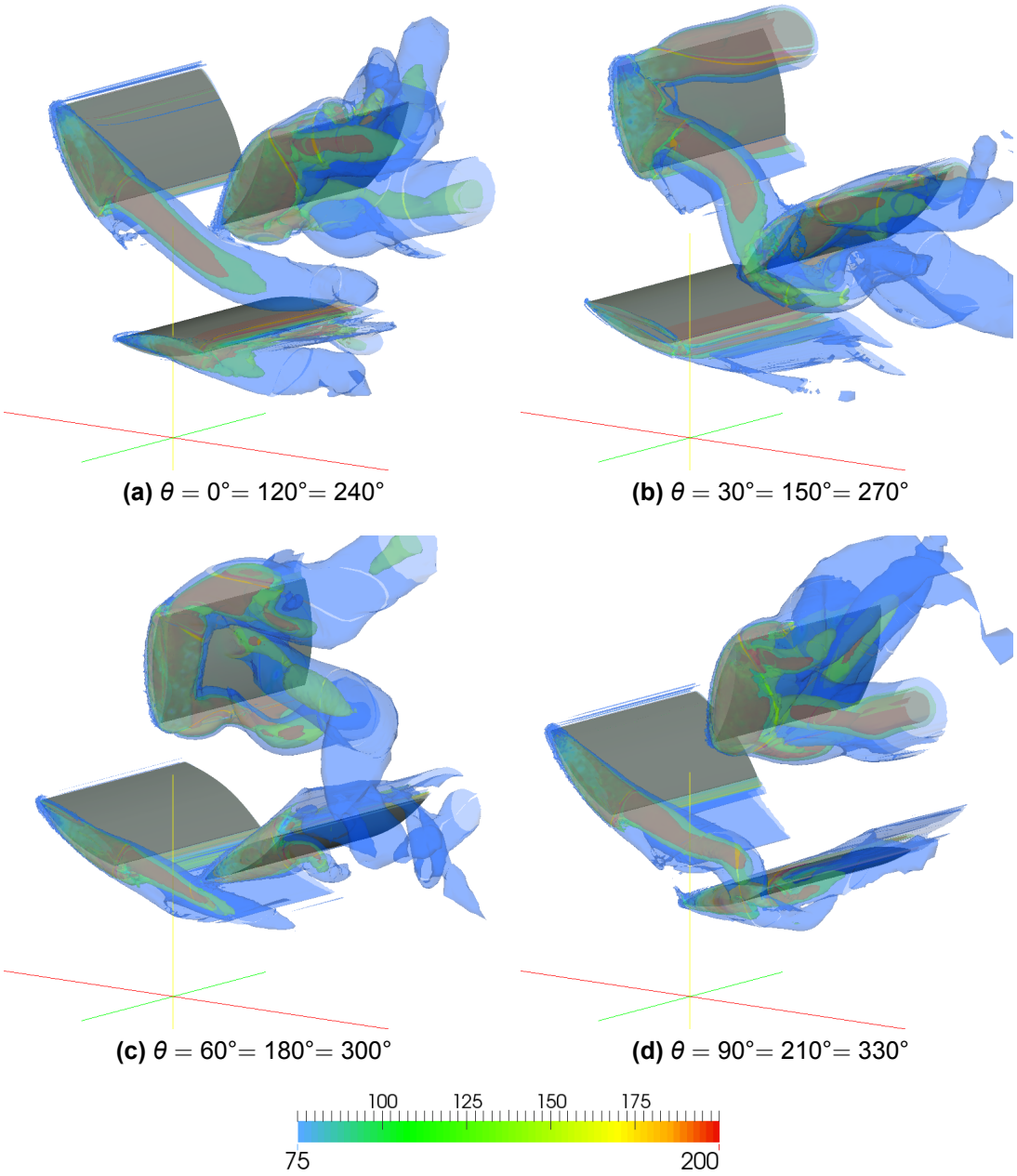

(a) $\theta = 0° = 120° = 240°$ **(b)** $\theta = 30° = 150° = 270°$

(c) $\theta = 60° = 180° = 300°$ **(d)** $\theta = 90° = 210° = 330°$

Figure 5.3.9: Variation of vorticity magnitude with rotor angle, for 3D flume simulation ($BSR = 0.2$)

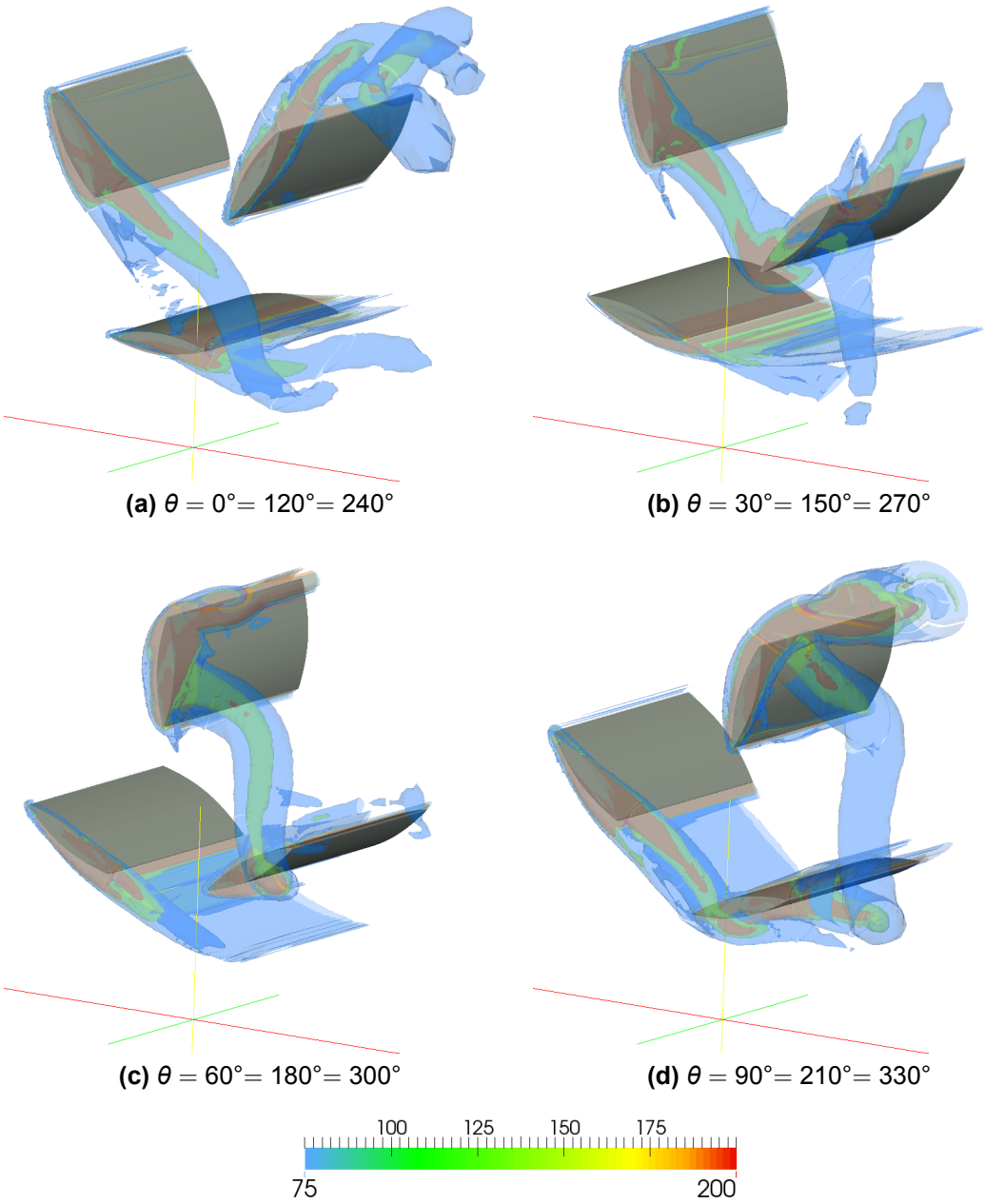

(a) $\theta = 0° = 120° = 240°$ **(b)** $\theta = 30° = 150° = 270°$

(c) $\theta = 60° = 180° = 300°$ **(d)** $\theta = 90° = 210° = 330°$

Figure 5.3.10: Variation of vorticity magnitude with rotor angle, for 3D flume simulation ($BSR = 0.35$)

The three-dimensional simulations reduce the gradient at lower *BSR* values, as the absolute magnitude of torque reduction is greater at $BSR = 0.2$ than at $BSR = 0.35$ and 0.5. However, between $BSR = 0.5$ and $BSR = 0.9$ the magnitude of reduction is more consistent and therefore the gradient appears to still diverge from that of the experimental results.

The power coefficient simulation and experimental curves show a similar shape, with an increase up to an initial peak that occurs in the range of $0.3 < BSR < 0.5$. At higher values the experimental results decrease towards zero, but the simulation results continue to increase. This is an effect of both the overall higher magnitude of simulation torque results, and the observed gradient decrease at values of $BSR > 0.5$. The three-dimensional results appear to match the gradient at lower *BSR* values to that of the experimental results, and diverge to a lesser degree at higher values (due to the relative reduction in torque magnitudes).

Magnitude

There is a large difference in magnitude between simulation and experimental results throughout the *BSR* range investigated. For example, at $BSR = 0.2$, the two-dimensional simulation torque coefficient is approximately 140% higher than the experimental result (at $\bar{U}_0 = u_{inlet} = 0.87\,m/s$), although at $BSR = 0.5$ this difference is reduced to approximately 110% (at $\bar{U}_0 = u_{inlet} = 1.04\,m/s$). As previously discussed, the three-dimensional simulation results are reduced significantly from the two-dimensional results, which brings the results closer to those from the experimental work. However, the simulation results are still 82% and 70% higher than the experimental results at $BSR = 0.2$ and $BSR = 0.5$ respectively.

Three potential reasons for the large variation between simulation and experimental results are suggested below:

1. The CFD simulations are significantly over-predicting the magnitude of forces acting on the blades and in turn, the torque acting about the central axis

2. The experimental method significantly under-estimated the model resistance torque

3. Comparison of simulated 0.22 m span blades to the experimental results is not fully valid, due to the particular geometry of the experimental model

The first point may account for part of the discrepancy between results, due to the tendency of the CFD simulations to over-predict the peak lift and drag forces acting on a rotating blade. There are no time-varying force and torque results available for a blade or plate undergoing MRL motion, and so conclusions must be inferred from the simply-pitching plate results presented in Chapter 4.

That work shows that at the lower pitch rates tested (e.g. $0.03 \leq K \leq 0.1$) the first peak lift force was overestimated by between 7% and 23%, in comparison to experimental data. Also, the peak drag force was overestimated by between 40% and 120%. This range of pitching frequency theoretically corresponds to the range of conditions encountered by blades in an MRL turbine rotating at $BSR = 0.2$, which suggests the turbine CFD torque results at the lowest *BSR* values could be over-predicted by significant amounts. It also corresponds to the range of conditions encountered through the majority of a turbine cycle (up to $\theta = 120°$), for *BSR* values up to 0.6. However, at higher values of angular position (up to $\theta = 180°$), these *BSR* values yield reduced frequencies up to $K = 1.0$. In this range, the pitching plate CFD results yielded much better agreement to experimental data, although final drag was still over-predicted by 33% in some cases.

The above serves to highlight the magnitude of uncertainty that is inherent in the CFD results, which may well be over-predicting the forces and torque developed by the physical model. However, as the flow developed by the motion of the blades is so complex (as highlighted previously during this chapter), and it is not possible to directly compare the flow at the majority of *BSR* values to that around a simply-pitching plate (as discussed in Chapter 4), it is very difficult to confidently state the uncertainty inherent in the CFD results.

The second point, that the experimental method used significantly under- estimates the model resistance torque, may also account for part of the discrepancy between simulation and experimental results. However, the uncertainty in the experimental results was discussed in detail in Chapter 2, and while there are a relatively large number of estimations made, it is unlikely the resistance torque is under-estimated by between 70% and 80%.

The third point is considered the most likely source of error between the simulation and experimental results. This is because of the geometry and support

structure of the physical turbine model, as presented in Chapter 2, which makes direct comparison of experimental and simulation results less reliable.

If the turbine model had a high aspect ratio (e.g. 10), with a large span in comparison to the total swept height, the two-dimensional simulations would give a more valid representation of the physical situation. However, the aspect ratio of the turbine model was relatively low (i.e. 1.57) and therefore three-dimensional effects are expected to have had a relatively large impact on the experimental results. This suggests the three-dimensional simulation results are more valid than the two-dimensional results in this case.

The three-dimensional simulations included representations of the blades tips, but no support structure such as end plates. In some cases, end plates in physical turbine models can help make the flow more "two-dimensional", by limiting the span wise flow and end losses. However, the three-dimensional simulations showed the velocity of flow in the span-wise direction was relatively low, but vortices formed at the blade ends had a large impact on the reduction of torque developed by downstream blades.

In the physical model, the blade tips were separated 1.6 *cm* from the end plates by a bearing housing and spacer, rather than being directly attached as in many Darrieus turbine models, and so tip vortices may have been able to form within this space. This means the three-dimensional simulations may give a valid representation of how the flow over downstream blades is affected by the upstream tip vortices, which leads to large reductions in overall torque and power.

However, the rotating end plates may have also developed a complex spinning boundary layer on their inner faces, and this vorticity would have interacted with the flow at both ends of the blades, possibly further reducing the span of blade that effectively generated driving torque.

In addition, one of the end plates had a significantly larger diameter than the other, as it was attached to the pulley-system housing. This housing would have created a significant amount of local blockage, accelerating flow around it. Evidence for this can be seen in Figure 5.3.7a, where the general shape of the experimental x-direction velocity profile matches reasonably to the simulation results, but only for one side of the turbine span (i.e. y<0). Here the velocity is reduced directly downstream of the blades, accelerated in the side bypass region (i.e. at $y = -0.18\,m$) and decelerating near the flume wall. In contrast,

at the $y > 0$ side, the flow is reduced to a lesser extent directly downstream of the blades, and also reduced where the pulley housing is located (i.e. at $y = 0.18\,m$), before being accelerated near the flume wall (i.e. at $y = 0.24\,m$). This inconsistency of wake profile across the blade span indicates the asymmetrical turbine geometry had a significant effect on the total generated torque. Any span wise flow would have interacted with the end plates and increased the complexity of the flow structures in the turbine. Overall this may have led to a significant reduction in torque generated by the turbine blades, when compared to a more uniform flow situation.

5.3.3.7 Conclusion of section

This section presented results from two- and three-dimensional simulations of the MRL turbine operating in equivalent conditions to the experimental work presented in Chapter 2. The magnitude and trends of simulated performance coefficients were compared to those from the experimental work and the following was observed:

- The *BSR* values where peak experimental torque and power occur are well predicted by the CFD simulations
- The trend of decreasing torque coefficient with increasing *BSR* is well matched between experimental and simulation results
- The three-dimensional simulations introduce flow structures that cause a significant reduction in the torque developed by the turbine
- Both sets of simulations yielded significantly higher torque and power values than the experimental work

A range of reasons for the large discrepancy between simulation and experimental results were discussed, but ultimately, without more detailed experimental results, it is not possible to determine the exact reason(s). However, as the general trends match, especially for torque coefficient, it is considered that the two-dimensional simulations yield a generally reliable representation of the flow structures developed within the turbine. As the two-dimensional simulations are much less computationally expensive than the three-dimensional alternative, the latter are more suitable for use in analysis and development of the turbine design.

5.4 Simulation of Alternative Turbine Geometry

5.4.1 Aim of analysis

This section presents results from simulations that were run with a number of geometry variations, including chord length and total number of blades. The aim is to use CFD simulations as a tool in the development of the turbine design, in order to maximise the power output throughout the BSR range.

5.4.2 Approach

A number of simulations have been run using the standard setup used previously in this and preceding chapters. In particular, the infinite domain and MRL blade profiles were simulated (rather than flat plates). Two sets of simulations were run, with further details shown in Table 5.4.1.

A blade mid-span thickness of 18% of the chord length was maintained throughout the simulations, except for a second set of simulations at $c = 0.085\,m$; here the mid-span thickness was matched to that of the $c = 0.05\,m$ blade, giving a thickness value of 10%. The aim was to assess the effect of blade length separately from thickness.

A chord length of $c = 0.085\,m$ was the largest that could be simulated using the sliding mesh technique, and this was achieved by minimising the distance between the blade tips and rotor boundary, and also the distance between Rotors 1-3, as shown in Figure 5.4.1.

5.4.3 Results

5.4.3.1 Effect of chord length

Figure 5.4.2 shows the variation of torque, power and thrust coefficient with BSR, for the four simulated chord lengths (and two thicknesses at $c = 0.085\,m$).

The results show that increasing chord length generally leads to a decrease in torque and power coefficient, and an increase in thrust coefficient magnitude, at a given BSR value. The effect is significant, with peak power coefficient at $BSR = 0.4$ reducing by 36% from $c = 0.03\,m$ to $c = 0.085\,m$. An exception

Table 5.4.1: Turbine simulation geometry and operating condition values

Parameter	n	c	R_b	u_{inlet}	Ti	TVR	Mesh	$\Delta\theta$	x_{max}/D	B	σ
	(-)	(m)	(m)	(m/s)	(%)	(-)	(-)	(°)	(-)	(%)	(-)
Value	3	0.030	0.055	1.0	1.0	150	As Test 22	0.5	10	5	0.64
		0.050									1.07
		0.070									1.50
		0.085									1.82
	2	0.050	0.055	1.0	1.0	150	As Test 22	0.5	10	5	0.71
	3										1.07
	4										1.43
	5										1.79

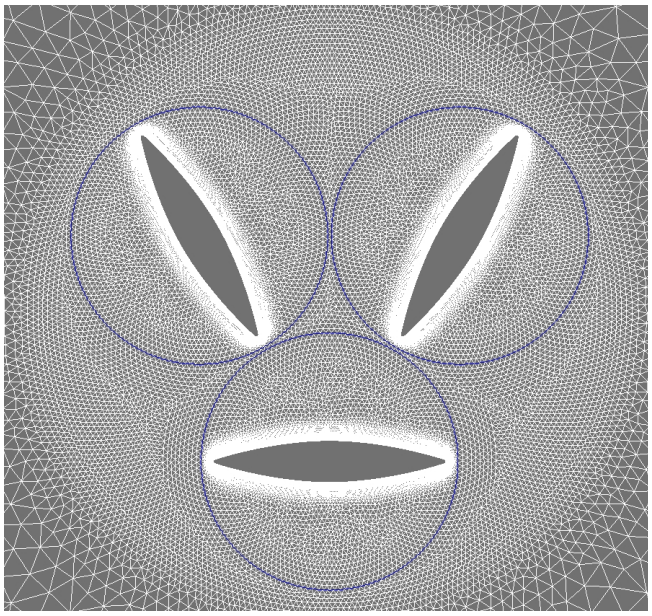

Figure 5.4.1: Diagram of $c = 0.085\,m$ mesh, with boundaries of Rotors 1-3 shown in blue

to this trend is at $BSR = 0.2$, where the maximum torque is produced by the $c = 0.07\,m$ turbine and the minimum by the $c = 0.03\,m$ turbine. The results also show minimal variation between the two sets of results at $BSR = 0.085\,m$, indicating that chord length, rather than blade thickness, is primarily responsible for the general observed behaviour.

The sets of results generally converge to similar values as BSR increases, although this effect is also dependent on chord length, with the higher values converging sooner, and $c = 0.03\,m$ results not converging by $BSR = 0.9$.

Figure 5.4.3 shows the effect of chord length on the time-dependent development of torque by both an individual blade within the turbine and the total of all three blades.

The individual blade results show that, generally, the same variation of torque with angular position is simulated at all chord lengths, albeit with differing magnitudes. At $BSR = 0.5$ (which is representative of all other values except $BSR = 0.2$), increasing chord length generally increases the torque magnitude in the upstream half-cycle, but in turn decreases the downstream magnitude. The former behaviour is directly linked to the length of blade, with a greater surface area increasing the magnitude of forces developed. However, increasing blade length increases the solidity of the turbine, and therefore blockage of blades in the downstream half-cycle. This likely leads to a reduction in flow velocity (i.e.,

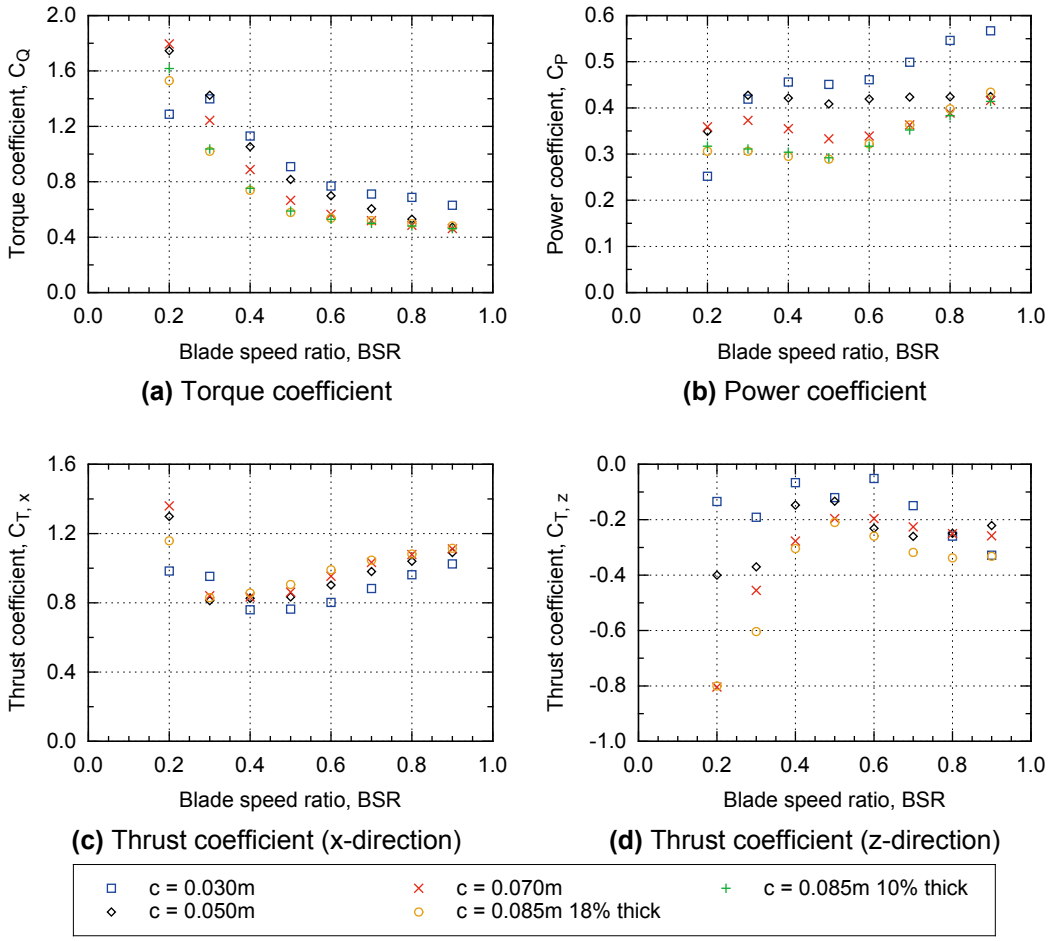

Figure 5.4.2: Variation of performance coefficients with BSR value, comparing blade chord length ($n = 3$)

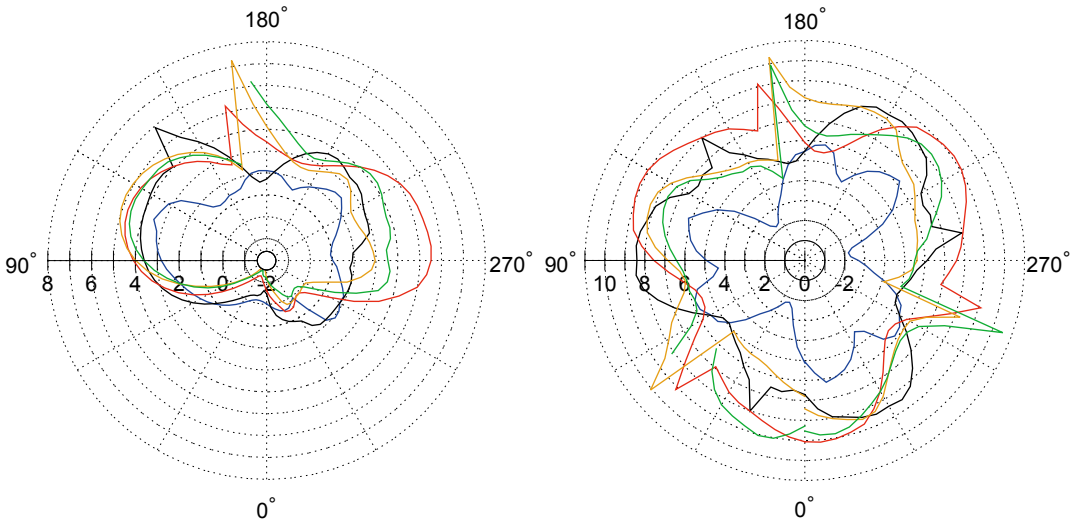

(a) $BSR = 0.2$

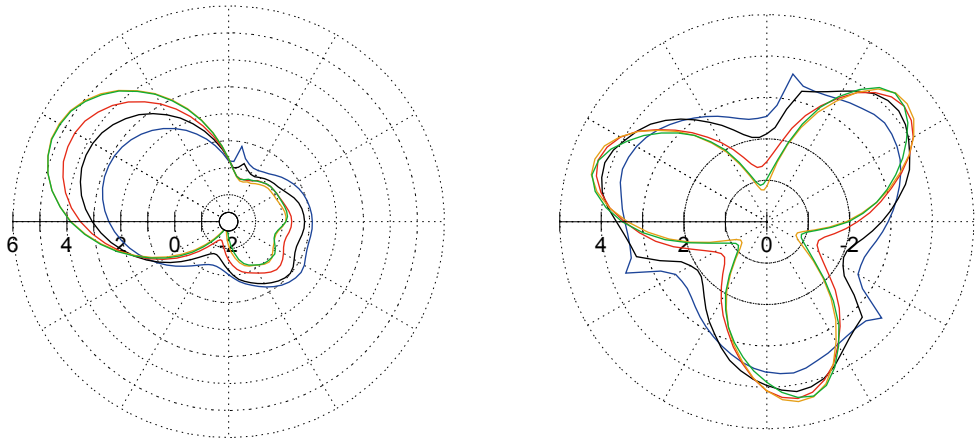

(b) $BSR = 0.5$

i) Individual blade ii) All blades

c = 0.03m
c = 0.05m
c = 0.07m
c = 0.085m 18% thick
c = 0.085m 10% thick

Figure 5.4.3: Variation of individual blade and total torque with rotor angle, comparing the effect of blade chord length ($n = 3$)

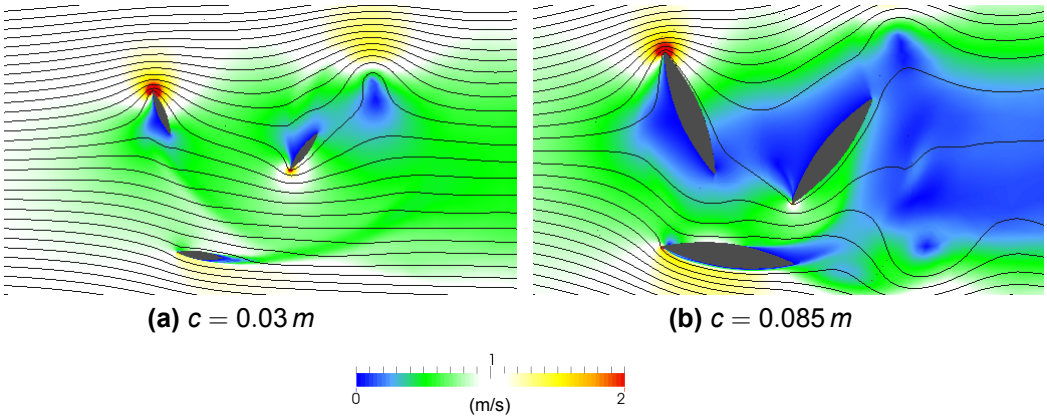

Figure 5.4.4: Visualisation showing effect of chord length on flow velocity streamlines around a three-blade turbine at $BSR = 0.5$ ($\theta = 15°= 135°= 255°$)

an increase in the induction factor for downstream blades) and reduction in the magnitude of developed forces.

A further and very important observation is that increasing chord length leads to a greater magnitude of negative, parasitic torque at approximately $\theta = 20 - 30°$. It is likely that the reduction is partly due to increased body drag and skin friction linked to increased frontal and surface areas. However, Figure 5.4.4 shows that flow deflection also has an significant impact when the blade is at $\theta = 15°$. From visualisation of the $c = 0.03\,m$ results at this position, it can be seen that the flow impinging on the blade leading edge is nearly aligned with the blade chord. In contrast, the $c = 0.085\,m$ results show the impinging flow is at a significantly negative angle of attack, therefore producing higher forces acting in the positive x-direction and negative z-direction (contributing to parasitic torque). This deflection of flow is due to the increased size of the preceding blade, which strongly affects the flow field within the turbine region.

The total torque curves are strongly affected by the magnitude of this negative value, with greater chord lengths yielding a greater degree of torque variation throughout a cycle. At $BSR = 0.5$, the peak total torque values are also relatively equal (apart from $c = 0.03\,m$), which is a result of the interaction between the torques developed by the three separate blades at any point in the cycle. Therefore, increased upstream peak values developed by one blade are offset by reduced torque values developed by the other blades at the same point in time.

At $BSR = 0.2$, an increase in upstream torque is observed for increasing chord

length, and the majority of results follow similar shaped profiles. However, the $c = 0.03\,m$ results are notably different in profile, with a sudden reduction in torque at approximately $\theta = 120°$. This is likely due to the shedding of an attached vorticity region that is not simulated at higher chord lengths. In the downstream half-cycle, the results do not follow the same trend as at higher *BSR* values; instead, the torque values increase up to a peak at $c = 0.07\,m$ before reducing at $c = 0.085\,m$. This accounts for the torque coefficient values discussed previously.

Overall, the simulations generally show that increasing chord length leads to a decrease in cycle-averaged total torque throughout the *BSR* range. The optimum chord length tested is $c = 0.03\,m$, which gives the maximum (or very close) power coefficient at all *BSR* values apart from $BSR = 0.2$. Whilst individual blades develop lower magnitudes of peak torque in the upstream half-cycle, the down-stream blades are less effected by blockage and turbulence, producing higher magnitudes of torque in comparison to higher chord length turbines.

5.4.3.2 Effect of total blade number

Figure 5.4.5 shows the variation of torque, power and thrust coefficient with *BSR*, for the four simulated total blade numbers.

The results show that a turbine with three blades develops the maximum torque and power coefficients at *BSR* values of 0.4 or less, and a two-blade turbine develops the maximum at higher *BSR* values. Increasing the total blade number to four or five generally reduces the coefficients at all *BSR* values.

Increasing blade number also generally increases the magnitude of thrust coefficient. One exception to this is the z-direction thrust coefficient at high BSR values, where the trend reverses. A second exception is the x-direction coefficient at values of $BSR = 0.3$ or less, where values are generally similar. However, simulated thrust coefficients for a turbine with MRL blade profiles are less reliable at lower BSR values, as discussed in Section 5.2.3.2. Therefore the effect of blade number on thrust at these BSR values cannot be reliably analysed from these results.

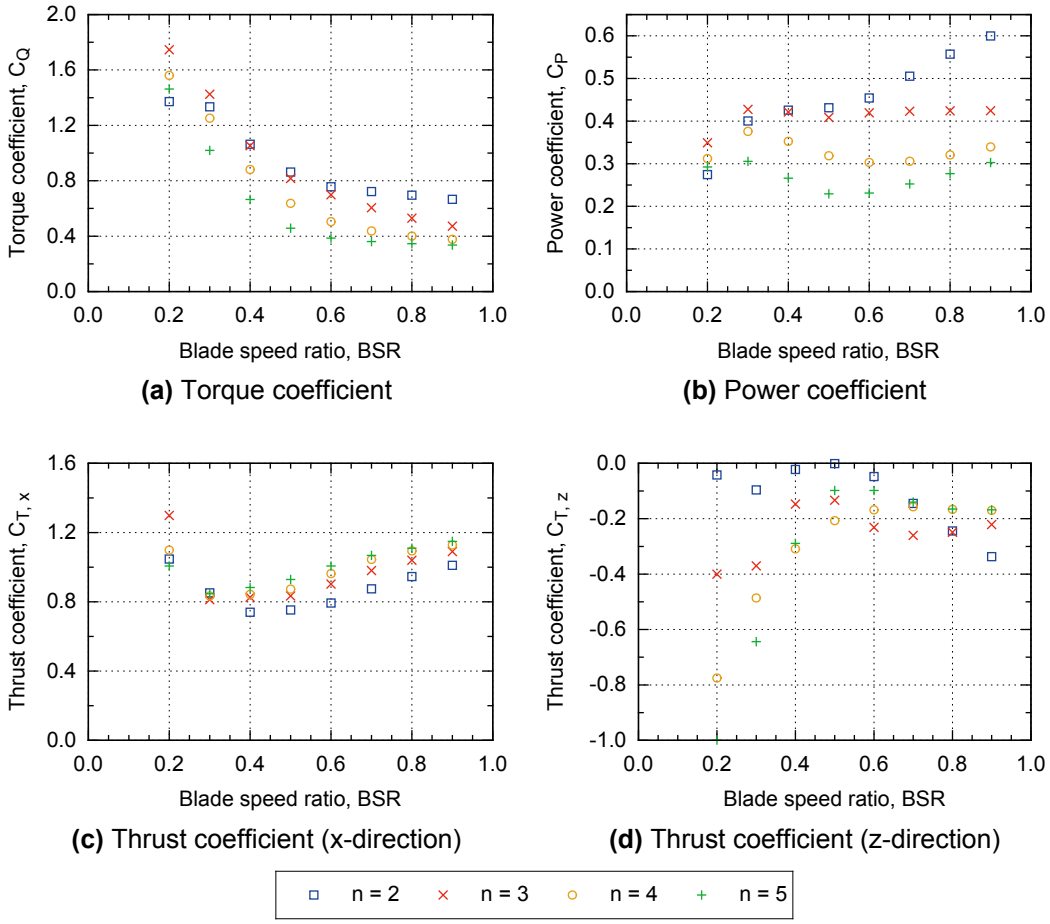

(a) Torque coefficient

(b) Power coefficient

(c) Thrust coefficient (x-direction)

(d) Thrust coefficient (z-direction)

Figure 5.4.5: Variation of performance coefficients with BSR value, comparing total number of turbine blades ($c = 0.05\,m$)

Figure 5.4.6 shows the effect of total blade number on the time-dependent development of torque by both an individual blade within the turbine and the total of all three blades.

The individual blade results show that, generally, the same variation of torque with angular position is simulated for all total blade numbers, albeit with differing magnitudes. At $BSR = 0.5$ (which is representative of all other values except $BSR = 0.2$), increasing blade number generally decreases the torque magnitude in both the upstream and downstream half-cycles. This is likely due to the increasing solidity of the turbine, and the related increase in pressure within the turbine region due to the presence of other blades . This likely leads to a reduction in flow velocity (i.e., an increase in induction factor) and reduction in magnitude of developed forces.

This effect is visualised in Figure 5.4.7, where the velocity field around the blade at $\theta = 120°$ is shown for both three- and four-blade turbines. The results indicate the flow field at the upstream face is very similar in both cases. However, around the leading edge and at the downstream face of the four blade turbine the velocity is generally reduced and therefore pressure increased, leading to to a reduction in developed torque. This reduction in velocity appears to be due to the closer proximity of the preceding blade (at a spacing of $\theta = 90°$ rather than $\theta = 120°$. This flow field behaviour will also affect blades in downstream positions and therefore reduce the developed torque through the full cycle.

When combining the individual blade torque values into a total value for the turbine, higher total blade numbers might be expected to yield higher overall torque values. However, Figure 5.4.6 also shows this is not the case. Higher blade numbers do yield more consistent torque values throughout a cycle, but due to the decrease in individual blade peak torque, the total peak values are also lower. A four-blade turbine appears to give the most consistent total torque profile, which is likely due to the shape of torque curves for individual blades, i.e, two major peaks and two local minimums per cycle, spaced at approximately $\theta = 90 - 100°$. Therefore, when four blades are combined, the peak values directly cancel the minimum values. In contrast, the two-blade turbine yields the most fluctuating total torque profile, as peaks are reinforced by peaks and minimums reinforced by minimums. The two-blade turbine is therefore the only design where the total torque profile approaches a value of zero, and even reaches negative values. This design is unlikely to self-start and would also

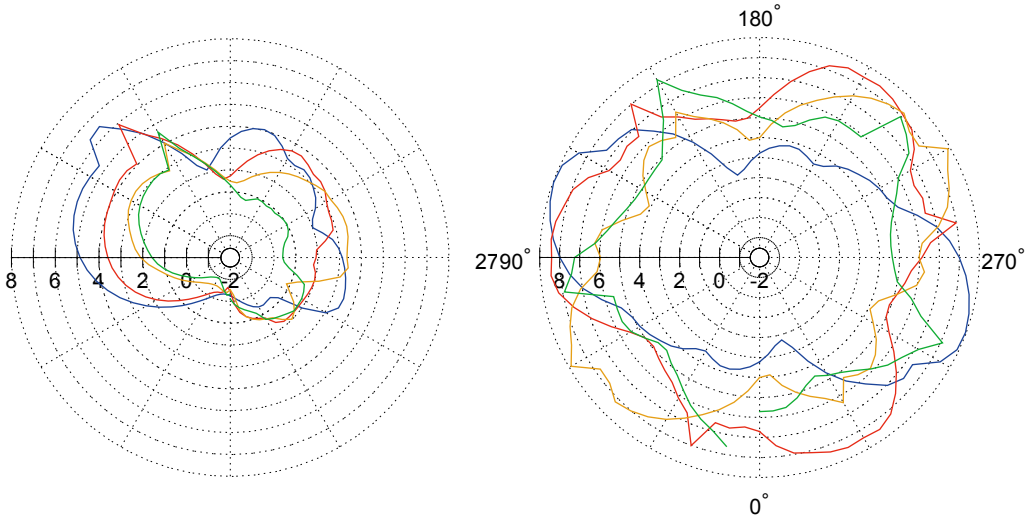

(a) $BSR = 0.2$

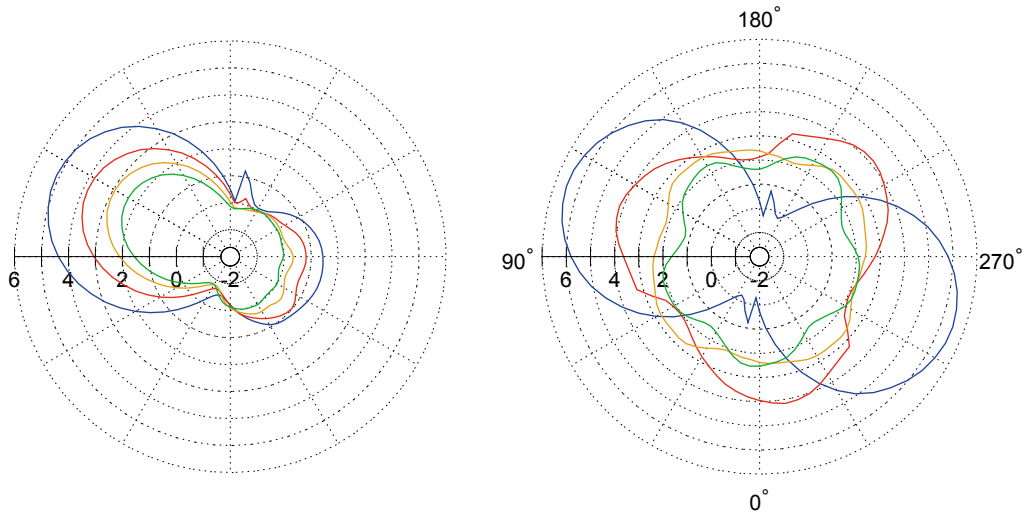

(b) $BSR = 0.5$

i) Individual blade ii) All blades

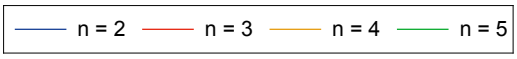

Figure 5.4.6: Variation of individual blade and total torque with rotor angle, comparing the effect of total blade number ($c = 0.05\,m$)

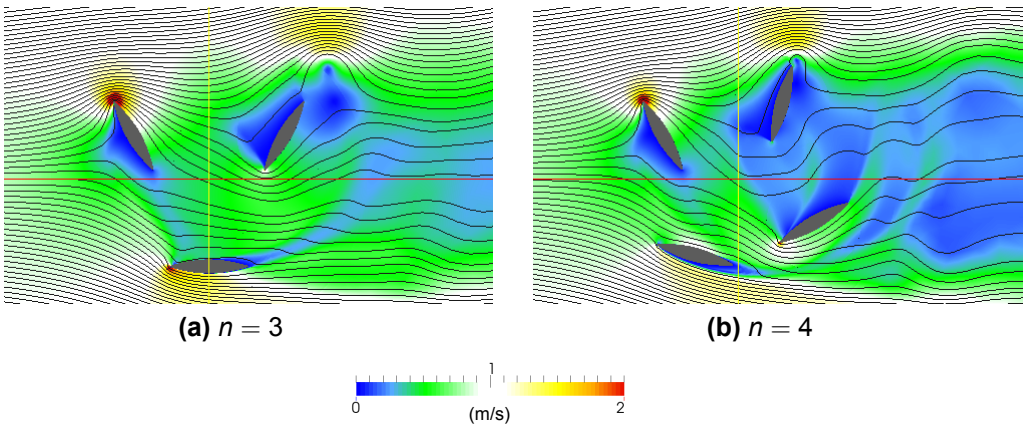

(a) $n = 3$ **(b)** $n = 4$

Figure 5.4.7: Visualisation showing effect of total blade number on flow velocity streamlines around a three-blade turbine at $BSR = 0.5$ ($c = 0.05\,m$,$\theta = 120°$)

cause fluctuating torque to be transferred to the power generation mechanisms, increasing the risk of wear and failure.

Overall, the simulations have shown that increasing total blade number generally decreases the torque and power coefficient values through the *BSR* range. However, a turbine with only two-blades is impractical and therefore three-blades is considered the optimum number for maximising magnitude of total power output, while four-blades gives the most consistent output, albeit with a significantly reduced cycle-mean value.

5.4.4 Conclusion of section

This section presented simulation results for a number of turbine solidity values. Increased solidity was achieved by either increasing chord length or total number of blades.

The simulations showed that increasing solidity generally decreased turbine torque and power output, and increased the magnitude of thrust coefficients, across the *BSR* range. Increasing the chord length results in an increased upstream torque peak but both decreased downstream peak values and decreased minimum torque values, for each individual blade. When combined, the total torque curves become less consistent and the cycle-mean torque is generally reduced. Increasing the total number of blades leads to decreased upstream and downstream peak values for an individual blade, although the minimum values remain relatively equal. When combined, increasing blade

number results in more consistent total torque profiles, but lower cycle-mean values.

It is concluded that a chord length of $c = 0.03\,m$ and total blade number of $n = 3$ yields the highest practical power output, although this combination has not been modelled directly.

5.5 Chapter Conclusions

This chapter has presented results from CFD simulations of primarily three-blade turbines, in both an effectively infinite sized domain and an experimental flume domain. The torque and power coefficient results have been compared to experimental results and the thrust coefficients and time-varying torque profiles and flow structure also analysed. Results from simulations with varying turbine solidity have also been presented.

The results firstly showed that the torque developed by each blade in a three-blade turbine is similar in profile to that developed by a single blade in MRL motion. However, the magnitude of both the upstream and downstream peaks is significantly reduced, which is likely a result of decreased velocity and increased pressure within the turbine region.

The second section presented results from two- and three-dimensional simulations of the MRL turbine operating in equivalent conditions to the experimental work presented in Chapter 2. It was observed that the *BSR* values where peak experimental torque and power occur, and the trend of decreasing torque with increasing *BSR* are well predicted by the CFD simulations. However, the simulated power coefficient trend at values of $BSR \geq 0.5$ does not match well to experimental results. This increasing power coefficient trend occurs because the simulated torque coefficient trend does not follow as steep a negative gradient as the experimental results.

In comparison to the two-dimensional simulations, the three-dimensional simulations introduce flow structures that cause a significant reduction in the torque developed by the turbine, although both sets of simulations yielded significantly higher torque and power values than the experimental work. It is suggested the discrepancy may be due to the 3D CFD simulations not modelling the support structure and asymmetrical geometry of the turbine model (in the spanwise direction).

However, as all sets of torque coefficient results follow a similar trend with *BSR*, and as three-dimensional simulations are significantly more expensive than two-dimensional simulations, the latter have been used to investigate the effect of turbine solidity on output torque and power.

Increased solidity was achieved by either increasing chord length or the total number of blades. The simulation results showed that increasing solidity generally decreased turbine torque and power output, and increased thrust coefficient magnitude, across the *BSR* range. The individual blade torque profiles showed this behaviour occurs for different reasons when varying chord length versus varying number of blades. Varying these values also has a strong impact on the consistency of the output torque profiles, and therefore it is concluded that a chord length of $c = 0.03\,m$ and total blade number of $n = 3$ yields the highest practical power output.

This page is intentionally left blank.

CHAPTER 6

CONCLUSIONS AND FURTHER WORK

6.1 Overview of study

The primary aim of this study has been to further understanding of the performance characteristics of the Momentum-Reversal and Lift (MRL) tidal-stream energy conversion device. In particular, the study has focused on the performance of a laboratory-scale device, and analysed both the time-averaged and time-varying torque and power output, and the associated fluid-dynamic structure of flow through the turbine.

In order to develop the approach of the investigation, existing studies of cross-flow wind and tidal turbines were firstly reviewed. It was found that time-dependent computational fluid dynamics (CFD) simulations are a powerful tool and offer advantages over traditional mathematical models, mainly in the ability to both model the vortex shedding behaviour within the rotor volume, and model high solidity rotors such as the MRL turbine. CFD simulations are also relatively cheap in comparison to physical experiments, especially when investigating the effect of varying design geometry and operating conditions.

If computing power is adequate, the most accurate CFD models tend to be three-dimensional time-dependent studies, using a sliding mesh approach and either LES, DES or advanced RANS techniques to model the effects of turbulence. However, two-dimensional simulations using two-equation RANS techniques are relatively inexpensive and give an insight into the flow structures that occur at the centre span of high aspect ratio turbines.

Successful CFD simulations must incorporate a detailed sensitivity analysis, ensuring that the results are independent of the key simulation parameters

such as cell size and time-step. It is also important that simulation results are compared to a set of physical experimental results in order to determine the relative accuracy of results. Cycle-mean values of torque and power, and the variation with turbine rotational speed are generally the minimum requirement for validation. Time-dependent torque development and flow visualisation allow much more detailed comparisons to be made but are relatively expensive to obtain.

Given the above findings, this study has used OpenFOAM to develop a time-dependent RANS CFD model and investigate the performance of the MRL turbine.

To allow validation of the CFD model, experiments were firstly undertaken in order to measure the cycle-mean torque and power output of the turbine when operating in a laboratory flume. Measurements of the flow velocity at a number of upstream and downstream locations were also taken, in order to allow comparison with the CFD simulation results, where appropriate.

Also, in order to allow validation of the CFD approach against time-varying data, the motion of the turbine blades was analysed. This allowed suitable experimental test cases to be identified from the literature and CFD simulation results have been compared to these.

A detailed sensitivity analysis of the MRL turbine CFD model was carried out, followed by two-dimensional simulations of the turbine involving a single-blade and three-blades. Three-dimensional simulations were also undertaken, with results compared to the gathered experimental results. Finally, the effect of varying turbine solidity was investigated with the CFD model.

This chapter firstly presents a summary of the detailed research findings and secondly discusses recommendations for further work.

6.2 Conclusions

Detailed findings of the study have previously been discussed in the various chapter conclusions. The following is a summary of the most important points.

6.2.1 Experimental analysis

6.2.1.1 Energy conversion

The existing laboratory-scale model of the MRL turbine was refitted with $c = 0.05\,m$ blades and tested in the experimental flume at Plymouth University's COAST laboratory. At this facility the turbine model was operated in current flow with measured peak velocity in the range of $\bar{U}_0 = 0.87\,m/s$ to $\bar{U}_0 = 1.40\,m/s$. The rotational velocity of the turbine was measured and the rotational resistance torque varied in order to characterise the energy conversion performance over a range of blade speed ratio (*BSR*) values. The turbine was primarily operated without side-plates, although they were added for a small number of tests.

In order to estimate the rotational resistance of the turbine, preliminary experiments and analysis were also undertaken. This work indicated that the majority of resistance inherent to the model was provided by the blade-pitch pulley control mechanism and this was relatively constant with rotational speed. Additional resistance was provided by the rotational damper pulley system, and this could be varied by selection of pulley ratio. The uncertainty in the resistance analysis method was also estimated and found to increase with rotational speed.

The flume experiment results showed a peak torque coefficient in the approximate range of $0.75 < C_Q < 0.93$ occurred at a blade speed ratio in the range of $0.2 < BSR < 0.3$. A peak power coefficient in the approximate range of $0.25 < C_P < 0.33$ occurred in the range $0.35 < BSR < 0.45$. At higher values of *BSR* both coefficients reduced towards zero at $BSR = 0.9 - 1.0$. The results from different inlet flow velocities were relatively well correlated, although variation and uncertainty in the results increased with *BSR* value. The use of side plates did not appear to increase the magnitude of peak torque or power coefficient values, but extended the width of the peak region to higher values of *BSR*.

6.2.1.2 Wake characterisation

During the COAST laboratory experiments, acoustic Doppler velocimetry (ADV) probes were used to measure the velocity at multiple locations upstream and

downstream of the turbine. The aim was to gather data that would be useful for validation of a CFD model and prove useful for other researchers focusing on the MRL turbine.

The ADV results contained significant amounts of noise and therefore a post-processing approach, based on existing de-spiking and classification techniques was presented and tuned for use with the gathered data. It was found that the modified phase-space threshold technique was successful at reducing the noise levels of both relatively clean and noisy data. However, noise levels varied significantly within each measured batch of time-series and this led to discrepancies between adjacent batch results when plotting mean velocity profiles. The cells with the most reliable results were identified by comparing the gradient of the results to the theoretical -5/3 value, when plotted in the frequency domain. The most reliable results occurred near the centre of each batch and these were used to plot time-averaged velocity profiles.

The measured velocity profiles showed the centre-span wake was not symmetrical about the central-axis depth, with a deeper wake created directly downstream of the face-on blade. The maximum velocity deficit tended to endure for a distance of approximately 5 turbine diameters downstream before recovery occurred, with 95% recovery by approximately 15 D. However, the near wake values were not uniform with transverse position, indicating the asymmetrical turbine model structure may have had a strong affect on the flow structure through the turbine.

6.2.2 Computational analysis

6.2.2.1 Development of sliding mesh RANS model

A time-dependent CFD model has been successfully developed; the model employs a sliding mesh technique to model the novel motion of the MRL turbine, and a $k-\omega$ SST sustain wall-resolved RANS approach for modelling turbulent flow. The key parameters influencing the setup of the model were defined, including a number of computational cell sizes, time-step and domain size. A sensitivity analysis was undertaken in order to find parameter values that yielded independent results, whilst minimising the duration of computations, for the full range of BSR values investigated. The selected setup yielded simulation

durations between approximately 0.4 and 1.0 hours per turbine cycle, with at least 5-10 cycles required in order to gain periodically repeating results.

6.2.2.2 Simulation of a pitching plate

The selected simulation parameters were also used in simulations of a single flat plate pitching at a constant rate about its mid axis. The aim of this work was to assess the ability of the CFD approach for modelling flow physics relevant to the MRL turbine. In order to identify suitable test cases, the motion of a blade in MRL motion was analysed, and the relationships were derived that link resultant velocity, angle of attack and reduced frequency with rotor angle. This analysis yielded a set of graphs that describe the variation of these parameters through a turbine cycle, and how these relationships vary with blade speed ratio. Generally the graphs highlighted the large variation in resultant velocity, angle of attack, and reduced frequency, K, that occur both throughout a cycle, and between different BSR values.

The most suitable pitching plate test case was identified and the CFD lift and drag coefficient profiles were compared to published experimental results. Vorticity plots also provided a qualitative insight into the flow structure formed and showed a series of leading and trailing edge vorticity regions form and shed as the plate angle of attack increases. The success of the CFD simulations in predicting physically accurate behaviour was mixed and dependent upon angle of attack and pitch rate for both lift and drag forces. The simulations were more successful at lower values of K, when focusing on lower angles of attack (where lift is dominant). In contrast, the behaviour at higher angles of attack (where drag is dominant) is better predicted at higher values of K.

An important observation from the pitching plate simulations concerns the thickness of the plate. The simulations of 2% thick plates (matching the published experimental setup) introduced sudden jumps or spikes in the force coefficient that did not appear in the simulation of a 0.4% thick plate. In the latter case the results are better matched to experimental data and the vorticity plots show the behaviour is the result of physically inaccurate sudden vorticity formation. The CFD simulation was unable to simulate the accurate development of vorticity at certain pitch rates, without a sharp leading edge.

6.2.2.3 Simulation of a single blade in MRL motion

CFD simulations were carried out that focused on a single blade undergoing MRL motion. Two thicknesses of flat plate, as well as the experimental blade profile were simulated with *BSR* values ranging from 0.2 to 0.9.

All values of *BSR* greater than 0.2 yielded a torque curve with two major peaks per cycle. The torque profiles were generally very similar regardless of blade or plate profile, except for the occurrence of a sudden spike near the mid cycle point, for thick plate and blade profiles. This sudden spike occurs in the same way as for a simple pitching plate, where the simulated leading edge vorticity region suddenly forms and sheds. It is therefore not considered an accurate representation of physical flow behaviour.

Regardless of this spike, the mean values of cycle torque for the different blade/plate profiles lay within 10% of each other at each *BSR* value, apart from $BSR = 0.4$. Here the thick plate and blade results were 20% lower than the thin plate result, which is primarily due to a significantly lower magnitude of the second torque peak. The results also show the maximum mean torque was developed when a blade/plate travels at a *BSR* value of 0.3; at higher values the mean developed torque reduces significantly, although the values levelled off at $BSR \geq 0.7$.

From visualisation of the simulated time-varying flow structure, the torque generation behaviour was linked to the formation and shedding of leading and trailing edge vorticity regions, which occur more frequently at lower values of *BSR*. At $BSR = 0.2$ and $BSR = 0.3$, the initial development of torque has been successfully compared to the flow field around a simply pitching flat plate at equivalent values of angle of attack and reduced frequency. At higher *BSR* values only a single vorticity shedding event occurs per cycle, near $\theta = 180°$. This is qualitatively similar to behaviour observed for plates pitching at reduced frequencies of $K \geq 0.2$, which is theoretically reached for all *BSR* values greater than 0.3.

From analysis of the theoretical pitch rate of a blade in MRL motion, and the accuracy of simulated pitching plate lift and drag results, it was estimated that the simulated mean torque of a turbine operating at $BSR = 0.3$ is over-predicted by approximately 20%. However, it is also noted that the the actual blade conditions of the MRL turbine include varying pitch rate and varying relative velocity, whereas the validation cases involved constant pitch rates and flow

velocity. It is therefore difficult to accurately predict the reliability of results with greater confidence.

6.2.2.4 Simulation of the MRL turbine

Simulations of three-blade turbines were carried out, in both an effectively infinite sized domain, and a domain size representing the physical experiments. The results showed that the torque developed by each blade in a three-blade turbine is similar in profile to that developed by a single blade in MRL motion. However, the magnitude of both the upstream and downstream peaks is significantly reduced, which is likely a result of decreased velocity and increased pressure within the turbine region.

Both two- and three-dimensional simulations were carried out with the experimental flume domain size. The two-dimensional simulations represent the centre span of a high aspect ratio turbine, and the three-dimensional simulations introduce blade-ends, but no support structure. The latter simulations took between 4.6 and 8.1 times as long to simulate a single turbine cycle, and were ran on 60 times the number of processors.

Peak simulated torque coefficient occurred at $BSR = 0.25$ and peak power coefficient at $BSR = 0.40 - 0.45$. These values, and the trend of decreasing torque with increasing *BSR*, are well predicted in comparison to the physical experiment results. However, the simulated power coefficient trend at values of $BSR \geq 0.5$ does not match well to experimental results. This increasing power coefficient trend occurs because the simulated torque coefficient trend does not follow as steep a negative gradient as the experimental results at the upper *BSR* range. This may be due to high levels of blockage, particularly in the two-dimensional simulations.

The three-dimensional simulations introduced flow structures that cause a significant reduction of approximately 20-25% in the torque developed by corresponding two-dimensional simulations. However, the former simulation results are still approximately 70-80% higher than the physical experimental results at corresponding *BSR* values. This discrepancy may be due to the following reasons:

1. The CFD simulations are significantly over-predicting the magnitude of forces acting on the blades and in turn, the torque acting about the central axis

2. The experimental method significantly under-estimated the model resistance torque

3. Comparison of simulated 0.22 m span blades to the experimental results is not fully valid, due to the particular geometry of the experimental model

The first reason may be responsible for part of the discrepancy (in the region of 20% as discussed above) but it is unlikely to account for a greater amount. It is more likely that the discrepancy is due to the 3D CFD simulations not modelling the support structure and asymmetrical geometry of the turbine model (in the span-wise direction). The experimental wake measurements indicated that the flow structure through the turbine was not consistent with blade span, and therefore comparing the experimental results to 3D simulations involving only open ended blades is not fully valid.

However, as all sets of torque coefficient results follow a similar trend with *BSR*, and as three-dimensional simulations are significantly more expensive than two-dimensional simulations, the latter were used to investigate the effect of turbine solidity on output torque and power. Increased solidity was achieved by either increasing chord length or the total number of blades. The simulation results showed that increasing solidity generally decreased turbine torque and power output across the *BSR* range. Varying these values also has a strong impact on the consistency of the output torque profiles, and therefore it is concluded that a chord length of $c = 0.03\,m$ and total blade number of $n = 3$ yields the highest practical power output for the options tested.

6.2.3 Performance of the MRL turbine

6.2.3.1 Energy conversion

The experimental and computational results indicate that a (three-dimensional) MRL turbine can operate with a peak power coefficient in the range of $C_P \approx 0.3 - 0.4$. This compares to a typical peak of $C_P \approx 0.4$ and $C_P \approx 0.15$ for Darrieus and Savonius turbines respectively. This suggests the MRL turbine

could be a viable alternative to the Darrieus design, in situations where cross-flow turbines are to be used (e.g. shallow water environments).

It is recognised that the MRL design operates at relatively low rotational speeds ($0 < BSR < 1$), compared to Darrieus turbines ($3 < BSR < 7$). The former operating range is similar to Savonius turbines, but the MRL turbine offers significantly better peak performance than this design. The MRL turbine is therefore a promising solution where low rotational speed operation is desired, which may be beneficial for protection of aquatic species from the effects of blade strike (Amaral et al., 2015) or noise (Frid et al., 2012).

6.2.3.2 Torque production

Although the peak power coefficient is similar to the Darrieus turbine, the magnitude of torque coefficient is generally much greater (as expected due to the significant difference in typical rotational speed). For example, the experimental and computational results indicate a torque coefficient in the range of $C_Q \approx 0.8 - 1.2$ is achieved at the rotational speed of peak power output. This compares to $C_Q \approx 0.1$ for the Darrieus turbine. This shows the MRL design is capable of harnessing a much higher proportion of the flow force acting on the blades, and converting these forces into useful torque.

The effect of MRL blade motion was discussed in detail in Chapter 4 and the analysis showed the peak conversion of lift force into driving torque is theoretically 100% for the MRL turbine, compared to 20% for the Darrieus turbine. The MRL turbine is designed to also convert 100% of drag forces into useful torque at the mid-cycle position, whereas drag forces consistently contribute 100% to parasitic torque in the Darrieus turbine.

The reason for this is the combination of operating at $BSR < 1$ and employing the MRL blade pitch motion. The former ensures the x-direction component of relative flow velocity always acts in the positive direction, and results in the following:

- Developed lift force contributes highly to tangential force during the mid-portion of each half-cycle (e.g., peak conversion of lift into torque occurs in the range of $90° < \theta < 160°$)

- Developed drag force contributes highly to tangential force during the mid-portion of the complete cycle (e.g., peak conversion of drag into torque occurs at $\theta = 180°$)

The above is only beneficial if the angle of attack of the blade results in high lift and drag forces being developed at these angular locations. For example, if the Darrieus turbine operates at $BSR < 1$, the generated lift and drag forces are near zero at these positions and the generation of positive torque is limited.

In comparison, the MRL blade motion results in near-peak, or peak, lift and drag forces being developed at the locations of maximum conversion into tangential force. This occurs as the angle of attack varies in the range $0° < \alpha < 90°$ throughout a turbine cycle, compared to a maximum of approximately $\alpha < 18°$ for the Darrieus turbine.

The wide range of angle of attack values also results in a wide range of pitch rates occurring during the cycle. The pitch rates are also generally higher than the Darrieus turbine. As shown in Chapter 4, the magnitude of peak lift and drag coefficients generally increase with pitch rate, and this mechanism likely contributes significantly to the generation of high forces and torque driving the MRL turbine.

However, the relatively slow rotational speed also results in low relative flow velocities, compared to Darrieus turbines. This has a significant effect, as the magnitude of developed lift and drag force increases with the square of flow velocity. This offsets the advantage the MRL turbine holds in terms of conversion of forces into useful torque.

Operation in the range $0 < BSR < 1$ also results in wider variations in relative flow velocity, compared to Darrieus turbines operating in the range $3 < BSR < 7$. For example the MRL turbine operating at $BSR = 0.5$ develops values in the range $1.5U_0 > U_R > 0.5U_0$ (ignoring the inevitable reduction in flow velocity that occurs upstream of the turbine). This generally results in higher magnitudes of generated lift force in comparison to drag force, due to the angular location each is predominantly generated at. The generation of drag force (where relative velocity magnitude is lowest) is also most affected by induction factor, i.e., the reduction of upstream flow velocity due to energy extraction at the turbine.

However, the CFD results indicate that drag forces do make a significant contribution to driving torque, especially at lower BSR value (e.g., $BSR = 0.3$),

where relative flow velocity remains high at the mid-cycle position. This drag force contributes to high cycle-mean torque generated by a single blade. This is in contrast to the Darrieus turbine, where there is a large variation between maximum and minimum blade torque values during a cycle, as peak lift forces are only generated once each half-cycle.

6.2.3.3 Mechanical considerations

There are a number of challenges posed to the mechanical design of a real MRL turbine, as discussed below.

The relatively low rotational speeds and related high levels of torque developed by MRL turbine have consequences for drive-trains linking the turbine to an electricity generator. In particular, the transfer of high torque and forces through the gearbox may contribute to high levels of wear and increase maintenance costs in comparison to the Darrieus design.

The MRL blade motion requires that individual blades rotate and this rotation is controlled reliably. Such mechanisms are liable to wear, especially in harsh ocean or river environments, and would likely give rise to additional maintenance costs in comparison to fixed-blade Darrieus turbines.

The CFD thrust coefficient results indicate that significantly high cycle-mean forces act on the turbine, particularly in the direction of flow. These forces have a direct impact on mooring requirements, and are therefore an important consideration when planning deployment of a real turbine. At the peak power operating point, the simulations gave a minimum x-direction thrust coefficient of $C_{T,x} \approx 0.8$, which is similar to Darrieus turbines operating at peak performance (Gretton et al., 2009). Z-direction thrust can also be significant, due to the asymmetry of blade motion and developed forces. For example, at peak power operating speed, the simulations gave an optimum value of $C_{T,z} \approx -0.2$. It should also be noted that these coefficients represent the mean forces acting on the turbine during one cycle, and peak instantaneous forces are expected to be significantly higher.

6.2.3.4 Design improvements

The CFD results indicate that lower solidity turbines give better performance, in terms of increased power and reduced thrust magnitudes. This is likely due to

a reduction in induction factor, i.e., higher flow velocities and lower pressure at the turbine due to reduced blockage by the blades. Higher flow velocities lead to higher generated forces and torque, and this compensates for the reduction in blade surface area related to reduced solidity. This is particularly important for blades in the second half-cycle, where lower upstream blockage allows higher velocities to reach downstream blades.

The MRL blade motion could be adapted, with a variable pitch mechanism. By further controlling the variation of angle of attack throughout the complete cycle, the magnitude of developed forces could be increased and/or the contribution of developed forces to useful torque could be increased. This may allow the turbine to operate at peak performance over a wide range of blade speed ratios, and in a wide range of operating conditions.

6.3 Further work

The work presented in this study can be improved and expanded upon in a number of ways. The following sections discuss recommendations for further experimental and computational investigation of the MRL turbine design.

6.3.1 Experimental work

The reliability of the physical experiments can be greatly improved, which would allow greater confidence in the study conclusions. It is suggested a higher aspect ratio turbine model is built and tested in a low blockage flume. The frontal area of the blade-pitch control mechanism should be minimised, possibly with use of a low profile gear system. This should also reduce the inherent resistance provided by the model and allow a greater range of total resistance to be controlled. More advanced systems for measuring and/or controlling the total resistance torque would also reduce the uncertainty of results.

Further experimental work employing flow visualisation techniques (e.g. particle image velocimetry) in order to analyse the time-varying flow structure within the turbine volume would be highly valuable. This would enable time-dependent validation of the vortex shedding behaviour predicted by the CFD simulations.

6.3.2 Computational work

The computational model can be further developed by incorporating the full support structure of the experimental turbine. This would require modelling of the full span width, due to the asymmetry of the model, and would be highly expensive. It may also be difficult to achieve, due to the difficulty of generating reliable meshes at the interface between the blade ends and end plates (which rotate in relation to each other).

The current three-dimensional CFD model could also be developed with use of a detached-eddy simulation (DES) approach to modelling turbulence. The $k-\omega$ SST sustain RANS model could be used near blade-surfaces and LES elsewhere. This may model the behaviour and breakdown of three-dimensional detached eddies more accurately. This would likely affect the total torque output of the simulation, especially at lower values of *BSR* where detached eddies have a strong influence.

Two-dimensional simulations could also be further developed with more advanced, or alternative, RANS models. For example, use of the $k-\varepsilon$ RNG or transitional SST models could be investigated in simulations of pitching flat plates. If lift and drag results from these simulations were to more successfully match the pitching plate data, further simulations of the MRL turbine would be justified.

A number of further geometry variations can also be simulated. These include the use of side plates, as in the physical experiments, and the effect of plate size and proximity should be investigated. The effect of varying inlet conditions, such as flow direction and consistency could also be investigated. Design improvements such as further investigation of the effects of solidity, or variable pitch rate, could be investigated.

If confidence in the two-dimensional simulations is improved, the simulations can be developed by increasing the downstream length of the domain and allowing the wake to fully develop. This would allow comparison to the gathered experimental wake results and the results of CFD simulations undertaken by other researchers (i.e. Gebreslassie et al.)

This page is intentionally left blank.

BIBLIOGRAPHY

T. A. Adcock, S. Draper, G. T. Houlsby, A. G. Borthwick, and S. Serhadlıoğlu. The available power from tidal stream turbines in the Pentland Firth. In *Proc. R. Soc. A*, volume 469, page 20130072. The Royal Society, 2013.

J. V. Akwa, H. A. Vielmo, and A. P. Petry. A review on the performance of Savonius wind turbines. *Renewable and Sustainable Energy Reviews*, 16 (5):3054--3064, 2012.

A. Alaimo, A. Esposito, A. Messineo, C. Orlando, and D. Tumino. 3D CFD analysis of a vertical axis wind turbine. *Energies*, 8(4):3013--3033, 2015.

K. M. Almohammadi, D. B. Ingham, L. Ma, and M. Pourkashanian. Effect of transitional turbulence modelling on a straight blade vertical axis wind turbine. In *Alternative Energies*, pages 93--112. Springer, 2013a.

K. M. Almohammadi, D. Ingham, L. Ma, and M. Pourkashanian. CFD sensitivity analysis of a straight-blade vertical axis wind turbine. *Wind Engineering*, 36 (5):571--588, 2012.

K. Almohammadi, D. Ingham, L. Ma, and M. Pourkashan. Computational fluid dynamics (CFD) mesh independency techniques for a straight blade vertical axis wind turbine. *Energy*, 58:483--493, 2013b.

S. V. Amaral, M. S. Bevelhimer, G. F. Čada, D. J. Giza, P. T. Jacobson, B. J. McMahon, and B. M. Pracheil. Evaluation of behavior and survival of fish exposed to an axial-flow hydrokinetic turbine. *North American journal of fisheries management*, 35(1):97--113, 2015.

E. Amet, T. Maître, C. Pellone, and J.-L. Achard. 2D numerical simulations of blade-vortex interaction in a Darrieus turbine. *Journal of fluids engineering*, 131(11):111103, 2009.

M. M. Aslam Bhutta, N. Hayat, A. U. Farooq, Z. Ali, S. R. Jamil, and Z. Hussain. Vertical axis wind turbine--a review of various configurations and design techniques. *Renewable and Sustainable Energy Reviews*, 16(4):1926--1939, 2012.

M. T. Asr, E. Z. Nezhad, F. Mustapha, and S. Wiriadidjaja. Study on start-up characteristics of H-Darrieus vertical axis wind turbines comprising NACA 4-digit series blade airfoils. *Energy*, 112:528--537, 2016.

F. Balduzzi, A. Bianchini, E. A. Carnevale, L. Ferrari, and S. Magnani. Feasibility analysis of a Darrieus vertical-axis wind turbine installation in the rooftop of a building. *Applied Energy*, 97:921--929, 2012.

F. Balduzzi, A. Bianchini, R. Maleci, G. Ferrara, and L. Ferrari. Critical issues in the CFD simulation of Darrieus wind turbines. *Renewable Energy*, 85: 419--435, 2016.

H. Beri and Y. Yao. Effect of camber airfoil on self starting of vertical axis wind turbine. *Journal of Environmental Science and Technology*, 4(3):302--312, 2011a.

H. Beri and Y. Yao. Computational analysis of vertical axis wind turbine with open-able airfoil. In *Power and Energy Engineering Conference (APPEEC), Asia-Pacific*, pages 1--5. IEEE, 2011b.

M. Bhargav, V. R. Kishore, and V. Laxman. Influence of fluctuating wind conditions on vertical axis wind turbine using a three dimensional CFD model. *Journal of Wind Engineering and Industrial Aerodynamics*, 158:98--108, 2016.

P. Bradshaw. The turbulence structure of equilibrium boundary layers. *Journal of Fluid Mechanics*, 29(04):625--645, 1967.

T. Burton, N. Jenkins, D. Sharpe, and E. Bossanyi. *Wind energy handbook*. John Wiley & Sons, 2011.

T. J. Carrigan, B. H. Dennis, Z. X. Han, and B. P. Wang. Aerodynamic shape optimization of a vertical-axis wind turbine using differential evolution. *ISRN Renewable Energy*, 2012:528418, 2012.

L. Cea, J. Puertas, and L. Pena. Velocity measurements on highly turbulent free surface flow using ADV. *Experiments in Fluids*, 42(3):333--348, 2007.

J. Chapman, I. Masters, M. Togneri, and J. Orme. The Buhl correction factor applied to high induction conditions for tidal stream turbines. *Renewable energy*, 60:472--480, 2013.

A. M. Chowdhury, H. Akimoto, and Y. Hara. Comparative CFD analysis of vertical axis wind turbine in upright and tilted configuration. *Renewable Energy*, 85:327--337, 2016.

W. G. Cochran. The flow due to a rotating disc. *Mathematical Proceedings of the Cambridge Philosophical Society*, 30:365--375, July 1934.

P. Cooper and O. C. Kennedy. Development and analysis of a novel vertical axis wind turbine. Technical report, University of Wollongong, 2004.

C. Croarkin and P. Tobias. NIST/SEMATECH e-handbook of statistical methods. *Available online: http://www.itl.nist.gov/div898/handbook*, 2006.

J. W. Daily and R. E. Nece. Chamber dimension effects on induced flow and frictional resistance of enclosed rotating disks. *Journal of Fluids Engineering*, 82:217--230, March 1960.

L. Daróczy, G. Janiga, K. Petrasch, M. Webner, and D. Thévenin. Comparative analysis of turbulence models for the aerodynamic simulation of H-Darrieus rotors. *Energy*, 90:680--690, 2015.

G. Darrieus. Turbine having its rotating shaft transverse to the flow of the current, December 1931. US Patent 1,835,018.

P.-L. Delafin, T. Nishino, A. Kolios, and L. Wang. Comparison of low-order aerodynamic models and RANS CFD for full scale 3D vertical axis wind turbines. *Renewable Energy*, 109:564--575, 2017.

D. L. Donoho and J. M. Johnstone. Ideal spatial adaptation by wavelet shrinkage. *Biometrika*, 81(3):425--455, 1994.

M. Elkhoury, T. Kiwata, and E. Aoun. Experimental and numerical investigation of a three-dimensional vertical-axis wind turbine with variable-pitch. *Journal of Wind Engineering and Industrial Aerodynamics*, 139:111--123, 2015.

S. Eriksson, H. Bernhoff, and M. Leijon. Evaluation of different turbine concepts for wind power. *Renewable and Sustainable Energy Reviews*, 12(5):1419--1434, 2008.

E. Esmailian, H. Ghassemi, and S. A. Heidari. Numerical investigation of the performance of Voith Schneider propulsion. *American Journal of Marine Science*, 2(3):58--62, 2014.

P. Farrell and J. Maddison. Conservative interpolation between volume meshes by local Galerkin projection. *Computer Methods in Applied Mechanics and Engineering*, 200(1):89--100, 2011.

C. S. Ferreira, H. Bijl, G. van Bussel, and G. van Kuik. Simulating dynamic stall in a 2D VAWT: modeling strategy, verification and validation with particle image velocimetry data. In *Journal of Physics: Conference Series*, 75. IOP Publishing, 2007. The Science of Making Torque from Wind.

C. Frid, E. Andonegi, J. Depestele, A. Judd, D. Rihan, S. I. Rogers, and E. Kenchington. The environmental interactions of tidal and wave energy generation devices. *Environmental Impact Assessment Review*, 32(1):133--139, 2012.

D. Frölich, B. Magyar, and B. Sauer. A comprehensive model of wear, friction and contact temperature in radial shaft seals. *Wear*, 311(1):71--80, 2014.

R. E. Froude. On the part played in propulsion by differences of fluid pressure. *Trans. Inst. Naval Architects*, 30:390, 1889.

L. Gagnon, G. Quaranta, M. Morandini, P. Masarati, M. Lanz, C. M. Xisto, and J. C. Páscoa. Aerodynamic and aeroelastic analysis of a cycloidal rotor. *AIAA Paper 2014-2450*, (2014-2450), 2014.

M. G. Gebreslassie, G. R. Tabor, and M. R. Belmont. CFD simulations for sensitivity analysis of different parameters to the wake characteristics of tidal turbine. *Open Journal of Fluid Dynamics*, 2:56, 2012.

M. G. Gebreslassie, G. R. Tabor, and M. R. Belmont. Numerical simulation of a new type of cross flow tidal turbine using OpenFOAM--part I: Calibration of energy extraction. *Renewable Energy*, 50:994--1004, 2013a.

M. G. Gebreslassie, G. R. Tabor, and M. R. Belmont. Numerical simulation of a new type of cross flow tidal turbine using OpenFOAM--part II: Investigation of turbine-to-turbine interaction. *Renewable Energy*, 50:1005--1013, 2013b.

M. G. Gebreslassie, M. R. Belmont, and G. R. Tabor. Comparison of analytical and CFD modelling of the wake interactions of tidal turbines. University of Exeter, 2014.

M. G. Gebreslassie, G. R. Tabor, and M. R. Belmont. Investigation of the performance of a staggered configuration of tidal turbines using CFD. *Renewable Energy*, 80:690--698, 2015.

M. G. Gebreslassie, S. O. Sanchez, G. R. Tabor, M. R. Belmont, T. Bruce, G. S. Payne, and I. Moon. Experimental and CFD analysis of the wake characteristics of tidal turbines. *International Journal of Marine Energy*, 16: 209--219, 2016.

D. G. Goring and V. I. Nikora. Despiking acoustic Doppler velocimeter data. *Journal of Hydraulic Engineering*, 128(1):117--126, 2002.

D. G. Goring and V. I. Nikora. Closure to depiking acoustic Doppler velocimeter data by Derek G. Goring and Vladimir I. Nikora. *Journal of Hydraulic Engineering*, 129(6):487--488, 2003.

J. Gorle, L. Chatellier, F. Pons, and M. Ba. Flow and performance analysis of H-Darrieus hydroturbine in a confined flow: A computational and experimental study. *Journal of Fluids and Structures*, 66:382--402, 2016.

A. M. Gorlov. Unidirectional helical reaction turbine operable under reversible fluid flow for power systems, September 1995. US Patent 5,451,137.

K. O. Granlund, M. V. Ol, and L. P. Bernal. Unsteady pitching flat plates. *Journal of Fluid Mechanics*, 733:R5, 2013.

G. I. Gretton, T. Bruce, and D. M. Ingram. Hydrodynamic modelling of a vertical axis tidal current turbine using CFD. In *Proceedings of the 8th European Wave and Tidal Energy Conference*, pages 468--476, Uppsala, Sweden, 2009.

M. S. Güney and K. Kaygusuz. Hydrokinetic energy conversion systems: A technology status review. *Renewable and Sustainable Energy Reviews*, 14 (9):2996--3004, 2010.

R. Gupta and A. Biswas. Computational fluid dynamics analysis of a twisted three-bladed H-Darrieus rotor. *Journal of Renewable and Sustainable Energy*, 2(4):043111, 2010.

M. Hansen and D. Sørensen. CFD model for a vertical axis wind turbine. In *Wind Energy for the New Millenium - Proceedings of the European Wind Energy Conference*, Copenhagen, Denmark, 2001.

E. Hau. *Wind turbines: fundamentals, technologies, application, economics*. Springer Science & Business Media, 2013.

L. A. Horve. Understanding the sealing mechanism of the radial lip seal for rotating shafts. In *Fluid Sealing*, pages 5--19. Springer Netherlands, 1992.

W. G. Howe. Two-sided tolerance limits for normal populations-some improvements. *Journal of the American Statistical Association*, 64(326):610--620, 1969.

R. Howell, N. Qin, J. Edwards, and N. Durrani. Wind tunnel and numerical study of a small vertical axis wind turbine. *Renewable Energy*, 35(2):412--422, 2010.

I. S. Hwang, Y. H. Lee, and S. J. Kim. Optimization of cycloidal water turbine and the performance improvement by individual blade control. *Applied Energy*, 86(9):1532--1540, 2009.

IEA. CO_2 emissions from fuel combustion. Technical report, International Energy Agency, Paris, France, 2016a.

IEA. Key world energy statistics. Technical report, International Energy Agency, Paris, France, 2016b.

IEA. Energy, climate change & environment 2016 insights. Technical report, International Energy Agency, Paris, France, 2016c.

M. Islam, D. S.-K. Ting, and A. Fartaj. Aerodynamic models for Darrieus-type straight-bladed vertical axis wind turbines. *Renewable and Sustainable Energy Reviews*, 12(4):1087--1109, 2008.

R. I. Issa. Solution of the implicitly discretised fluid flow equations by operator-splitting. *Journal of computational physics*, 62(1):40--65, 1986.

P. Jain and A. Abhishek. Performance prediction and fundamental understanding of small scale vertical axis wind turbine with variable amplitude blade pitching. *Renewable Energy*, 97:97--113, 2016.

A. P. Janssen and M. R. Belmont. Initial research phase of MRL turbine. Project summary technical report 200064, Project No. MO 562L, 2009.

M. Jesson, M. Sterling, and J. Bridgeman. Despiking velocity time-series--optimisation through the combination of spike detection and replacement-methods. *Flow Measurement and Instrumentation*, 30:45--51, 2013.

X. Jin, G. Zhao, K. Gao, and W. Ju. Darrieus vertical axis wind turbine: Basic research methods. *Renewable and Sustainable Energy Reviews*, 42:212--225, 2015.

M. J. Khan, G. Bhuyan, M. T. Iqbal, and J. E. Quaicoe. Hydrokinetic energy conversion systems and assessment of horizontal and vertical axis turbines for river and tidal applications: A technology status review. *Applied Energy*, 86(10):1823--1835, 2009.

B. Khorsandi, L. Mydlarski, and S. Gaskin. Noise in turbulence measurements using acoustic Doppler velocimetry. *Journal of Hydraulic Engineering*, 138 (10):829--838, 2012.

B. K. Kirke and L. Lazauskas. Limitations of fixed pitch Darrieus hydrokinetic turbines and the challenge of variable pitch. *Renewable Energy*, 36(3):893--897, 2011.

A. N. Kolmogorov. The local structure of turbulence in incompressible viscous fluid for very large Reynolds numbers. In *Dokl. Akad. Nauk SSSR*, volume 30, pages 299--303, 1941.

L. I. Lago, F. L. Ponta, and L. Chen. Advances and trends in hydrokinetic turbine systems. *Energy for Sustainable Development*, 14(4):287--296, 2010.

H. Lamb. *Hydrodynamics*. Cambridge University Press, 6 edition, 1932.

R. Lanzafame, S. Mauro, and M. Messina. 2D CFD modeling of H-Darrieus wind turbines using a transition turbulence model. *Energy Procedia*, 45:131--140, 2014.

H. Larsen. Summary of a vortex theory for the cyclogiro. In *Proceedings of the 2nd US National conference on Wind Engineering Research.(1975-8), Colorad State University*, volume 8, page 1, 1975.

B. E. Launder and D. Spalding. The numerical computation of turbulent flows. *Computer methods in applied mechanics and engineering*, 3(2):269--289, 1974.

N. D. Laws and B. P. Epps. Hydrokinetic energy conversion: Technology, research, and outlook. *Renewable and Sustainable Energy Reviews*, 57: 1245 -- 1259, 2016. ISSN 1364-0321.

Y.-T. Lee and H.-C. Lim. Numerical study of the aerodynamic performance of a 500W Darrieus-type vertical-axis wind turbine. *Renewable Energy*, 83: 407--415, 2015.

J. G. Leishman. Challenges in modelling the unsteady aerodynamics of wind turbines. *Wind energy*, 5(2-3):85--132, 2002.

C. Li, S. Zhu, Y.-l. Xu, and Y. Xiao. 2.5D large eddy simulation of vertical axis wind turbine in consideration of high angle of attack flow. *Renewable energy*, 51:317--330, 2013.

K. Lu, Y. Xie, and D. Zhang. Numerical study of large amplitude, nonsinusoidal motion and camber effects on pitching airfoil propulsion. *Journal of Fluids and Structures*, 36:184--194, 2013.

D. MacPhee and A. Beyene. Recent advances in rotor design of vertical axis wind turbines. *Wind Engineering*, 36(6):647--666, 2012.

B. MacVicar, S. Dilling, and J. Lacey. Multi-instrument turbulence toolbox (MITT): Open-source MATLAB algorithms for the analysis of high-frequency flow velocity time series datasets. *Computers & Geosciences*, 73:88--98, 2014.

T. Maître, E. Amet, and C. Pellone. Modeling of the flow in a Darrieus water turbine: Wall grid refinement analysis and comparison with experiments. *Renewable Energy*, 51:497--512, 2013.

J. F. Manwell, J. G. McGowan, and A. L. Rogers. *Wind energy explained: theory, design and application*. John Wiley & Sons, 2010.

Z. Mao, W. Tian, and S. Yan. Influence analysis of blade chord length on the performance of a four-bladed Wollongong wind turbine. *Journal of Renewable and Sustainable Energy*, 8(2):023303, 2016.

C. Masson, J. Johansen, N. Sorensen, F. Zahle, C. Bak, H. Madsen, E. Politis, G. Schepers, K. Lindenburg, H. Snel, et al. IEA wind annex XX: HAWT aerodynamic and models from wind tunnel measurements-final report. Technical report, National Renewable Energy Laboratory, 2008.

I. Masters, A. Williams, T. N. Croft, M. Togneri, M. Edmunds, E. Zangiabadi, I. Fairley, and H. Karunarathna. A comparison of numerical modelling techniques for tidal stream turbine analysis. *Energies*, 8(8):7833--7853, 2015.

K. McLaren, S. Tullis, and S. Ziada. Computational fluid dynamics simulation of the aerodynamics of a high solidity, small-scale vertical axis wind turbine. *Wind Energy*, 15(3):349--361, 2012.

J. McNaughton, F. Billard, and A. Revell. Turbulence modelling of low Reynolds number flow effects around a vertical axis turbine at a range of tip-speed ratios. *Journal of Fluids and Structures*, 47:124--138, 2014.

F. R. Menter. Two-equation eddy-viscosity turbulence models for engineering applications. *AIAA journal*, 32(8):1598--1605, August 1994.

F. R. Menter. Review of the shear-stress transport turbulence model experience from an industrial perspective. *International Journal of Computational Fluid Dynamics*, 23(4):305--316, 2009.

F. R. Menter, M. Kuntz, and R. Langtry. Ten years of industrial experience with the SST turbulence model. In *Turbulence, Heat and Mass Transfer 4*, Antalya, Turkey, October 2003.

F. Menter. Influence of freestream values on k-omega turbulence model predictions. *AIAA journal*, 30(6):1657--1659, 1992.

M. Mohamed, A. Ali, and A. Hafiz. CFD analysis for H-rotor Darrieus turbine as a low speed wind energy converter. *Engineering Science and Technology, an International Journal*, 18(1):1--13, 2015.

F. O Rourke, F. Boyle, and A. Reynolds. Tidal energy update 2009. *Applied Energy*, 87(2):398--409, 2010.

M. V. Ol. The high-frequency, high-amplitude pitch problem: Airfoils, plates and wings. In *39th AIAA Fluid Dynamics Conference*, number AIAA 2009-3686, San Antonio, TX, USA, jun 2009.

R. K. Pachauri, M. R. Allen, V. Barros, J. Broome, W. Cramer, R. Christ, J. Church, L. Clarke, Q. Dahe, P. Dasgupta, et al. *Climate change 2014: Synthesis Report. Contribution of working groups I, II and III to the fifth assessment report of the intergovernmental panel on climate change*. IPCC, 2014.

I. Paraschivoiu. Double-multiple streamtube model for studying vertical-axis wind turbines. *Journal of propulsion and power*, 4(4):370--377, 1988.

I. Paraschivoiu. *Wind turbine design: with emphasis on Darrieus concept*. Presses inter Polytechnique, 2002.

H. C. Parker. *Rotary Seal Design Guide*. Parker Hannifin Corporation, 2006.

M. Parsheh, F. Sotiropoulos, and F. Porté-Agel. Estimation of power spectra of acoustic-Doppler velocimetry data contaminated with intermittent spikes. *Journal of Hydraulic Engineering*, 136(6):368--378, 2010.

S. V. Patankar and D. B. Spalding. A calculation procedure for heat, mass and momentum transfer in three-dimensional parabolic flows. *International journal of heat and mass transfer*, 15(10):1787--1806, 1972.

C. Pellone, T. Maitre, and E. Amet. 3D RANS modeling of a cross flow water turbine. In *Advances in Hydroinformatics*, Springer Hydrogeology, pages 405--418. Springer Singapore, 2014.

S. Plath, S. Meyer, and V. M. Wollesen. Friction torque of a rotary shaft lip type seal - a comparison between test results and finite element simulation. *Mechanika*, 4(54):55--59, 2005.

N. Qin, R. Howell, N. Durrani, K. Hamada, and T. Smith. Unsteady flow simulation and dynamic stall behaviour of vertical axis wind turbine blades. *Wind Engineering*, 35(4):511--528, 2011.

M. Raciti Castelli, A. Englaro, and E. Benini. The Darrieus wind turbine: Proposal for a new performance prediction model based on CFD. *Energy*, 36(8):4919--4934, 2011.

M. Raciti Castelli, S. De Betta, and E. Benini. Numerical investigation of the optimal spatial domain discretization for the 2-D analysis of a Darrieus vertical-axis water turbine. In *Proceedings of World Academy of Science,*

Engineering and Technology, number 64. World Academy of Science, Engineering and Technology, 2012a.

M. Raciti Castelli, S. De Betta, and E. Benini. Numerical analysis of the performance of a shrouded vertical-axis water turbine based on the NACA 0025 blade profile. In *Proceedings of World Academy of Science, Engineering and Technology*, number 63. World Academy of Science, Engineering and Technology, 2012b.

M. Raciti Castelli, S. De Betta, and E. Benini. Effect of blade number on a straight-bladed vertical-axis darreius wind turbine. *World Academy of Science, Engineering and Technology*, 61:305--3011, 2012c.

W. Rankine. On the mechanical principles of the action of propellers. *Trans. Inst. Naval Architects*, 6:13--39, 1865.

A. M. Roa, V. Aumelas, T. Maître, and C. Pellone. Numerical and experimental analysis of a Darrieus-type cross flow water turbine in bare and shrouded configurations. In *IOP Conference Series: Earth and Environmental Science*, volume 12. IOP Publishing, 2010.

A. Rossetti and G. Pavesi. Comparison of different numerical approaches to the study of the H-Darrieus turbines start-up. *Renewable Energy*, 50:7--19, 2013.

C. L. Rumsey and P. R. Spalart. Turbulence model behavior in low Reynolds number regions of aerodynamic flowfields. *AIAA journal*, 47(4):982--993, 2008.

SailPoweredEnergy. Design credentials. http://sailpoweredenergy.com/designcredentials.php. Accessed 25 October 2016.

S. Salter. Are nearly all tidal stream turbine designs wrong? In *4th International Conference on Ocean Energy. Dublin*, 2012.

B. Sanderse, S. Pijl, and B. Koren. Review of computational fluid dynamics for wind turbine wake aerodynamics. *Wind Energy*, 14(7):799--819, 2011.

S. J. Savonius. Rotor adapted to be driven by wind or flowing water, January 1929. US Patent 1,697,574.

H. Schlichting. *Boundary-Layer Theory*. McGraw-Hill, NY, USA, 7 edition, 1979.

A. Sengupta, A. Biswas, and R. Gupta. Studies of some high solidity symmetrical and unsymmetrical blade H-Darrieus rotors with respect to starting characteristics, dynamic performances and flow physics in low wind streams. *Renewable Energy*, 93:536--547, 2016.

D. Sharpe. A general momentum theory applied to an energy-extracting actuator disc. *Wind Energy*, 7(3):177--188, 2004.

R. E. Sheldahl and P. C. Klimas. Aerodynamic characteristics of seven symmetrical airfoil sections through 180-degree angle of attack for use in aerodynamic analysis of vertical axis wind turbines. Technical Report SAND80-2114, Sandia National Laboratories, Albuquerque, NM, USA, mar 1981.

P. R. Spalart and C. L. Rumsey. Effective inflow conditions for turbulence models in aerodynamic calculations. *AIAA journal*, 45(10):2544--2553, 2007.

M. J. L. Stakenborg. On the sealing mechanism of radial lip seals. *Tribology International*, 21(6):335--340, 1988.

J. H. Strickland and G. M. Graham. Force coefficients for a NACA-0015 airfoil undergoing constant pitchrate motions. *AIAA journal*, 25(4):622--624, 1987.

J. H. Strickland. Darrieus turbine: a performance prediction model using multiple streamtubes. Technical report, Sandia Labs., Albuquerque, N. Mex.(USA), 1975.

R. Templin. Aerodynamic performance theory for the NRC vertical-axis wind turbine. Technical report, National Aeronautical Establishment, Ottawa, Ontario (Canada), 1974.

H. Tennekes and J. L. Lumley. *A first course in turbulence*. MIT press, 1972.

G. Tescione, C. S. Ferreira, and G. van Bussel. Analysis of a free vortex wake model for the study of the rotor and near wake flow of a vertical axis wind turbine. *Renewable Energy*, 87:552--563, 2016.

T. Theodorsen and A. Regier. Experiments on drag of revolving disks, cylinders, and streamline rods at high speeds. Report 793, National Advisory Commitee for Aeronautics, 1944.

W. Tjiu, T. Marnoto, S. Mat, M. H. Ruslan, and K. Sopian. Darrieus vertical axis wind turbine for power generation I: Assessment of Darrieus VAWT configurations. *Renewable Energy*, 75:50--67, 2015.

A. Tummala, R. K. Velamati, D. K. Sinha, V. Indraja, and V. H. Krishna. A review on small scale wind turbines. *Renewable and Sustainable Energy Reviews*, 56:1351--1371, 2016.

R. Urbina, M. L. Peterson, R. W. Kimball, G. S. deBree, and M. P. Cameron. Modeling and validation of a cross flow turbine using free vortex model and a modified dynamic stall model. *Renewable Energy*, 50:662--669, 2013.

J. C. Vassberg. Revisiting the vertical-axis wind-turbine design using advanced computational fluid dynamics. In *43rd AIAA Aerospace Sciences Meeting*, number 2005-0047, Reno, NV, USA, 2005.

H. K. Versteeg and W. Malalasekera. *An introduction to computational fluid dynamics: the finite volume method*. Pearson Education, 2007.

M. R. Visbal and J. Shang. Investigation of the flow structure around a rapidly pitching airfoil. *AIAA journal*, 27(8):1044--1051, 1989.

T. Von Kármán. Über laminare und turbulente reibung. *Zeitschrift für Angewandte Mathematik und Mechanik*, 1(4):233--252, August 1921.

G. Voulgaris and J. H. Throwbridge. Evaluation of the acoustic doppler velocimeter (ADV) for turbulence measurements. *Journal of Atmospheric & Oceanic Technology*, 15:272--289, 1998.

T. L. Wahl. Discussion of despiking acoustic doppler velocimeter data by Derek G. Goring and Vladimir I. Nikora. *Journal of Hydraulic Engineering*, 129(6): 484--487, 2003.

S. Wang, M. Machado, A. Camacho, M. S. Gómez, and P. Escobar. Study on a low starting torque vertical axis wind turbine. In *The International Conference on Green Technologies*. National Pingtung University of Science and Technology, Pingtung, Taiwan, oct 2010.

F. M. White. *Fluid Mechanics*. McGraw-Hill, 6 edition, 2008.

D. C. Wilcox. Reassessment of the scale-determining equation for advanced turbulence models. *AIAA journal*, 26(11):1299--1310, 1988.

D. C. Wilcox. Comparison of two-equation turbulence models for boundary layers with pressure gradient. *AIAA journal*, 31(8):1414--1421, 1993.

M. H. Worstell. Aerodynamic performance of the 17-metre-diameter Darrieus wind turbine. Technical Report SAND78-1737, Sandia National Laboratories, Albuquerque, NM, USA, 1979.

M. H. Worstell. Aerodynamic performance of the 17-metre-diameter Darrieus wind turbine in the three-bladed configuration: An addendum. Technical Report SAND79-1753, Sandia National Laboratories, Albuquerque, NM, USA, 1980.

C. M. Xisto, J. C. Páscoa, J. A. Leger, P. Masarati, G. Quaranta, M. Morandini, L. Gagnon, D. Wills, and M. Schwaiger. Numerical modelling of geometrical effects in the performance of a cycloidal rotor. In *6th European Conference on Computational fluid dynamics*, 2014.

J. Zhang and J. N. Sørensen. Numerical modeling of vertical axis wind turbine (VAWT). Master's thesis, Technical University of Denmark, dec 2004.

L. Zhang, S. Zhang, K. Wang, X. Liu, and Y. Liang. Study on synchronous variable-pitch vertical axis wind turbine. In *Power and Energy Engineering Conference*, pages 1--5. IEEE, 2011.